THE FLAVOUR OF DARK MATTER

A SEARCH FOR DARK MATTER IN ASSOCIATION WITH A HIGGS BOSON DECAYING TO BOTTOM QUARKS WITH THE ATLAS DETECTOR

Proefschrift

ter verkrijging van de graad van doctor
aan de Radboud Universiteit Nijmegen
op gezag van de rector magnificus prof. dr. J. H. J. M. van Krieken,
volgens besluit van het college van decanen
in het openbaar te verdedigen op vrijdag 5 juni 2020
om 11:00 uur precies

door

VERONICA FABIANI

geboren op 8 december 1991
te Ascoli Piceno, Italië

PROMOTOREN — Prof. dr. N. DE GROOT
Dr. F. FILTHAUT

MANUSCRIPTCOMMISSIE — Prof. dr. P. G. JONKER
Prof. dr. R. H. P. KLEISS
Prof. dr. M. P. DECOWSKI (Universiteit van Amsterdam)
Dr. A. C. KÖNIG
Dr. C. J. M. NELLIST

The flavour of Dark Matter - A search for Dark Matter in association with a Higgs boson decaying to bottom quarks with the ATLAS detector
Thesis, Radboud University Nijmegen
ISBN: 978-94-028-2008-9
Cover design and printing by Ipskamp Printing

This work is part of the research programme of the Foundation for Fundamental Research on Matter (FOM), which is part of the Netherlands Organisation for Scientific Research (NWO).

"A chi è andato a vivere a Londra
Berlino, a Parigi, Milano, Bologna
ma le paure non han fissa dimora
le vostre svolte son sogni di gloria."

(The Zen Circus)

Contents

Preface

In the last decades, critical goals have been achieved by the whole scientific community towards a deeper understanding of our Universe. In the context of particle physics, the Standard Model (SM) has proved to be the most complete and valid theoretical model that is able to explain three of the four interactions among the fundamental constituents of matter. After a long series of breakthrough results, from the deep inelastic scattering experiments that revealed the internal structure of hadrons up to the discovery of the W/Z bosons and top quark, the last missing piece of the SM puzzle was added in 2012, when a new particle consistent with the Higgs boson predicted in the 1960s was discovered by the A Toroidal LHC ApparatuS (ATLAS) and Compact Muon Solenoid (CMS) experiments at the Large Hadron Collider (LHC), the largest particle accelerator in the world.

The discovery of the Higgs boson represented the most compelling proof of the validity of the SM. However, even after the inclusion of the Higgs boson, the SM of particle physics is in practice able to explain just about 5% of the whole Universe. The bulk of matter in our Universe is actually made of a non-luminous source of matter, commonly called Dark Matter (DM).

Although several astrophysical and cosmological measurements have proved in different ways the existence of an enormous amount of DM in the Universe, its nature is still unknown. Several properties, as the fact that it must have neutral electric charge, it must be stable (at least compared to the age of the Universe) and that it must interact very weakly with the SM particles, are inferred from such observations. Based on these findings, it is possible to probe the existence of DM with several detectors built on Earth or even attached to a satellite orbiting in the outer space. In particular, at the LHC, where head-on proton-proton collisions take place, the potential presence of DM particles, which do not interact with the detector, can be inferred by an imbalanced amount of energy (*missing energy*) in the plane that is transverse to the beam axis.

The main subject of this thesis is the search for DM signals in events with a SM Higgs boson decaying to b-quarks plus *missing energy* with the ATLAS detector at the LHC. This type of signature defines the mono-H($b\bar{b}$) final state.

The thesis is organised as follows.

Chapter 1 presents an overview of the most relevant aspects of the SM of particle physics. A brief description of the basic ingredients of the theoretical model is followed by a discussion about its current limitations concerning several phenomena that cannot be properly explained within the SM framework. Among those is the DM puzzle that represents the central theme of this thesis.

Chapter 2 is dedicated to the problem of DM. Starting from a review of the cosmological and astrophysical evidences for the existence of DM, some important aspects that characterise a potential DM particle candidate are examined. This discussion is aimed at setting the stage for a more detailed discussion about the search for DM through direct and indirect detection as well as collider experiments, such as the one led by the ATLAS experiment at the LHC.

Chapter 3 is aimed at describing the physics behind the pp collisions that take place at the LHC. First, the whole accelerator complex is described, then the key features of each component of the ATLAS multi-purpose detector are illustrated.

Chapter 4 consists in a summary of the most relevant techniques adopted for the reconstruction of the final state objects, arising from each pp collision occurring inside the ATLAS detector, that are relevant for the analysis presented in this thesis.

Chapter 5 is entirely dedicated to the description of the search for DM through the mono-H($b\bar{b}$) channel. First, the main features of the probed signal are illustrated. The most relevant aspects concerning the event selection, the estimation of the background and the final statistical analysis are then discussed in detail. My personal contribution to the results presented in this chapter comprises the implementation and validation of the 0ℓ Signal Region (SR) event selection in the analysis framework, the validation of the event selection across different versions of the ATLAS reconstruction software, the validation and optimisation studies related to the usage of Variable-Radius (VR) track jets in the *boosted* regime, including also the calibration of their b-tagging performance in data. Furthermore, I worked on a new estimate of the signal and background theory modelling uncertainties whose results are going to be used for the upcoming analysis of the full Run 2 dataset.

Chapter 6 describes in detail the method adopted in order to extract the b-tagging efficiency of VR track jets from pp collision data. All the material presented in this chapter represents entirely the results of the work I did in the context of the b-tagging calibration, aimed at commissioning the usage of VR track jets in the mono-H($b\bar{b}$) analysis.

Chapter 7 presents the results of a work aimed at reinterpreting the mono-H($b\bar{b}$) ATLAS results in the context of a new dark Higgs model through the usage of the Request Efficiency Computation for Alternative Signal Theories (RECAST) framework. My personal contribution to this work, in addition to sharing the knowledge about the mono-H($b\bar{b}$) analysis strategy, consists in a dedicated evaluation of the theory uncertainties on the new signal model.

Chapter 8 is aimed at giving a small taste of the future directions of the mono-H($b\bar{b}$) search towards the analysis of the data recorded by the ATLAS detector during the full Run 2 of the LHC. While the analysis is still in preparation, some aspects concerning several potential improvements are examined. For the work presented in this chapter, my personal contribution concerns the usage of the `DL1r` tagger as potential alternative b-tagging algorithm.

1 The Standard Model and beyond

The SM of particle physics represents the most robust and solid theory that nowadays is able to describe matter at the subatomic level. Its validity and robustness have been established by several experimental results culminating with the discovery of the Higgs boson at the LHC. In this chapter, the main aspects of the SM are presented and a dedicated examination of its current limitations is aimed at setting the stage for the discussion of the DM problem.

1.1 The Standard Model of particle physics

The SM of particle physics is the relativistic quantum field theory that describes all the fundamental constituents of matter as well as the interactions between them, with the exception of the gravitational force (whose magnitude is negligible at the subatomic scale that we have been able to probe so far). In the SM, the fundamental constituents of matter can be divided in two categories of fermion particles: *leptons* and *quarks*. They can interact via the *electromagnetic*, *weak* and *strong* forces by exchanging of particles with integer spin, called *gauge bosons*.

The SM is a Yang-Mills theory [1] based on the local gauge symmetry group $SU(2)_L \times U(1)_Y \times SU(3)_C$ where:

- $SU(2)_L$ is the *weak isospin* $\vec{I}$ symmetry group, whose three generators correspond to the three gauge fields W^1_μ, W^2_μ and W^3_μ,
- the $U(1)_Y$ group, whose corresponding gauge field is B_μ, is the *weak hypercharge* $Y = 2(Q - I_3)$ symmetry group, where Q is the electric charge and I_3 is the third component of the weak isospin vector,
- $SU(3)_C$ is the *colour* symmetry group which has eight generators, associated to eight *gluons*, and represents the strong interaction.

The label "L" for the $SU(2)_L$ group refers to the fact that the vector bosons mediating the charged weak interactions couple only to left-handed fermions[1].

[1] The right-handed and left-handed projections of a spin-1/2 field are determined by the action of the chirality operator $P_{R,L} = \frac{1}{2}(1 \pm \gamma^5)$, where $\gamma^5 \equiv i\gamma^0\gamma^1\gamma^2\gamma^3$ and γ^μ (μ=0,1,2,3) are the 4×4 Dirac matrices acting on the four dimensional spinor, representing the fermion field. In the massless case, the $P_{R,L}$ operators project the fermion field onto states of definite (positive or negative) *helicity*, which is represented by the operator $\vec{S} \cdot \hat{p}$, where $\vec{S} = \frac{1}{2}\vec{\Sigma} = \frac{1}{2}\begin{bmatrix} \vec{\sigma} & 0 \\ 0 & \vec{\sigma} \end{bmatrix}$, in which $\vec{\sigma}$ are the 2×2 Pauli matrices, and $\vec{p}$ is the momentum of the particle.

The theory describing the electromagnetic interactions is called Quantum ElectroDynamics (QED), initially formulated by Paul Dirac in the 1920s. The treatment of QED and weak interaction has been unified by Glashow [2], Weinberg [3] and Salam [4] who, thanks to this important contribution, were awarded the Nobel Prize in 1979. They suggested the $SU(2)_L \times U(1)_Y$ as the symmetry group for the *electroweak* force, such that the associated four gauge fields can be written as:

$$\begin{aligned} A_\mu &= B_\mu \cos\theta_W + W^3_\mu \sin\theta_W, \\ Z_\mu &= W^3_\mu \cos\theta_W - B_\mu \sin\theta_W, \\ W^\pm_\mu &= \frac{1}{\sqrt{2}}(W^1_\mu \pm W^2_\mu)s \end{aligned} \tag{1.1}$$

where $W^\pm_\mu$ and Z_μ are the massive vector bosons mediating, respectively, the charged current and the neutral current weak processes while A_μ represents the photon γ (massless) which is the mediator of the electromagnetic interactions. The $W^\pm$ bosons couple only with left-handed particles while the Z boson couples with both right-handed and left-handed particles. On the other hand, the coupling of the photon with the fermions is proportional to the fermion electric charge.

In Equation 1.1, the weak angle θ_W is defined by the couplings g and g' of $SU(2)_L$ and $U(1)_Y$:

$$\sin\theta_W = \frac{g'}{\sqrt{g^2 + g'^2}}, \tag{1.2}$$

$$\cos\theta_W = \frac{g}{\sqrt{g^2 + g'^2}}. \tag{1.3}$$

The electric charge can at this point be written as:

$$e = g\sin\theta_W = g'\cos\theta_W. \tag{1.4}$$

An overview of gauge bosons associated to each fundamental interaction is shown in Table 1.1.

In the SM, all the fermions (leptons and quarks) are arranged in different families. The left-handed fermions exist as $SU(2)_L$ doublets with $I = 1/2$, while the right-handed fermions are singlets ($I = 0$). The quarks exist in six flavours: *up*, *down*, *charm*, *strange*, *top* and *bottom*, and they are distinguished between up-type and down-type depending on the value of their electric charge:

$$\begin{pmatrix} u \\ d' \end{pmatrix}_L \quad \begin{pmatrix} c \\ s' \end{pmatrix}_L \quad \begin{pmatrix} t \\ b' \end{pmatrix}_L \qquad u_R \quad d_R \quad c_R \quad s_R \quad t_R \quad b_R.$$

where d', s' and b' are the weak eigenstates that are obtained from a rotation of the mass eigenstates d, s, b described by the Cabibbo-Kobayashi-Maskawa (CKM) matrix:

$$\begin{pmatrix} d' \\ s' \\ b' \end{pmatrix} = V_{CKM} \begin{pmatrix} d \\ s \\ b \end{pmatrix} \tag{1.5}$$

whose elements have absolute values corresponding to (values taken from Ref. [5]):

$$\begin{pmatrix} |V_{ud}| & |V_{us}| & |V_{ub}| \\ |V_{cd}| & |V_{cs}| & |V_{cb}| \\ |V_{td}| & |V_{ts}| & |V_{tb}| \end{pmatrix} \simeq \begin{pmatrix} 0.975 & 0.225 & 0.004 \\ 0.224 & 0.974 & 0.042 \\ 0.009 & 0.041 & 0.999 \end{pmatrix}. \tag{1.6}$$

Transitions between different quark generations can occur through the interaction with the $W^{\pm}$ bosons. Diagonal elements of the matrix, referring to transitions within the same family, are close to unity, while off-diagonal elements refer to transitions between different families which are suppressed.

The same categorisation is done also for leptons, which consist of the electron e, muon μ and τ lepton and their associated neutrinos:

$$\begin{pmatrix} e \\ \nu_e \end{pmatrix}_L \quad \begin{pmatrix} \mu \\ \nu_\mu \end{pmatrix}_L \quad \begin{pmatrix} \tau \\ \nu_\tau \end{pmatrix}_L \quad e_R \quad \mu_R \quad \tau_R.$$

It is worth noticing here that right-handed neutrinos (as well as left-handed anti-neutrinos) have not been observed so far in Nature, hence they are not included in the list of SM particles above.

For what concerns the strong sector, the theory describing the interaction between quarks and gluons is called Quantum ChromoDynamics (QCD). Gluons are electrically neutral and massless particles which carry the *colour* charge. Following the analogy to the primary colours used on our TV screen, the colour charge comes in three variants: "red", "green" and "blue". The three colours combined together yield a total null colour charge (a "white" state) and each anti-colour combined with the other two colours gives again a "white" state.

Interaction	Gauge Boson	Mass [GeV]	Charge
electromagnetic	photon (γ)	0	electric
weak	Z^0 $W^{\pm}$	~ 91.2 ~ 80.4	weak isospin
strong	8 gluons (g)	0	colour (r,g,b)

TABLE 1.1: Overview of the three fundamental forces described by the SM with their corresponding gauge bosons and charges.

Contrary to the photon, which is electrically neutral, gluons carry colour charge hence they can also interact among themselves. One of the most relevant differences of QCD with respect to QED is the dependence of their coupling constant on the energy scale. While QED coupling constant decreases at large distances (i.e. low energy) due to the screening of e^+e^- pairs of the vacuum, the QCD coupling constant shows the opposite behaviour and it decreases with the energy. At high energies, the strong coupling constant $\alpha_s(Q^2)$ can be approximated as:

$$\alpha_s(Q^2) = \frac{12\pi}{(33 - 2N_f)\ln\left(\frac{Q^2}{\Lambda^2_{QCD}}\right)} \tag{1.7}$$

where N_f is the number of flavours that are accessible at the chosen energy scale Q^2 and Λ_{QCD} corresponds to the non-perturbative scale of QCD.

The two main features of QCD are the:

- *confinement*: the colour is not an observable property of particles, so quarks and gluons cannot exist as isolated particles and they must combine together in order to produce colour neutral ("white") particles, the *hadrons*;
- *asymptotic freedom*: at high energies (i.e. short distances) the strong force becomes so weak that quarks and gluons behave as free point-like particles.

The confinement phenomenon, even if not yet proved mathematically, has a crucial role in the understanding of the hadron's structure. In fact, most of the hadrons known up to the present day appear either as a quark-antiquark pair (*mesons*) or as a three quarks state (*baryons*)[2]. Confinement has hence a direct impact on collider experiments: quarks and gluons produced in particle accelerators will always appear in the detector as a spray of several colour-neutral particles, which are usually referred to as *jets*. While a mathematical description of the colour confinement in QCD is still missing (at that low energy the perturbative treatment breaks down), asymptotic freedom has been explained by Gross, Wilczek [9] and Politzer [10] (Nobel Prizes in 2004) and successfully observed in deep inelastic scattering experiments.

1.1.1 The Higgs boson

The last missing piece of the SM theory is related to the problem of masses. We know, from several experimental results, that the $W^{\pm}$ and Z boson (as well as most of the fermions) are massive, however adding a mass term for the gauge bosons (and also for the fermions) explicitly in the Lagrangian density would break the local gauge invariance of the theory. Spontaneous electroweak symmetry breaking finally solved this problem through the *Brout-Englert-Higgs mechanism* [11, 12, 13, 14]. The power of this solution is in the fact that the mass terms are spontaneously originated, hence preserving the local gauge invariance.

The simplest realisation of this mechanism consists in adding a generic left-handed isospin complex scalar doublet to the SM Lagrangian:

$$\phi = \begin{pmatrix} \phi^+ \\ \phi^0 \end{pmatrix}, \qquad (I = 1/2, Y = 1) \tag{1.8}$$

where $\phi^+ = \frac{\phi_1(x)+i\phi_2(x)}{\sqrt{2}}$, $\phi^0 = \frac{\phi_3(x)+i\phi_4(x)}{\sqrt{2}}$ and $\phi_i(x)$ with i=1,...,4 are real scalar fields. The Lagrangian of the Higgs sector can then be written as:

$$\mathcal{L}_H = (D_\mu\phi)^\dagger(D^\mu\phi) - V(\phi) \tag{1.9}$$

where $V(\phi) = \mu^2\phi^\dagger\phi + \lambda(\phi^\dagger\phi)^2$ and D_μ is the covariant derivative of the field $\phi(x)$. The shape of the potential V depends on the parameters μ and λ. The parameter λ needs to be positive for the theory to remain stable. On the other hand, the sign of μ^2 is not defined a priori and can be either positive or negative. The vacuum state is the lowest energy state of the field ϕ and corresponds to the minimum of the potential $V(\phi)$. For $\mu^2 < 0$, the lowest energy state does not occur at $\phi = 0$ and the field is said to have a non-zero Vacuum Expectation Value (VEV), also named as v. Moreover, as shown in Figure 1.1, due to the symmetry of the potential, the vacuum state of the field is also degenerate. By choosing a particular minimum, the symmetry of the

[2]Actually, several "exotic" baryons with more than three valence quarks have been discovered in the recent years, for example the *tetraquark* state, named $Z(4430)$ [6, 7], and the two *pentaquark* states $P_c^+(4380)$ and $P_c^+(4450)$ [8]. Also a combination of such different number of quarks will result in a total null colour charge.

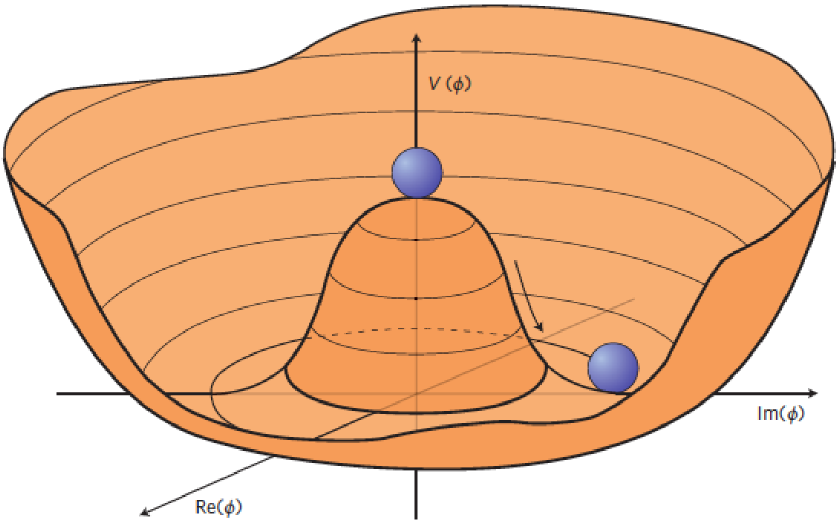

FIGURE 1.1: Schematic representation of the potential V of the scalar field ϕ in the case $\mu^2 < 0$. Figure taken from Ref. [15].

Lagrangian is spontaneously broken and the ground state can be written as:

$$\phi_0 = \langle 0|\phi|0\rangle = \frac{1}{\sqrt{2}}\begin{pmatrix}0\\ v\end{pmatrix}, \qquad v = \sqrt{\frac{-\mu^2}{\lambda}}. \tag{1.10}$$

The VEV can also be written as $(\sqrt{2}G_F)^{-1/2} = \frac{2M_W}{g}$ (where G_F is the reduced Fermi constant and g is the weak isospin coupling) and corresponds approximately to a value of 246 GeV. The particle states, which correspond to excitations of the field, can now be described by expanding the field ϕ around the minimum configuration. In order to do that, let us consider a small excitation of the complex scalar doublet (in unitary gauge):

$$\phi(x) = \frac{1}{\sqrt{2}}\begin{pmatrix}0\\ v + h(x)\end{pmatrix} \tag{1.11}$$

where the Higgs boson is represented by the real scalar $h(x)$ with a mass $m_h = \sqrt{2\lambda}v$. The Higgs mass m_h thus depends on μ and is a free parameter of the theory. As a consequence of this mechanism, mass terms for each of the electroweak gauge bosons originate spontaneously in the Lagrangian and the following relations are obtained:

$$m_W = \frac{1}{2}gv, \quad m_Z = \frac{1}{2}v\sqrt{g^2 + g'^2}, \quad m_\gamma = 0. \tag{1.12}$$

Hence the photon, which does not couple with the Higgs boson, remains massless. For what concerns the fermion masses instead, the interaction term between the Higgs doublet scalar field and the fermion fields gives rise to a mass term for each fermion f, which is proportional to their *Yukawa* coupling λ_f with the Higgs scalar field:

$$m_f = \frac{\lambda_f v}{\sqrt{2}} \tag{1.13}$$

which shows that the interaction of the Higgs boson with the fermions is proportional to the fermion mass. On 4 July 2012, the ATLAS [16] and CMS [17] experiments at Conseil Européen pour la Recherche Nucléaire (CERN) announced the observation of a new particle around the mass region of 125 GeV which was consistent with the SM Higgs boson, predicted by the theory. On 8 October 2013, François Englert and Peter W. Higgs were jointly awarded the Nobel Prize in Physics "for the theoretical discovery of a mechanism that contributes to our understanding of the origin of mass of subatomic particles", hence solving the last missing piece of the SM puzzle.

1.2 Limitations of the Standard Model

The discovery of the SM Higgs boson in 2012 represented a great achievement for the whole scientific community and allowed closing a chapter of the particle physics programme, which had lasted about 50 years, acknowledging the SM as the most complete and solid theoretical framework of particle physics. However, this cannot be the full story, as there are several phenomena that escape our comprehension and cannot be explained within the SM.

As already anticipated, the SM framework does not include gravity and this is already a severe limitation of the theory. It has also been discussed that the strong, weak and electromagnetic coupling constants depend on the energy; and at very high energy scales, around 10^{16} GeV, they have similar magnitudes. So how to reconcile this energy scale with the Planck scale ($\sim 10^{19}$ GeV) at which the gravitational effects cannot be neglected anymore? In particular, why does the Higgs boson mass (as the only dimensional parameter of the SM Lagrangian) happen to be so small compared to the Planck scale? This is usually referred to as the "hierarchy problem".

Moreover, if we assume that the SM can be interpreted as an effective field theory able to describe the physics up to a certain energy scale, the physical mass of the Higgs boson can be written as :

$$\mathrm{m}_h{}^2 = \mathrm{m}_h^{0\,2} + (\Delta\mathrm{m}_h)^2 \tag{1.14}$$

where m_h^0 is the *bare* Higgs boson mass and $\Delta\mathrm{m}_h$ represents the higher order corrections from fermion loops, which can be written as:

$$(\Delta\mathrm{m}_h)^2 = -\frac{|\lambda_f|^2}{8\pi^2}[\Lambda_{UV}^2 + ...] \tag{1.15}$$

in which λ_f represents the Yukawa coupling of the fermions with the Higgs field and Λ_{UV} is the ultraviolet cut-off energy scale of the theory (e.g. the Planck scale). Therefore for the Higgs mass to be finite at the electroweak scale, the bare mass should be set to a large value such that the resulting physical mass is at the measured value of 125 GeV. This is usually called the "fine-tuning" problem and at the present day is still considered an "accident" of the theory.

Another weakness of the SM concerns the neutrino sector. In the SM all the neutrinos are considered as massless particles, which is in contrast with the experimental observation of flavour oscillations (Nobel Prize to Kajita [18] and McDonald [19] in 2015). Therefore neutrinos do have a (even very tiny) mass and their oscillation is parametrised by the Pontecorvo-Maki-Nakagawa-Sakata (PMNS) matrix, similarly to the CKM matrix in the case of quarks. There should then be three mass eigenstates with two possible arrangements: the *normal* and the *inverted* hierarchy and in both of them there is a "doublet" of close mass states and a "lone" mass state. While our current knowledge about neutrinos is still very limited, several experiments are aiming at a direct measurement of the neutrinos masses and have provided an upper limit which is $\mathcal{O}$(eV).

Another big open question concerns the matter-antimatter asymmetry. It is evident that our Universe is dominated by matter, although it is a natural assumption that in the early instants after the Big Bang the amount of matter and antimatter should have been identical. Within the SM, the matter-antimatter asymmetry can be qualitatively explained by a violation of the CP symmetry. The CP symmetry refers to the combination of the charge conjugation C and parity P operators. The charge conjugation C transforms a particle into its anti-particle, while the parity P operation reflects the particle with respect to the origin of the space coordinates. In the SM, the existence of a complex phase in the CKM matrix implies a violation of the combined CP transformation (observed for the first time in the decay of neutral kaons in the 1960s, leading to the Nobel Prize in physics to Cronin [20] and Fitch [21] in 1980). Hence the particle-antiparticle asymmetry in our Universe might be explained by the fact that CP is not a symmetry of all fundamental interactions. However, the magnitude of the CP violation in the SM is not sufficient to explain this asymmetry, which still remains an unsolved problem.

Lastly, and probably most importantly, all the physics discussed in these pages, and successfully described by the SM, refers only to just about the 5% of the whole Universe. Cosmological and astrophysical observations are demonstrating that the rest of the Universe is made by Dark Energy (DE), that would be responsible for the accelerating expansion of the Universe, and DM, a non-luminous source of matter which seems not to interact with the "ordinary" matter described by the SM.

The most attentive reader would at this point notice, from the title of this thesis, that the search for DM is the main topic of this work, hence a dedicated discussion about the astrophysical and cosmological evidences as well as the current search strategies at the LHC will be discussed more extensively in Chapter 2.

2 Dark Matter

In the last decades, several astrophysical measurements have proved that we still do not know the origin of almost the 95% of the world around us. The matter successfully described by the SM only accounts for about the 5% of the whole Universe while the rest is made by DM ($\sim$ 24%) and DE ($\sim$ 71%) [22], whose nature is still unknown. Starting from the discussion of the most relevant astrophysical evidence for the existence of DM, this chapter presents an overview of the main features associated to it, as well as a discussion of the strategies behind the various searches for DM performed up to the present day.

2.1 Astrophysical evidence

The first evidence of the existence of a non-luminous source of matter in the Universe dates back to the 1930's, when Fritz Zwicky measured the velocity dispersion of the galaxies in the Coma Cluster [23]. He made use of the virial theorem to infer that galaxies cannot only be made by visible matter but a "dunkle materie" must also exist and should correspond to six times the amount of visible matter. Nevertheless, almost another 30 years must have passed before this important result was properly acknowledged. In the 1970's, Vera Rubin and others observed a constant rotation speed v as a function of the radius r beyond the visible disk. If galaxies were only made from visible matter, according to Kepler's Third Law, their rotation velocity should correspond to:

$$v(r) = \sqrt{\frac{GM(r)}{r}} \tag{2.1}$$

where $M(r) = 4\pi \int \rho(r) r^2 dr$, indicating with $\rho(r)$ the density of visible matter at a distance r from the galactic centre and with G the gravitational constant. Therefore, at distances larger than the radius of the galaxy the rotation curve is expected to decrease as $\frac{1}{\sqrt{r}}$, while experimental results showed a rotation curve which tends to be constant at higher distances. Hence, not only an additional source of mass is present beyond the visible disk, but its content must grow proportionally to r [24]. In the following years, such observations have been confirmed for a quite large sample of galaxies. An example is shown in Figure 2.1.

The content of DM in the Universe can also be inferred by studying how the light originating from a luminous source is deflected and distorted due to the large amount of matter between the source and the observer. This phenomenon, predicted

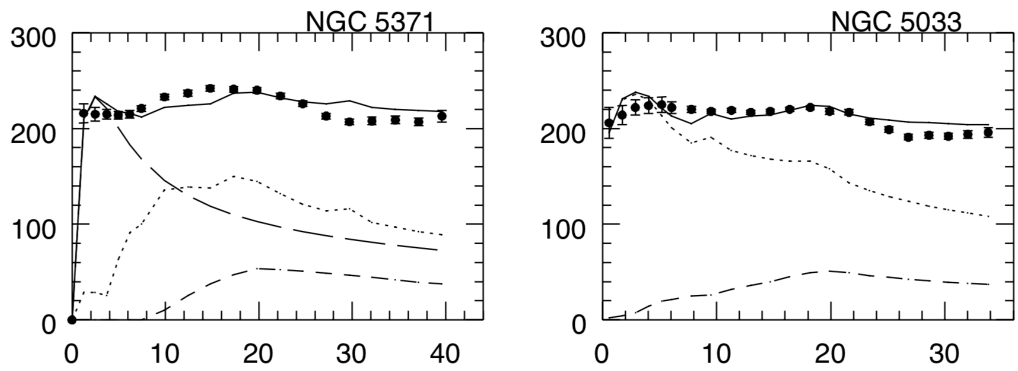

FIGURE 2.1: Rotation curve of galaxies NGC 5371 and NGC 5033. The radius (horizontal axis) is given in kpc and the rotation velocity (vertical axis) in km/s. The observed data are compared with the fitted MOdified Newtonian Dynamics (MOND) rotation curve (solid line) [25]. The other curves represent the Newtonian rotation curves of the various separate components: the long dashed curve is the rotation velocity resulting from a central bulge, if present, the short dashed line is the rotation curve of the gaseous disk, the dotted curve is that of the luminous disk. Figure taken from Ref. [26].

by Einstein's theory of general relativity, is called "gravitational lensing" and dedicated measurements of such effect can provide constraints on the density of DM in our Universe [27].

Perhaps one of the most spectacular applications of the gravitational lensing effect is the one related to the "Bullet Cluster". In 2003, the Chandra telescope [28] measured the mass distribution of this system of two colliding clusters of galaxies and found that the centre of total mass of galaxies was shifted with respect to the visible matter distribution (see Figure 2.2), suggesting once again that an additional non-luminous, and non-interacting, source of matter must also be present.

(a)

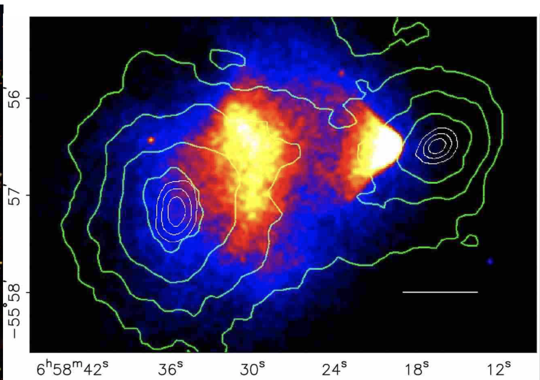

(b)

FIGURE 2.2: The Bullet Cluster (1E 0657-558). On the left, the pink regions correspond to the visible mass distribution of the cluster as measured by the Chandra X-ray Observatory [29, 28]. On the right, the green lines represent the gravitation lensing contours and the blue regions correspond to the inferred mass distribution due to the presence of DM [30].

2.2 The Dark Matter relic density

A quantity that is worth discussing is the abundance of DM remaining in the Universe after the Big Bang, at the present day. Usually, when thinking about a possible DM particle candidate, a distinction is made between the case in which DM is produced in collisions between particles of the thermal plasma in the early Universe (radiation-dominated era) or it is created non-thermally (for example from the decay of other particles, which themselves may or may not have a thermal abundance) during a phase transition.

In case of an initial state of thermal equilibrium, the evolution of the number density n_χ of DM particles χ, and the relative antiparticles $\bar{\chi}$, can be written as[1]:

$$\frac{dn_\chi}{dt} = -3Hn_\chi - \langle\sigma_A v\rangle(n_\chi^2 - (n_\chi^{\text{eq}})^2) \tag{2.2}$$

where $H \equiv \frac{\dot{a}}{a}$ is the Hubble parameter, which determines the expansion rate of the Universe, a is the scale factor of the Universe, σ_A is the $\chi\bar{\chi}$ annihilation cross-section (brackets denote thermal average), v is the relative speed of the annihilating DM particles and n_χ^{eq} is the number density at thermal equilibrium [31, 32]. For massive particles (i.e. non-relativistic limit), the number density at thermal equilibrium n_χ^{eq} can be expressed, following the Maxwell-Boltzmann approximation, as:

$$n_\chi^{\text{eq}} = g\left(\frac{m_\chi T}{2\pi}\right)^{3/2} e^{-m_\chi/T} \tag{2.3}$$

where g is the χ number of degrees of freedom. In order for the thermal equilibrium to take place, the interaction rate must be sufficiently larger than the expansion rate. Hence, already from Equation 2.2 it is possible to notice that if the expansion rate is much greater than the reaction rate, the first term dominates and Equation 2.2 becomes [33]:

$$\frac{dn_\chi}{dt} = -3Hn_\chi = -3\frac{\dot{a}}{a}n_\chi \quad \Rightarrow \quad \frac{d(n_\chi a^3)}{dt} = 0 \tag{2.4}$$

and n_χ falls as a^{-3}. Otherwise, if the reaction rate is large compared to the expansion rate, the derivative of the number density is negative if n_χ is greater than the equilibrium value n_χ^{eq}. In this case, the number density is a function of the temperature T and is pushed toward the equilibrium value. We can therefore distinguish two regimes:

$$\begin{aligned} n_\chi &\sim n_\chi(T) & T &\gg T_f \\ n_\chi a^3 &\sim \text{constant} & T &\ll T_f \end{aligned} \tag{2.5}$$

where T_f is usually called the “freeze-out” temperature at which the annihilation rate becomes equal to the expansion rate. Figure 2.3 shows an example of the numerical solution of the number density as a function of m/T (thus time).

The thermal relic density can finally be estimated by equating the annihilation rate and the expansion rate [33] and, once divided by the critical density ρ_c[2], it is

[1] Assuming that χ and $\bar{\chi}$ can only annihilate and be created in $\chi\bar{\chi}$ pairs and there is no particle-antiparticle asymmetry, i.e. $n_\chi = n_{\bar{\chi}}$.

[2] The critical density ρ_c is the value of the total energy density such that the Universe is spatially flat: $\rho_c \equiv \frac{3H^2}{8\pi G}$.

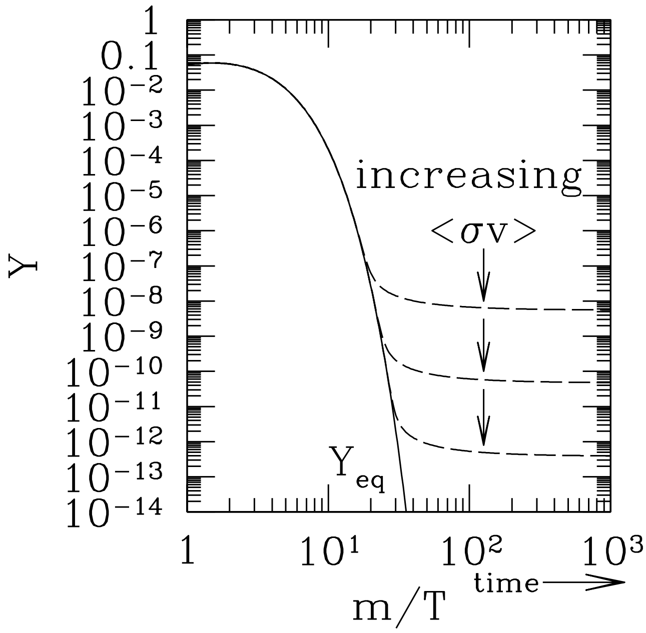

FIGURE 2.3: Typical evolution of the WIMP number density in the early Universe during the epoch of freeze-out. Figure taken from Ref. [34].

found to be:

$$\Omega_\chi h^2 \sim \frac{3 \times 10^{-37} \mathrm{cm}^3 s^{-1}}{\langle \sigma v \rangle} \tag{2.6}$$

where h is the rescaled Hubble constant $\left(h = H/(100\,\mathrm{km\,s^{-1}\,Mpc^{-1}})\right)$. It is possible to measure the value of Ω_χ, as well as the one of several other cosmological parameters, through the analysis the Cosmic Microwave Background (CMB), the primordial radiation of photons originated in the early Universe, predicted by George Gamow and others [35, 36, 37] in 1948 and "accidentally" discovered by Arno Penzias and Robert Wilson in 1965 (Nobel Prize in Physics in 1978). The study of the temperature fluctuations of the CMB is a powerful tool to derive stringent constraints on several cosmological parameters. The Planck satellite is dedicated to these measurements and from the position, shape and relative height of the "acoustic peaks" of the power spectrum, like the one shown on the right of Figure 2.4, can extract information about the amount of matter in the Universe. In particular, the second and third peaks provide a direct information about the amount of DM and DE in the Universe. The most recent results of the Planck collaboration are [38]:

$$\Omega_b h^2 = 0.02237 \pm 0.00015 \qquad \Omega_c h^2 = 0.1200 \pm 0.0012 \tag{2.7}$$

where $\Omega_b h^2$ is the baryon density and $\Omega_c h^2$ is the cold DM density.

Therefore, for cross-section values comparable with those of the weak interaction, Equation 2.6 yields a DM density of this order of magnitude. This is usually referred to as the "WIMP miracle". Moreover, from such calculations, the freeze-out seems to occur at $T_f \sim m_\chi/20$, which corresponds to a DM particle produced before the Big Bang Nucleosynthesis (BBN) era, which is the first one from which we have a trace. As a consequence, a possible discovery of DM would shed light, for the first time, on the pre-BBN era.

Nevertheless, it is important to notice that several assumptions went into the

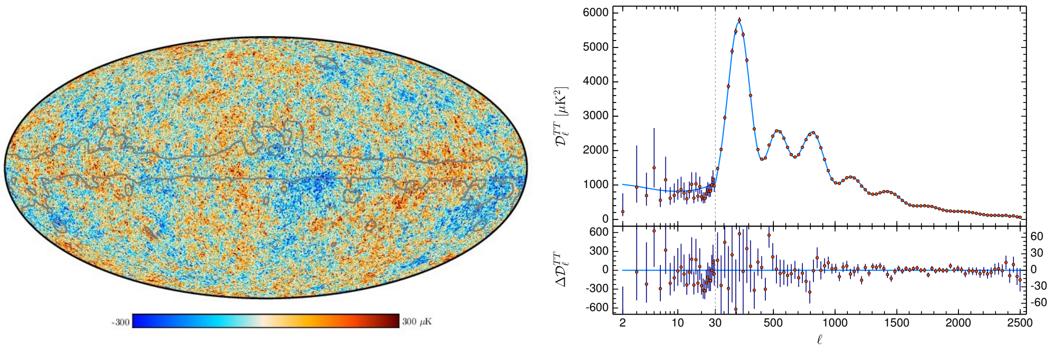

(a)

(b)

FIGURE 2.4: Temperature map of the CMB (on the left) and the Planck 2018 temperature power spectrum (on the right). Figures taken from Ref. [38, 22].

calculations presented above, among them the fact that DM is in thermal equilibrium and decouples when the Universe is radiation dominated, that there is no DM particle-antiparticle asymmetry and that DM particles are stable. Any deviation from these assumptions would change the DM relic density considerably. Furthermore, also the presence of an additional particle with similar mass and same quantum numbers of the DM particle can alter the result significantly. A more detailed discussion about these aspects can be found in Ref. [39]. It is therefore crucial to be aware of the caveats hiding behind our current knowledge in order to keep our minds as open as possible when thinking about a possible DM particle candidate, as discussed in the next section.

2.3 What do we know about Dark Matter?

Nowadays, several extensions of the SM of particle physics are able to provide their own DM candidate particle. A pragmatic approach consists in considering DM within a more general category of particles that are neutral, stable, non-relativistic and that can match the appropriate relic abundance. Particles fulfilling all these criteria are generally called Weakly Interactive Massive Particle (WIMP)s and in most of the Beyond Standard Model (BSM) theories the DM candidate falls into the WIMPs category.

In this context, one of the most famous theories is SUperSYmmetry (SUSY) in which a super-partner is associated to each SM particle with the same quantum numbers apart from the spin, which differs by half a unit. Therefore, the partners of fermions are bosons and viceversa. One of the most striking consequences of this new model is a solution of the fine-tuning problem (see Section 1.2) as the higher order corrections to the Higgs mass would have two contributions with opposite sign, one from the SM fermions and one from their super-symmetric partners, hence they cancel out each other exactly, and naturally.

Let us take a step back and have a deeper look at these properties in general.

Is DM neutral? The starting point is that DM is dark, i.e. non-luminous, because it does not seem to interact with light of any frequency. Hence DM must be neutral, or at least have a very small effective electric charge. It is possible to imagine that the DM particle is part of a “dark sector” and couples with a charge Q' to a dark photon and with charge $\epsilon Q'$ to the SM photon. This is the case of the so-called “Millicharged DM” [40]. Alternative models suggest instead a charged DM particle that has a sufficiently large mass preventing it from interacting electromagnetically [41]. This is the case of Charged Massive Particles (CHAMPs), discussed in Ref. [42], which would also solve several long-standing astrophysical problems, like the fact that the number of dwarf galaxies is orders of magnitude smaller than what expected from simulation (missing satellites problem [43]).

Is DM stable? In order to ensure its stability, the DM particle lifetime must exceed the present age of the Universe, which is about 4.3×10^{17} s (13.8 billion years). In several theories beyond the SM, the stability of DM is guaranteed by the presence of an additional symmetry that forbids the decay of DM into SM particles. For example, SUSY introduces a new symmetry, called R-parity, defined as:

$$R = (-1)^{3(B-L)+2S} \tag{2.8}$$

where B is the baryon number, L is the lepton number and S is the spin. Thus SM particles have positive R-parity while SUSY particles have negative R-parity, since they have the same value of B and L but the value of S differs by half unit. For R-parity to be conserved, a SUSY particle can only decay into a SUSY particle plus a SM particle whereas the decay in two SUSY particles is not allowed. Hence, the most plausible DM candidate in SUSY is the Lightest Supersymmetric Particle (LSP), which cannot further decay and remains stable. The LSP can be either the neutralino $\tilde{\chi}_1^0$ or the gravitino $\tilde{G}$ (in Gauge Mediated SUSY Breaking models).

Is DM cold? DM must also be cold, in other words it must be made of particles that have become non-relativistic before the matter domination era. DM is therefore usually classified as cold, warm or hot, depending on how relativistic it is. In the Cold Dark Matter (CDM) framework, structures must grow hierarchically, with smaller structures merging first and creating more massive objects, like galaxies and clusters. In the Hot Dark Matter (HDM) framework, galaxies are instead created from the fragmentation of superclusters, in contrast with cosmological observations which show that galaxies are older than superclusters [32]. HDM models are thus nowadays disfavoured while in principle both CDM and Warm Dark Matter (WDM) models are able to explain the current structure of the Universe [44]. CDM candidates can include both the WIMPs thermal relics like SUSY neutralinos as well as the non-thermal axions, light pseudoscalar particles introduced by Roberto D. Peccei and Helen R. Quinn to solve the strong CP problem [45]. Possible WDM candidates are instead light thermal gravitinos (even if already excluded as they are not able to reproduce the abundance of DM) or sterile neutrinos, a hypothetical new type of right-handed neutrinos, which interact only gravitationally with SM particles [46].

Does it match the expected relic abundance? The other key ingredient is the DM relic abundance, discussed in Section 2.2. For a new particle to be considered a valid DM candidate, its production mechanism must be able to reproduce the appropriate value of the relic density. WIMPs are usually very favoured because they are able to naturally achieve the expected abundance, whereas SM neutrinos are ruled out because (in addition to the fact they are not "cold") they are not able to reproduce the total amount of DM ($\Omega_\nu h^2 \sim 6 \times 10^{-4}$, from Ref. [38]). Nevertheless, other thermal relics can also originate from the decay of a more massive species that has previously decoupled from the thermal bath. This is the case of the LSP gravitino and the first excitation of the graviton in Universal Extra-Dimensions (UED), which are produced by late decays of the next to the lightest particles in the respective theories. Another case is the one of "WIMPzillas" which, having masses around 10^{15} GeV, cannot have thermal equilibrium hence different hypotheses are being discussed about the production mechanism that can be behind them (among others, possible creation during reheating after inflation, pre-heating stage, Planck scale or even creation of gravitational nature) [47].

Clearly, this section is not meant to be an exhaustive overview of possible DM candidates but rather its aim is to give a small taste of the general picture under which the current, diversified, DM searches are performed.

2.4 Dark Matter searches

DM searches can be distinguished in three main complementary categories:

- direct detection
- indirect detection
- pair production at colliders

whose approaches can be schematically depicted as in Figure 2.5.

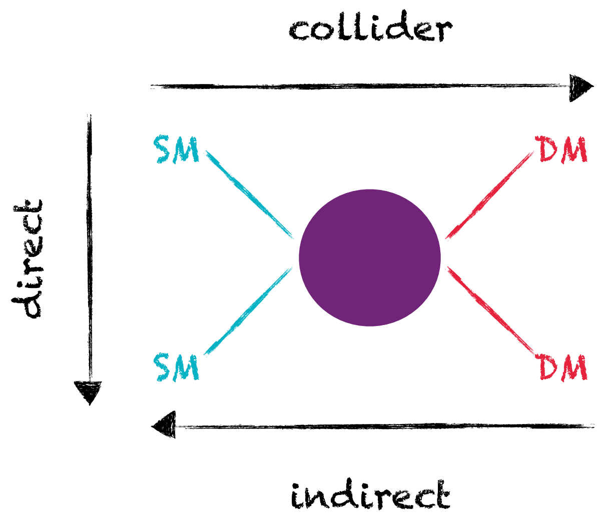

FIGURE 2.5: Scheme of the possible interaction between DM and SM particles as probed by the direct, indirect and collider searches.

Direct searches The rotation of the Milky Way through the (non-rotating) DM halo causes the solar system to experience an effective DM wind. Direct searches are aimed at detecting the interaction of DM with the SM particles from the nuclear recoil of the target material of a detector placed on Earth (usually underground, in order to minimise the background).

The expected DM flux $nv = \rho_{DM} v/m$ can in principle be very large therefore for a WIMP mass around 100 GeV, assuming a speed of the Earth through the DM halo of 230 km/s and a local DM density of the order of 0.3 GeV/cm^3, it is possible to experience a flux of 10^5 cm^{-3}s^{-1}. Of course, the other missing piece is the magnitude of the DM scattering cross-section: in principle, this type of searches can be very sensitive also to WIMPs with a relatively small relic density, as long as their scattering cross-section is large enough. On the other hand, direct searches lose sensitivity at low masses of the DM particle, where the signal goes below the detection threshold. Direct detection experiments usually distinguish between Spin Independent (SI) and Spin Dependent (SD) WIMP-nucleon interactions, in which DM couples, respectively, to the nuclear density or to the nuclear spin density. The SD interactions result from an axial-vector coupling and their cross-sections depend on the spin content J of the nucleon, while SI scattering cross-sections, arising from scalar or vector couplings, are proportional to A^2, where A is the number of nucleons in the nucleus. Direct detection experiments therefore usually probe SI interactions using heavy atoms as targets.

Another remarkable feature of the direct searches is the so-called *annual rate modulation*. Due to the Earth's orbital motion around the Sun, the direction of the DM wind with respect to an observer on the Earth changes throughout the year: the flux is maximal in June and minimal in December. The count rate is therefore expected to exhibit a sinusoidal dependence on time. This is a very distinctive feature of the DM signal, as the majority of the background does not show the same time dependence. Indications of an annual modulation initially came from the DAMA/LIBRA experiment [48, 49] but were found to be inconsistent with several other experiments. Recently, the COSINE-100 experiment attempted to reproduce such results in an independent way, using the same target material of the DAMA/LIBRA experiment. Although more statistics is needed to be able to fully confirm or refute these results, the COSINE-100 results seem to disfavour the WIMP-nucleon spin independent interaction as the origin of the annual modulation signal claimed by DAMA/LIBRA [50, 51].

In addition to the energy of the DM particle, several direct detection experiments attempt also to measure the recoil direction and possibly identify the origin of the DM signal. Figure 2.6 shows an overview of the current limits on the WIMPs-nucleon cross-section, including also the sensitivity of the XENON1T, which in 2019 announced the first observation of the two-neutrino double electron capture process, thus proving its sensitivity to this kind of extremely rare processes [52].

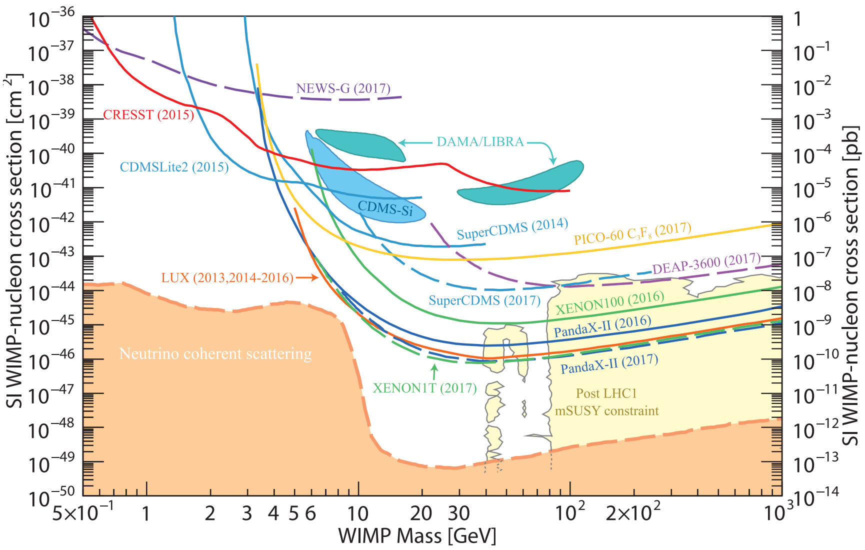

FIGURE 2.6: 90% Confidence Level (CL) upper limits to SI WIMPs-nucleon interaction for several direct detection experiments. Figure taken from Ref. [53].

Indirect searches Indirect searches are aimed at detecting the products of DM particle annihilation, as γ rays, $p\bar{p}$, e^+e^- and neutrinos, looking for anomalies that might indicate the presence of DM in a certain region of the Universe. The potential capture of WIMPs inside the Sun or the Earth would increase their density and then enhance their probability to annihilate.

Searches for γ rays are usually done in space, as in the GeV-TeV energy range photons interact with matter mostly producing e^+e^- pairs, hence they would not reach the Earth. Nevertheless, both ground-based and space-based telescopes are currently performing this type of DM search. Within the second category of telescopes, the Fermi-LAT collaboration has observed an excess of events in the few GeV range from a region around the galactic centre, consistent with several WIMPs hypotheses [54]. However, the current range of explored uncertainties on the modelling of the background emission is still not complete and the spectrum and morphology of the excess are not yet obviously consistent with the expectations from a DM signal. The result is therefore currently used only to derive constraints on the annihilation cross-section of DM particle candidates.

Several other experiments are instead designed to specifically detect neutrinos. Such neutrinos are expected to escape from the Sun or Earth and travel a large distance (through ice or underwater) before being detected. The signal rate is therefore expected to be very low, however a signal like this would point directly to the Sun, therefore removing most of the background. In this context, the strongest limits actually come from Super-Kamiokande which, by including in the selection also events with a muon produced inside the detector, extended its sensitivity down to the few GeV regime [55].

The flux of antiprotons and positrons is instead probed by experiments like PAMELA and AMS. Unlike photons and neutrinos, these charged particles interact with the magnetic field in the galaxy and therefore they will not point to their source. Nevertheless, studying the flux of this type of particles is extremely interesting given the limited amount of anti-matter in the Universe. Both PAMELA and AMS observed a quite clear rise of the positron fraction in an energy regime between 10 and 200

GeV [56, 57]. However, the behaviour of this flux at higher energy seems to be different among the two experiments and several signal hypotheses are currently being considered, including pulsars, supernovas and also antideuteron signals.

Lastly, if DM is not too heavy it might be possible to produce it with one of our powerful accelerators of SM particles, like the LHC. As the main focus of this thesis consists in one of these searches, a dedicated discussion about the DM searches at the LHC is presented in the next section.

2.5 The search for Dark Matter at the LHC

As for the direct and indirect detection, the main assumption behind the search for DM at colliders is the existence of a certain kind of interaction between SM and DM particles. A direct production of DM at colliders, as the LHC, would then be crucial in understanding the interaction of DM with the ordinary matter in the first instants after the Big Bang.

A DM particle produced at the LHC would almost pass invisibly through the detector and, exactly as the SM neutrinos, its signal would be characterised by a large amount of missing transverse momentum, $E_{\mathrm{T}}^{\mathrm{miss}}$, which qualitatively refers to the imbalance in the energy measured by the detector (a more detailed discussion will be presented in Sections 3.2-4.7).

In general, it is possible to extend the SM in order to account for a new DM candidate by allowing the Higgs boson or the Z boson to mediate the interaction between DM and SM particles. These are usually called "portal models". Alternatively, a large set of theory models assume that the mediator of the DM-SM interaction is also a new particle, which can either be a heavier version of the Z boson, usually called Z', or a new scalar particle. In this context, a distinction is usually made between the so-called Effective Field Theory (EFT) and simplified models. The first approach, in which the interaction between DM and SM particles is described as a contact interaction, is only valid when the energy scale of the process is much lower than the scale of the microscopic interaction (also referred to as "suppression scale") and therefore not sufficient to create the mediator particle itself. When the collision energy is close to the mediator mass, such models must be replaced with the simplified models. In this case, the DM particle is produced by the exchange of a new mediator particle and, unlike the EFT models, the process depends on several parameters, as the nature of the mediator particle, its couplings to the DM and the SM particles, and the mass of the DM particle itself.

Depending on the process involving the mediator particle, searches with *invisible* or *visible* final states can be performed. In the first case, the DM particles, produced by the mediator particle, leave a large amount of $E_{\mathrm{T}}^{\mathrm{miss}}$ in the final state therefore additional particles from Initial State Radiation (ISR) or from associated productions are used to define the signature of the event which can be:

- Jets/γ + $E_{\mathrm{T}}^{\mathrm{miss}}$,
- W/Z + $E_{\mathrm{T}}^{\mathrm{miss}}$,
- a SM Higgs boson + $E_{\mathrm{T}}^{\mathrm{miss}}$,
- heavy flavour quarks + $E_{\mathrm{T}}^{\mathrm{miss}}$.

One of the most inclusive searches is the one looking just for events with jets and $E_{\mathrm{T}}^{\mathrm{miss}}$, in which a new mediator particle Z' decays to DM and the only visible object

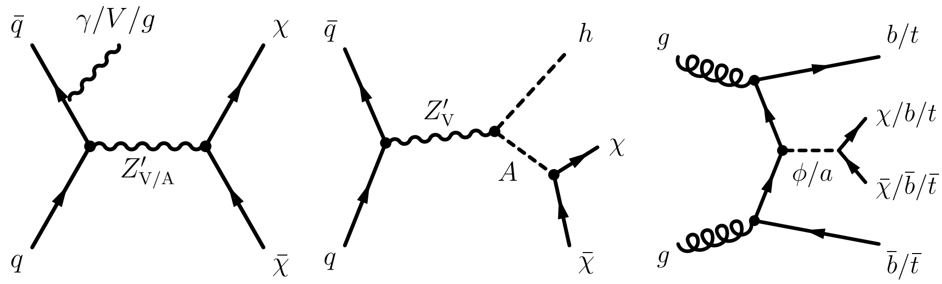

FIGURE 2.7: Feynman diagrams of some "invisible" state signatures. Figures taken from Ref. [58].

originates from a gluon emitted from the initial state quarks, as shown in Figure 2.7a, giving rise to the so-called "mono-jet" signature. Actually, due to gluon splitting, more than one ISR jet can arise, therefore this type of searches looks for up to three or four jets in the event.

Another possibility is the emission of a photon from the initial state partons. The presence of a high $p_{\rm T}$ photon makes the event selection very clean with respect to the jet case, but it also suffers from lower statistics due to the smaller magnitude of the electromagnetic coupling constant with respect to the one of the strong interaction.

Equivalently, also the W and Z vector bosons can be emitted from the initial quarks. In the case of fully hadronic decays, the signature results very similar to the "mono-jet" one. In addition, dedicated searches for $Z(\ell\ell)+E_{\rm T}^{\rm miss}$ final states are also carried out.

It is also possible to exploit the properties of the SM Higgs boson to look for the so-called "mono-Higgs" final states. Figure 2.7b shows how this type of signature can arise, in the specific case of the Z'-Two Higgs Doublet Model (2HDM) model, in which the mediator Z' produces a new pseudo-scalar Higgs boson a which is assumed to decay to a pair of DM particles. The final state visible objects are therefore the decay products of the Higgs boson which can originate from processes with high Branching Ratio (BR) (and relatively high background level), like $H \rightarrow b\bar{b}$, or processes with a much cleaner signature (and also much lower statistics), like $H \rightarrow \gamma\gamma$.

Another interesting signature would also be characterised by an invisible decay of the SM Higgs boson. Due to the very tiny BR associated to this process in the SM (BR($H \rightarrow Z(\nu\nu)Z(\nu\nu)$) $\sim$ 0.1%), an observation of a large BR for this process would certainly imply physics BSM.

Lastly, as shown in Figure 2.7c, through the exchange of a new scalar particle ϕ or a pseudo-scalar a, it is possible to produce final states with heavy flavour quarks (such as top and bottom) plus $E_{\rm T}^{\rm miss}$ from DM particles.

The various "invisible" final state searches described so far are also usually referred to as "mono-X" searches.

Another possibility is to probe the so-called "visible" final states, whose signatures are defined by the decay of the new mediator particle into SM particles. This type of BSM searches includes the:

- di-jet,
- Trigger-object Level Analysis (TLA) di-jet,
- di-jet + ISR,

- di-bjet,
- di-lepton,
- and $t\bar{t}/t\bar{t}t\bar{t}$

final states.

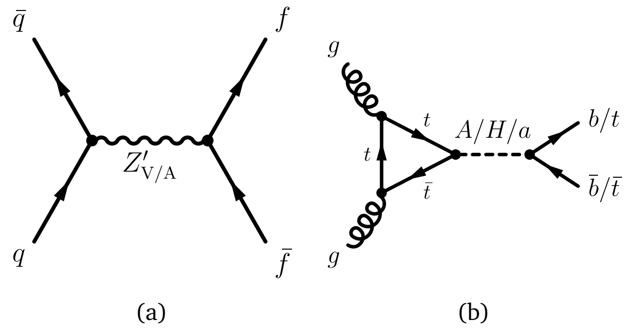

FIGURE 2.8: Feynman diagrams of some "visible" state signatures. Figures taken from Ref. [58].

Di-jet searches aim at observing events with exactly two energetic hadronic jets, hoping to see a bump in the invariant mass of the di-jet system consistent with the mass of the new mediator particle. Some di-jet analyses perform an angular analysis in order to exploit also the difference between the rapidities of the two jets (see Section 3.2) in order to look for deviations with respect to the SM.

Traditionally, the focus of the di-jet searches has been the high mass regime (above 900 GeV), mainly because low mass searches are severely limited by the restrictions in the data-taking (both for the ATLAS and CMS experiments) for low p_{T} jets. In fact, at lower p_{T}, the single jet triggers only record a fraction of the events (*prescaling*). In the recent years, an innovative approach has been developed in order to record and analyse only a reduced set of information from the trigger system, leading to the so-called TLA. Following this strategy, events passing the single-jet First Level Trigger (L1) trigger, with lower threshold than the High Level Trigger (HLT) (for a more detailed discussion about the ATLAS trigger system see Section 3.2.5), can be recorded with minimal bandwidth increase, making it finally possible to probe also the mass region below 1 TeV.

Alternative strategies consist in looking for a pair of jets recoiling against a photon or an additional jet from the initial state. This is the case of the di-jet+ISR analyses. Dedicated searches are also performed for events in which the two jets originate from bottom or anti-bottom, or other heavy flavour, quarks.

Lastly, narrow di-lepton resonances are also predicted by several BSM theories, hence dedicated searches with events containing exactly two same flavour leptons are carried out.

A comparison of the sensitivity of all these searches performed by the ATLAS experiment is shown in Figures 2.9, for the case of vector and axial-vector mediator models, and is more extensively discussed in Ref. [58].

It is also interesting to compare the results of all these searches with the ones of the direct detection experiments by converting the ATLAS exclusion limits to bounds on the DM–nucleon scattering cross-section. This conversion can be done for vector, axial-vector and scalar mediator models, following the procedure described in Ref. [59]. Furthermore, following the same method, the pseudo-scalar mediator results, for which the direct searches lose sensitivity, can be compared to the indirect

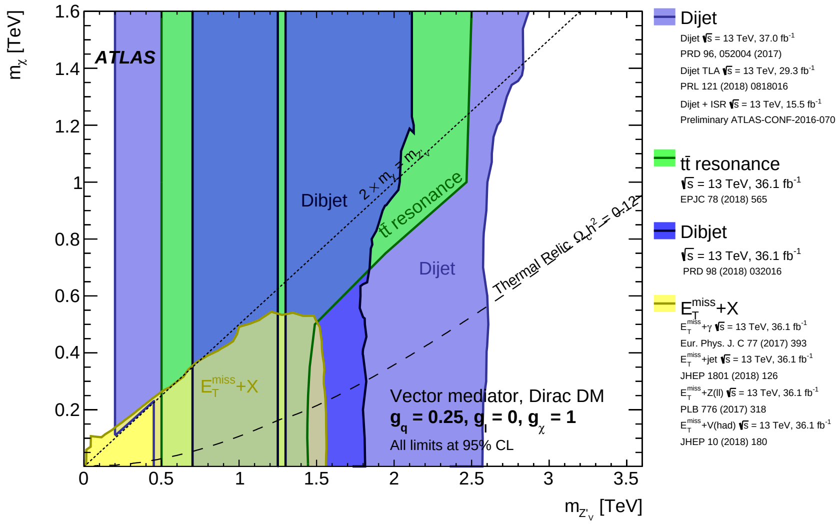

(a)

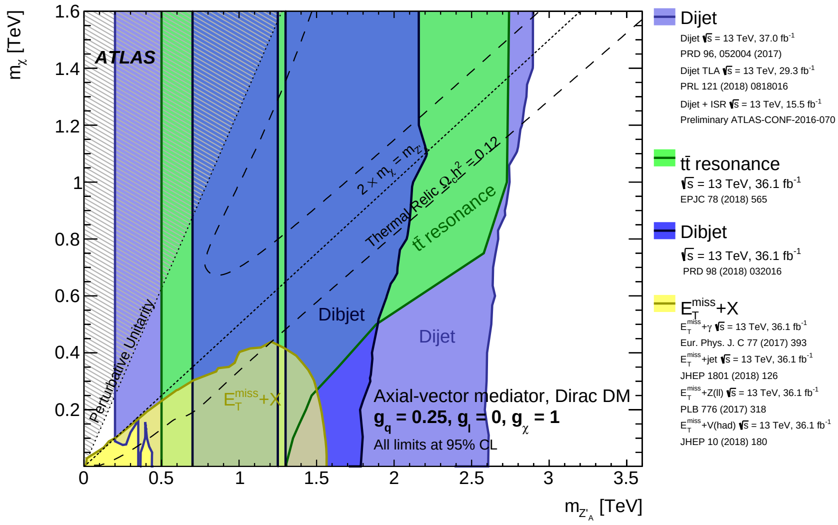

(b)

FIGURE 2.9: Regions in the mediator mass - DM mass plane excluded at 95% CL by di-jet, di-lepton and $E_T^{\text{miss}} + X$ searches for vector (top) and axial-vector simplified models (bottom). Figures taken from Ref. [58].

search results, by converting the exclusion limits into the DM annihilation cross-section limits. The result of this comparison, for what concerns the ATLAS results, is shown in Figure 2.10.

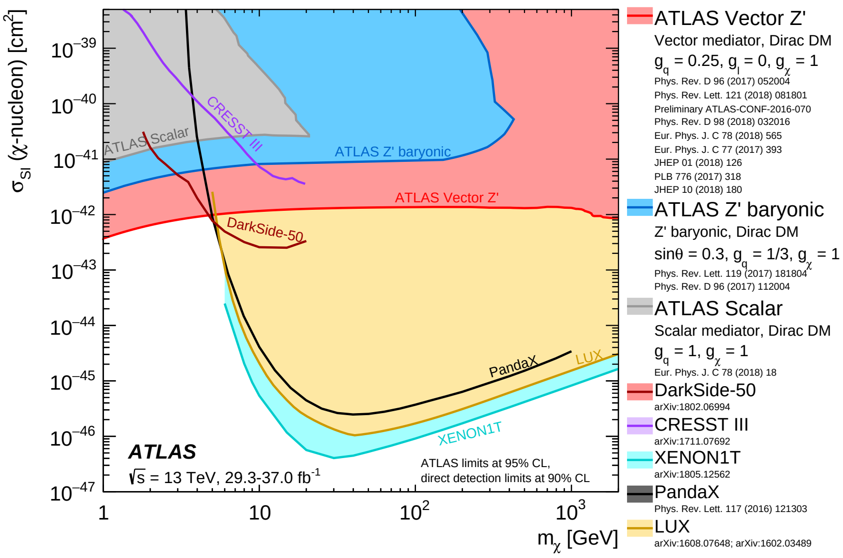

FIGURE 2.10: A comparison between the constraints at 90% CL from direct detection experiments on the SI WIMPs–nucleon scattering cross-section and the ATLAS exclusion limits at 95% CL. Figure taken from Ref. [58].

3 The LHC and the ATLAS experiment

The data used for the work presented in this thesis have been collected by the ATLAS experiment, which is one of the four main experiments operating at the LHC: the largest and most powerful particle accelerator in the world. This chapter is dedicated to the discussion of the physics behind the high energy proton-proton (pp) collisions taking place at the LHC, starting from the illustration of the accelerator complex and ending with the description of the ATLAS multi-purpose detector.

3.1 The Large Hadron Collider

Based at CERN near Genève, in Switzerland, the LHC [60] is mainly designed to collide proton beams at a centre-of-mass energy up to 14 TeV and to reach a luminosity of 10^{34} cm^{2}s^{-1}. Nevertheless, the LHC can also collide heavy ions (Pb) as well as lighter nuclei like xenon whose collisions are able to provide information about the quark-gluon plasma, reproducing the phenomena occurred in the first instants of the Universe. The LHC is a circular hadron accelerator with a circumference of 27 km and it is placed in the pre-existing tunnel already built for the Large Electron Positron collider (LEP) [61].

3.1.1 The accelerator complex

When protons reach the LHC, they have already gone through several accelerating steps. The proton source is created by injecting hydrogen gas into a metal cylinder, placed at one end of LINAC2. An electric field surrounding the cylinder strips the hydrogen atoms off their electrons, leaving only protons to enter the accelerator. Inside LINAC2, protons are accelerated up to 50 MeV. Subsequently, protons are injected into the Proton Synchrotron Booster (PSB) where they reach the energy of 1.4 GeV. A second ring, the Proton Synchrotron (PS), brings them to 25 GeV and protons are then "clumped" in bunches spaced by 25 ns from each other. Finally, just before the injection in the LHC, they are accelerated up to 450 GeV in the Super Proton Synchrotron (SPS). A scheme of the accelerator system is shown in Figure 3.1.

The beam particles are forced in a circular orbit by the magnetic field which, through the Lorentz force, curves the trajectories in a direction orthogonal with respect to the plane of the velocity and the magnetic field. Since the collisions occur

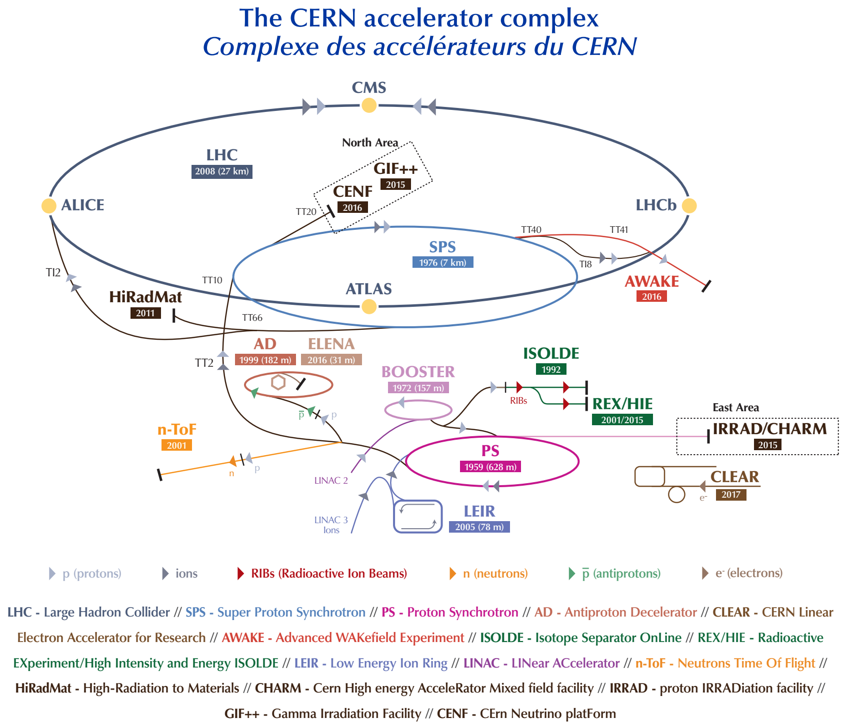

FIGURE 3.1: Scheme of the LHC injection system. Figure taken from Ref. [62].

between particles with the same electric charge, two different magnetic fields in different rings are needed in order to allow the two beams to circulate in opposite directions.

3.1.2 Proton-proton collisions

In a pp collision, the interaction occurs between the fundamental constituents of each proton (quarks and gluons, also generally called as *partons*) in the initial state. Such interactions are usually referred to as hard-scattering processes. The outgoing partons produced in such interaction will then start emitting QCD radiation, creating parton showers. At the end, partons have to recombine in order to produce colour singlet particles (see Section 1.1), through the hadronisation process. The resulting hadrons decay afterwards into other stable particles, which we try to detect with our detectors. In addition to the particles produced during the hard-scattering process, ISR and Final State Radiation (FSR) processes can take place, as a result of the remaining activity due to the breakup of the proton. These are usually defined as Underlying Events (UE). An illustration of a hard-scattering process in a pp collision is shown in Figure 3.2.

The effective centre-of-mass energy $\sqrt{\hat{s}}$ is determined by the momentum carried by the partons involved in the collision:

$$\sqrt{\hat{s}} = \sqrt{s x_1 x_2} \tag{3.1}$$

where x_1 and x_2 represent the fractions of the total momentum of the proton carried by the two partons in the initial state. The probability that a parton i carries a fraction x of the total momentum of the proton at a momentum transfer Q^2 is given by the

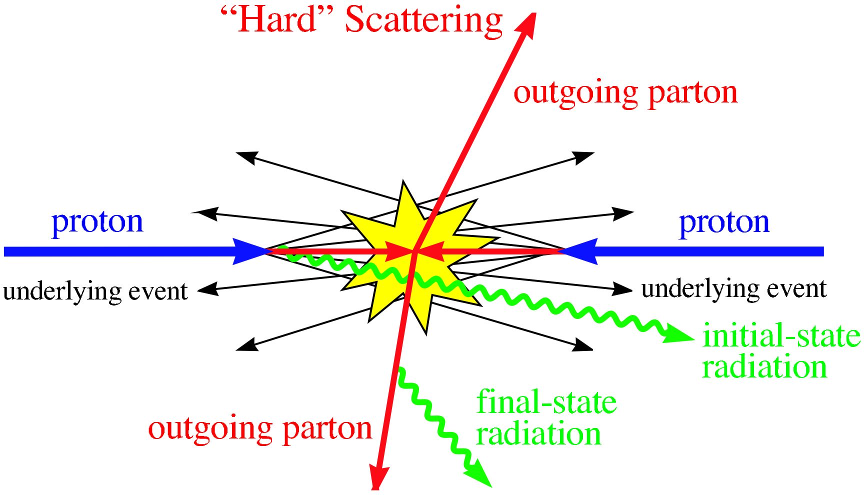

FIGURE 3.2: Pictorial representation of a hard-scattering event. Figure taken from Ref. [63].

Parton Density Function (PDF) $f_i(x, Q^2)$. The dependence of the PDF on Q^2 can be predicted by QCD and is described by the Dokshitzer-Gribov-Lipatov-Altarelli-Parisi (DGLAP) equation [64], while the dependence on x is parametrised at fixed Q^2. As shown in Figure 3.3, *valence* quarks (i.e. the quarks defining the hadron quantum numbers) of the proton are able to carry a large fraction of momentum, while gluons and *sea* quarks (originating from the $q\bar{q}$ pairs produced by gluon splitting) dominate at small values of x. In particular, the gluon PDF is extremely peaked at low x, therefore gluon-gluon fusion is the dominant process at the LHC. By knowing the PDFs of the initial state partons, it is possible to calculate the total hadronic cross-section for a given process in a pp collision, using the *factorisation theorem* [65]:

$$\sigma_{AB\to X} = \sum_{a,b} \int dx_a dx_b f_{a/A}(x_a, Q^2) f_{b/B}(x_b, Q^2) \hat{\sigma}_{ab\to X} \tag{3.2}$$

where A and B refer to the two protons in the initial state, while a and b are the partons involved in the hard-scattering process and $\hat{\sigma}$ is the cross-section of the process at parton-level.

3.1.3 The machine performance

The rate of events generated in the LHC pp collisions is given by:

$$\frac{dN_{\text{events}}}{dt} = \mathcal{L}\sigma_{\text{event}} \tag{3.3}$$

where σ_{event} is the cross-section of the process under study and $\mathcal{L}$ is the machine instantaneous luminosity. The machine luminosity depends only on the beam parameters and can be written, assuming a Gaussian beam profile in all directions, in this way [60, 67]:

$$\mathcal{L} = \frac{N_b^2 n_b f_{rev} \gamma_r}{4\pi\varepsilon_n \beta^*} F \tag{3.4}$$

where N_b is the number of protons in each bunch, n_b is the number of bunches in the beam, f_{rev} is the revolution frequency and γ_r is the relativistic γ factor. ε_n corresponds to the beam emittance ε (which is a property of a particle beam characterising its size)

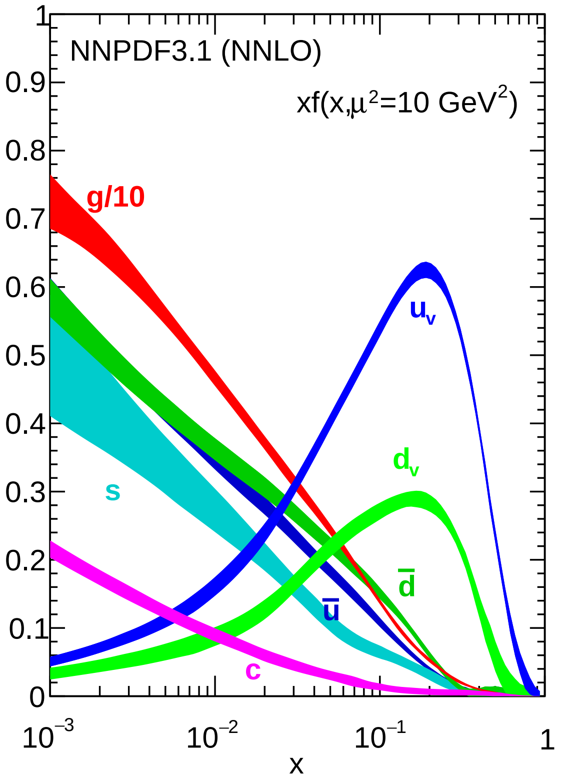

FIGURE 3.3: The quark and gluon PDFs calculated by the NNPDF3.1 analysis at Next-to-Next-to-Leading Order (NNLO). Figure taken from Ref. [66].

scaled to the energy of the beam itself. The β^* parameter corresponds instead to the value of the β-function (which, in accelerator physics, relates the width of the beam to its emittance ε) measured at the interaction point. The last term F represents the geometric luminosity reduction factor due to the crossing angle or transverse offset at the interaction point and at the LHC it has been measured to be very close to unity [68].

At the LHC, the collisions of proton bunches result not only in a hard-scattering interaction but also in additional collisions accompanying the signal. These further collisions usually occur at low transverse momentum and are referred to as *pile-up* interactions. Such events can arise from the superposition of two consecutive bunch-crossings (*out-of-time*) or from different interactions taking place within the same bunch-crossing (*in-time*).

The two proton beams are designed to collide in exactly four interaction points, corresponding to the four main experiments that are operating at the LHC: ATLAS [70], CMS [71], LHC beauty (LHCb) [72] and A Large Ion Collider Experiment (ALICE) [73]. ATLAS and CMS are the two high luminosity experiments designed to reach a peak luminosity of $\mathcal{L} = 10^{34}$ cm^{2}s^{-1}. LHCb focuses on B-physics and is aiming at a peak luminosity of 10^{32} cm^{2}s^{-1}, while ALICE is dedicated to the heavy ion collisions and it is expected to reach a maximum peak luminosity of 10^{27} cm^{2}s^{-1}.

The number of pp inelastic collisions that occur in each bunch crossing can be modelled as a Poisson random variable with mean value $\langle\mu\rangle$. Figure 3.4 shows the distribution of $\langle\mu\rangle$ for the different years of data taking of Run 2 of the LHC. The value

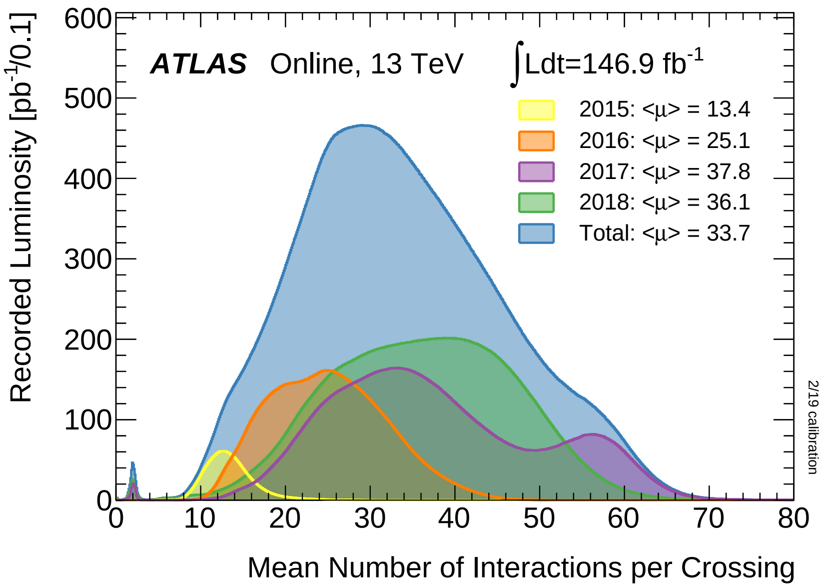

FIGURE 3.4: Luminosity-weighted distribution of the mean number of interactions per crossing for all data periods, from 2015 until 2018, at 13 TeV centre-of-mass energy in Run 2 of the LHC. Figure taken from Ref. [69].

of $\langle \mu \rangle$ corresponds to the mean value of the Poisson distribution of the number of interactions per crossing which is calculated for each bunch as $\mu = \mathcal{L}_{\text{bunch}} \times \sigma_{\text{inel}} / f_{\text{rev}}$ where $\mathcal{L}_{\text{bunch}}$ is the per-bunch instantaneous luminosity, σ_{inel} is the inelastic cross-section[1] and f_{rev} is the LHC revolution frequency.

The data used for this thesis have been collected during Run 2 of the LHC, which started in June 2015 and ended in October 2018. Figure 3.5, shows the integrated luminosity delivered by the LHC over these years, together with the one recorded by the ATLAS detector, which corresponds to 147 fb^{-1}.

3.2 The ATLAS detector

ATLAS [70] is a multi-purpose detector with forward-backward symmetry with respect to the interaction point. It extends for a length equal to 44 meters, it has a diameter of 25 meters and a weight of approximately 7000 tons. An overview of the whole ATLAS detector is illustrated in Figure 3.6.

ATLAS uses a right-handed coordinate system whose origin is placed at the nominal interaction point, which is located at the centre of the detector. The x-axis points from the interaction point towards the centre of the LHC, while the y-axis points vertically upwards. In these coordinates, θ represents the polar angle in the y-z plane, while ϕ represents the azimuthal angle in the transverse x-y plane. A sketch of the ATLAS coordinate system is shown in Figure 3.7.

Defining quantities in this reference frame is very handy as, in head-on collisions, like the ones taking place at the LHC, the momentum of the two initial partons is directed along the beam axis z, while the transverse components, x and y, are null.

[1]The inelastic cross-section is measured, by the ATLAS detector, from events with a very loose trigger selection applied in order to minimise the selection bias as much as possible (*minimum bias events*).

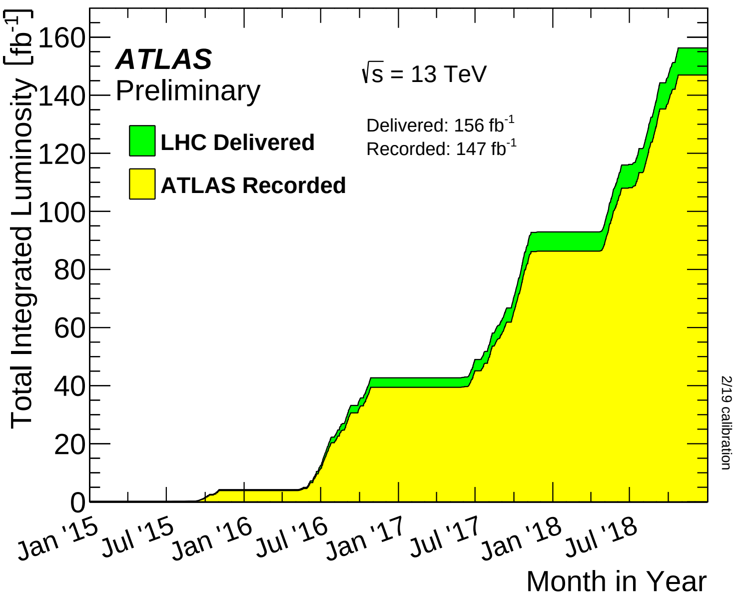

FIGURE 3.5: Cumulative luminosity versus time delivered to ATLAS (green) and recorded by ATLAS (yellow) during stable beams for pp collisions at 13 TeV centre-of-mass energy in Run 2 of the LHC. Figure taken from Ref. [69].

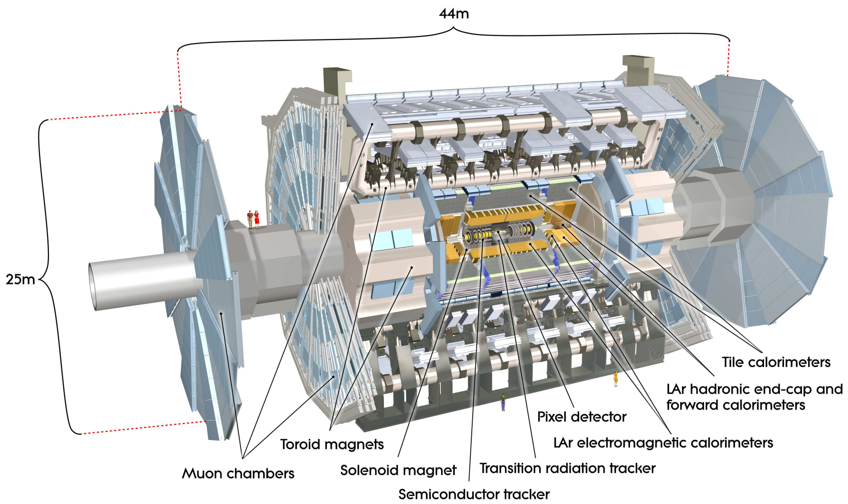

FIGURE 3.6: Cut-away view of the ATLAS detector. Figure taken from Ref. [70].

This allows us to apply the conservation of energy and infer that in the transverse plane the vectorial sum of all particles' momenta in the final state must also be zero, unless in the event there are neutrinos or any other weakly interacting particles escaping detection. Since the boost along the z axis is not known a priori, as it depends on the fraction of momentum carried by the single partons, the collision can happen everywhere along the beam axis. It is therefore important to define quantities which are invariant under Lorentz boosts along the z axis. For this purpose, let us introduce the *rapidity* which is defined as:

$$y = \frac{1}{2} \ln \frac{E + p_z}{E - p_z} \tag{3.5}$$

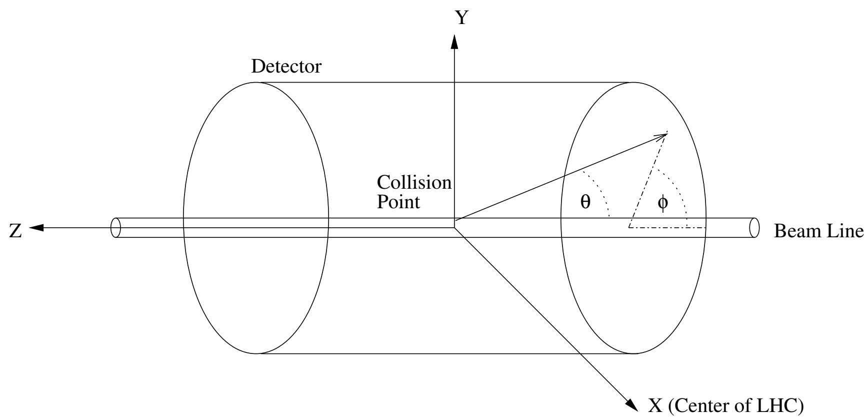

FIGURE 3.7: Illustration of the ATLAS coordinate system. Figure taken from Ref. [74].

where E and p_z represent, respectively, the energy and the z-component of the particle momentum. In the relativistic case, $E \gg m$, the rapidity becomes equal to the *pseudo-rapidity*:

$$\eta = -\ln \tan(\theta/2) \tag{3.6}$$

and it is possible to show that intervals of η are invariant under longitudinal boosts. Moreover, the transverse momentum p_{T}, whose components are the projections of the momentum along the x and y axes, is by definition also an invariant under boosts along the beam axis. For these reasons, differential cross-sections are usually studied as a function of η (or y) and p_{T}.

The ATLAS detector aims at reconstructing and identifying all the particles produced in the pp collisions at the Point-1 the LHC. As every particle interacts differently with matter, ATLAS is made of several sub-detectors and each of them is designed to yield a specific signal allowing the particle identification. From the inside out, ATLAS is made of:

- an Inner Detector (ID), which allows for the track and vertex identification,
- a Solenoid, which surrounds the ID and provides a 2 T magnetic field,
- an Electromagnetic Calorimeter (ECAL), dedicated to the measurement of the energy of electrons and photons,
- a Hadronic Calorimeter (HCAL), which measures the energy of hadrons,
- a Muon Spectrometer (MS) for the measurement of the muons' momentum.

The ATLAS detector is commonly subdivided into the central region (called also *barrel*) and the two forward regions (also referred to as *end-caps*). Hence this terminology will be used in the following.

The magnet system The whole magnet system of the ATLAS detector [75] consists of a central solenoid, aligned with the beam axis, and a superconducting air-core toroidal system in the outermost region of the detector. The central solenoid is placed between the ID and the ECAL and it provides a 2 T axial magnetic field. It extends for a length of 5.8 m, with inner and outer diameters equal to 2.46 m and 2.56 m, respectively. In order to keep the material thickness in front of the calorimeter as low as possible, the solenoid windings and the Liquid Argon (LAr) calorimeter (see Section 3.2.2) share a common vacuum vessel. The toroidal magnet system consists of three parts: a barrel and two end-caps. Each system is made of eight separate coils assembled radially and symmetrically around the beam axis. The barrel system extends for a length of 25.3 m with inner and outer diameters equal to 9.4 m and 20.1 m, respectively. The two end-caps coils are rotated by 22.5° with respect to the barrel system, in order to realise radial overlap and optimise the bending power in the transition region between the two systems. Each coil in the barrel has its own cryostat while the end-cap coils are housed in a common cryostat. The toroidal system provides a bending power[2] that varies from 1.5 Tm to 5.5 Tm in the barrel and from 1 Tm to 7.5 Tm in the end-cap regions. The bending power provided by the solenoid system is instead around 2 Tm.

The presence of a magnetic field is essential for the measurement of the momentum of a particle. The Lorentz force bends the trajectory of the particle, without changing its energy. Therefore, assuming a uniform magnetic field B acting over a length L, the p_{T} of a particle entering the region can be evaluated, assuming unit electric charge, as:

$$p_{\mathrm{T}}(\mathrm{GeV}) = 0.3\rho(\mathrm{m})B(\mathrm{T}) \tag{3.7}$$

where ρ represents the radius of curvature.

3.2.1 Tracking system

The ID of the ATLAS detector aims at reconstructing the tracks originating from the interaction point, as well as the identification of the vertex at which the hard-scattering collision takes place. Given the high track density originating from the pp collisions taking place at the LHC, it is crucial to employ high-granularity detectors and at the same time use a minimal amount of material, in order to reduce multiple scattering effects.

As illustrated in Figure 3.8, the ID consists of two precision tracking detectors, employing silicon pixels and microstrips and covering the pseudo-rapidity range $|\eta| < 2.5$, and a gas detector, the Transition Radiation Tracker (TRT), which extends up to $\eta = 2$.

[2] The bending power is given by the integral $\int B dl$, where B is the azimuthal magnetic field component and dl is a straight line covering the distance between the inner and the outer radius of the toroids.

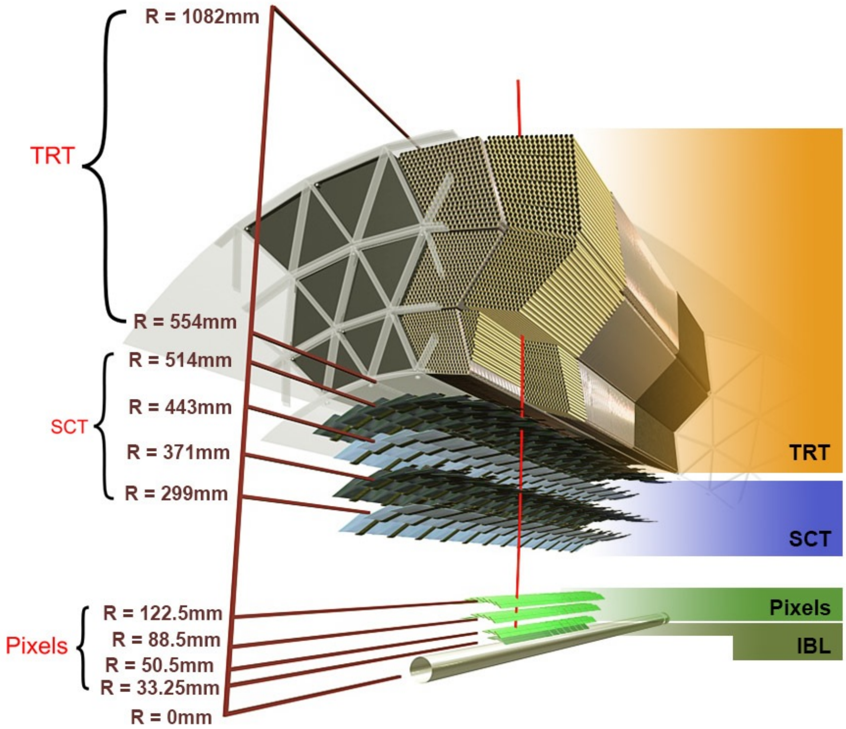

FIGURE 3.8: Illustration of the ATLAS tracking system. Figure taken from Ref. [76].

The Pixel detector The silicon pixel detector is placed in the innermost region, in order to provide a finer granularity around the vertex region. It consists of four barrel layers, with the outermost layer placed at a distance of 122.5 mm, while in the end-cap regions, disks are placed perpendicular to the beam axis. The innermost pixel layer is the Insertable B-Layer (IBL) [77] which is placed at a distance of 3 cm with respect to the beam axis. In the three outermost layers, the nominal pixel size is 50×400 μm^2, which yields an intrinsic resolution of 14×115 μm^2 while in the IBL the tracking resolution improves due to the usage of pixels with size equal to 50×250 μm^2, providing a resolution of approximately 10 μm in the R-ϕ plane and 66.5 μm in the z direction.

The Semi-Conductor Tracker The Semi-Conductor Tracker (SCT) is the second sub-detector of the ATLAS ID and it is made of silicon microstrips. They are arranged in four concentric layers in the barrel region, while the end-cap regions consist of 9 disks on each side. In the barrel region, where the strips are placed at a distance of 80 μm, the SCT uses small-angle (40 mrad) stereo strips to measure both coordinates, yielding an accuracy of 17 μm in the R-ϕ direction and 580 μm in the z direction.

The Transition Radiation Tracker The third sub-system of the ID is the TRT, which is made by 4 mm straw tubes filled with a xenon-based gas mixture. The presence of the TRT in the tracking system allows also a better electron identification, through the detection of transition radiation photons, which can originate from the xenon contained in the straw tubes. In addition to the electron identification, although designed to be complementary to the silicon-based tracking systems, the TRT contributes also to the combined tracking system p_{T} resolution, thanks to the high number of hits per track and the long lever arm.

3.2.2 Calorimeter system

The ATLAS calorimeter system is made of several detectors with full ϕ symmetry and covering the pseudo-rapidity range equal to $|\eta| < 4.9$, as illustrated in Figure 3.9. The purpose of the calorimeter system is to measure the energy lost by electrons, photons and hadrons inside the detector. In order to have a precise measurement, it is therefore important to force the particles to deposit all their energy within the volume of the detector. The ECAL and HCAL are hence designed to contain, respectively, the full electromagnetic and hadronic showers. One additional goal of the calorimeter system is also to limit the amount of particles reaching the MS. Therefore, the depth of each of the two systems is a crucial parameter.

In general, the depth of an electromagnetic calorimeter is given in terms of the radiation length X_0 which represents, for a given material, both the mean distance travelled by a high energy electron before losing all but $1/e$ of its energy by bremsstrahlung and 7/9 of the mean free path of a high-energy photon before creating e^+e^- pairs. The size of hadronic calorimeters is instead usually given in terms of the interaction length λ which is the mean distance travelled by a hadron, in a certain material, before undergoing an inelastic nuclear interaction [5].

The ECAL extends for more than 22 X_0 in the barrel and more than 24 X_0 in the end-caps, while the total thickness of the HCAL is instead equal to 9.7 interaction lengths of active material in the barrel and 10 λ in the end-caps. All the calorimeters adopt a sampling technique, where active material layers alternate with layers of passive material. LAr is usually preferred as active material, due to its linear behaviour, stability of the response over time and intrinsic radiation hardness.

The Electromagnetic Calorimeter Similarly to all the sub-detectors already described, also the ECAL is subdivided in a Barrel Electromagnetic Calorimeter (EMB) and in an End-Cap Electromagnetic Calorimeter (EMEC). For both regions, an accordion geometry has been chosen, as illustrated in Figure 3.10. This peculiar shape provides a full coverage in ϕ around the beam axis as well as a fast extraction of the signal at the far ends of the electrodes. The active material of the detector is LAr while the absorbers are made of lead plates. The barrel module extends up to $|\eta| < 1.475$ and consists of three longitudinal layers (front, middle and back as viewed from the interaction point), preceded by an additional thin LAr layer, called *presampler*, which estimates the energy loss before the calorimeter. As shown in Figure 3.10, the granularity in each layer is different. The first layer has a high granularity for π/γ discrimination, the second one is designed to contain the major part of the cascade while the last one is dedicated to the measurement of the electromagnetic shower tails, improving the rejection with respect to the hadron showers. At each side of the barrel system, the EMEC system extends over the range $1.375 < |\eta| < 3.2$. The EMEC is made of two co-axial wheels, one covering the range $1.375 < |\eta| < 2.5$ and the other extending from $|\eta| = 2.5$ up to $|\eta| = 3.2$. As for the barrel, the precision

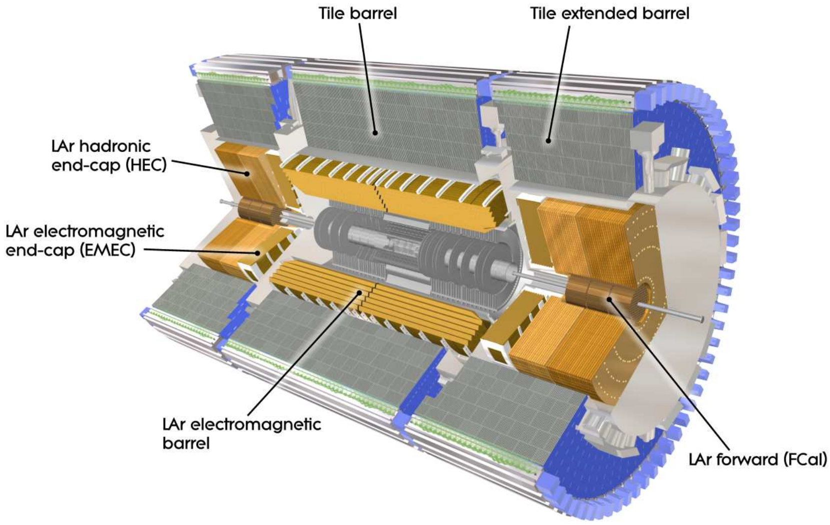

FIGURE 3.9: Cut-away view of the ATLAS calorimeter system. Figure taken from Ref. [70].

measurement region ($1.5 < |\eta| < 2.5$) is divided in depth in three longitudinal layers with different granularity in η. The transition region between the EMB and EMEC consists of several X_0 of inactive material and therefore produces non-negligible energy losses. For this reason, it is usually recommended not to consider electrons or photons in the region $1.37 < |\eta| < 1.52$.

The Hadronic Calorimeter The HCAL consists of the Tile Calorimeter (TileCal), the End-Cap Hadronic Calorimeter (HEC) and the Forward Calorimeter (FCal). The TileCal [78] is a sampling calorimeter made of steel as absorber and tiles of scintillating material as active medium. It covers the region $|\eta| < 1.7$ and is subdivided into a central barrel and two extended barrels. The HEC is instead made of copper and LAr and covers the range $1.5 < |\eta| < 3.2$. It consists of two wheels at each end of the barrel system, each of them containing two longitudinal sections. Lastly, the full coverage of the system is provided by the FCal which covers the region $3.1 < |\eta| < 4.9$. In the FCal, LAr is still used as active material while the absorber is copper in the layer closest to the interaction point, designed to measure the electromagnetic showers, and tungsten in the following two layers measuring the remaining hadron showers.

3.2.3 The Muon System

Unlike electrons and hadrons, which lose energy in the calorimeters, muons are minimum ionising particles: they can travel across the whole detector losing only a small fraction of energy. For this reason, the MS is placed in the outermost region of the ATLAS detector. It extends up to $|\eta| < 2.7$ and is dedicated to the measurement of the muon's momentum through the magnetic deflection caused by the large superconducting air-core toroid magnets, described in Section 3.2, which provide a magnetic field mostly orthogonal to the muon's trajectory. In the MS barrel region ($|\eta| < 1.4$) the magnetic field is provided by the large central toroid, while in the end-cap region ($1.6 < |\eta| < 2.7$), the magnetic deflection is caused by the two smaller magnets placed at the end of each barrel side. In the transition region $1.4 < |\eta| < 1.6$, the magnetic deflection is provided by a combination of the barrel and end-cap fields.

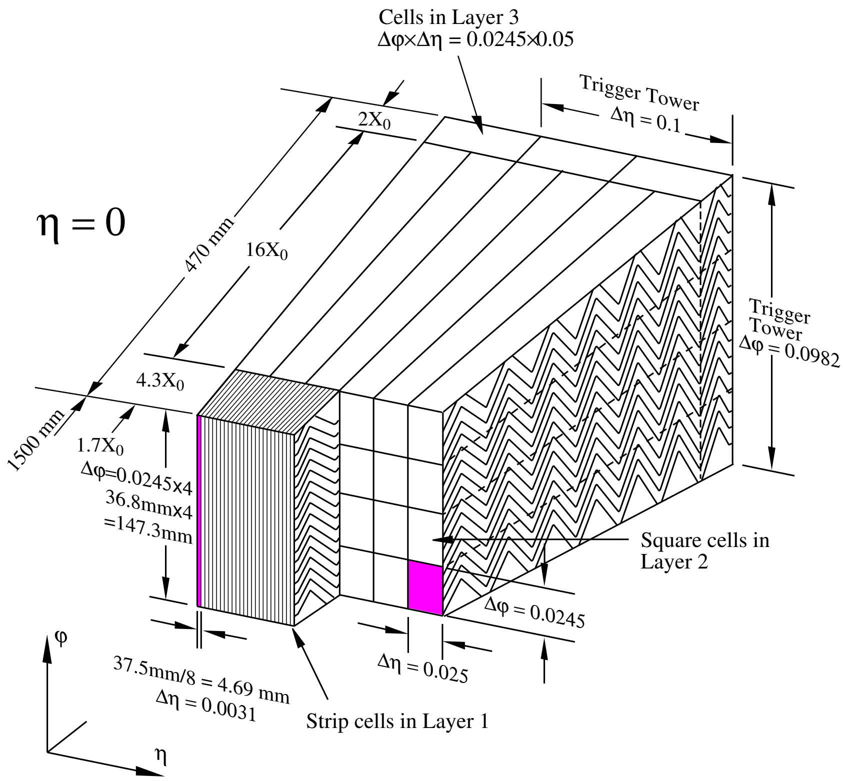

FIGURE 3.10: Sketch of the ECAL barrel module. Figure taken from Ref. [70].

The muon chambers in the barrel region of the MS are arranged in three cylindrical layers around the beam axis while in the two end-cap regions the muon chambers form large wheels placed in planes perpendicular to the beam axis. The major part of the MS consists of Monitored Drift Tubes (MDTs), operating with a gas mixture of Ar (93%) and CO_2 (7%), which measure the coordinate of the track in the bending plane with good precision. In the region $2 < |\eta| < 2.7$, Cathode Strip Chambers (CSCs) are instead preferred as they are more resistant to the higher particle fluxes occurring in this forward region. They consist of multiwire proportional chambers with cathodes segmented into strips. Lastly, the muon trigger system covers the range $|\eta| < 2.4$ and it consists of Resistive Place Chambers (RPCs), which are placed in the barrel and allow the measurement of the muon coordinate in non-bending plane, and Thin Gap Chambers (TGCs) for the end-caps. The RPCs are used due to their good spatial and time resolution as well as their adequate rate capability, while the TGCs work as multi-wire proportional chambers and provide good time resolution and high rate capability.

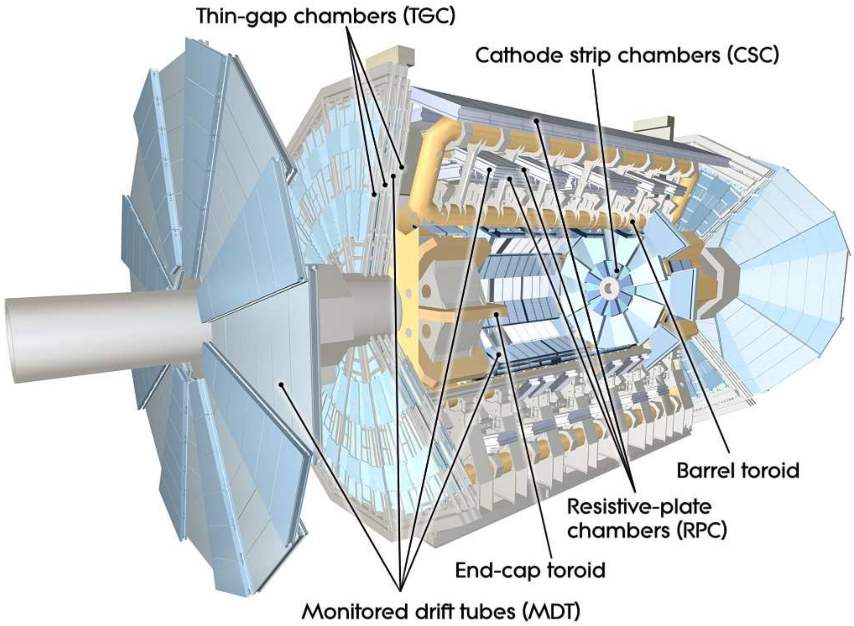

FIGURE 3.11: Cut-away view of the ATLAS muon system. Figure taken from Ref. [70].

3.2.4 The luminosity detectors

An accurate measurement of the luminosity, as well as the systematic uncertainty associated to it, is essential for the precision measurements performed in ATLAS. In order to perform this measurement, the luminosity, already defined in Equation 3.4, can be re-written as:

$$\mathcal{L} = \frac{\mu_{\text{vis}} n_b f_{rev}}{\sigma_{\text{vis}}} \tag{3.8}$$

where σ_{vis} and μ_{vis} represent, respectively, the visible inelastic cross-section and interaction rate [79, 80].

In ATLAS, the measurement of μ_{vis} is commonly done using *event counting* algorithms in which each particular bunch crossing is categorised depending on a specific selection designed to detect the presence of at least one inelastic pp collision. Assuming a Poisson probability distribution for the number of interactions in a bunch crossing, the probability to observe at least one event is given by [81]:

$$P_{\mu_{\text{vis}}}(n \geqslant 1) = 1 - e^{-\mu_{\text{vis}}} \tag{3.9}$$

hence by measuring the fraction of bunch crossings satisfying the event selection criteria of the algorithm is possible to determine μ_{vis}. The results obtained with this approach are also compared with the results of the track-counting method [81] in which μ_{vis} is taken as the number of tracks per bunch crossing averaged over a given time window. The two primary sub-detectors which are dedicated to the measurement of μ_{vis} are:

- the Beam Conditions Monitor (BCM) diamond sensors, designed to protect the detector from the damage originating from potential uncontrolled beam, which at the same time measure the instantaneous rate of collisions and monitor potential beam losses;

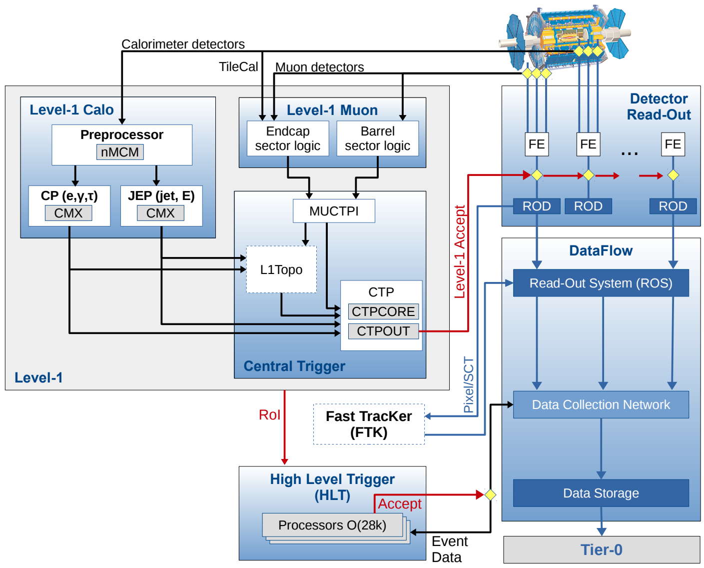

FIGURE 3.12: Schematic view of the ATLAS TDAQ system in Run 2. Figure taken from Ref. [86].

- the LUminosity Cherenkov Integrating Detector (LUCID) [82], placed around the beam pipe at a position of about 17 m from the nominal interaction point, and specifically designed to measure the luminosity in ATLAS, by detecting Cherenkov light signals.

On the other hand, the measurement of σ_{vis} is commonly performed during the van der Meer (vdM) scans [83], in which the beams are separated by a known distance, in both the x and y transverse directions, such that a direct measurement of their transverse sections is possible.

3.2.5 The trigger system

In a dense environment like the one of the LHC, the trigger system is a crucial component of the experiment. It allows to select the events of interest at a recording rate of approximately 1 kHz from up to 40 MHz of collisions. The Trigger and Data Acquisition (TDAQ) system adopted by the ATLAS detector consists of a hardware-based L1 [84] and a software-based HLT [85], as illustrated in Figure 3.2.5. The L1 trigger decision is formed by the Central Trigger Processor (CTP), which receives inputs mostly from the L1 calorimeter trigger (L1Calo) and L1 muon trigger (L1Muon). Designed for a target latency of 2 μs, the L1 brings the event rate from the bunch crossing rate of 40 MHz down to 100 kHz. After the L1 trigger selection, the events are buffered in the Read-Out System (ROS) and processed by the HLT. The HLT algorithms exploit the full granularity and precision of the various sub-detectors to refine the trigger selection. In the HLT, the event rate is further reduced from the L1 output to approximately 1 kHz. Only the events selected by the HLT are transferred to a data storage system and used to perform the offline analysis. In addition to that, a L1 topological trigger (L1Topo) uses the information provided by L1Calo and L1Muon to apply further selections, allowing also a refined calculation of the $E_{\text{T}}^{\text{miss}}$ (see Section 4.7). A more comprehensive description of the ATLAS trigger system can be found in Ref. [86].

4 Physics objects

As illustrated in Chapter 3, each ATLAS sub-detector is designed to yield a different signal depending on the nature of the particle produced in a pp collision. In this chapter, the techniques adopted by the ATLAS experiment for the reconstruction of the final state objects relevant for the analysis presented in this thesis are described.

4.1 Tracks and vertices

As mentioned in Section 3.2.1, the purpose of the ATLAS ID is to reconstruct the trajectory of all charged particles as well as to identify the position along the beam axis at which the hard-scattering process takes place. This is generally referred to as Primary Vertex (PV) and it is reconstructed as the vertex corresponding to the highest sum of the squared transverse momenta of its associated tracks. The reconstruction of the PV is essential as it defines the reference point for the definition of the impact parameters and the identification of the displaced vertices.

The track reconstruction starts from the measurements in the pixel and SCT detectors. The information is then propagated to the TRT using a combinatorial Kalman filter [87]. A score is assigned to each track candidate, depending on the presence of holes (i.e. a missing hit in a region of the detector where one is expected) and weighting the measurement in each sub-detector depending on its precision. A preference is also given to high p_{T} tracks in order to discard the large number of low p_{T} tracks formed from incorrect combination of clusters.

Some of the most important quantities defining the particle trajectory are the transverse and longitudinal projections of the distance of closest approach with respect to the PV, usually referred to as d_0 and z_0, respectively, as illustrated in Figure 4.1.

The track candidates are selected depending on a certain number of quality criteria and are then divided in two different categories:

- `Loose`: all tracks with $p_{\mathrm{T}} > 500$ MeV and $|\eta| < 2.5$ with at least seven hits in the silicon detectors, not more than one shared module (pixel and SCT), not more than two missing hits in the silicon detectors and not more than one missing hit in the pixel detectors;

- `Tight Primary`: all tracks passing the `Loose` requirements and having at least nine hits in the silicon detectors if $|\eta| \leq 1.65$ or at least eleven hits if $|\eta| > 1.65$,

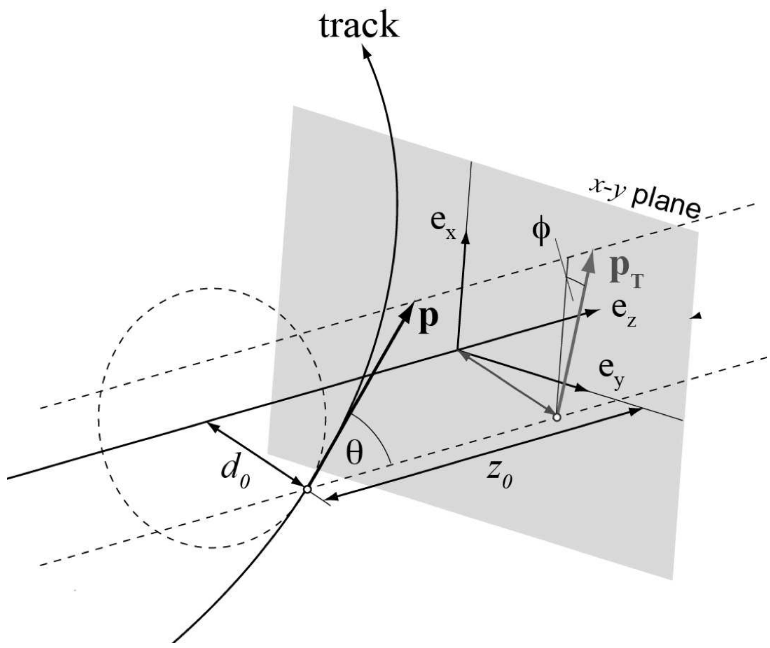

FIGURE 4.1: Illustration of the track helix parameters defined in the perigee representation in the ATLAS detector. Figure taken from Ref. [88].

at least one hit in the two innermost pixel layers and no missing hits in the pixel detectors.

The track reconstruction efficiency for `Loose` (`Tight Primary`) tracks, as calculated from minimum bias simulated events, varies from a maximum value of 90% (84%) in the region $|\eta| \leqslant 0.1$ to a minimum of 71% (62%) in the region $2.3 \leqslant |\eta| \leqslant 2.5$. The resolutions of the impact parameters d_0 and z_0 are usually extracted by performing a gaussian fit of such distributions in bins of p_{T} and η. An iterative method is applied in order to reduce the dependence on the PV position resolution [89]. In order to cover a wide range in track p_{T}, minimum bias events are analysed for tracks with $p_{\mathrm{T}} < 15$ GeV while $Z \to \mu\mu$ events are used for tracks with $p_{\mathrm{T}} \geqslant 15$ GeV. The final uncertainty is parameterised as a function of the track p_{T} and η and provided in the form of two-dimensional histograms. Figure 4.2 shows the intrinsic transverse impact parameter resolution of d_0 and z_0 for `Tight Primary` tracks associated to jets with $p_{\mathrm{T}} > 20$ GeV measured in di-jet events using data collected in 2017 and 2018.

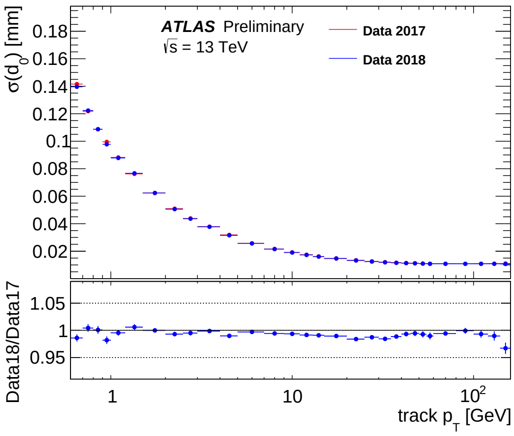

(a)

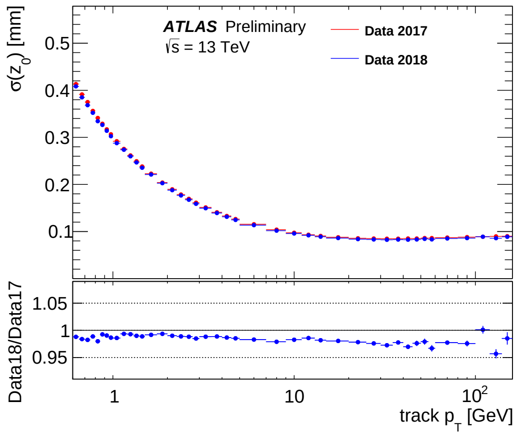

(b)

FIGURE 4.2: Intrinsic resolutions of the d_0 (on the left) and z_0 (on the right) impact parameters of `Tight Primary` tracks measured in di-jet triggered pp collision data taken in 2017 and 2018. Figure taken from Ref. [90].

4.2 Jets

As already anticipated in Section 1.1, the partons produced in the pp collisions taking place at the LHC cannot be observed as free particles. Due to the confinement phenomenon, the objects measured by the ATLAS detector are actual "jets" of particles, originating from the hadronisation and fragmentation processes of quarks and gluons. Such hadronic jets are measured using either the topological calorimeter clusters ("calorimeter jets"), constructed as adjacent calorimeter cells with an absolute value of their energy significantly above the noise threshold [91], or the ID tracks ("track jets") as inputs for the jet clustering algorithm. In the case of calorimeter jets, the topological clusters can be reconstructed at the electromagnetic scale, which correctly measures the energy deposited in the calorimeter by particles produced in electromagnetic showers. Alternatively they can be calibrated in order to take into account the response of the calorimeter to hadrons. In this case the calibration makes use of the Local Calibration Weighting (LCW) method, which first classifies the clusters as either electromagnetic or hadronic and then, based on such classification, applies correction from Monte Carlo (MC) simulation of neutral and charged pions [92, 93, 94].

All the inclusive jet clustering algorithms start by introducing a distance d_{ij} between the constituents i and j and a distance d_{iB} between the i-th entity and the beam B:

$$d_{ij} = \min(k_{ti}^{2p}, k_{tj}^{2p})\frac{\Delta_{ij}^2}{R^2} \qquad d_{iB} = k_{ti}^{2p} \tag{4.1}$$

where $\Delta_{ij}^2 = (y_i + y_j)^2 + (\phi_i + \phi_j)^2$, where k_{ti}, y_i and ϕ_i are respectively the transverse momentum, rapidity and azimuth of particle i and R is the chosen distance parameter ($R = 0.4$, 0.2, 1.0 etc). If d_{ij} is smaller than the distance d_{iB}, the constituents i and j are combined (i.e. their momenta are summed together), otherwise

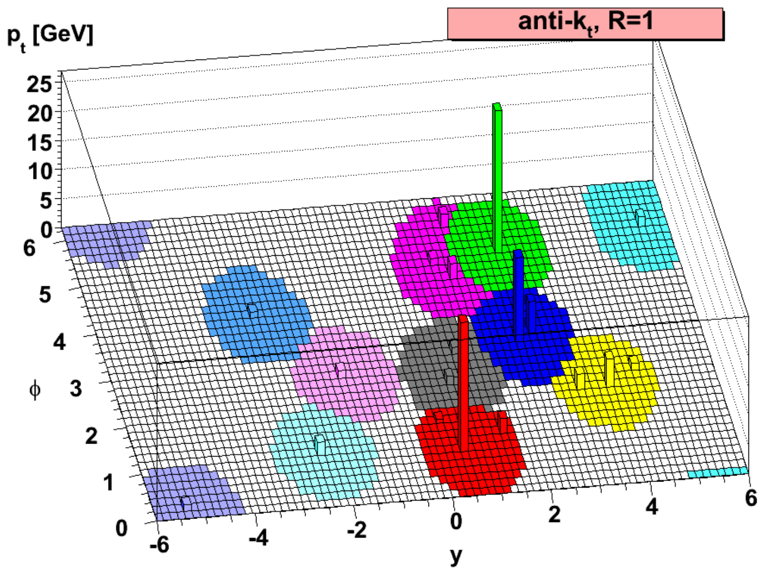

FIGURE 4.3: Illustration of the anti-k_t algorithm. Figure taken from Ref. [95].

the object i is considered a jet and is removed from the list of jet constituents. The distances are then recalculated and the procedure is repeated until no entities are left. The parameter p determines the power of the geometrical scale which in the anti-k_t algorithm is set to -1. The choice of this metric makes the clustering start from the hardest constituents and the results are conical jets, as illustrated in Figure 4.3.

One of the main property of the anti-k_t algorithm is the Infrared and Collinear (IRC) safety, which ensures that the set of hard jets found in an event remains unchanged in case the event is modified by a collinear splitting or the addition of a soft emission [96].

The energy of the reconstructed calorimeter jets in then calibrated in order to correct for several detector effects that can affect the measurement, as the calorimeter non-compensation, dead material, leakage, limited acceptance, noise threshold and pile-up. This calibration is performed using truth jets reconstructed at the particle-level energy scale and it is typically referred to as the Jet Energy Scale (JES) correction. This procedure follows several steps, as illustrated in Figure 4.4: first, the jet direction is corrected to point to the PV of the event[1], then the contribution of pile-up is subtracted and finally the JES derived from MC is applied to the reconstructed jets. Further corrections are then applied in order to reduce the difference between the jet responses of quarks and gluons and to correct high p_T jets which are not fully contained in the calorimeter, following the Global Sequential Calibration (GSC). The final step consists in comparing the p_T of the calibrated jets with respect to some reference objects in both data and MC and applying this residual correction to the reconstructed jets. In addition to the central value of the JES, another important quantity that needs to be estimated is the precision of the jet energy measurement,

[1] By default, during the jet clustering, the direction of the topological calorimeter clusters is set to point towards the centre of the detector. After the full event reconstruction, it is then possible to correct for that and point the topological calorimeter cluster towards the actual hard-scattering position.

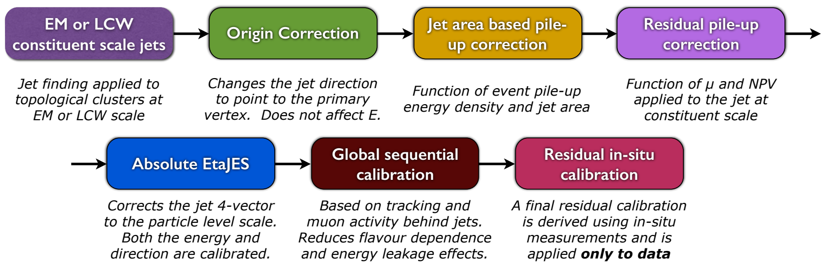

FIGURE 4.4: Scheme of the stages used in the calibration of electromagnetic and LCW jets. Figure taken from Ref. [92].

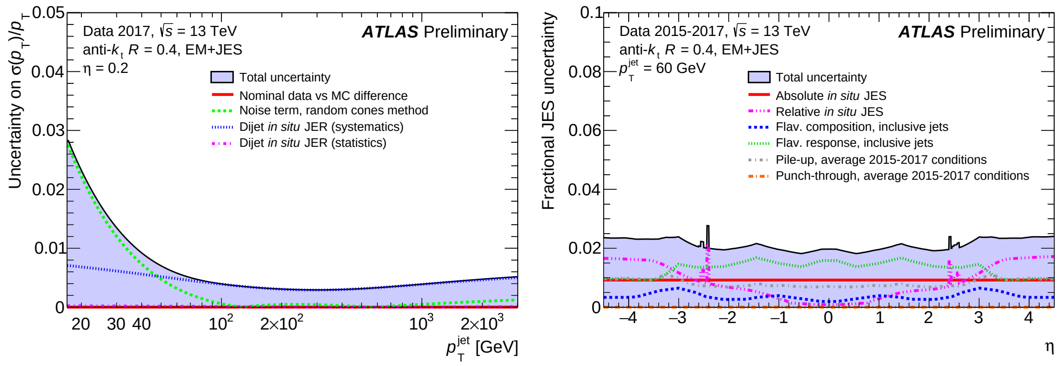

(a) (b)

FIGURE 4.5: Uncertainty on the relative jet energy resolution as a function of the jet p_{T} (on the left) and jet energy scale systematic uncertainty components as a function of the jet η (on the right) for anti-k_t calorimeter jets. Figures taken from Ref. [97, 98]

.

usually referred to as Jet Energy Resolution (JER), which can be parametrised as:

$$\frac{\sigma(p_{\mathrm{T}})}{p_{\mathrm{T}}} = \frac{N}{p_{\mathrm{T}}} \oplus \frac{S}{\sqrt{p_{\mathrm{T}}}} \oplus C \tag{4.2}$$

where N represents the noise term, S describes the stochastic effect, C is p_{T} independent constant term and the symbol $\oplus$ indicates a quadratic sum. Each of these terms is extracted using dedicated methods, as described in Ref. [92].

Depending on the topology of the event and on the specific needs of the analysis, jets with different radius parameters R can be used. The most common objects supported by the ATLAS collaboration are small-R and large-R calorimeter jets with radius equal to 0.4 and 1.0, respectively, as well as Fixed-Radius (FR) (generally $R = 0.2$) and VR track jets. In the following sections, a brief overview of the different techniques and calibrations for each of these jet definitions is presented.

4.2.1 Small-R calorimeter jets

Small-R calorimeter jets are reconstructed from topological clusters, calibrated to the electromagnetic energy scale, using the anti-k_t algorithm with radius parameter equal to 0.4.

Jets coming from pile-up interactions are suppressed by making use of the Jet Vertex Tagger (JVT) [99] discriminant variable which is a multivariate combination of the Jet Vertex Fraction (JVF), defined as the fraction of the total momentum of tracks in the jet which is associated with the PV[2], and the R_{p_T} variable, which represents the scalar p_T sum of tracks associated to the jet and associated to the PV divided by the p_T of the fully calibrated jet. The usage of the JVT variable has proved to strongly suppress the contribution from pile-up jets, while maintaining a good stability with respect to the pile-up conditions. The JVT cut is recommended to be applied to small-R jets with 20 GeV < p_T < 60 GeV and $|\eta| < 2.4$.

Furthermore, a jet cleaning cut must also be applied in order to reject fake jets arising from non-collision backgrounds, like Beam Induced Background (BIB), cosmic rays and calorimeter noise [100, 101]. In order to suppress the contribution from such bad quality jets, a combination of cuts on some of the most sensitive variables, like the fraction of energy measured by the ECAL and by the HCAL, the maximum energy fraction released in each calorimeter layer as well as the charged fraction and the shape of the signal in the LAr calorimeter, is applied.

4.2.2 Large-R calorimeter jets

Large-R calorimeter jets, also colloquially referred to as "fat jets", are generally dedicated to the reconstruction of the decay products of very energetic objects. In fact, in the two-body decay of a high p_T (*boosted*) particle with mass m, the angular separation between the decay products can be approximated as [102]:

$$\Delta R \sim \frac{1}{\sqrt{z(1-z)}} \frac{m}{p_T}, \quad (p_T \gg m) \tag{4.3}$$

where z and $1 - z$ represent the momentum fractions carried by the two daughter particles.

This means that, in such energetic cases, it is not optimal anymore to reconstruct the two decay products as two distinguished small-R jets but rather they would be fully contained inside a single jet with a larger radius. As an example, in the case of a $H \to b\bar{b}$ process, when the Higgs boson p_T is higher than 250 GeV, the two b-quarks will be contained inside a single jet with $R = 1.0$.

The large-R jets are built from topological clusters, calibrated with the LCW scheme, using the anti-k_t algorithm with a distance parameter of $R = 1.0$. The jets reconstructed in this way undergo a grooming procedure in order to remove the soft radiation component originating from pile-up, ISR and UE. The grooming technique adopted in ATLAS is the trimming [103] which consists in reclustering the constituents of the initial jet into subjets of radius R_{sub}, following the k_t algorithm, and discarding any subjet that has a transverse momentum that is less than f_{cut} times the transverse momentum of the parent jet. Usually, the values of $R_{\text{sub}} = 0.2$ and $f_{\text{cut}} = 0.05$ are adopted in this procedure. The four-momentum of the final trimmed jet is therefore the sum of the four-momenta of the remaining constituents. Figure 4.6 shows an illustration of a general trimming procedure.

The large-R jet mass reconstruction makes use of both the calorimeter and tracking information, combining the calorimeter mass m^{calo}, deduced from the four-momentum sum of all calorimeter jet constituents, and the track-assisted mass m^{TA},

[2]Actually, the variable adopted in the JVT calculation considers an adjusted definition of the JVF which corrects for the linear dependence of the p_T sum of pile-up tracks on the number of vertices [99].

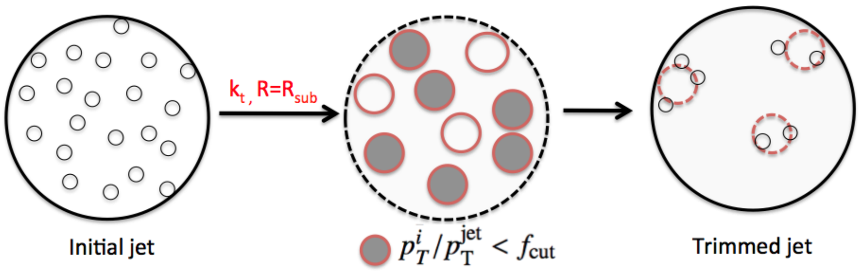

FIGURE 4.6: Illustration of the jet trimming procedure. Figure taken from Ref. [104].

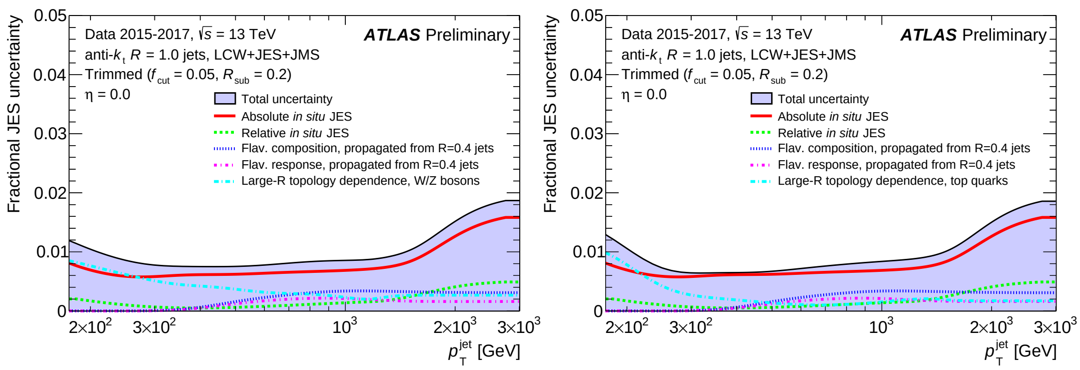

(a) (b)

FIGURE 4.7: JES systematic uncertainty components as a function of jet transverse momentum for trimmed $R=1.0$ anti-k_t jets. Figures taken from Ref. [106]

.

defined as [105]:

$$m^{\rm TA} = \frac{p_{\rm T}^{\rm calo}}{p_{\rm T}^{\rm track}} \times m^{\rm track} \tag{4.4}$$

where $p_{\rm T}^{\rm calo}$ is the transverse momentum of a large-R calorimeter jet while $p_{\rm T}^{\rm track}$ and $m^{\rm track}$ are the transverse momentum and the invariant mass[3] of the four-vector sum of tracks associated to the large-R calorimeter jet. The final large-R jet mass in hence defined as:

$$m^{\rm comb} = a \times m^{\rm calo} + b \times m^{\rm TA} \tag{4.5}$$

where $a = \frac{\sigma_{\rm calo}^{-2}}{\sigma_{\rm calo}^{-2} + \sigma_{\rm TA}^{-2}}$ and $b = \frac{\sigma_{\rm TA}^{-2}}{\sigma_{\rm calo}^{-2} + \sigma_{\rm TA}^{-2}}$, where $\sigma_{\rm calo}$ and $\sigma_{\rm TA}$ are, respectively, the calorimeter-based and the track-assisted mass resolutions.

[3]A mass equal to the pion mass is assumed for all tracks.

4.2.3 Track jets

The track jets are reconstructed from the ID tracks, using the anti-k_t algorithm. The considered tracks are required to pass the `Loose` criteria, described in Section 4.1. Additional requirements on the longitudinal impact parameter ($|z_0 \sin(\theta)| < 3$ mm) with respect to the PV allow to reduce the pile-up contribution and to improve the efficiency in selecting tracks from the hard-scattering vertex. Track jets are generally used to identify the flavour content of large-R jets in dense environments, using either the FR or the VR algorithm. The first step consists in associating the track jets to the trimmed large-R jet, through the Ghost Association (GA) procedure [107], and then looking at the flavour content of each track jet in order to establish whether the large-R jet contains one or more subjets originating from a b-hadron decay.

The GA procedure consists in creating a replica of the jet constituents with the same η and ϕ but a negligible energy ("ghosts"). The jet clustering algorithm is then run on both the actual and the new *ghost* jet constituents such that a list of *ghost* particles matched to the jet can be extracted. As the k_t and anti-k_t algorithms are IRC safe (see Section 4.2), the very small energy attributed to the *ghost* particles does not alter the resulting jets.

The identification of jets coming from fragmentation of b-quarks is the procedure called b-tagging, whose main features are discussed in the following section.

4.3 *b*-tagging

The ability of identifying jets containing b-hadrons (commonly referred to as b-jets) is an essential ingredient for the work presented in this thesis and for many physics processes taking place at the LHC, from several SM precision measurements to searches for new phenomena. The distinct signature left by a b-jet is mainly caused by the long lifetime of b-hadrons ($\sim$ 1.5 ps) which can travel significantly away from the PV, giving rise to at least one displaced vertex with respect to the hard-scattering collision point, as illustrated in Figure 4.8. Such long lifetime leads to a measurable decay length of 3 mm for energies of about 50 GeV.

The b-tagging procedure in ATLAS consists of a two-stage approach: a first one ("low-level tagger") exploiting the main features of the charged particle tracks and their association to a displaced vertex and a second one ("high-level tagger") consisting of Multivariate (MVA) classifiers and aiming at maximising the b-tagging efficiency from the output of the low-level taggers.

The low-level b-tagging algorithms are distinguished between:

- the Impact Parameter (IP) based algorithms, `IP2D` and `IP3D` [108], relying on the information of the impact parameters and their significances[4],
- the `SV1` finding algorithm [109], reconstructing the single displaced vertex inside the jet,
- topological multi-vertex finding algorithm, `JetFitter` [110], dedicated to the reconstruction of the full decay chain of the b-hadron, exploiting the topological features of the weak b-hadron and c-hadron decays inside the jet.

[4]The impact parameter significance is defined as the impact parameter divided by its estimated uncertainty.

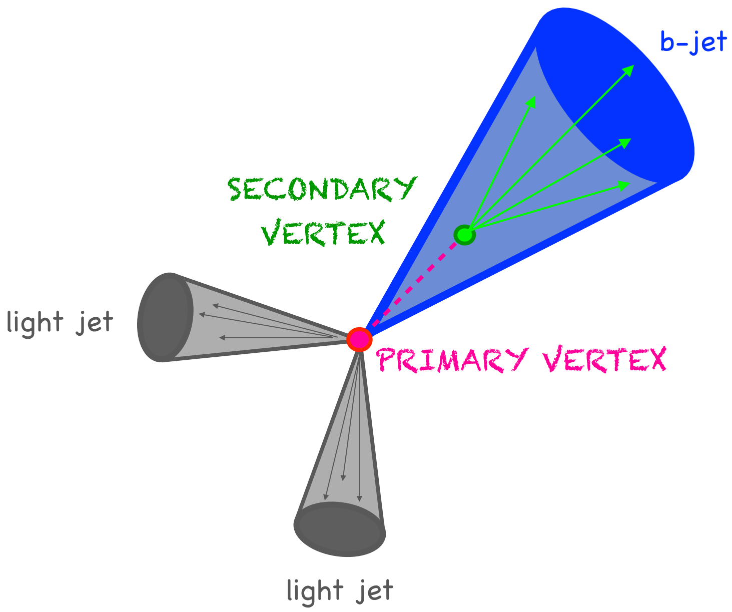

FIGURE 4.8: Illustration of a *b*-hadron decay.

The outputs of the IP2D and IP3D algorithms are based on a Log-Likelihood Ratio (LLR) discriminant which is computed as the sum of the per-track contributions. JetFitter is based instead on a modified Kalman-Filter algorithm [87].

The flavour of each jet is determined by investigating the track and vertex information from the tracks associated to a given jet. The tracks are associated exclusively to the jet based on their angular separation, $\Delta R(\text{track, jet})$, applying a selection that depends on the jet p_{T} as:

$$\Delta R(\text{track, jet}) < 0.239 + e^{-1.220-1.64\times 10^{-5} p_{\text{T}}} \tag{4.6}$$

where the jet p_{T} is expressed in MeV. These tracks are then provided as inputs to the *b*-jet identification algorithms that individually exploit, in addition to the kinematic variables, the impact parameter information (IP2D, IP3D), Secondary Vertex (SV) information and *b*- to *c*-hadron decay chain information (JETFITTER).

In simulation, a flavour label is assigned to each jet using particle-level information by matching jets to *b*- and *c*-hadrons, as well as to τ leptons. In order for a jet to be labelled as a *b*-jet, a truth *b*-hadron must be contained inside a cone of radius $\Delta R = 0.3$ with respect to the jet axis. If no *b*-hadrons are found, the search is repeated to *c*-hadrons, then for τ leptons. If no match is found for *b*, *c* and τ, the jet is labelled as a light-flavour jet. The flavour labelling is exclusive hence the truth hadron is matched only to the closest jet.

The inputs of the different low-level taggers are combined in the high-level taggers using MVA techniques, in order to maximise the *b*-tagging efficiency. The two main high-level taggers commonly used in ATLAS are:

- the MV2 Boosted Decision Tree (BDT), which combines the output variables reconstructed from the low-level taggers,
- the DL1 Deep Neutral Network (DNN), which uses the same input variables of the MV2 algorithm together with the JetFitter *c*-tagging variables, containing information about the secondary and tertiary vertices.

Recently, several improvements to the traditional b-tagging procedure have been implemented. One of the most relevant one consists in the usage of Recurrent Neural Networks (RNN) [111] as low-level tagger. The main difference with respect to the baseline IP based algorithms is given by the fact that, while the `IP3D` assumes each track in the jet to be independent of all other tracks, the RNN is able to learn the dependencies of a certain sequence of variables, like the ones defined for the tracks in a jet, giving a more reliable description of the b-jet properties. Such RNN can then be used as input for the high-level taggers, hence providing an improved version of the high-level taggers, usually referred to as `MV2r` and `DL1r`. In addition to the RNN implementation, a further improvement can be achieved by including the Soft Muon Tagger (SMT) information to the list of input variables of the high-level taggers. The SMT algorithm [108] is based on the reconstruction of muons originating from semi-leptonic decays of b-hadrons. Such muons are characterised by a relatively soft p_{T} (with respect the leptons coming from electroweak boson decays) and a large transverse momentum relative to the jet axis, $p_{\mathrm{T}}^{\mathrm{rel}}$. The muons from such semi-leptonic decays are required to be reconstructed both in the ID and in the MS (see definition of Combined muon (CB) in Section 4.5) and are then associated to the closest jet. From these muons, it is possible to compute different variables (like the ΔR between the muon and the selected jet, the muon d_0 and $p_{\mathrm{T}}^{\mathrm{rel}}$) which can help in further discriminating between the b-, c- and light-flavour jets. The SMT variables can then be added to either `MV2` or `DL1`, whose outputs are provided in the form of the `MV2r`μ and `DL1r`μ taggers.

The high-level algorithms are trained using a hybrid sample that contains both $t\bar{t}$ and Z' events, in order to populate both the low p_{T} (below 250 GeV) and high p_{T} region (above 250 GeV).

The performance of the different b-tagging algorithms is evaluated based on their ability of selecting b-jets while rejecting light-flavour jets. The light-flavour and c-jet rejections are shown in Figure 4.9 as a function of the b-jet tagging efficiency.

Once the several b-tagging algorithms have been optimised, it is crucial to measure the b-tagging efficiency in data in order to account for possible imperfections of the detector response or of the modelling of physics processes. Dedicated calibrations are therefore carried on in order to estimate from collision data the efficiency of tagging b-jets or misidentifying them as c- or light-jets, analysing clean samples of b-, c- or light-jets, respectively. The calibration results are therefore provided, as a function of the jet p_{T}, in the form of Scale Factors (SFs): $\frac{\varepsilon^{\mathrm{data}}}{\varepsilon^{\mathrm{MC}}}$, where $\varepsilon^{\mathrm{data}}$ and $\varepsilon^{\mathrm{MC}}$ represent the efficiency measured in data and estimated from simulation, respectively. The SFs are then applied as additional weights to the simulated events on a jet-by-jet basis in order to correct the efficiency in MC to the one observed in data.

The main feature that distinguishes b-jets from light-flavour jets is the presence of tracks originating from the SV. In order to exploit this feature, the transverse impact parameter d_0 is signed with the sign defined by the angle between the jet axis and the line between the PV and the point of closest approach of the track. This entails that the resolution effect is mostly symmetric with respect to the PV hence the amount of positive and negative d_0 tracks is almost identical, while the tracks originating from the SV are more likely to have positive d_0. Under the assumption that the misidentification is mainly coming from the finite resolution of the reconstructed tracks and the IP, the signed IP distributions are expected to be symmetric around zero for tracks associated to light-flavour jets. Therefore the tagging rate obtained after flipping the sign of the IP and decay length when running the `IP2D` and `IP3D` algorithms can be considered a good estimate for the light-jets misidentification rate.

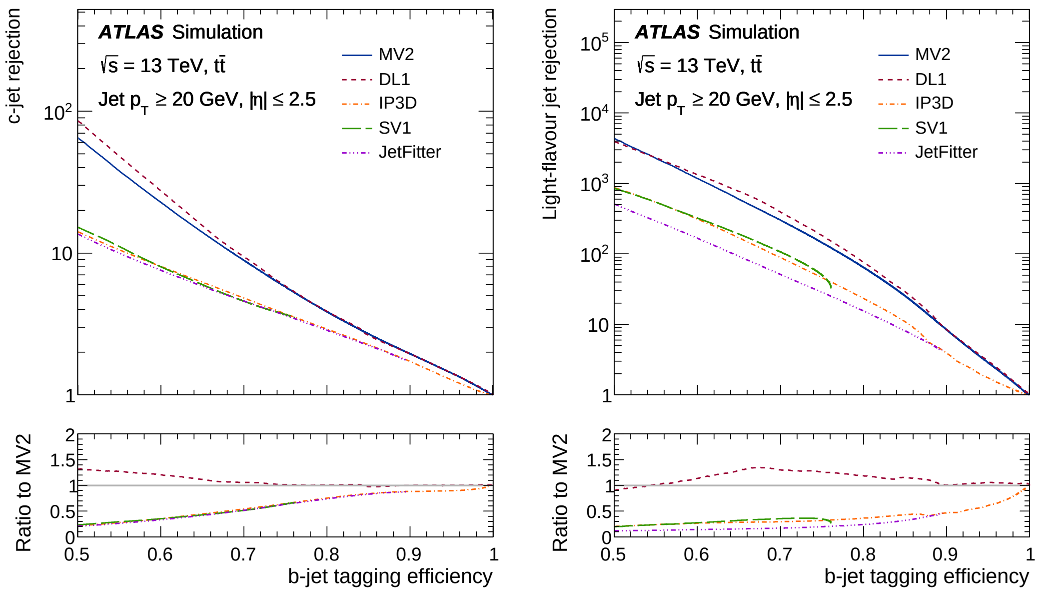

(a) (b)

FIGURE 4.9: *c*-jet (on the left) and light-flavour jet (on the right) rejection as a function of the *b*-jet tagging efficiency for the `IP3D`, `SV1`, `JetFitter`, `MV2` and `DL1` *b*-tagging algorithms. Figures taken from Ref. [112].

This is the main feature of the so-called *flipped* taggers which are used to extract the light mistag rate from $Z(\rightarrow ll)$ + jets or di-jet events (*negative tag* method) [113].

On the other hand, in order to extract the *c*-jet mistag rate, a sample of semi-leptonic $t\bar{t}$ events, where one of the two W bosons decays hadronically and the other leptonically (l=e,μ), can be analysed. At least one of the two quarks originating from the W boson is required to have charm flavour and therefore the *c*-jet misidentification rate is extracted by evaluating how many times the *c*-jet candidate is wrongly classified as *b*-jet [114].

Lastly, the *b*-tagging efficiency is measured in data from a clean sample of *b*-jets coming from di-leptonic $t\bar{t}$ events with opposite sign leptons and exactly two jets. In order to further increase the purity of *b*-jets, additional requirements are applied on variables which do not use the *b*-tagging information, such that both the *b*-jet identification efficiency and the flavour fractions can be extracted from a combinatorial likelihood fit [115, 112]. The method is described in more details in the Section 6.1, where the results obtained in the case of VR track jets are discussed.

Both *b*-tagging efficiency and the light/*c*-jets mistag rate SFs are derived in a limited p_{T} range. At high p_{T}, where the statistics becomes too poor, an alternative assessment of the uncertainty on the measured *b*-tagging efficiency is developed. The value of the SFs is fixed to the one in the highest calibrated p_{T} bin while an additional high p_{T} uncertainty is derived by varying sensitive quantities in simulation and recomputing the *b*-jet tagging efficiency for each variation [112].

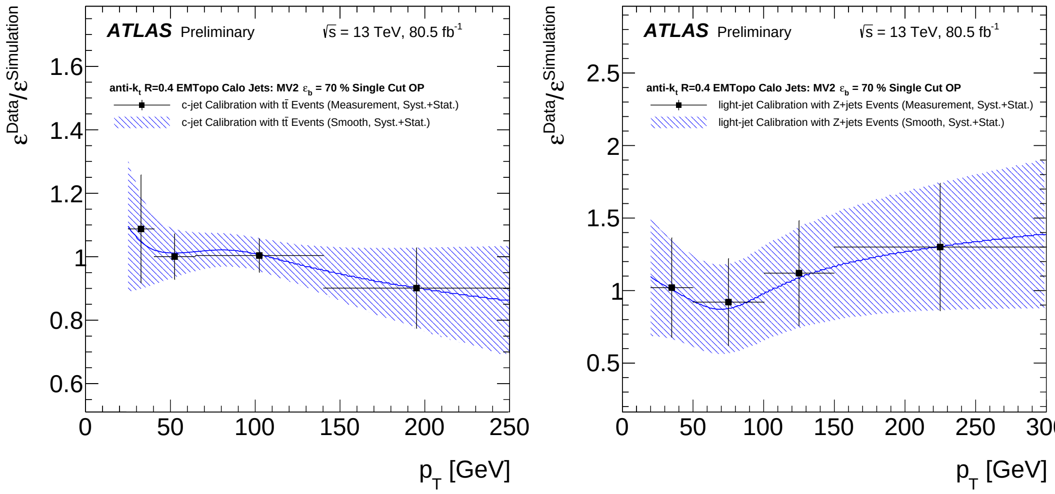

(a) (b)

FIGURE 4.10: *c*-jet (on the left) and light-jet (on the right) mistag rate data/MC SFs derived for the anti-k_t R=0.4 calorimeter jets, calibrated at the electromagnetic scale. Both single data/MC SFs correction factors and the smoothed curve are shown. Figures taken from Ref. [116].

4.4 Electrons

As described in Section 3.2, an electron passing through the ATLAS detector gives rise to a track in the ID and energy deposits in the ECAL. The information of the two sub-detectors are combined in order to identify the electron candidate. As the acceptance of the ID extends up to $|\eta| = 2.5$, no distinction can be made between electrons and photons in the forward region, where only the EMEC information can be used. For this reason, only electrons in central region $|\eta| < 2.47$ are usually considered for physics analyses. Further selections and quality requirements are then applied in order to distinguish signal-like electrons from background-like objects like hadronic jets or electrons from photon conversion. The performance of the electron reconstruction, identification, isolation, and charge identification algorithms is evaluated in data and in simulated samples using electrons from $Z \to ee$ and $J/\psi \to ee$ decays.

The baseline identification algorithm is based on a likelihood method consisting of a MVA technique which takes into account different properties of the electron candidate. In addition to the likelihood discriminant variable, also the number of hits per track is used as information to define the electron candidate. Three levels of identifications are defined (`Loose`, `Medium` and `Tight`), each of them applying a different selection on the final likelihood discriminant. Each operating point is then optimised with respect to η and the sum of transverse energies of the topological clusters [91] E_{T} in the ECAL, as shown in Figure 4.11. The identification efficiency varies from 58% at E_{T} = 4.5 GeV to 88% at E_{T} = 100 GeV for the `Tight` operating point, and from 86% at E_{T} = 20 GeV to 95% at E_{T} = 100 GeV for the `Loose` operating point. The uncertainties on the efficiency are about ± 7% at E_{T} = 4.5 GeV and decrease at high E_{T} to less than ± 1% for 30 GeV < E_{T} < 250 GeV [117]. The drop in efficiency around $|\eta| = 1.5$ is due to the electrons coming from the transition region between the EMB and the EMEC which contains a large amount of inactive material (as discussed in Section 3.2.2).

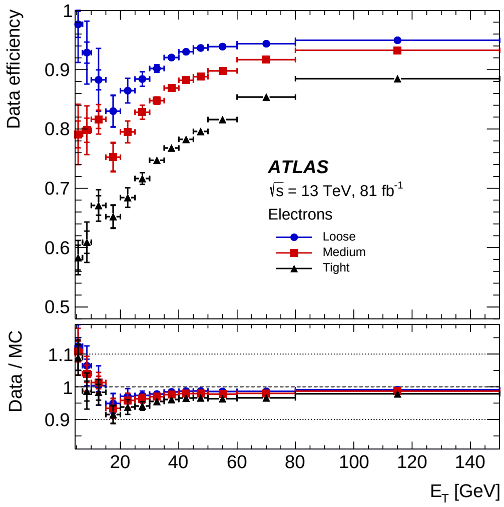

(a)

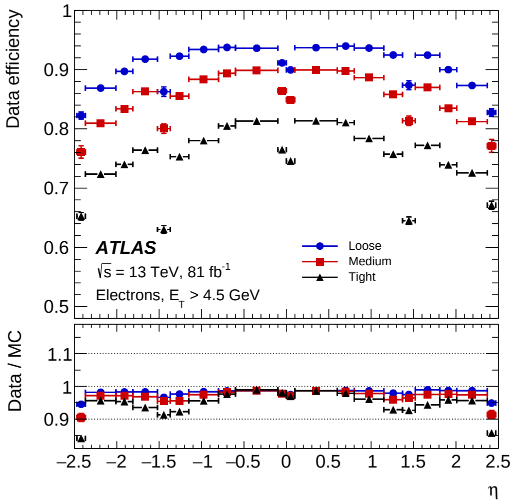

(b)

FIGURE 4.11: Electron-identification efficiency in $Z \to ee$ events for the `Loose` (blue circle), `Medium` (red square) and `Tight` (black triangle) operating points as a function of η (on the right) and E_T (on the left). The efficiencies are obtained by applying data-to-simulation efficiency ratios measured in $J/\psi \to ee$ and $Z \to ee$ events to $Z \to ee$ simulation. Figures taken from Ref. [117].

A signal-like electron is also expected to have little activity, both in the ECAL and ID systems, in its surrounding area. For this reason, specific requirements are also applied on the amount of activity, usually defined as the sum of transverse energies in the calorimeter clusters or transverse momenta of tracks (excluding the candidate itself) in a cone of radius $\Delta R = \sqrt{\Delta\phi^2 + \Delta\eta^2}$ with respect to the direction of the electron candidate. Two possible isolation variables can therefore be defined. When using only the calorimeter information, the activity is defined as $E_{\mathrm{T,cone}}^{\mathrm{isol}}$:

$$E_{\mathrm{T,cone}}^{\mathrm{isol}} = E_{\mathrm{T,raw}} - E_{\mathrm{T,core}} - E_{\mathrm{T,leakage}} - E_{\mathrm{T,pile\text{-}up}} \tag{4.7}$$

where $E_{\mathrm{T,raw}}$ is the sum of the transverse energies of all the topological clusters whose barycentres fall within the cone of radius ΔR, including the transverse energy of the electron candidate $E_{\mathrm{T,core}}$, while $E_{\mathrm{T,leakage}}$ and $E_{\mathrm{T,pile\text{-}up}}$ are the corrections for the average leakage, pile-up and underlying events. Alternatively, a track-based definition of the activity can be used by summing the transverse momenta of the tracks found within the ΔR cone, excluding the candidate's own contribution. Given the finer granularity of the ID it is possible to exploit also very narrow cones. For this reason, when using only tracking information, a variable-cone size can be defined as a function of p_{T} of the candidate object:

$$\Delta R = \min\left(R_{\mathrm{max}}, \frac{10\ \mathrm{GeV}}{p_{\mathrm{T}}}\right). \tag{4.8}$$

A value of 0.2 is generally chosen for electrons for both the cone size of the $E_{\mathrm{T,cone}}^{\mathrm{isol}}$ variable and for R_{max} in the case of the tracking-based approach. The isolation efficiency is therefore optimised with respect to these parameters and different operating points are distinguished depending whether a fixed value of the efficiency is targeted or a fixed cut on the isolation variable is performed. The `Gradient` criterium targets a fixed value of the isolation efficiency, dependent on the p_T and uniform in η of the electron while other three `FixedCut` selections (`Loose`, `Tight` and `HighPtCaloOnly`) are defined by applying a specific cut on the isolation variable. Figure 4.12 shows the isolation efficiencies measured in data recorded in 2017, using a tag-and-probe method, and the corresponding ratios with respect to the simulation are shown for different operating points. The overall differences between data and simulation are in general smaller than 1–5 % depending on the working point, with the largest difference observed for `Fixed Cut Tight` isolation.

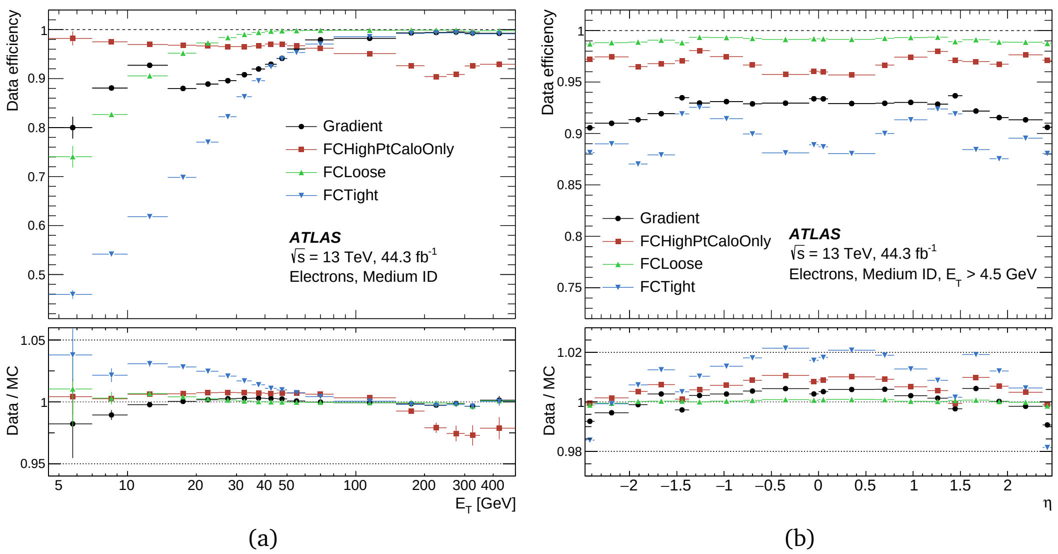

FIGURE 4.12: Efficiency of the different isolation operating points for electrons from inclusive $Z \to ee$ events as a function of E_T (at the top) and p_T (at the bottom). The electrons are required to fulfil the `Medium` selection from the likelihood-based electron identification. The lower panel shows the ratio of the efficiencies measured in data and in MC simulations. Figures taken from [117].

4.5 Muons

The muon reconstruction and identification rely on the information obtained from the ID, the MS and the calorimeters. The reconstruction is first performed independently in each sub-detector and then combined. The muon candidate is then classified in different categories:

- Standalone muon (SA): the muon candidate is identified using only the track reconstructed in the MS,
- CB: the reconstruction is performed separately in the ID and in the MS and a combined track is formed by performing a global fit on the hits from the ID and MS,
- Calorimeter-Tagged muon (CT): in this case, the track reconstructed in the ID is required to match an energy deposit in the calorimeter compatible with the one of a minimum ionising particle,

- Segmented-Tagged muon (ST): the muon track candidate reconstructed in the ID, once extrapolated to the MS, is required to match at least one segment in the MDTs or CSCs,
- SiliconAssociatedForward muon (SiA): the muon candidate is identified using a SA track matched to segments in the silicon tracker.

Based on these categories, four inclusive muon identification selections are defined, aimed at improving either the purity or the acceptance of signal-like muons: `Loose`, `Medium`, `Tight`, `Low-`p_T and `High-`p_T. The `Medium` selection is the most widely used as it provides good acceptance with relatively small fake-rate and uncertainties. The `Loose` and `Tight` working points are dedicated to improve, respectively, the acceptance and the purity with respect to the `Medium` selection. Lastly, the `High-`p_T selection aims at optimising the reconstruction efficiency for muons up to several TeV, while the `Low-`p_T one is dedicated at the reconstruction of muons with p_T down to 5 GeV, while maintaining a reasonable fake rate.

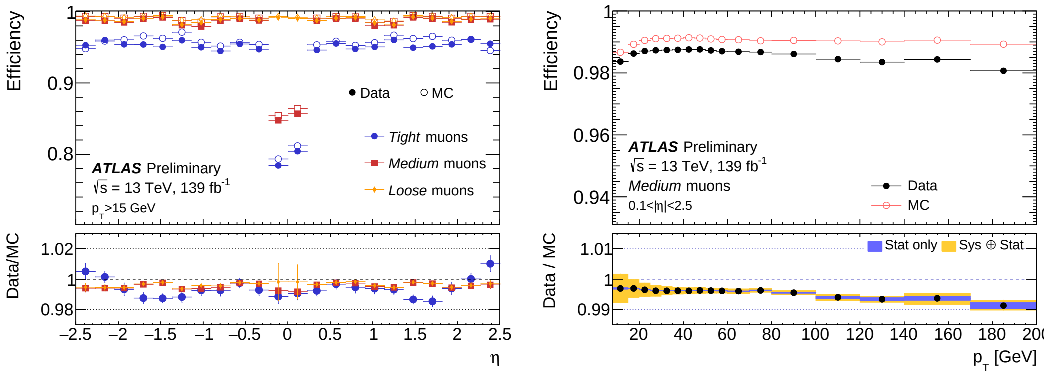

(a) (b)

FIGURE 4.13: Muon reconstruction efficiency measured in $Z \to \mu\mu$ as a function of η for the `Loose-Medium-Tight` selections (on the left) and as a function of p_T for the `Medium` selection (on the right). The results are based on the pp collision data collected during Run 2 of the LHC at 13 TeV. Figures taken from Ref. [118].

As the measurement is performed independently with two different sub-detectors in the $|\eta| < 2.5$ region, a tag-and-probe method using $Z \to \mu\mu$ and $J/\psi \to \mu\mu$ events is used to evaluate the muon reconstruction efficiency, as shown in Figure 4.13. A different approach is instead used in the region $2.5 < |\eta| < 2.7$ where muons are reconstructed using only the MS detector [119].

It is important also in the case of muons to apply specific isolation requirements in order to mitigate the contribution from background-like objects. A track-based and a calorimeter-based isolation variable are usually adopted, following the same definitions illustrated in Equations 4.7 and 4.8. For the track-based term, the transverse momenta of tracks with $p_T > 1$ GeV falling into a variable radius defined in Equation 4.8 with $R_{max} = 0.3$ around the muon candidate axis are summed together. This sum hence defines the $p_T^{varcone30}$ isolation variable. For the calorimeter term, the transverse energies of the topological clusters within a cone of $R_{max} = 0.2$ (or 0.3, 0.4) around the muon direction are combined together and corrections for pile-up and underlying events are also applied, defining the $E_T^{topocone20}$ variable. Several isolation working points are defined using these variables and, as for the electrons, they can be distinguished in two main categories: the first one simply applies a fixed cut on the selected isolation variable (either calorimeter-based or track-based) while the second one is designed to target a specific value of the efficiency dependent on the muon p_{T}.

4.6 τ leptons

Jets originating from hadronically decaying τ leptons are usually classified into the one-prong or three-prong categories, corresponding to the number of charged pions ($\pi^{\pm}$) produced by the τ decay. In addition to that, a significant fraction of the energy is deposited in the ECAL by the photons originating from the decay of neutral pions. Such typical signatures are hence exploited in order to develop dedicated τ identification algorithms, as described more extensively in Ref. [120, 121]. A τ candidate jet is required to have $p_{\mathrm{T}} > 20$ GeV, $|\eta| < 2.5$ and to be outside of the transition region between the barrel and forward calorimeters ($1.37 < |\eta| < 1.52$). The τ vertex is chosen as the one with the largest fraction of momentum from tracks (with $p_{\mathrm{T}} > 1$ GeV) associated within $\Delta R = 0.2$ with respect to the jet axis. Additional requirements are also applied on the transverse and longitudinal impact parameter of each track with respect to the τ vertex. The baseline τ identification procedure consists in processing both the tracking and calorimeter information in order to build a BDT discriminant. Three operating points (`Loose`, `Medium` and `Tight`) are defined, each of them corresponding to different τ identification efficiency values (designed to be independent of p_{T}). The performance of the reconstruction and identification algorithms are then measured, using a tag-and-probe method, from $Z \to \tau\tau$ events where one τ lepton decays hadronically and the other decays leptonically to a muon and a neutrino.

4.7 $E_{\mathrm{T}}^{\mathrm{miss}}$

Once all the objects in the final state have been reconstructed, it is possible to calculate the missing transverse momentum $E_{\mathrm{T}}^{\mathrm{miss}}$, which is defined as the negative vectorial sum of the transverse momenta of all the calibrated objects present in the final state. The $E_{\mathrm{T}}^{\mathrm{miss}}$ reconstruction consists of a *hard* term, which evaluates the contribution from all the fully reconstructed and calibrated objects like electrons, muons, τ leptons, photons (γ) and jets (hard objects), and the *soft* term, arising from reconstructed soft charged particle tracks associated with the hard-scattering process but not with any hard object (soft signals). The $E_{\mathrm{T}}^{\mathrm{miss}}$ components can therefore be defined as [122]:

$$E_{\mathrm{x(y)}}^{\mathrm{miss}} = -\sum_{i\in\{\text{hard objects}\}} p_{x(y),i} - \sum_{j\in\{\text{soft signals}\}} p_{x(y),j}. \tag{4.9}$$

The $E_{\mathrm{x(y)}}^{\mathrm{miss}}$ components are then used to build the following variables:

$$\begin{aligned} \mathbf{E}_{\mathrm{T}}^{\mathrm{miss}} &= (E_{\mathrm{x}}^{\mathrm{miss}}, E_{\mathrm{y}}^{\mathrm{miss}}) \\ E_{\mathrm{T}}^{\mathrm{miss}} &= |\mathbf{E}_{\mathrm{T}}^{\mathrm{miss}}| = \sqrt{(E_{\mathrm{x}}^{\mathrm{miss}})^2 + (E_{\mathrm{y}}^{\mathrm{miss}})^2} \\ \phi^{\mathrm{miss}} &= \tan^{-1}(E_{\mathrm{y}}^{\mathrm{miss}}/E_{\mathrm{x}}^{\mathrm{miss}}) \end{aligned} \tag{4.10}$$

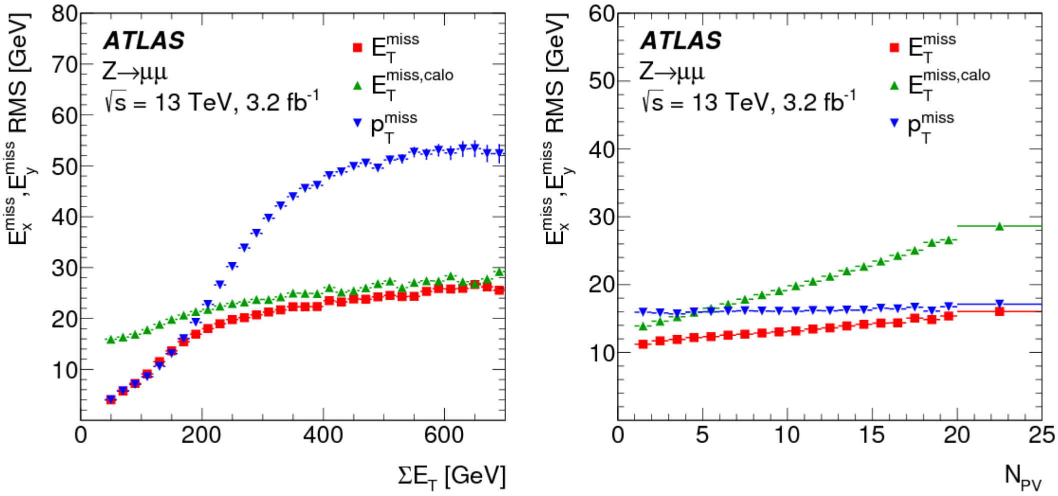

(a) (b)

FIGURE 4.14: Comparison of the reference $E_{\mathrm{T}}^{\mathrm{miss}}$ resolution (in red) with respect to the track-only-based variant (in blue) and calorimeter-based variant (in green), measured from an inclusive $Z \to \mu\mu$ sample in data, as a function of $\sum E_{\mathrm{T}}$ (on the left) and number of PV (on the right). Figures taken from Ref. [122].

where $E_{\mathrm{T}}^{\mathrm{miss}}$ and ϕ^{miss} represent, respectively, the magnitude and the direction in the transverse plane of the $\mathbf{E}_{\mathrm{T}}^{\mathrm{miss}}$ vector. So the $E_{\mathrm{T}}^{\mathrm{miss}}$ vector can finally be defined as:

$$\begin{aligned} \mathbf{E}_{\mathrm{T}}^{\mathrm{miss}} = - \sum_{\text{selected electrons}} \mathbf{p}_{\mathrm{T}}^{e} - \sum_{\text{accepted photons}} \mathbf{p}_{\mathrm{T}}^{\gamma} - \sum_{\text{accepted } \tau \text{ leptons}} \mathbf{p}_{\mathrm{T}}^{\tau_{\mathrm{had}}} \\ - \sum_{\text{selected muons}} \mathbf{p}_{\mathrm{T}}^{\mu} - \sum_{\text{accepted jets}} \mathbf{p}_{\mathrm{T}}^{\mathrm{jets}} - \sum_{\text{unused tracks}} \mathbf{p}_{\mathrm{T}}^{\mathrm{track}}. \end{aligned} \tag{4.11}$$

In addition to the $E_{\mathrm{T}}^{\mathrm{miss}}$, other variables, like $\sum E_{\mathrm{T}}$, are sometimes also used to estimate the event activity:

$$\sum E_{\mathrm{T}} = \sum p_{\mathrm{T}}^{\mu} + \sum p_{\mathrm{T}}^{e} + \sum p_{\mathrm{T}}^{\gamma} + \sum p_{\mathrm{T}}^{\tau} + \sum p_{\mathrm{T}}^{\mathrm{jets}} + \sum p_{\mathrm{T}}^{\mathrm{soft}} \tag{4.12}$$

or its hard object equivalent variable, called H_{T}, which is defined as:

$$H_{\mathrm{T}} = \sum p_{\mathrm{T}}^{\mu} + \sum p_{\mathrm{T}}^{e} + \sum p_{\mathrm{T}}^{\gamma} + \sum p_{\mathrm{T}}^{\tau} + \sum p_{\mathrm{T}}^{\mathrm{jets}}. \tag{4.13}$$

The soft term of the $E_{\mathrm{T}}^{\mathrm{miss}}$ is of crucial importance for the estimation of the $E_{\mathrm{T}}^{\mathrm{miss}}$ scale and resolution, in particular in events with low jet activity. In the Run 2 analyses, the soft-term used is the Track-based Soft Term (TST), which only uses reconstructed tracks from the ID associated to the PV and having $p_{\mathrm{T}} > 500$ MeV, $|\eta| < 2.5$ (full ID coverage) and $|d_0/\sigma(d_0)| < 2$, $|z_0 \sin(\theta)| < 3$ mm. In addition to these criteria, further cuts are applied on the angular separation between tracks and electrons, photons and τ leptons. The TST term has found to have a better stability with respect to pile-up and provides a better resolution in events with low $\sum E_{\mathrm{T}}$, as shown in Figure 4.14.

As the $E_{\mathrm{T}}^{\mathrm{miss}}$ performance is affected by the selection of jets used for its calculation, a few alternative operating points are defined:

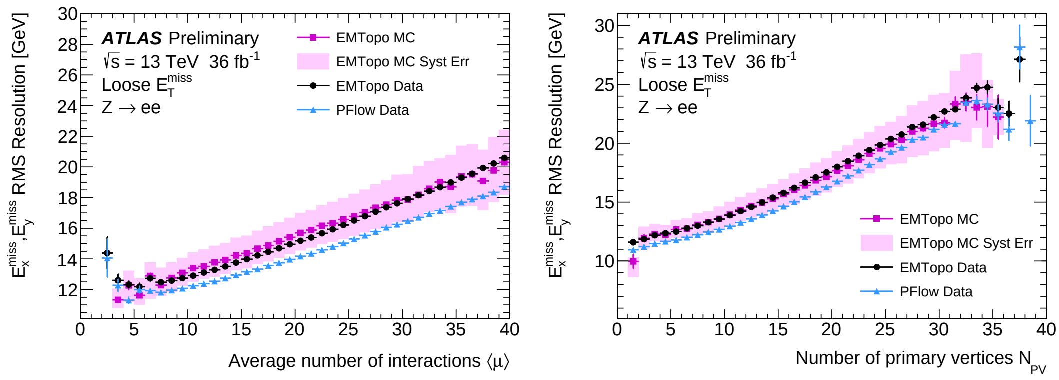

(a) (b)

FIGURE 4.15: Distribution of the $E_{\mathrm{T}}^{\mathrm{miss}}$ Root Mean Squared (RMS), for the case of the Loose $E_{\mathrm{T}}^{\mathrm{miss}}$ operating point, shown as a function of the average number of interactions per bunch-crossing $\langle\mu\rangle$ (on the left) and as a function of the number of PV (on the right), as estimated after a $Z \to ee$ event selection. Different curves are shown for the case of small-R calorimeter jets calibrated at the electromagnetic scale (EMTopo) and Particle-Flow jets [125] and simulation with EMTopo jets. Figures taken from Ref. [124].

- `Loose`: includes all jets with $p_{\mathrm{T}} > 20$ GeV and passing the JVT requirements (see Section 4.2.1),
- `Tight`: discard all forward jets with $|\eta| > 2.4$ and $20 \text{ GeV} < p_{\mathrm{T}} < 30$ GeV in order to reduce the pile-up dependence of the $E_{\mathrm{T}}^{\mathrm{miss}}$ (at the price of a worse scale and resolution),
- `Forward-JVT (fJVT)`: also developed in order to suppress the forward pile-up jet contamination, it still considers all jets with $p_{\mathrm{T}} > 20$ GeV, except the forward jets with $|\eta| > 2.5$ and $20 \text{ GeV} < p_{\mathrm{T}} < 50$ GeV and failing the `Loose` fJVT cut[5]. A JVT requirement is still applied to jets with $p_{\mathrm{T}} < 60$ GeV.

For what concerns the evaluation of the systematic uncertainties on the $E_{\mathrm{T}}^{\mathrm{miss}}$, it is important to notice that, while for the *hard* term the uncertainties affecting each object entering in the $E_{\mathrm{T}}^{\mathrm{miss}}$ reconstruction are directly propagated to the $E_{\mathrm{T}}^{\mathrm{miss}}$ calculation, the uncertainty on the *soft* term must be evaluated separately. A comprehensive description of such uncertainty can be found in Ref. [124].

[5]Fully described in Ref. [123], the fJVT is a novel technique that exploits the correlation between central and forward jets in order to suppress the forward pile-up jet contribution.

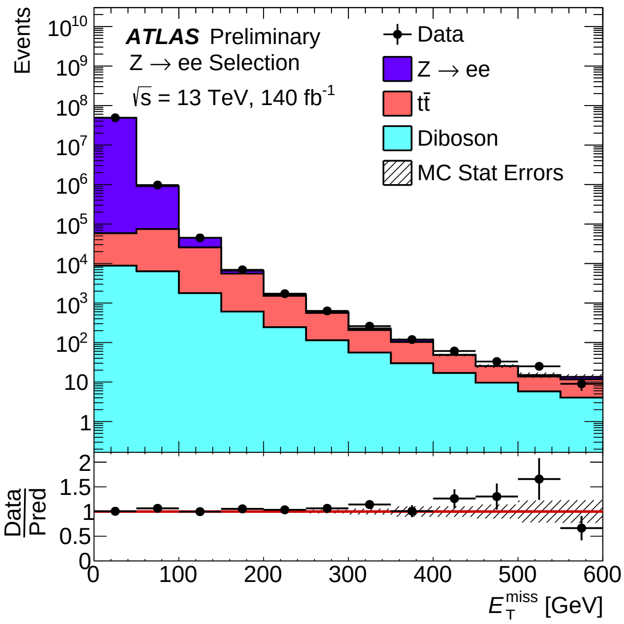

FIGURE 4.16: Data to simulation comparison of the E_T^{miss} spectrum, using the full Run 2 dataset of the LHC, as estimated from $Z \to ee$ events. Figure taken from Ref. [126].

4.7.1 E_T^{miss} significance

As already anticipated, the conservation of the momentum in the transverse plane implies that the vectorial sum of the momenta of all objects in the final state should be zero. Any imbalance in the transverse plane gives rise to E_T^{miss} and it can be attributed to invisible particles, such as neutrinos or more exotics weakly interacting particles. However, fake E_T^{miss} can arise from jets not falling into the acceptance of the detector or inaccurately reconstructed, or due to resolution effects. It is therefore crucial to be able to distinguish events with *fake* and *real* E_T^{miss}. A useful quantity that can help in discriminating these two categories is the E_T^{miss} significance, $\mathcal{S}$, which evaluates how likely is that there is genuine E_T^{miss} from undetectable particles in the event. On an event-by-event basis, $\mathcal{S}$ is determined from the LLR that the reconstructed E_T^{miss} is consistent with the null hypothesis of having zero real E_T^{miss}. In the past, in ATLAS and also in previous experiments, the following two event-based definitions of $\mathcal{S}$ have been used:

$$\mathcal{S} = \frac{E_T^{miss}}{\sqrt{\sum E_T}} \quad \text{or} \quad \mathcal{S} = \frac{E_T^{miss}}{\sqrt{H_T}} \tag{4.14}$$

as $\sqrt{\sum E_T}$ and $\sqrt{H_T}$ can be considered as event-based approximations of the E_T^{miss} total resolution. Such approximation is valid as long as only the calorimeter information is used in calculation of the E_T^{miss} but, as discussed in Section 4.7, the E_T^{miss} reconstruction involves also other sub-detectors. For this reason, a new approach has been developed in order to construct a new definition of $\mathcal{S}$ at the object-level, taking into account all the expected resolutions and directional correlations of all the objects entering in the E_T^{miss} reconstruction [127]. As the goal is to test the hypothesis that the total transverse momentum carried by the invisible particles, p_T^{inv}, is zero against

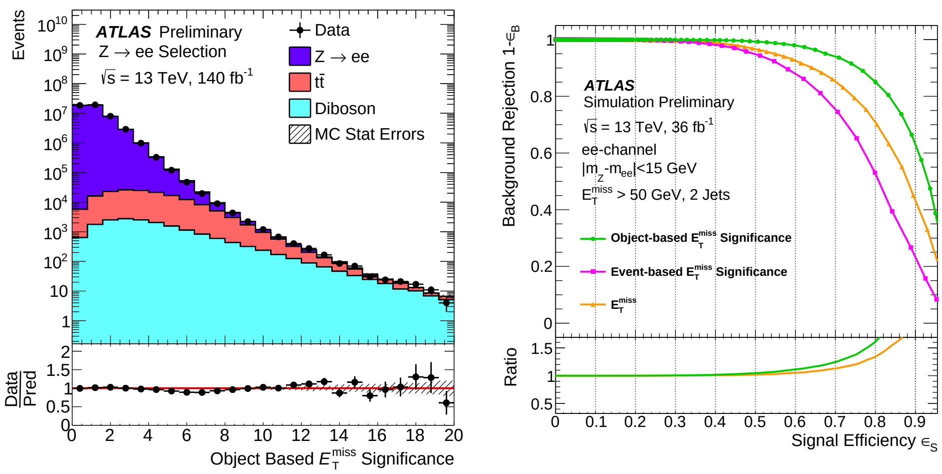

(a) (b)

FIGURE 4.17: On the left, data to simulation comparison of the object-based E_T^{miss} significance spectrum, using the full Run 2 dataset of the LHC, as estimated from $Z \to ee$ events. Figure taken from Ref. [126]. On the right, object-based E_T^{miss} significance background rejection versus signal efficiency in simulated $Z \to ee$ and $ZZ \to ee\nu\nu$ events compared with the previous event-based definitions. Figure taken from Ref. [127].

the hypothesis that p_T^{inv} is different from zero, $\mathcal{S}$ can defined as the following LLR:

$$\mathcal{S}^2 = 2\ln\left(\frac{\mathcal{L}(E_T^{miss}|E_T^{miss})}{\mathcal{L}(E_T^{miss}|0)}\right) = (E_T^{miss})^T\left(\sum_i V^i\right)^{-1}(E_T^{miss}) \tag{4.15}$$

where the index i indicates each object entering in the E_T^{miss} reconstruction and V^i the corresponding covariance matrix. It is possible to appreciate, from this χ^2 definition of the E_T^{miss} significance, the strong dependence between the E_T^{miss} and the resolution effects propagated inside the covariance matrix. A small value of $\mathcal{S}$ is expected in case the event is compatible with the hypothesis of having fake E_T^{miss} from detector effects, whereas large values of $\mathcal{S}$ should indicate the presence of real E_T^{miss}. The Equation 4.15 can be further simplified and $\mathcal{S}$ can be reduced to:

$$\mathcal{S}^2 = \frac{|E_T^{miss}|^2}{\sigma_L^2(1-\rho_{LT}^2)} \tag{4.16}$$

where σ_L is the total variance in the direction longitudinal to E_T^{miss} and ρ_{LT} is the correlation factor between the transverse (T) and longitudinal (L) measurements with respect to the direction of the E_T^{miss} vector. A detailed description of the object-based E_T^{miss} significance can be found in Ref. [127]. The performance of this variable has been studied in $Z \to ee$ and $ZZ \to ee\nu\nu$ events and its discriminating power with respect to the previous event-based definitions is shown in Figure 4.17b.

4.8 Overlap removal

In order to resolve ambiguities between leptons and jets, an overlap removal procedure must be applied in each physics analysis. The standard method proceeds through a list of consecutive steps, where only the surviving objects participate in the subsequent steps. Initially, electrons are removed if they share a track with another electron candidate with higher p_{T} or with a muon candidate. Next, τ candidates are removed if they are within $\Delta R = 0.2$ of an electron or a muon candidate. Photons are also rejected against leptons in case they overlap within $\Delta R = 0.4$. Small-R jets are then removed if they lie within $\Delta R = 0.2$ with respect to any remaining electrons. Successively, a lepton (either an electron or a muon) is removed if it lies within $\Delta R = \min(0.4, 0.04 + 10\ \mathrm{GeV}/p_{\mathrm{T}}^{\mathrm{lepton}})$ with respect to the small-R jet. Small-R jets are further removed if they are within $\Delta R = 0.2$ of any surviving muon, in case the jet has less than three tracks or the muon p_{T} is greater than half the jet p_{T} and greater than 70% of the p_{T} sum of the tracks associated to the jet. Moreover, muons are removed if they are within $\min(0.4, 0.04 + 10\ \mathrm{GeV}/p_{\mathrm{T}}^{\mathrm{lepton}})$ of a small-R jet. Lastly, large-R jets are removed if they are separated from an electron by less than $\Delta R = 1.0$.

4.9 Pile-up reweighting

The last missing piece of the event reconstruction, for what concerns the work presented in this thesis, is related to the modelling of *pile-up*. As already mentioned in Section 3.1.3, the pile-up can be interpreted as the amount of uncorrelated energy flow originating from additional collisions occurring in the event or due to the "hardness" of a single collision. The presence of additional energy flow in the detector can have a strong impact on physics analyses, as it would lead to a lower or higher number of events passing certain selection criteria. It is therefore important to model properly the amount of pile-up events in simulation. The pile-up reweighting procedure aims at correcting for the difference between data and simulation by scaling the selection efficiency of an event such that *on average* the predicted $<\mu>$ distribution matches the one observed in data.

The amount of pile-up is related to the average number of interactions in a bunch crossing which is measured in data from the inelastic collisions occurring in minimum bias events. However, the visible inelastic cross section in simulation has found to be higher than the one measured in data [128]. Furthermore, MC events are simulated for a given value of the beamspot length, which instead can vary in collision data. As a result, the estimated number of interactions per crossing as well as other pile-up sensitive variables, as the number of vertices, is known to be wrong. The generated discrete values of $\langle\mu\rangle$ are therefore corrected in simulation by the offset due to the inelastic cross-section mismodelling. Only after this correction, it is possible to derive an event weight which modifies the effective efficiency for an event to pass the selection of the analysis.

5 The mono-H($b\bar{b}$) analysis

As anticipated in Chapter 2, the search for events with a large amount of $E_{\mathrm{T}}^{\mathrm{miss}}$ recoiling against a SM particle is a probe for detecting DM at the LHC. The discovery of the Higgs boson h (see Refs. [16, 17]) opens a new opportunity through the $h+E_{\mathrm{T}}^{\mathrm{miss}}$ signature, with the highest probability for the Higgs boson to decay to bottom quarks (b), thus defining the mono-H($b\bar{b}$) final state. The mono-H($b\bar{b}$) channel has proved to have a leading role in the search for DM at the LHC, as it allows to probe a substantial region of the phase space while being complementary to several other mono-X searches. This chapter is dedicated to the description of the mono-H($b\bar{b}$) analysis performed using pp collisions at a centre-of-mass energy of 13 TeV and a dataset corresponding to 79.8 fb^{-1} of integrated luminosity.

5.1 Analysis strategy

One of the BSM theories that motivates the search for mono-H($b\bar{b}$) events is the Type-II 2HDM with an additional U(1)$_{Z'}$ gauge symmetry, referred to as Z'-2HDM [129]. The 2HDM model predicts the existence of five physical Higgs bosons: a light scalar h, which is identified with the SM Higgs boson, a heavy scalar, denoted as H, the pseudo-scalar A and the two charged scalar bosons $H^{\pm}$. The process yielding the signature of h+DM is $pp \to Z' \to Ah$, with the subsequent decay of A to $\chi\bar{\chi}$, as illustrated in Figure 5.1. The relevant model parameters are therefore the masses of the involved particles, m_A, $m_{Z'}$, m_χ, as well as the gauge coupling of the Z', $g_{Z'}$, and $\tan\beta$, which denotes the ratio of the vacuum expectation values of the two Higgs fields coupling to the up- and down-type quarks.

Depending on the mass of the new mediator particle, the topology of the event can be very different. At low masses, the p_{T} of the Higgs boson can be still sufficiently low that the Higgs candidate can be reconstructed as a pair of two single small-R calorimeter jets, corresponding to the two b-quarks. On the other hand, when the energy is sufficiently high, the Higgs boson can become very energetic and its decay products tend to be very collimated; in this regime the Higgs candidate is reconstructed as a single large-R calorimeter jet having a substructure consistent with the fragmentation of two b-quarks. An illustration of the two different topologies is shown in Figure 5.2.

The $E_{\mathrm{T}}^{\mathrm{miss}}$ originating from the DM particles and the jet system recoil against each other, thus their transverse momenta are highly correlated. For this reason, in order to maximise the sensitivity of the analysis, a distinction is made between the *resolved*

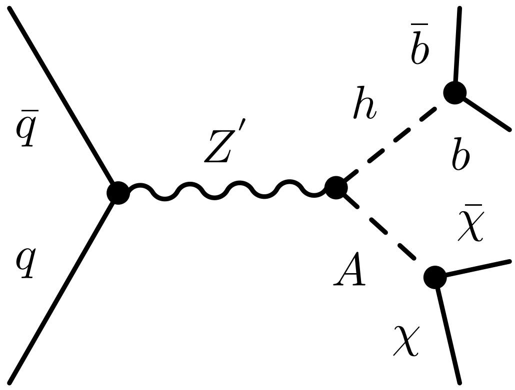

FIGURE 5.1: The leading-order contribution of the production of DM and a Higgs boson through a new Z' mediator coupled to a pseudo-scalar Higgs boson A, where the latter decays primarily to $\chi\bar{\chi}$. Figure taken from Ref. [130].

regime ($E_{\mathrm{T}}^{\mathrm{miss}} < 500$ GeV) and the *merged* (or *boosted*) regime ($E_{\mathrm{T}}^{\mathrm{miss}} \geqslant 500$ GeV). Signal events are expected to have two b-tagged jets coming from the $H \to b\bar{b}$ decay. In the resolved case, the b-tagging is applied to the leading two central small-R jets, while in the merged case, the identification of the flavour content of the large-R jet is based on track jets ghost-associated [107] with the ungroomed jet (see Sections 4.2.2-4.2.3).

The SR is characterised by the presence of high $E_{\mathrm{T}}^{\mathrm{miss}}$ and no isolated electrons (e) or muons (μ). The main backgrounds that contaminate the SR originate from the Z+jets, W+jets and $t\bar{t}$ processes.

In order to reduce the impact of the systematic uncertainties arising from a direct estimation of the background contribution purely from MC simulation, a semi data-driven approach is adopted [131, 132]. This method consists in defining a dedicated Control Region (CR), CR$_i$, which is orthogonal to the SR and mostly populated by a specific background BG_i. The contribution of this background in the SR can then be expressed as:

$$N_{BG_i,\mathrm{data}}^{SR} = \frac{N_{BG_i,MC}^{SR}}{N_{BG_i,MC}^{CR_i}} \times N_{BG_i,\mathrm{data}}^{CR_i} \tag{5.1}$$

where $N_{BG_i,\mathrm{data}}^{CR_i}$ corresponds to the contribution of BG_i, as extracted from data, in the CR$_i$ while $N_{BG_i,MC}^{SR}$ and $N_{BG_i,MC}^{CR_i}$ are the contributions of BG_i, predicted by MC simulation, in the SR and in the CR$_i$, respectively. The contribution of BG_i is therefore extrapolated from the CR$_i$ to the SR through the *transfer factor* $\frac{N_{BG_i,MC}^{SR}}{N_{BG_i,MC}^{CR_i}}$ which allows most of the systematic uncertainties to cancel out or to be significantly reduced in the ratio. Moreover, as the term $N_{BG_i,\mathrm{data}}^{CR_i}$ can also be expressed as $N_{\mathrm{data}}^{CR_i} - N_{\mathrm{other\ backgrounds}}^{CR_i}$, it is possible to define the *normalisation factor* as:

$$\frac{N_{\mathrm{data}}^{CR_i} - N_{\mathrm{other\ backgrounds}}^{CR_i}}{N_{BG_i,MC}^{CR_i}}. \tag{5.2}$$

As a given background process can contribute to several CRs, the normalisation factors depend on each other and the purer is the selection of each CR, the smaller is the impact of the $N^{CR_i}_{\text{other backgrounds}}$ term.

In the context of the mono-H($b\bar{b}$) analysis, 1μ-CR is used to estimate the contribution of the W+jets and $t\bar{t}$ processes, while a 2ℓ-CR (ℓ=e,μ) is used to constrain the Z+jets background.

The last step of the analysis consists in performing a simultaneous profile-likelihood fit to all the CRs and SR in order to constrain the backgrounds and extract information about the potential presence of a signal.

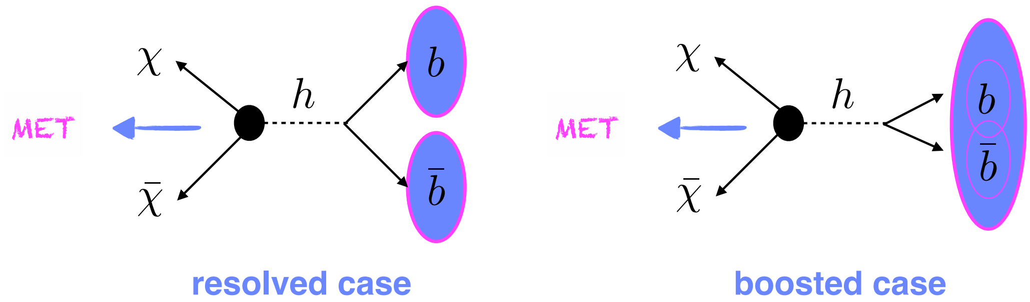

FIGURE 5.2: Illustration of the different reconstruction of the Higgs candidate in the resolved and in the merged (or *boosted*) region.

5.2 Datasets and triggers

The search is performed using the pp collision data at $\sqrt{s}$ = 13 TeV recorded by the ATLAS detector during 2015, 2016 and 2017. Only data collected with all detector components and good operating conditions, included in the so-called Good Run Lists (GRLs), are analysed.

Events in the 0 and 1 lepton regions are selected using $E_{\mathrm{T}}^{\mathrm{miss}}$ triggers, whose thresholds increase from 70 GeV for 2015 data to 110 GeV for 2017 data. Events used for control samples with two leptons are selected using the lowest unprescaled single lepton triggers with p_{T} thresholds that vary with data-taking periods. For electrons the thresholds vary from 24 GeV to 26 GeV, while for muons the p_{T} thresholds increase over time from 20 GeV to 26 GeV. All these triggers include isolation requirements. Additional triggers without isolation requirements but higher p_{T} thresholds are used to preserve trigger efficiency at high p_{T} values.

It is also important to notice that, as this analysis uses events with $E_{\mathrm{T}}^{\mathrm{miss}}$ as low as 150 GeV, where some of the triggers are not fully efficient yet, the trigger efficiencies are measured in data as a function of the $E_{\mathrm{T}}^{\mathrm{miss}}$ and correction factors for simulated samples are derived in order to match the efficiencies obtained in data.

5.3 Simulated samples

The W/Z+jets processes are simulated using the SHERPA v2.2.1 [133, 134] event generator with the NNPDF30NNLO [135] PDF set and filters corresponding to the flavour content of the final state jets. The matrix elements are computed at Next-to-Leading Order (NLO) for up to two partons and at Leading Order (LO) for up to four partons. They are merged with the SHERPA parton shower using the MEPS@NLO prescription [136]. The normalisations are determined at NNLO in QCD.

A similar setup is also used to simulate the diboson background samples using the SHERPA generator. With respect to the V+jets case, no flavour filtering is applied and only up to three additional partons are included in the matrix element, with up to one parton at NLO accuracy.

The other dominant background is top quark pair production, whose events, together with the single top quark processes, are generated at NLO using the POWHEG-BOX v2 [137] generator interfaced with PYTHIA 8.230 [138] with the A14 set of tuned parameters [139] and NNPDF30NNLO [135] PDFs in order to simulate the parton shower and hadronisation processes. The $t\bar{t}$ predictions are normalised to a cross-section calculation at NNLO in QCD, including NNLO corrections for soft-gluon radiation. The cross-section used to normalise the single-top-quark samples is calculated at NLO in QCD.

Additional backgrounds such as Vh processes are generated with the POWHEGBOX v2 generator interfaced with PYTHIA 8.230 using the NNPDF30NNLO PDF set.

Signal events corresponding to the Z'-2HDM simplified model are produced at tree-level using `MadGraph5 aMC@NLO` [140] interfaced to `Pythia8` using the NNPDF3.0 PDF set and the A14 tune. The relevant signal theory parameters are fixed to $\tan\beta = 1.0$, $g_{Z'} = 0.8$ and $m_\chi = 100$ GeV, $m_H = m_{H^\pm} = 300$ GeV and a $\mathrm{BR}(A \to \chi\bar{\chi}) = 100\%$ is assumed.

All simulated samples include detector effects as well as the impact of multiple pp interactions per bunch crossing. All samples are processed with the GEANT 4 [141] based ATLAS detector simulation [142].

5.4 Object and event selection

In this analysis, various physics objects are reconstructed and selected in order to categorise the events in different SRs and CRs. A summary of the criteria used for the reconstruction of the physics objects used in this analysis is presented in Table 5.1 for what concerns jets and $E_\mathrm{T}^\mathrm{miss}$. A summary of the electron and muon selection criteria is instead shown in Tables 5.2 and 5.3.

In addition to the data quality and trigger requirements, at least one PV with at least two associated tracks with $p_\mathrm{T} > 500$ MeV must be present in order for the event to be selected. An event veto is also applied in case a jet fails the LOOSEBADJET jet cleaning requirement (see Section 4.2), which would compromise the measurement of the $E_\mathrm{T}^\mathrm{miss}$. Events are also required to have $E_\mathrm{T}^\mathrm{miss} > 150$ GeV. In each region, a proxy for the $E_\mathrm{T}^\mathrm{miss}$ is used in order to apply the cut on the missing transverse momentum. In signal events the $E_\mathrm{T}^\mathrm{miss}$ is expected to come from DM particles while $W(l\nu)$+jets and $Z(ll)$+jets events can end up in the SR in case the leptons are wrongly reconstructed. In order to mimic the way these processes can contaminate the SR selection, in the 1μ region the muon is added to the missing transverse momentum vector and the corresponding $E_\mathrm{T}^\mathrm{miss}$ term is usually referred to as $E_\mathrm{T}^{\mathrm{miss,no}\mu}$. Similarly, in the 2ℓ region

Object	Kinematics	Type	Additional
Small-R jets *central*	$p_T > 20$ GeV $\|\eta\|$<2.5	anti-k_t R= 0.4 EMTopo	if $p_T < 60$ GeV, $\|\eta\| < 2.4$ then JVT > 0.59, b-tagging: 77% signal efficiency
Small-R jets *forward*	$p_T > 30$ GeV $2.5 < \|\eta\| < 4.5$	anti-k_t $R = 0.4$ EMTopo	
Large-R jets	$p_T > 200$ GeV $\|\eta\| < 2.0$	anti-k_t $R = 1.0$ LCTopoTrimmed $R_{\text{sub-jet}} = 0.2$, $f_{\text{cut}} = 5\%$	
Track jets	$p_T > 10$ GeV $\|\eta\| < 2.5$	anti-k_t variable-R	$N_{\text{tracks}} \geq 2$ b-tagging: 77% signal efficiency
τ leptons	$p_T > 20$ GeV $\|\eta\|$ = [0,1.37],[1.52,2.5] N_{tracks} = 1 or 3	BDT ID Loose Working Point (WP)	Extended selection: $1 \leq N_{\text{tracks}} \leq 4$ $\Delta\phi(\tau, E_T^{\text{miss}}) \leq 22.5°$
E_T^{miss}	$E_T^{\text{miss}} > 150$ GeV	E_T^{miss} TST	

TABLE 5.1: A concise summary of the jet and E_T^{miss} object selections used in the analysis.

Electron Type	p_T [GeV]	$\|\eta\|$	$d_0/\sigma(d_0)$	$\|z_0 \sin\theta\|$ [mm]	ID	Isolation
VH-loose	> 7 GeV	< 2.47	< 5	< 0.5	LooseLLHBLayer	LooseTrackOnly
ZH-signal	> 27 GeV	< 2.47	< 5	< 0.5	LooseLLHBLayer	LooseTrackOnly

TABLE 5.2: A summary of the electron object selections used in the analysis. The VH-loose definition is used in the 0ℓ and 1μ channels to veto electrons. The ZH-signal definition is used in the ee channel.

Muon Type	p_T [GeV]	$\|\eta\|$	$d_0/\sigma(d_0)$	$\|z_0 \sin\theta\|$ [mm]	ID	Isolation
VH-loose (veto, 0 lepton channel)	> 7 GeV	< 2.7	< 3	< 0.5	Loose	LooseTrackOnly
WH-signal (one muon channel)	> 25 GeV	< 2.5	< 3	< 0.5	Medium	FixedCutTight
ZH-signal (two muons channel)	> 25 GeV	< 2.5	< 3	< 0.5	Loose	LooseTrackOnly

TABLE 5.3: A summary of the muon object selections used in the analysis. The VH-loose definition is used in the 0 lepton channel to veto muons. The WH-signal and ZH-signal definitions are used in the 1μ and 2μ channels, respectively.

the p_T of the two-leptons system, $p_{T,\ell\ell}$, which corresponds to the p_T of the Z boson, is used as a proxy for the E_T^{miss}.

A source of background that can be easily reduced is the BIB which can arise from interactions of the beam with residual gas or beam collimators. In these interactions, secondary particles can be produced simulating high p_T fake jets with characteristic azimuthal distributions[1]. Since BIB particles have direction nearly parallel to the beam-pipe, there are usually no tracks associated to these fake jets. A cut on the track-based term of the E_T^{miss} (p_T^{miss}) is therefore applied and events with 0 or 1 b-tagged jet are required to have $p_T^{\text{miss}} > 30$ GeV, as illustrated in Figure 5.3. For events with two b-tagged jets, where the non-collision background contribution is already

[1] Mostly peaking at ϕ=0,$\pm\pi$, as a result of the arrangement of the dipole magnets and of the shielding effect of the tunnel floor [143].

quite low (due to the b-tagging requirement), no $p_{\mathrm{T}}^{\mathrm{miss}}$ cut is applied, in order to recover signal efficiency.

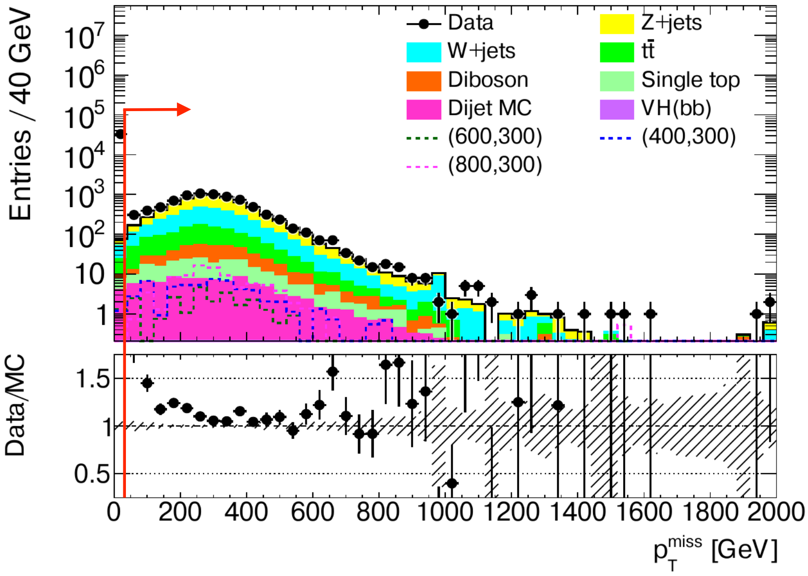

FIGURE 5.3: Exemplary distribution of the $p_{\mathrm{T}}^{\mathrm{miss}}$ variable for data and MC, including three representative Z'-2HDM scenarios corresponding to different masses ($m_{Z'}$,m_A) (dashed lines). The disagreement at low values is expected to be caused by multijet background.

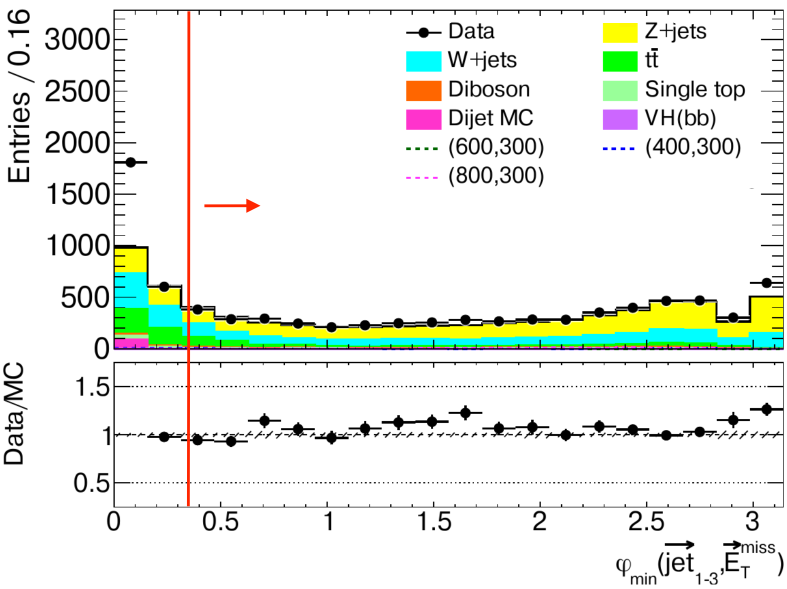

FIGURE 5.4: Exemplary distribution of the minimum $\Delta\phi$ between $E_{\mathrm{T}}^{\mathrm{miss}}$ and the three leading jets in the event, expressed in radians. The disagreement at low values is expected to be associated with multijet background events.

An important source of background that affects mostly the low $E_{\mathrm{T}}^{\mathrm{miss}}$ region is the one coming from QCD multijet processes. In case of a multijet event, the $E_{\mathrm{T}}^{\mathrm{miss}}$ is expected to point in the direction of the potential mismeasured jet, hence a cut on the azimuthal separation between the $E_{\mathrm{T}}^{\mathrm{miss}}$ and the total momentum of all central

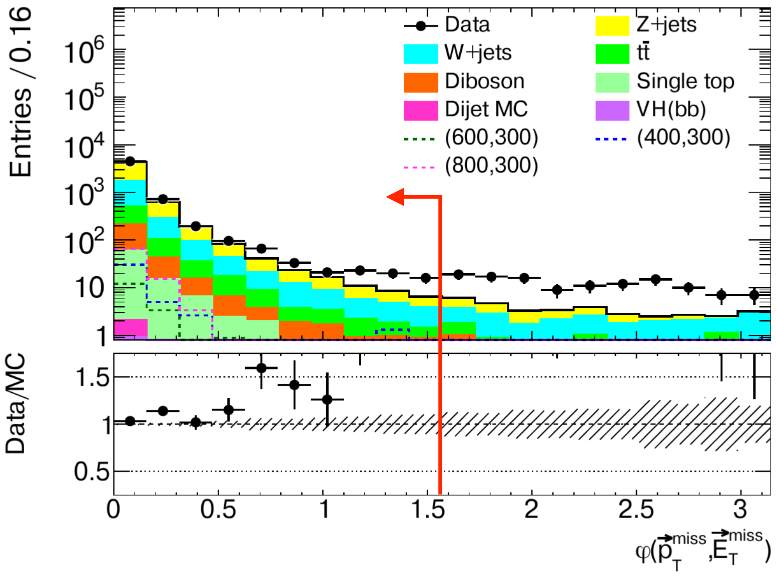

FIGURE 5.5: Exemplary distribution of the $\Delta\phi(E_T^{miss}, p_T^{miss})$ variable, expressed in radians, for data and MC, including three representative Z'-2HDM scenarios corresponding to different masses $(m_{Z'}, m_A)$ (dashed lines). The disagreement at high values is expected to be caused by multijet background.

and forward jets is expected to reduce the contamination originating from this background, as illustrated in Figure 5.4. Furthermore, while the E_T^{miss} is aligned along the direction of the mis-reconstructed jet, the p_T^{miss} is expected to remain small and without a preferred direction (see Figure 5.5). Therefore, in order to suppress this background the following cuts are applied:

- $\min(\Delta\phi(E_T^{miss}, \text{jets})) > 20°$,
- $\Delta\phi(E_T^{miss}, p_T^{miss}) < 90°$.

Once the baseline selection described above is applied, the events are divided into the resolved and merged region, depending on the amount of E_T^{miss}.

5.4.1 Resolved region

In the resolved region, the Higgs candidate h is reconstructed as the system made by the two leading central jets, j_1 and j_2, on which b-tagging is applied and which are required to have $p_T > 45$ GeV. Further requirements are applied to the scalar sum of the p_T of up to three jets, using all the jets both in the central and forward region of the ATLAS detector. For events with two (three or more) jets, the scalar p_T sum of the first two (three) jets has to be greater than 120 (150) GeV.

In order to further suppress the multijet background, two additional cuts are applied in the resolved region:

- $\Delta\phi(j_1, j_2) < 140°$,
- $\Delta\phi(E_T^{miss}, h) > 120°$.

These cuts are motivated by the fact that multijet events are usually back-to-back; therefore a cut on the angular separation between the two leading jets should already

Resolved	Merged
trigger	
lepton veto (SR) or selection (CRs)	
(modified) $E_{\mathrm{T}}^{\mathrm{miss}} > 150$ GeV	
min $\Delta\phi(E_{\mathrm{T}}^{\mathrm{miss}}$,jets) $> 20°$	
$\Delta\phi(E_{\mathrm{T}}^{\mathrm{miss}}, p_{\mathrm{T}}^{\mathrm{miss}}) < 90°$	
$\mathcal{S} > 16$ (SR only)	—
0ℓ-SR: $E_{\mathrm{T}}^{\mathrm{miss}} < 500$ GeV 1μ-CR: $E_{\mathrm{T}}^{\mathrm{miss,no}\mu} < 500$ GeV 2ℓ-CR: $p_{\mathrm{T}}^{\ell\ell} < 500$ GeV	0ℓ-SR: $E_{\mathrm{T}}^{\mathrm{miss}} > 500$ GeV 1μ-CR: $E_{\mathrm{T}}^{\mathrm{miss,no}\mu} > 500$ GeV 2ℓ-CR: $p_{\mathrm{T}}^{\ell\ell} > 500$ GeV
N(central small-R jets) ≥ 2	N(central large-R jets) ≥ 1
$p_{\mathrm{T}}^{\mathrm{jet}_1} > 45$ || $p_{\mathrm{T}}^{\mathrm{jet}_2} > 45$	—
$\sum_{i=1}^{2(3)} p_{\mathrm{T}}^{\mathrm{jet}_i} > 120(150)$ GeV	—
$\Delta\phi(\mathrm{jet}_1,\mathrm{jet}_2) < 140°$	—
$\Delta\phi(E_{\mathrm{T}}^{\mathrm{miss}}$,h) $> 120°$	—
τ-veto	
additional b-jet veto	
H_T ratio	
$\Delta R(\mathrm{jet}_1,\mathrm{jet}_2) < 1.8$	$\frac{\Delta R(\mathrm{VR}_1,\mathrm{VR}_2)}{R_{\mathrm{min}}} > 1$
b-tag requirement on	
small-R jets	track-jets

TABLE 5.4: Summary of the resolved and merged region event selection, in the category with two b-tagged jets.

suppress the contribution of this background. At the same time, in an event with real $E_{\mathrm{T}}^{\mathrm{miss}}$, the Higgs candidate h should recoil against the DM particles so an additional cut on the angular separation between the Higgs candidate and the $E_{\mathrm{T}}^{\mathrm{miss}}$ is also applied.

An important feature that has been introduced in the resolved region selection consists in the usage of the object-based definition of the $E_{\mathrm{T}}^{\mathrm{miss}}$ significance (see Section 4.7.1) to further suppress the multijet background. The improvement caused by this new variable in the analysis is more extensively discussed in Section 5.5.

Dedicated cuts are also applied in order to reduce the other dominant background at low $E_{\mathrm{T}}^{\mathrm{miss}}$, which originates from $t\bar{t}$ processes. As in signal events the b-jets are expected to come only from the $H \to b\bar{b}$ decay, the presence of additional b-jets would indicate the presence of background processes as $t\bar{t}$. A veto is therefore applied on events with more than two b-jets. The angular separation between the two leading jets is also a powerful variable that can help in discriminating signal from $t\bar{t}$ background events. While in signal events the two b-jets originate from the Higgs decay and are expected to be very close to each other, in a $t\bar{t}$ process they originate from the decay of each top quark ($t \to Wb$), hence their angular separation is expected to be quite large. For this reason, the $\Delta R(j_1, j_2)$ is required to be smaller than 1.8. In addition, a H_T ratio variable can be defined as the ratio of the scalar p_{T} sum of the jets which do not form the Higgs candidate over the total scalar p_{T} sum of all jets:

$$H_T \text{ ratio} = \frac{H_T(\text{non Higgs candidate})}{H_T(\text{all jets})}. \tag{5.3}$$

For signal-like events, one would expect this variable to be relatively small, as the remaining jets in the events, which are not coming from the $H \to b\bar{b}$ decay, mostly originate from ISR processes which have generally low p_{T} activity. On the other hand, in a $t\bar{t}$ process, the two b-jets which can potentially form the Higgs candidate are produced in association with the jets from the W boson which have, on average, a similar p_{T} magnitude as the b-jets. Applying a cut on the H_T ratio variable, whose numerator is calculated using all jets except the highest three ranked jets[2], is a powerful way to further suppress the contribution of the $t\bar{t}$ background. Lastly, an event veto is applied on events containing a hadronically decaying τ lepton candidate, which is not expected to be present in signal events but can originate from semi-leptonic and fully hadronic $t\bar{t}$ events. Furthermore, an *extended* version of this cut has been developed and it consists in defining a τ-jet candidate as a jet with a track multiplicity no lower than one nor larger than four and with an azimuthal separation with respect to the $E_{\mathrm{T}}^{\mathrm{miss}}$ equal or lower than 22.5°. An additional event veto is applied in the presence of such jets.

5.4.2 Merged region

The merged region is defined by applying all the baseline cuts and increasing the $E_{\mathrm{T}}^{\mathrm{miss}}$ cut up to 500 GeV. In this regime, the contamination from the multijet background is negligible, hence no further anti-QCD cuts are applied in this region. The Higgs candidate is reconstructed as the leading large-R jet in the event with at least two ghost-associated [107] track jets. In particular, VR track jets are used in the analysis. A cut on the minimum angular separation between the two leading associated VR track jets is applied as event cleaning in order to discard events with potential ambiguous b-tagging (see Section 6.1.1-6.3) . As the usage of VR track jets represents one of the key ingredients of this analysis in the merged regime, a dedicated discussion is postponed to Section 5.6.

Also in the merged region, optimised cuts have been developed in order to suppress the $t\bar{t}$ contamination. The H_T ratio cut is applied by considering all the small-R jets that are not associated to the leading large-R jet within its R=1.0 cone. The *extended* τ veto cut is applied by asking the events to have no jets that fulfil the track multiplicity and $\Delta\phi$(jet,$E_{\mathrm{T}}^{\mathrm{miss}}$) separation criteria described above and that are not associated to the leading large-R jet. The additional b-jet veto is applied by requiring the events to have no additional b-tagged VR track jets that are not ghost-associated to the leading large-R jet.

[2] By construction, all jets except the highest two ranked jets should be used in the calculation of the numerator of the H_T ratio variable. However, excluding also the third leading jet gives a slightly better significance gain therefore this modified version of the cut is employed in the analysis.

5.4.3 Signal and Control Region separation

After having applied the full list of requirements described above, events are further classified in different SR and CRs. The events that do not contain any loose electron or muon fall into the SR. Events containing leptons, on the other hand, are used to define CRs to constrain the main background contributions. The 1μ-CR is defined by requiring exactly one signal muon and no further loose muons or electrons. The 2ℓ-CR contains instead the events with exactly two signal leptons with same flavour. The ee and $\mu\mu$ channels are used together and the electron (muon) pair must have an invariant mass of 83 GeV < m_{ee} < 99 GeV (71 GeV < $m_{\mu\mu}$ < 106 GeV). In order to suppress the $t\bar{t}$ and single top background, the event based $E_{\mathrm{T}}^{\mathrm{miss}}$ significance (see Section 4.7.1) in the 2ℓ-CR is required to be smaller than 3.5 $\sqrt{\mathrm{GeV}}$.

5.5 The novelty of the $E_{\mathrm{T}}^{\mathrm{miss}}$ significance

As anticipated already in Section 4.7.1, the $E_{\mathrm{T}}^{\mathrm{miss}}$ significance $\mathcal{S}$ can help in distinguishing events with *real* $E_{\mathrm{T}}^{\mathrm{miss}}$ coming from weakly interacting particles from events in which *fake* $E_{\mathrm{T}}^{\mathrm{miss}}$ originates from particle mismeasurements and detector effects. This makes a cut on the $E_{\mathrm{T}}^{\mathrm{miss}}$ significance a promising choice to suppress multijet events, which represent a large source of background for this analysis at low $E_{\mathrm{T}}^{\mathrm{miss}}$. A new *object-based* definition of the $E_{\mathrm{T}}^{\mathrm{miss}}$ significance $\mathcal{S}$, which takes into account the resolution and directional correlations of the objects entering in the $E_{\mathrm{T}}^{\mathrm{miss}}$ reconstruction, rather than event-level quantities, has been used for this purpose [127].

As it is possible to construct this variable in several different ways, the first step consists in understanding which definition is more appropriate for this analysis. The performance of different possible definitions of $\mathcal{S}$ have been compared and among those the best discriminating power of the Z'-2HDM against the multijet background is provided by the definition that does not take into account the resolution of the pile-up jets and that of the $E_{\mathrm{T}}^{\mathrm{miss}}$ soft term. This specific definition of the object-based $E_{\mathrm{T}}^{\mathrm{miss}}$ significance is therefore employed in the analysis.

The performance of the object-based $E_{\mathrm{T}}^{\mathrm{miss}}$ significance is also compared against its event-based definition and the $E_{\mathrm{T}}^{\mathrm{miss}}$ itself, as shown in Figure 5.6. The cut on these three variables is applied in addition to a requirement on the angular separation between the $E_{\mathrm{T}}^{\mathrm{miss}}$ vector and the leading jets in the events.

The next step consists in identifying the cut value for this new variable. This has been chosen by comparing the expected signal significance corresponding to different possible cuts on the chosen definition of the object-based $E_{\mathrm{T}}^{\mathrm{miss}}$ significance variable, taking into account only the events in the resolved region. By introducing a requirement of $\mathcal{S} > 16$ more than 95% of the di-jet events are rejected while the signal efficiency remains stable at 90%.

After having included this new requirement in the analysis selection, a data-driven multijet estimate has been performed. The method consists in using two sufficiently uncorrelated variables, in this case $\min(\Delta\phi(E_{\mathrm{T}}^{\mathrm{miss}}, \mathrm{jets}))$ and $\mathcal{S}$, to define four different regions by applying and inverting the cuts used in the analysis. The region containing the events passing the requirements on both the two variables corresponds to our actual SR while the events failing both of the two requirements end up in a QCD-enriched region. From this last region, the contribution of the multijet background is extracted as the shape difference between data and the non-multijet processes in the invariant mass of the two jets system, m_{jj}. After having checked that the correlation between the two selected variables is sufficiently low, it is possible to express the

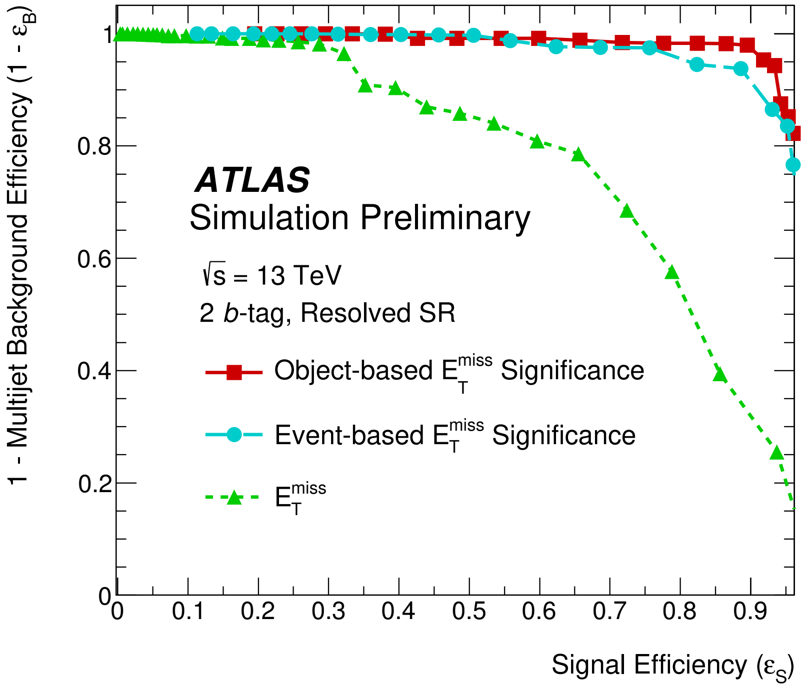

FIGURE 5.6: Performance of the object-based $E_{\mathrm{T}}^{\mathrm{miss}}$ significance, in terms of signal efficiency and background rejection, against the event-based definition and the $E_{\mathrm{T}}^{\mathrm{miss}}$ itself. Figure taken from Ref. [130].

number of multijet background events in the SR as:

$$N_{\mathcal{S}>16,\Delta\phi>20^\circ} = \frac{N_{\mathcal{S}>16,\Delta\phi<20^\circ} \cdot N_{\mathcal{S}<16,\Delta\phi>20^\circ}}{N_{\mathcal{S}<16,\Delta\phi<20^\circ}}. \tag{5.4}$$

In order not to compromise the estimate by the signal contamination, all the events are required to be outside of the Higgs mass window [70,140] GeV.

Sample	Region	$N_{\mathcal{S}<16,\Delta\phi<20^\circ}$	$N_{\mathcal{S}<16,\Delta\phi>20^\circ}$	$N_{\mathcal{S}>16,\Delta\phi<20^\circ}$	Prediction	$N_{\mathcal{S}>16,\Delta\phi>20^\circ}$
Data	150 GeV $< E_{\mathrm{T}}^{\mathrm{miss}} <$ 200 GeV	4573 ± 68	3452 ± 59	129 ± 11	–	7698 ± 88
Total background	150 GeV $< E_{\mathrm{T}}^{\mathrm{miss}} <$ 200 GeV	595 ± 13	2435 ± 28	50 ± 3	–	6397 ± 45
Multijet shape	150 GeV $< E_{\mathrm{T}}^{\mathrm{miss}} <$ 200 GeV	3978 ± 69	1017 ± 65	79 ± 12	20 ± 3.3	–
Data	200 GeV $< E_{\mathrm{T}}^{\mathrm{miss}} <$ 350 GeV	1705 ± 41	381 ± 20	355 ± 19	–	5429 ± 74
Total background	200 GeV $< E_{\mathrm{T}}^{\mathrm{miss}} <$ 350 GeV	282 ± 9	317 ± 10	174 ± 7	–	4731 ± 36
Multijet shape	200 GeV $< E_{\mathrm{T}}^{\mathrm{miss}} <$ 350 GeV	1423 ± 42	64 ± 22	181 ± 20	8 ± 2.9	–
Data	350 GeV $< E_{\mathrm{T}}^{\mathrm{miss}} <$ 500 GeV	66 ± 8	1 ± 1	94 ± 10	–	484 ± 22
Total background	350 GeV $< E_{\mathrm{T}}^{\mathrm{miss}} <$ 500 GeV	9 ± 1	0.9 ± 0.2	52 ± 4	–	434 ± 9
Multijet shape	350 GeV $< E_{\mathrm{T}}^{\mathrm{miss}} <$ 500 GeV	57 ± 8	0.1 ± 1	42 ± 11	0.1 ± 0.76	–

TABLE 5.5: Predicted amount of multijet background events in each region. Only events outside the Higgs mass window [70,140] GeV are used.

As shown in Table 5.5, thanks to the new requirement $\mathcal{S} > 16$ the remaining amount of the multijet background in the SR is significantly reduced and smaller than the statistical uncertainty on the data. Although the multijet background has already been found to be extremely small, an additional check has been performed including the multijet background (from the m_{jj} template extracted from the shape difference between data and non-multijet processes) in the final likelihood fit. In order to correct by the predicted fraction of multijet background in the SR, the m_{jj} template is scaled by the ratio of the full mass range over the blinded mass sideband. The impact on the final fit has found to be negligible; thus the multijet yield is entirely neglected in the final statistical analysis, described in Section 5.7, improving the level of complexity of the analysis with respect to the previous iterations [144, 145, 129].

5.6 The novelty of the Variable-Radius track jets

As anticipated in Section 5.1, in the *merged* (or *boosted*) regime the Higgs boson candidate is reconstructed as a single large-R jet with radius equal to 1.0 and the b-tagging is applied to the leading two track jets that are matched to it through GA [107] (see Section 4.2.3). In the previous iterations of the mono-H($b\bar{b}$) analysis, $R = 0.2$ track jets have been used in this regime. However, the more energetic is the Higgs candidate the more difficult is to reconstruct the two associated track jets as two separate objects. As the sensitivity of this search relies heavily on the ability to identify both b-jets from the Higgs boson decay, using a fixed radius parameter for the reconstruction of the track jets is not an optimal choice when probing high mass regimes. The first immediate solution to this problem consists in varying the radius parameter as a function of the jet transverse momentum. This represents the main feature of the VR jet reconstruction, in which the following p_{T} dependence of the jet radius is introduced [146]:

$$\mathrm{R} \rightarrow \mathrm{R}_{\mathrm{eff}}(p_{\mathrm{T}}) = \frac{\rho}{p_{\mathrm{T}}} \tag{5.5}$$

and the parameter ρ determines how the effective jet radius scales with the p_{T} of the jet during the jet finding procedure. Two additional parameters R_{min} and R_{max} are used to set, respectively, a lower and an upper cut on the jet radius. The optimal values of these three parameters, in terms of double b-labelling efficiency of Higgs candidate jets over a wide mass range, have been found to be: $\rho = 30$ GeV, $R_{\mathrm{min}} = 0.02$ and $R_{\mathrm{max}} = 0.4$ [147].

The VR track jets are reconstructed from the ID tracks using the anti-k_t algorithm. The considered tracks are required to have $p_{\mathrm{T}} > 500$ MeV and $|\eta| < 2.5$, in order to be in the fiducial region of the ATLAS tracking system. In addition, they must yield at least seven hits in the SCT and pixel detectors, not more than one hit shared by multiple tracks in the pixel detector, not more than one missing hit[3] in the pixel detector and not more than two missing hits in the SCT detector. Additional requirements on the longitudinal impact parameter ($|z_0 \sin(\theta)| < 3$ mm, see Section 4.1) with respect to the PV allow to reduce the pile-up contribution and to improve the efficiency in selecting tracks from the hard scattering vertex.

The effectiveness of VR track jets can be already observed when comparing the sub-jet multiplicity inside a large-R jet with respect to the case of FR track jets. This has been studied by evaluating the efficiency for a large-R jet with $R = 1.0$ ($p_{\mathrm{T}} > 200$ GeV, $|\eta| < 2.0$) matched to a truth Higgs boson to have also its two associated track jets matched to two truth b-hadrons (hence defining a “Higgs jet”) [147]. For this purpose, simulated Randall–Sundrum (RS) graviton G^* samples have been analysed, exploiting the decay chain $G^* \rightarrow HH \rightarrow b\bar{b}b\bar{b}$, combining together different m_{G^*} hypotheses, between 300 GeV and 6000 GeV. Such events are simulated with the `MadGraph5 aMC@NLO` generator interfaced with Pythia 8.230 and using the

[3]If no hit is observed in an active detector element where one is expected, this is referred to as a missing hit.

NNPDF2.3 PDF set and the ATLAS A14 set of tuned parameters. As shown in Figure 5.7, a large fraction of large-R jets (from 30% to 40%) has three associated VR track jets, in contrast with the FR track jets case in which the ability of resolving the two sub-jets system decreases rapidly at high Higgs jet p_T. In these cases, applying b-tagging only to the leading two associated VR track jets can lead to an inefficiency when trying to identify the flavour content of a Higgs jet. In fact, by recovering the third leading jet, the double b-labelling efficiency improves significantly, as can be observed by comparing Figure 5.8a with Figure 5.8b.

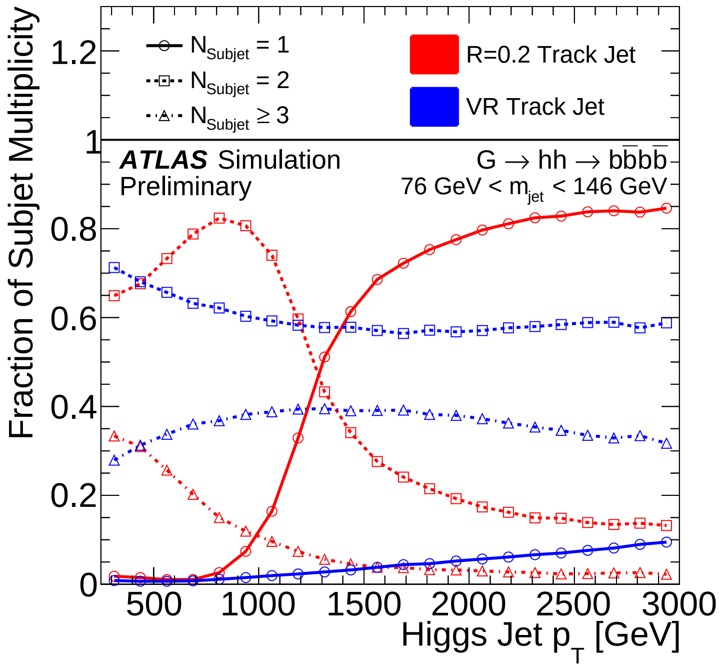

FIGURE 5.7: The sub-jet multiplicity fractions as a function of the Higgs jet p_T for Higgs jets with exactly 1 sub-jet (solid line), 2 sub-jets (dashed line) and at least 3 sub-jets (dotted line). Figure taken from Ref [147].

The possibility of applying b-tagging to the leading three VR track jets associated to the leading large-R jet has been studied also in the context of the mono-H($b\bar{b}$) analysis. Moreover, in order to exploit the full potential of the VR track jets, this study is performed for a (very boosted) Z'-2HDM signal model with $m_{Z'} = 2.8$ TeV and $m_A = 300$ GeV, on varying of the cut value applied on the `MV2c10` b-tagging discriminant. In this way, a complete re-evaluation of the b-tagging performance of VR track jets can be done, with respect to the previous approach based on the usage of FR track jets. The comparison, shown in Figure 5.9, is done in terms of the signal significance σ of the merged SR which is evaluated as [148]:

$$\sigma = \sqrt{2 \times ((s+b)\ln(1+\frac{s}{b}) - s)} \tag{5.6}$$

where s and b represent, respectively, the number of signal and background events in a given phase space region. Despite the increased signal selection efficiency, applying b-tagging to the three highest p_T jets in the event also leads to an increased background contamination which causes an overall decrease in sensitivity. For this reason, applying the b-tagging only to the leading two associated VR track jets still

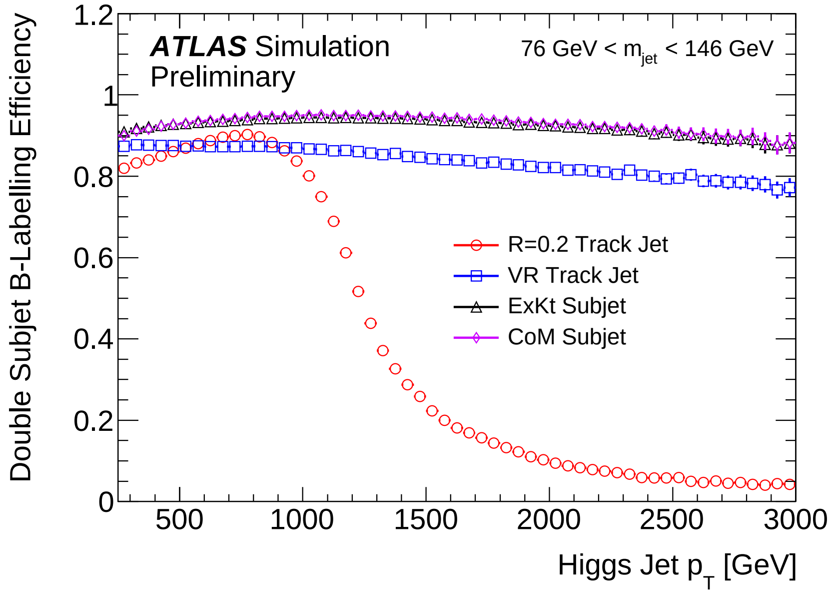

(a)

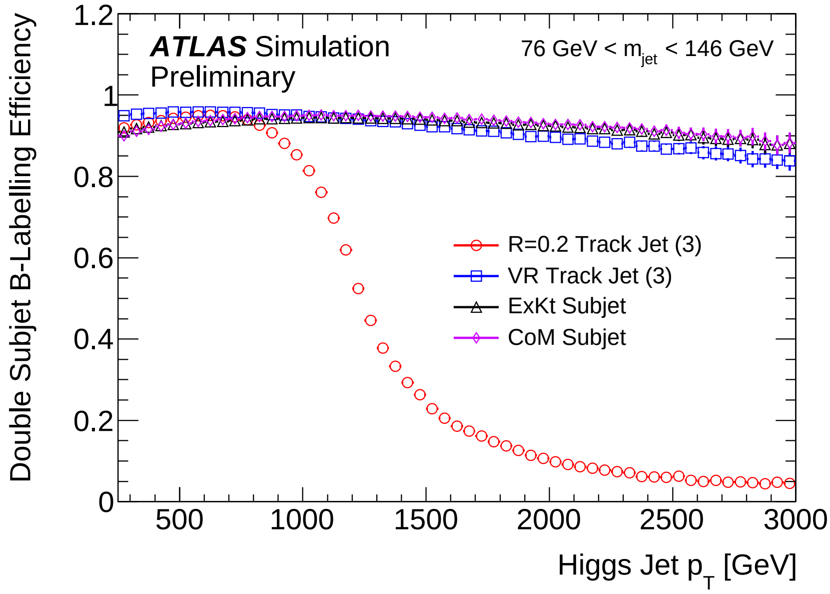

(b)

FIGURE 5.8: At the top (bottom), efficiency for a Higgs jet to have two of the leading two (three) associated track jets matched to truth b-hadrons vs Higgs jet p_T. Figure taken from Ref [147].

proves to be the most appropriate choice. Furthermore, by examining the full range of the MV2c10 possible cut values, it has been chosen to adopt the one corresponding to an average b-tagging efficiency of 77%, as it provides the best signal significance. This introduces an additional change with respect to the previous results in which the 70% MV2c10 WP was used for FR track jets.

Once the b-tagging procedure on VR track jets is established, it is possible to compare the performance of FR ($R = 0.2$) and VR track jets in terms of the signal significance gain in the merged SR over the whole phase-space of the Z'-2HDM benchmark model considered in this analysis. Figures 5.10a-5.10b show the signal significance,

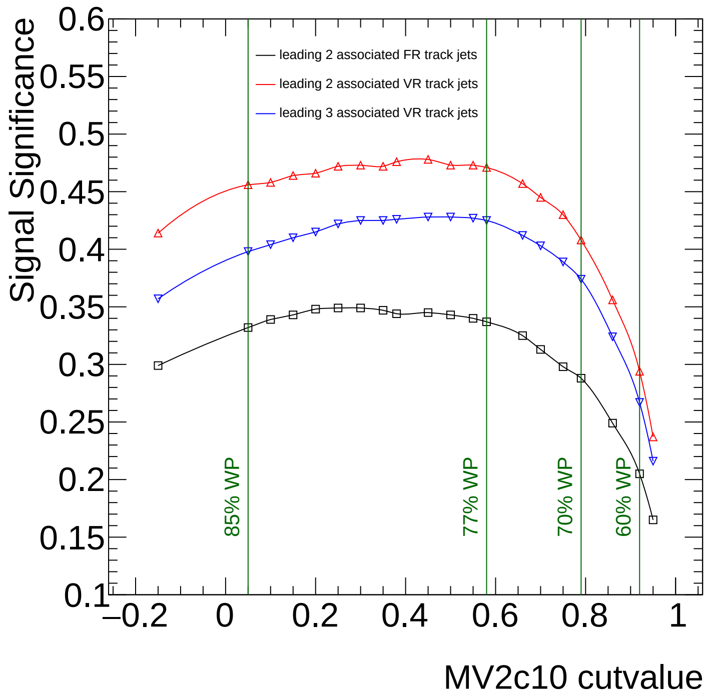

FIGURE 5.9: Signal significance of the merged SR selection (considering only events inside the Higgs mass window [70,140] GeV) as a function of the cut value applied on the `MV2c10` discriminant, comparing the cases in which the b-tagging is done on the leading two associated FR track jets (previous analysis) or on the leading two or three VR track jets.

computed using Equation 5.6, in the merged SR, of VR track jets compared to FR track jets, for the case of events with one (1 b-tag category) or two (2 b-tag category) b-tagged jets and with exactly two b-tagged jets, respectively.

As the signal events are expected to have exactly two b-tagged jets from the Higgs boson decay, it is also interesting to compare the signal significance of the 2 b-tag category with respect to the combined 1+2 b-tag category. Figure 5.11a shows that, when using VR track jets, including events with only one b-tagged jet leads only to a marginal improvement of the sensitivity. This allows for a removal of the 1 b-tag category, which simplifies the background modelling and the whole analysis strategy. Figure 5.11b shows also the comparison between the signal significance of the 2 b-tag category of VR track jets with respect to the combined 1+2 b-tag categories for the case of FR $R = 0.2$ track jets, with the latter representing exactly the approach adopted for the previous results [129]. At high $m_{Z'}$, the gain achieved by the usage of VR track jets is still significant, even when using only the 2 b-tag category.

Lastly, Figure 5.12a shows the signal selection efficiency for $E_{\mathrm{T}}^{\mathrm{miss}} > 500$ GeV for different b-tag multiplicities of a Z'-2HDM model with $m_A = 500$ GeV as a function of $m_{Z'}$, with the additional requirement that the Higgs candidate mass lies between 70 GeV and 140 GeV. Especially for $m_{Z'} > 2.5$ TeV the selection efficiency improves significantly both for the 1 b-tag and the 2 b-tag categories. Naturally, using a different jet definition implies also a different b-tagging performance. Hence, in order to understand the actual reason of the observed improvement, it is useful to study the relative efficiency of the 1 b-tag and 2 b-tag selections. As shown in Figure 5.12b, the b-tagging efficiencies for VR and FR track jets are very similar, hence the observed

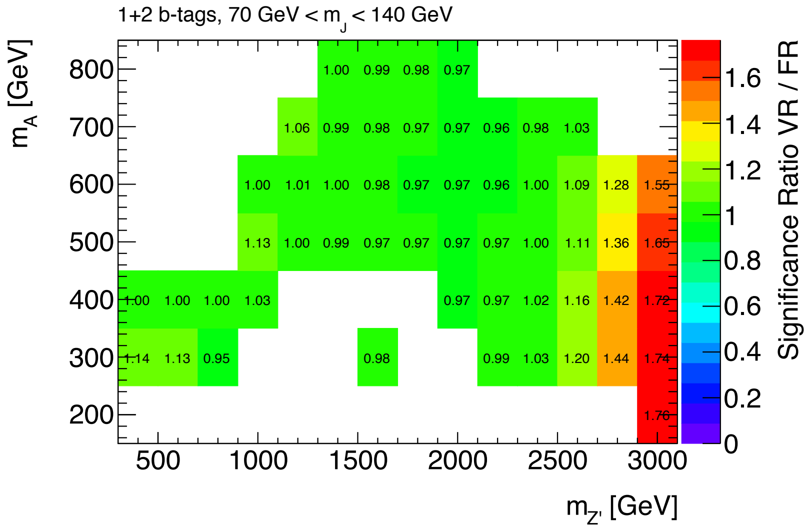

(a)

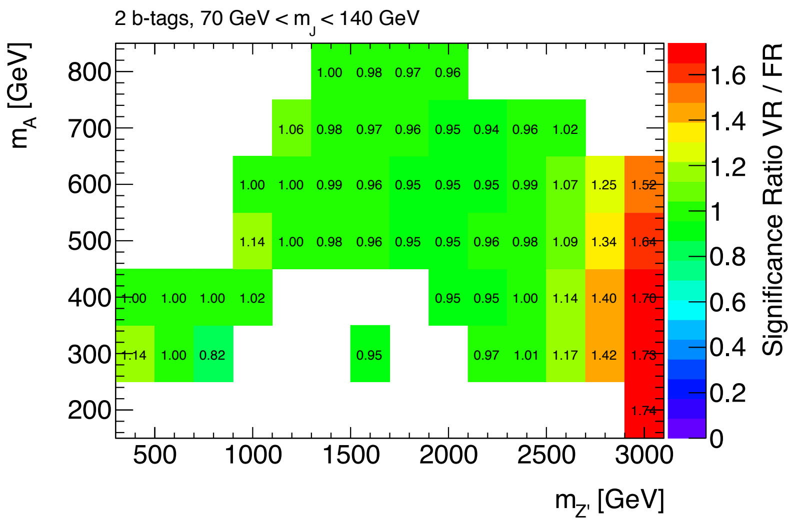

(b)

FIGURE 5.10: Ratio between the signal significance of the merged SR with one or two b-tagged jets (at the top) and with exactly two b-tagged jets (at the bottom) for VR and FR track jets. Only events inside Higgs mass window [70,140] GeV are considered.

enhancement in the signal acceptances originates primarily from the improved ability in resolving the two sub-jets system inside the large-R jet achieved with VR track jets, as shown in the inclusive b-tag (black filled markers) curve in Figure 5.12a.

As discussed above, for VR track jets a fixed cut on the MV2c10 discriminant corresponding to an average 77% b-tagging efficiency is used, similarly to the case of small-R jets in the resolved region. In order to finally use VR track jets in the analysis, it is crucial to measure the b-tagging efficiency of the chosen b-tagging algorithm in data and correct the b-tagging performance in simulation for detector effects and possible mismodelling of the simulated physics processes.

A dedicated discussion about the b-tagging calibration procedure adopted for the case of VR track jets is presented in Chapter 6. Although this separate chapter is aimed at presenting the most updated version of the b-tagging calibration exploiting the full statistics of Run 2 of the LHC, for the purpose of the mono-H($b\bar{b}$) search

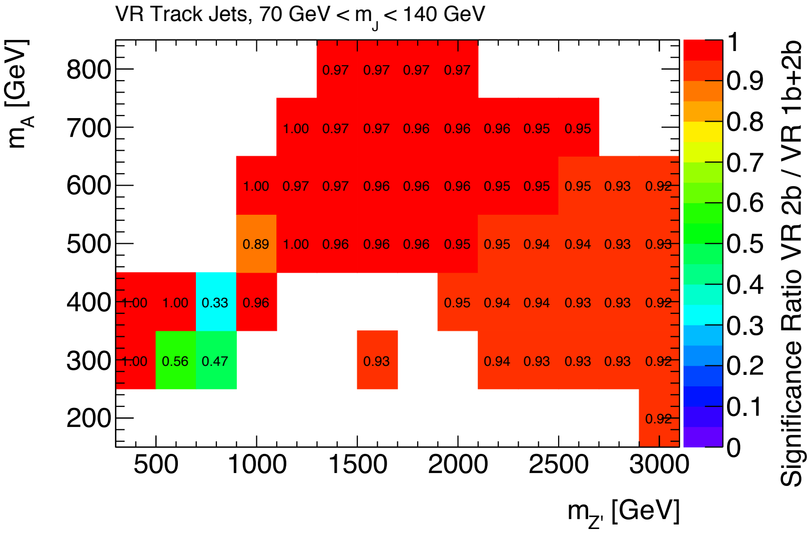

(a)

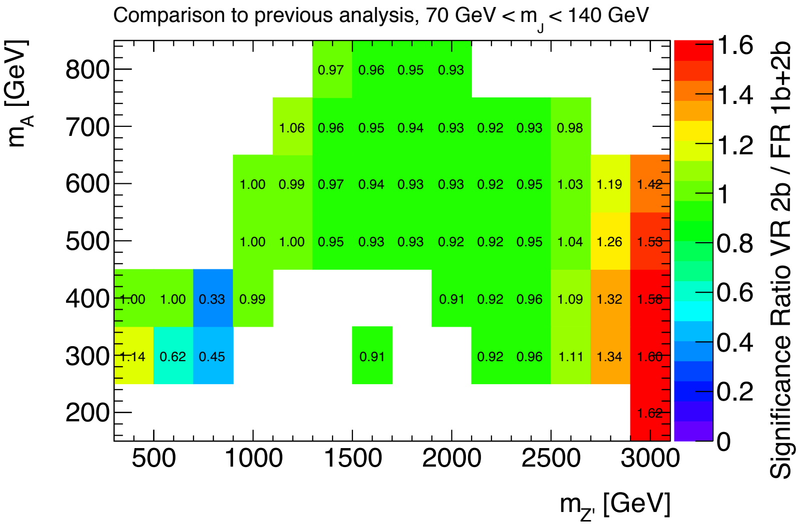

(b)

FIGURE 5.11: At the top, signal significance of the merged SR in the 2 b-tag category over the combined 1+2 b-tag category for VR track jets. At the bottom, signal significance ratio between the 2 b-tag category for VR track jets and the combined 1+2 b-tag category for FR $R = 0.2$ track jets. Only events inside Higgs mass window [70,140] GeV are considered.

described in this chapter only data recorded during 2015 and 2016 have been used. The most relevant difference applied to the analysis of the full Run 2 data concerns the usage of VR track jets with $p_T < 10$ GeV. As the event selection applied for the measurement of the b-tagging efficiency in data relies on the presence of exactly two VR track jets, a change in the p_T threshold implies also a different selection of events. In particular, by lowering the p_T down to 5 GeV a higher jet multiplicity is obtained hence more events are rejected. The impact on the final b-tagging SFs has found to be consistent with respect to the previous ones, within uncertainties. By using an extended dataset this effect is even more reduced therefore, since the calibration strategy stays identical, the impact of the b-tagging calibration results on

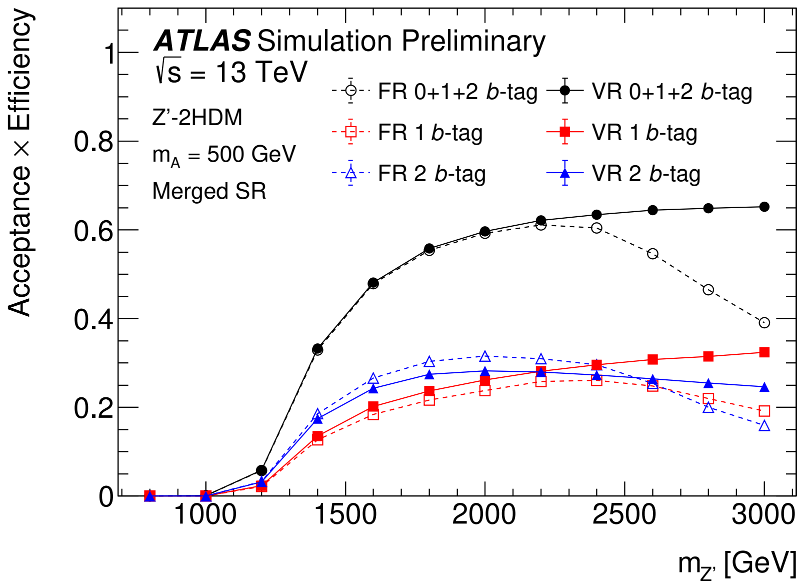

(a)

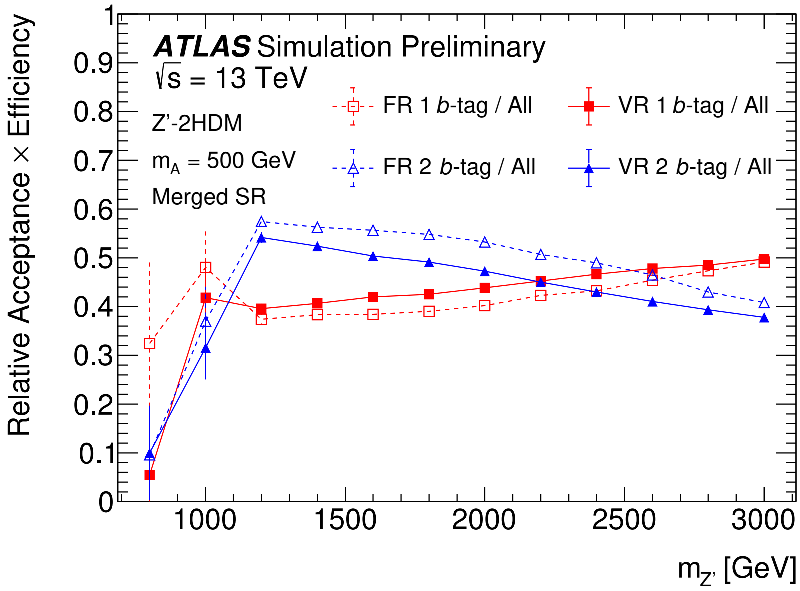

(b)

FIGURE 5.12: Acceptance × efficiency ($A \times \varepsilon$) of the merged SR selection for different b-tag multiplicity (at the top) and relative $A \times \varepsilon$ as a function of $m_{Z'}$ for a Z'-2HDM model with m_A = 500 GeV (at the bottom). Figures taken from Ref [130].

the mono-H($b\bar{b}$) analysis remains unchanged.

In addition to the description of the method used to measure the b-tagging efficiency of VR track jets in data, several other aspects concerning the usage of VR track jets for b-tagging are discussed in Chapter 6. In particular, Section 6.1.1-6.3 will discuss the importance of applying an additional requirement on the minimum angular separation between the leading two VR track jets used for b-tagging. Developed in the context of the b-tagging calibration, this requirement is then included to the baseline analysis event selection, as shown in Table 5.4.

5.7 Statistical evaluation

The statistical analysis of data is based on a binned likelihood function $\mathcal{L}(\mu, \vec{\theta})$ constructed as the product of the Poisson probability terms over the bins of the chosen discriminating variable:

$$\mathcal{L}(\mu, \vec{\theta}) = \prod_{\text{SR bins}:i} \text{Pois}(n_i, \mu S_i(\vec{\theta}) + B_i(\vec{\theta})) \prod_{\text{CR bins}:j} \text{Pois}(n_j, B_j(\vec{\theta})). \tag{5.7}$$

where S_i (B_i) represents the expected number of signal (background) events in a given bin i (j) in the SR (CR). The Parameter Of Interest (POI) μ is the signal strength, which is defined as the ratio of the observed signal yield to the theory prediction. Systematic uncertainties are instead included in the fit as Nuisance Parameter (NP)s, $\vec{\theta}$, most of them constrained with Gaussian or log-normal probability density functions. From this likelihood function, we can define the *test statistic* as:

$$q_\mu = -2\ln\frac{\mathcal{L}(\mu, \hat{\hat{\theta}})}{\mathcal{L}(\hat{\mu}, \hat{\theta})} \tag{5.8}$$

where $\hat{\theta}$ and $\hat{\mu}$ are the best values of the parameters obtained by maximising the likelihood, while $\hat{\hat{\theta}}$ are the values of the NPs obtained by maximising the likelihood for a given value of μ. The test statistic q_μ is therefore a function of μ and is called *profile likelihood ratio*.

A potential excess of events over the background prediction can only be established if the background-only (*null*) hypothesis can be rejected with a certain probability. Hence, the first step consists in performing a background-only fit, corresponding to the test statistic q_0 with $\mu = 0$. If q_0^{obs} is the observed value of q_0, it is possible to define the local p_0-value as:

$$p_0 = \int_{q_0^{\text{obs}}}^{\infty} f(q_0|0)dq_0 \tag{5.9}$$

where $f(q_\mu|\mu)$ is the probability distribution of the test statistics q_μ which asymptotically approaches a χ^2 distribution with one degree of freedom (*Wilks' theorem* [149]) [148]. Therefore, if the p_0-value is below a certain value, then the null hypothesis is excluded. Similarly, in order to test the presence of a specific signal model, the test statistic q_1 corresponding to $\mu = 1$ must be used. The quantity:

$$p_\mu = \int_{q_\mu^{\text{obs}}}^{\infty} f(q_\mu|\mu)dq_\mu \tag{5.10}$$

defines the CL at which a specific signal plus background hypothesis corresponding to a certain value of μ can be excluded and is usually also called CL_{s+b}. In order to extract exclusion limits on the signal strength μ, the signal plus background hypothesis is tested using q_μ as test statistic. Usually a modified frequentist approach, called CL_s method [150], is used in order to avoid excluding a signal hypothesis with a small sensitivity (e.g. for which the distributions of the signal and background-only hypotheses tend to overlap). The CL_s method consists in using as CL:

$$CL_s = \frac{CL_{s+b}}{CL_b} \tag{5.11}$$

where CL_b corresponds to $\int_{q_\mu^{\text{obs}}}^{\infty} f(q_\mu|0)dq_\mu$. As CL_s is by definition larger than CL_{s+b}, when using this scheme it is more difficult to exclude signals. Using the CL_s method, for each signal hypothesis of Z'-2HDM, a 95% CL upper limit on the signal strength is derived, which corresponds to the value of μ for which 1-CL_s is equal to 95%.

The final profile-likelihood fit is performed simultaneously in all SRs and CRs and the shape information of the most discriminating variables is exploited. In the 0ℓ-SR equidistant bins of the Higgs candidate mass distribution are used and the number of bins is optimised depending on the statistics of the region. On the other hand, in the 1μ-CR the information of the electric muon charge (resulting in just two bins) is instead used as it allows distinguishing $t\bar{t}$ events, in which similar amounts of μ^+ and μ^- are expected to be produced, from W+jets processes, which are characterised by the prevalence of μ^+ due to the doubled amount of u valence quarks in the initial state protons. Lastly, in the 2ℓ-CR, the fit uses only the total event yield due to limited data statistics.

The fit is performed for different Z'-2HDM signal mass points ($m_{Z'}$, m_A) and in the four different $E_{\text{T}}^{\text{miss}}$ bins: [150 GeV, 200 GeV),[200 GeV, 350 GeV),[350 GeV, 50 0 GeV),[500 GeV, ∞).

Apart from the signal strength μ, the fit also uses other freely-floating parameters related to the normalisation of the following processes:

- W + Heavy Flavour (HF) (i.e. bb,bc,bc,cc) jets,
- Z + HF (i.e. bb,bc,bc,cc) jets,
- $t\bar{t}$.

The contribution of V+jets events is divided based on the jet flavour estimated at parton-level (see Section 4.3). This choice is motivated by the fact that the amount of V+jets is expected to vary significantly depending on the considered $E_{\text{T}}^{\text{miss}}$ range and b-tag requirement that is applied. The most dominant background consists of $V+bb$, $V+bc$, $V+bl$ and $V+cc$ events. These categories are treated jointly as V+HF jets and are allowed to freely float in the fit. On the other hand, the normalisation of $V+ll$ and $V+cl$ events is constrained within theoretical uncertainties. In addition to the free parameters of the fit, NPs are also used in order to account for further background normalisations (such as the ones of the V+light-jets, single top and diboson processes), experimental and theory modelling uncertainties. A more extensive discussion about the treatment of these uncertainties is presented in Section 5.8.

5.8 Systematic uncertainties

Both experimental and theoretical uncertainties related, respectively, to the reconstruction of the physics objects and the prediction of the background and signal physics processes are taken into account in the analysis. Dominant sources of experimental uncertainties arise from the calibration of the b-tagging efficiency as well as from the scale and resolution of the energy and mass of the jets. As discussed separately in Chapter 6, the main uncertainty affecting the measurement of the b-tagging efficiency in data originates from the theory modelling of the $t\bar{t}$ physics processes. Moreover, a significant contribution is also attributed to the high p_{T} extrapolation procedure (see Section 4.3). An additional source of experimental uncertainty is related to the measurement of the $E_{\text{T}}^{\text{miss}}$ trigger efficiency, which is determined inclusively for all b-tagged jet multiplicities. An uncertainty on the $E_{\text{T}}^{\text{miss}}$ soft-term resolution and scale is also taken into account. Other uncertainties that have a smaller impact are related to the lepton energy and momentum scales and the lepton identification and trigger efficiencies. Dominant sources of theoretical systematic uncertainty originate from the number of simulated MC events and from the modelling of the signal and main background processes (V+jets and $t\bar{t}$).

Background modelling uncertainties While the amount of V+HF jets and $t\bar{t}$ background is estimated from the combined likelihood-fit, the normalisations of all the remaining backgrounds are taken from their theory expectation and have an uncertainty assigned. The uncertainties related to the modelling of the background are inherited from the SM $VH(bb)$ analysis [151] and considered to be applicable, due to the very similar event topology, to the mono-H($b\bar{b}$) case.

For single top processes, dedicated uncertainties that account for the variation of the renormalisation (μ_R) and factorisation (μ_F) scale, the α_s uncertainty and the error on the PDFs are derived[4]. The sum in quadrature of these uncertainties gives an overall normalisation uncertainty equal to 4.4%, 4.6% and 6.2% for the s-, t- and Wt-channel, respectively.

For diboson processes, an overall uncertainty on the cross-section caused by a variation of the μ_R and μ_F scales and of the parton shower model is applied in all regions and corresponds to 25%, 26% and 20% for the WW, WZ and ZZ processes, respectively.

For what concerns the V+jets background, an overall normalisation uncertainty, related to the parton shower and scale variations, estimated to be equal to 10% and 30% is assigned, respectively, to events with ll or cl jets. The normalisation of Z (W) + HF jets is decorrelated within 20% across the SR and 2ℓ-CR (1μ-CR). A common normalisation scale factor for the V + HF jets background is therefore used across all lepton multiplicities while an additional NP allows this normalisation to change in the 0ℓ regions. This specific source of uncertainty is expected to relieve the tension between the normalisation of the V+HF background across different lepton multiplicity channels which seems to be due by a different modelling of the kinematic variables of the W and Z bosons across different lepton regions which translates into uncertainties on the lepton selection efficiency itself. Furthermore, also the composition of the V + HF background is allowed to vary within uncertainties of 20%, individually for 0ℓ and 2ℓ channels. This allows the fit to have more flexibility in the estimation of the different components in the fit and to provide a better estimate of the Z+HF background from the high purity 2ℓ-CR.

Moreover, as the final likelihood fit is performed in the two dimensional space parameterised by the $E_{\mathrm{T}}^{\mathrm{miss}}$ (and equivalently $E_{\mathrm{T}}^{\mathrm{miss,no}\mu}$ and $p_{\mathrm{T},\ell\ell}$) and the Higgs candidate mass, it is important to assign a dedicated modelling uncertainty on the shape of such distributions. This is done by comparing the distributions of the two variables obtained in the case of a specific variation of the theory parameters, or also a different MC generator. In this comparison, the distributions are normalised to unity area in order to isolate shape differences and the maximal deviation is parameterised by an analytical function and taken as $\pm\sigma$ variation. This is done separately for $t\bar{t}$ and W/Z+jets processes and these functions are used to extract event-by-event scale factors to derive systematically varied templates for the final combined fit.

[4]A more general discussion about the different sources of the theory modelling uncertainties is presented in Section 5.10.

Source of uncertainty	Impact [%] (a)	(b)	(c)
b-tagging	4.0	8.0	10
V+jets modelling	3.5	6.0	5.0
Top modelling	3.7	4.8	4.5
MC statistics	1.8	5.4	4.9
SM $Vh(b\bar{b})$	0.8	3.2	2.1
Diboson modelling	0.8	1.5	1.1
Signal modelling	3.0	2.5	1.5
Luminosity	2.0	2.5	2.5
Small-R jets	1.4	3.0	2.0
Large-R jets	0.2	1.0	2.0
$E_{\mathrm{T}}^{\mathrm{miss}}$	1.2	1.7	1.1
Leptons	0.2	0.8	0.7
Total syst. uncert.	6.5	13	13
Statistical uncert.	2.3	20	22
Total uncertainty	7	24	25

TABLE 5.6: Impact of the dominant sources of systematic uncertainties, for three representative Z'-2HDM scenarios after the fit to simulated data including the signal: (a) $(m_{Z'},m_A)$=(0.6 TeV,0.3 TeV), (b) $(m_{Z'},m_A)$=(1.4 TeV,0.6 TeV), and (c) $(m_{Z'},m_A)$=(2.6 TeV,0.3 TeV).

Signal modelling uncertainties For what concerns the theory modelling uncertainties on the Z'-2HDM signal model, the values of the signal theory uncertainties used in the analysis correspond to the ones used for the publication of the mono-H($b\bar{b}$) results with 3.2 fb^{-1} of integrated luminosity [152]. These uncertainties are derived by taking into account the differences caused by the variation of the μ_R and μ_F scales, the uncertainty on the PDFs and the specific choice of *tuned* parameters [139][5]. For each source of systematic uncertainty, the relative difference of the SR acceptance in each $E_{\mathrm{T}}^{\mathrm{miss}}$ bin for each of the considered mass points is evaluated and the upward and downward variations are then symmetrised. The variations lead in general to changes in the acceptance that are smaller than 10%, although they can be larger for regions with low acceptance at either low or high $E_{\mathrm{T}}^{\mathrm{miss}}$ depending on the specific mass point.

In addition to the experimental and theory systematic uncertainties, also uncertainties due to the limited MC statistics of the background samples are included in the final fit, using a light version of the Beeston-Barlow technique [153]. This results in adding an extra NP representing the statistical uncertainty on the total MC background which is completely uncorrelated across bins. Table 5.6 summarises the dominant uncertainties in terms of the relative uncertainty on the signal strength μ, for three representative Z'-2HDM scenarios. While in the medium and high $E_{\mathrm{T}}^{\mathrm{miss}}$ regimes the analysis suffers mainly from the limited statistics in data, the most dominant systematic uncertainties are related to b-tagging measurement and the theory modelling of the main background and signal processes.

[5] Also in this case, for a more detailed discussion about these sources of theory modelling uncertainty I refer to Section 5.10.

5.9 Results

The results of the fit based on the binned likelihood approach described above are shown in Figure 5.13, for the four $E_{\mathrm{T}}^{\mathrm{miss}}$ regions considered in the analysis. The post-fit normalisation factors of $t\bar{t}$, W+HF and Z+HF correspond to 1.10±0.08, 1.52±0.22 and 1.42±0.10, respectively.

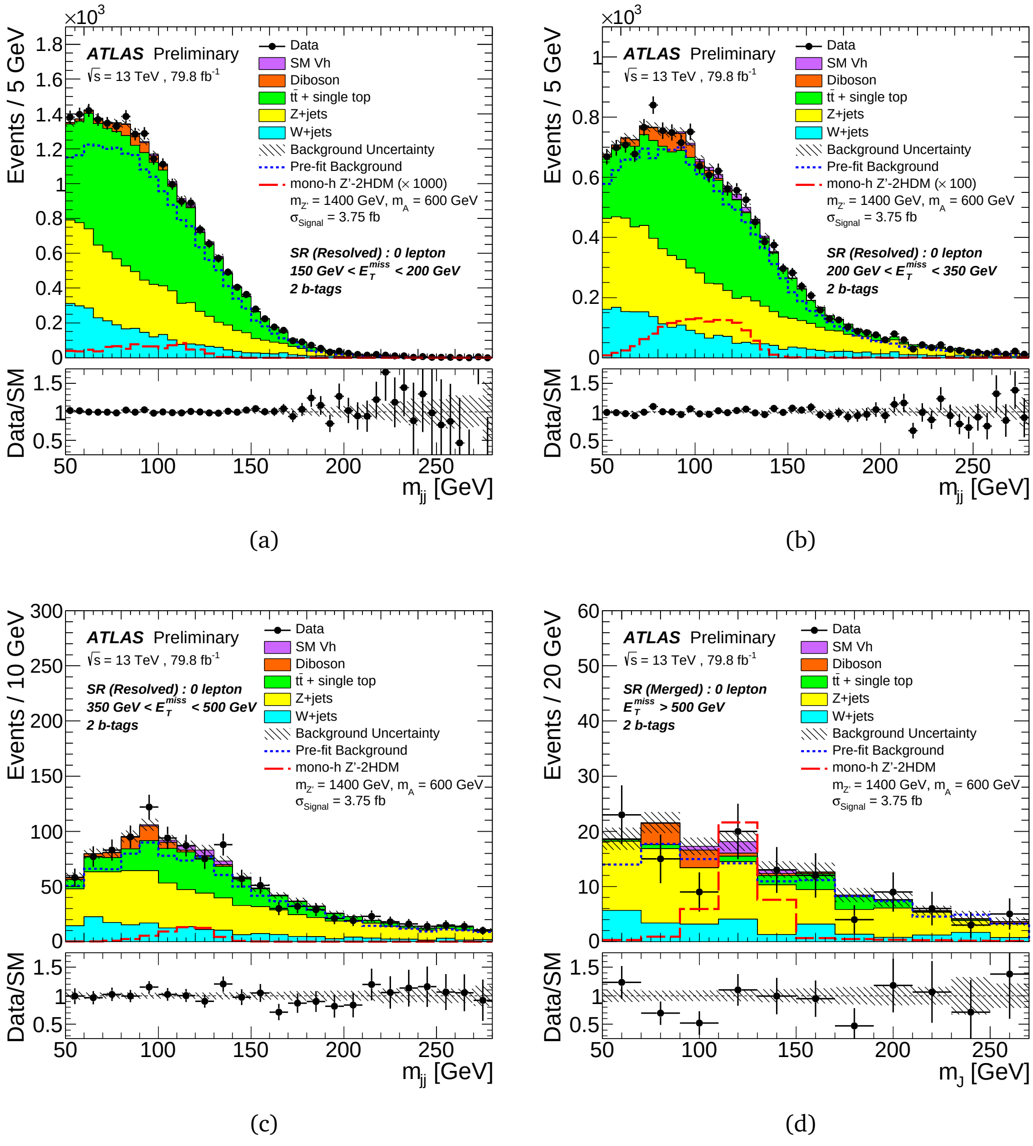

FIGURE 5.13: Distributions of the Higgs candidate mass m_h, calculated as the invariant mass m_{jj} of the di-jet system in the resolved regime and as the mass of the leading large-R jet m_J in the boosted regime. The SM expectation is shown before the fit (dashed blue line) and after the fit (solid histograms). The expected signal distribution for a representative Z'-2HDM model is also shown and is scaled up by a factor of 1000 and 100 for the lowest two $E_{\mathrm{T}}^{\mathrm{miss}}$ bins. Figures taken from Ref [130].

The distribution of the $E_{\mathrm{T}}^{\mathrm{miss}}$ in the 0ℓ-SR obtained after performing the background-only fit is shown in Figure 5.14, in which the dashed blue line represents the amount of total background estimated from simulation only. A similar comparison is shown in Figure 5.15 for what concerns the distribution of the $E_{\mathrm{T}}^{\mathrm{miss,no}\mu}$ and $p_{\mathrm{T},\ell\ell}$ in the 1μ-CR and 2ℓ-CR respectively.

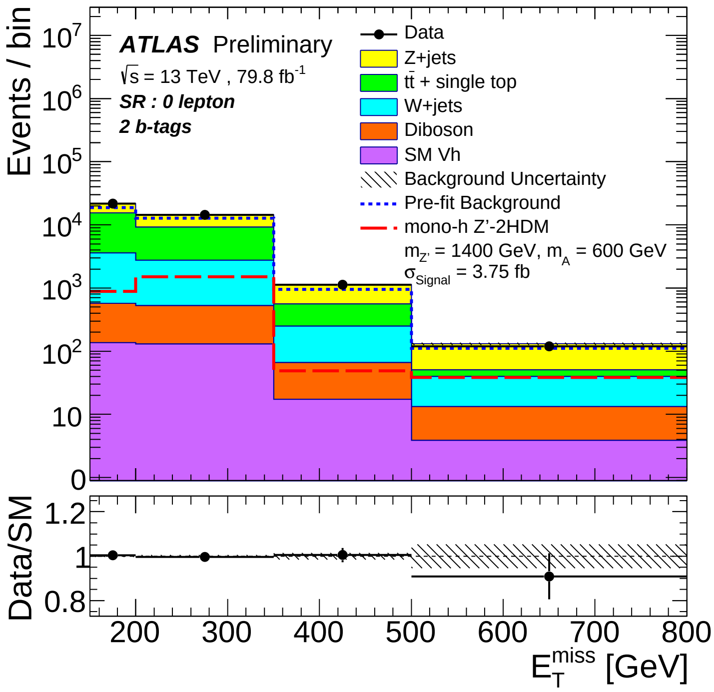

FIGURE 5.14: $E_{\mathrm{T}}^{\mathrm{miss}}$ distribution for the resolved and merged regions combined. Figure taken from Ref [130].

The number of expected background events extracted from the fit is shown in Table 5.7. No significant deviation from SM prediction is found; hence the results are used to extract 95% CL exclusion limits on the Z'-2HDM signal model.

Category	Range in $E_{\mathrm{T}}^{\mathrm{miss}}$ [GeV]			
	[150, 200)	[200, 350)	[350, 500)	[500, ∞)
W+jets	3020 ± 530	2240 ± 360	184 ± 32	26.4 ± 5.7
Z+jets	6330 ± 450	5180 ± 340	565 ± 37	80.5 ± 6.3
$t\bar{t}$ + single top quark	11 800 ± 350	6450 ± 200	308 ± 25	10.8 ± 2.5
Diboson	438 ± 67	400 ± 59	49.0 ± 11	9.37 ± 1.7
Vh	136 ± 39	129 ± 37	17.3 ± 5.0	3.86 ± 1.1
Bkg	21 700 ± 140	14 400 ± 110	1120 ± 25	131 ± 7.2
Data	21818	14350	1128	119

TABLE 5.7: Numbers of expected background events for each background process after the background-only profile likelihood fit compared with the number of observed data yields.

Figure 5.16 shows the exclusion contours in the ($m_{Z'}$,m_A) space in the Z'-2HDM scenario. The comparison with respect to the previous exclusion contours [129] corresponding to 36.1 fb^{-1} of integrated luminosity (blue dash-dotted line) shows the large improvement in the excluded phase-space region.

It is at this point important to understand whether the observed improvement is only caused by the doubled amount of luminosity or by the new techniques employed in the new iteration of the analysis. Figure 5.17 shows the comparison between the

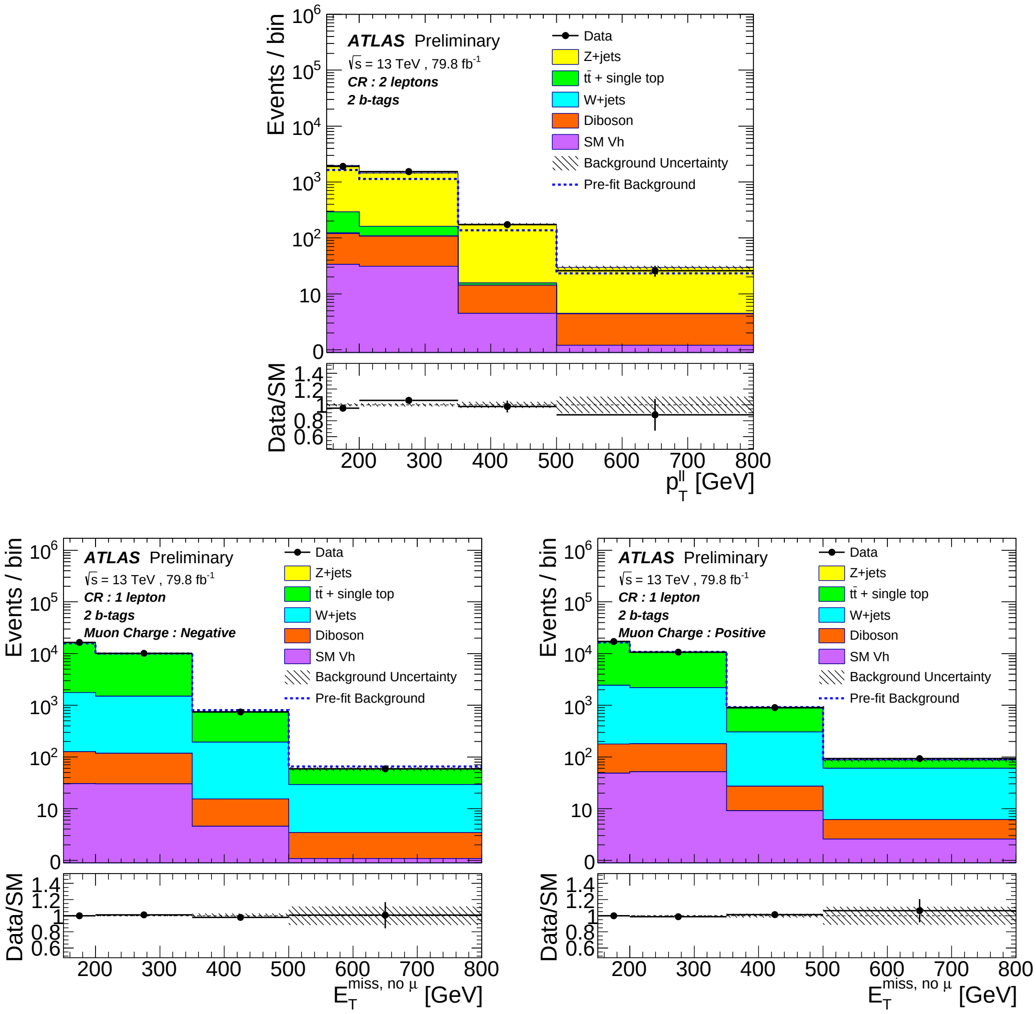

FIGURE 5.15: Distributions of $p_{\mathrm{T},\ell\ell}$ in the 2ℓ-CR (at the top) and $E_{\mathrm{T}}^{\mathrm{miss,no}\mu}$ in the 1μ-CR (at the bottom) before and after the background-only fit. The events in the 1μ-CR are separated by the sign of the electric charge of the muon. Figures taken from Ref [130].

expected upper limits on the signal strength μ as a function of $m_{Z'}$, obtained after performing the analysis using only the 2 b-tag category with VR track jets or the combined 1 b-tag and 2 b-tag categories with FR track jets. Both curves are scaled to the same integrated luminosity equal to 79.8 fb^{-1}. The ratio between the upper limits obtained in the two cases shows a significant improvement for high $m_{Z'}$, which is mostly caused by the usage of VR track jets.

The results of this work represent the first ever usage of VR track jets within the ATLAS collaboration. They have been published in the form of an ATLAS conference note [130] and presented at the 10th International Workshop on Boosted Object Phenomenology, Reconstruction and Searches in High Energy Physics [154] in July 2018.

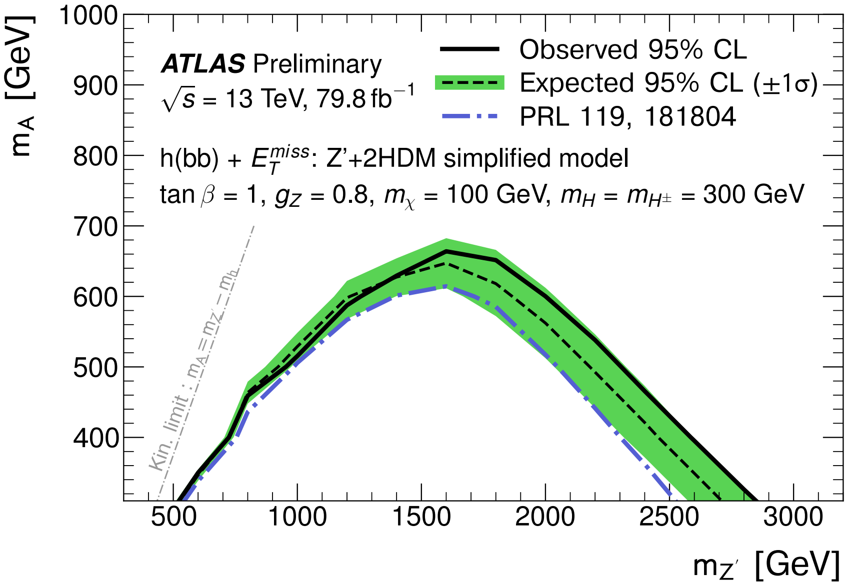

FIGURE 5.16: Exclusion contours for the Z'-2HDM scenario in the ($m_{Z'}$,m_A) plane for $\tan\beta = 1$, $g_Z = 0.8$, and $m_\chi = 100$ GeV. Observed limits from previous results at $\sqrt{s} = 13$ TeV and 36.1 fb^{-1} of integrated luminosity (see Ref. [129]) are also shown (dash-dotted line). Figure taken from Ref [130].

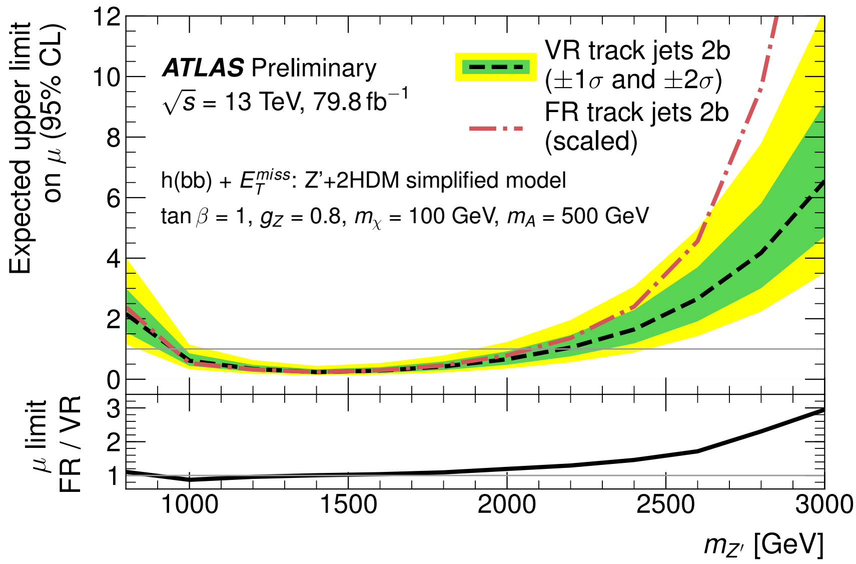

FIGURE 5.17: Comparison of the expected upper limits on the signal strength μ for the analysis using VR track jets against the previous iteration of the analysis performed with FR track jets, scaled to the same amount of luminosity of 79.8 fb^{-1}. Figure taken from Ref. [130].

5.10 Towards the full Run 2 results

As mentioned in Section 5.8, the theory modelling uncertainties used for the results presented so far are inherited from the SM $VH(b\bar{b})$ analysis which probes a very similar signature. Moreover, as the focus of the SM $VH(b\bar{b})$ analysis in recent years concerned the low/medium E_T^{miss} regime, the uncertainties in the merged region are extrapolated from the resolved one, without applying further corrections. Although Table 5.6 shows that the mono-H($b\bar{b}$) analysis performed with 79.8 fb^{-1} of integrated luminosity is statistically limited in the medium and high $E_{\mathrm{T}}^{\mathrm{miss}}$ regimes, a large impact on the total systematic uncertainty originates from the theory modelling of the V+jets, top quark and signal processes. A new dedicated estimate of these uncertainties is therefore desirable in order to improve the precision and the accuracy of the mono-H($b\bar{b}$) search.

Since several MC samples needed for the estimation of these uncertainties are not run through the ATLAS detector simulation but they are only available at truth-level, a new dedicated analysis framework that performs the full mono-H($b\bar{b}$) event selection at truth-level has been developed. Furthermore, this approach allows us to completely decouple the impact of the theory predictions from the detector effects, as the simulation of the ATLAS detector is not yet taken into account.

In the following, the description of the truth-level implementation of the 0ℓ SR event selection is discussed and a new estimate of the theory modelling uncertainties of Z'-2HDM signal model is presented. Additional studies on the alternative 2HDM+a signal model and $Z(\nu\nu)$+jets and $t\bar{t}$ background processes are presented in Appendix A.

5.10.1 Implementation of the 0ℓ truth-level analysis

In ATLAS, the production of the MC samples starts from the generation of particle-level events for the process of interest, in the form of Event Generator Output (EVNT) files. The following step consists in reproducing the interaction of the particle-level objects (jets, leptons, $E_{\mathrm{T}}^{\mathrm{miss}}$, etc) with the ATLAS detector. The last step involves the reconstruction of physics objects from detector-level information and takes into account the simulation of pile-up as well as the one of the trigger system. The final sample is then provided in a ROOT-readable format, known as Analysis Object Data (xAOD) [155]. Eventually, each physics analysis makes use of a dedicated *derivation* framework, which applies a basic event selection on the xAODs and save the selected events in a smaller sample, called Derived Analysis Object Data (DxAOD), having the same structure. While the actual analysis is performed at the reconstruction-level using DxAODs, in order to derive new values for the theory modelling uncertainties, the full event selection is applied directly on the EVNT samples.

The first step consists in replicating the definition of each cut that is part of the event selection of the original analysis, at truth-level. While most of the cuts can be implemented in a relatively straightforward way also on particle-level objects, a few aspects are conceptually non-trivial and need a dedicated discussion.

The first complication originates from the fact that pile-up is not simulated at truth-level while, as described in Section 4.2.2, the reconstruction of large-R jets relies heavily on the usage of the trimming procedure, whose aim is to mitigate the effect of additional radiation from pile-up and UE. In order to be consistent with the reconstruction-level analysis, it is therefore important to apply the same procedure also at truth-level. As shown in Figure 5.18, the effect of trimming on truth large-R jets is relatively small, as expected due to the absence of the soft component that characterises pile-up jets. As the resulting truth trimmed large-R jets show a similar distribution with respect to the jets reconstructed by the ATLAS detector and used in the actual mono-H($b\bar{b}$) analysis, this jet collection is employed in the truth-level analysis.

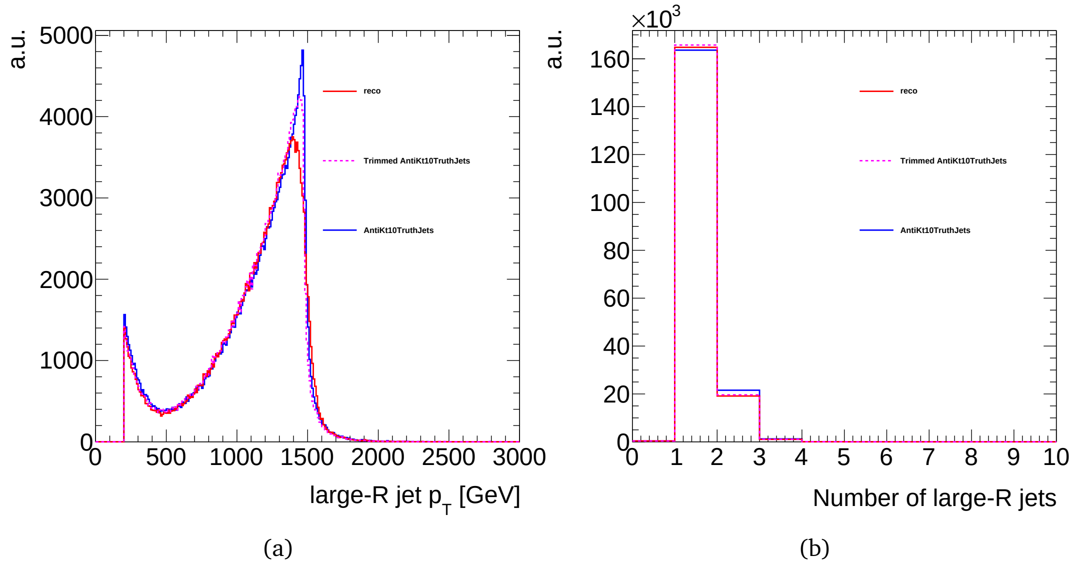

FIGURE 5.18: Comparison between p_T (on the left) and multiplicity (on the right) distribution of the trimmed $R = 1.0$ jets reconstructed by the ATLAS detector (in red) and the one at truth-level, before (blue curve) and after (magenta curve) applying the trimming procedure, for a representative Z'-2HDM signal with $m_{Z'} = 3.0$ TeV and $m_A = 400$ GeV.

Another difficulty that needs to be faced when implementing the mono-H($b\bar{b}$) analysis at truth-level is related to the definition of the object-based E_T^{miss} significance. As described in Sections 4.7.1-5.5, the new object-based definition of the E_T^{miss} significance takes into account the expected resolution and directional correlations of all the objects entering in the E_T^{miss} reconstruction. This brings a conceptual problem when trying to define the same variable using particle-level objects to which, by definition, no uncertainties are assigned. Nevertheless, as the uncertainties on the objects used for the E_T^{miss} reconstruction are estimated from simulation, in order to mimic the behaviour of the object-based E_T^{miss} significance at truth-level, it is possible to calculate a new approximated version of the object-based E_T^{miss} significance by assigning such uncertainties to particle-level objects. The new implemented version of the object-based E_T^{miss} significance can then be compared with the one adopted in the original analysis for both background and signal processes. Figure 5.19 shows the good agreement of the distribution of the original object-based E_T^{miss} significance with respect to its new approximated definition at truth-level. The quite similar shape of the two distributions can in part be explained by the fact that the original definition of the object-based E_T^{miss} significance adopted in the actual analysis does not take into account the resolution of pile-up jets, allowing to achieve a very similar definition of the same variable at truth-level.

The truth-level implementation of the mono-H($b\bar{b}$) 0ℓ SR is validated against the original one, by applying the full selection to the same set of simulated MC events and counting the number of events selected by both the original and truth-level analysis in each E_T^{miss} bin.

During this study, a large impact of the extended τ veto at truth-level has been observed, in contrast to the reconstruction-level analysis. As this aspect is still under investigation, this specific requirement has been temporarily excluded from the truth baseline selection. As the main purpose of the extended τ veto is a more aggressive

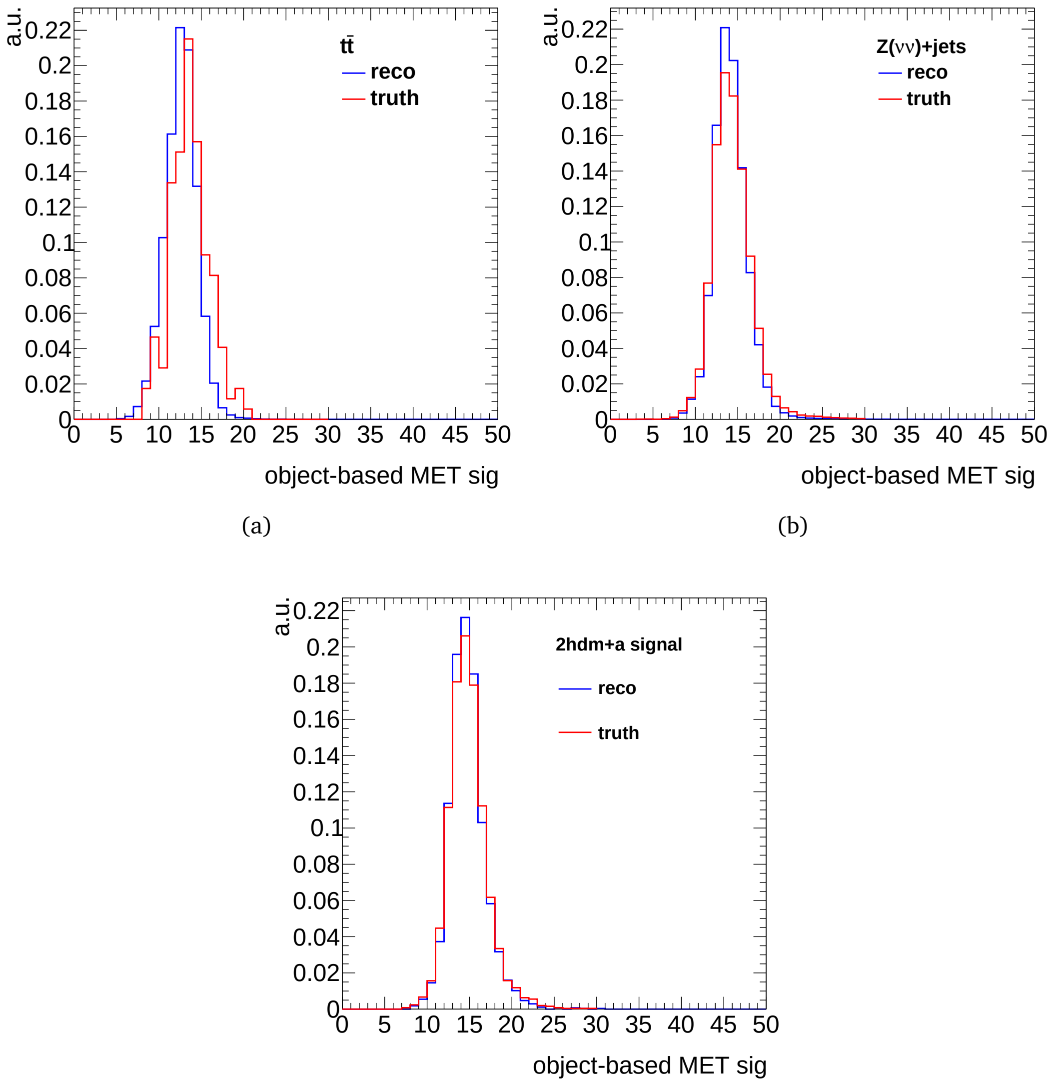

(a) (b)

(c)

FIGURE 5.19: Comparison between the original object-based definition, which does not include the resolution of pile-up jets and that of the $E_{\mathrm{T}}^{\mathrm{miss}}$ soft term, of the $E_{\mathrm{T}}^{\mathrm{miss}}$ significance as reconstructed by the ATLAS detector (in blue) and the one at truth-level (in red), for the case of a $t\bar{t}$ sample (at the top left), a $Z \to \nu\nu$+jets sample (at the top right) and a 2HDM+a signal model (at the bottom). All the histograms are scaled to unity.

suppression of the $t\bar{t}$ background, the final results presented in Section 5.10.3 for the Z'-2HDM signal model are not expected to change significantly after the inclusion of this cut, as the impact of this requirement on signal events is fairly small.

The rest of the event selection follows the same criteria illustrated in Table 5.4, including the final cut on the Higgs candidate mass which is required to be in the [50, 280] GeV window, except for two main differences that will characterise the event selection of the full Run 2 data. The first one is related to the cut value of the object-based $E_{\mathrm{T}}^{\mathrm{miss}}$ significance which is set to the looser value of 12. This new cut value is motivated by the observation, at reconstruction-level, of an object-based

E_T^{miss} significance spectrum shifted to lower values, with respect to the previous version of the analysis, which is likely caused by a new estimate of the JER. The second difference consists in the removal of the cuts involving p_T^{miss}, whose usage has been deprecated by the ATLAS collaboration due to the absence of dedicated systematic uncertainties, which are instead superseded by a tighter jet cleaning requirement (`TightBadJet` WP) in order to suppress the non-collision background. Figure 5.20 shows the number of events passing the SR selection criteria in both the truth-level and the reconstruction-level analysis, split in the usual four E_T^{miss} regions, for two representative Z'-2HDM signal samples. The majority of the events lies along the diagonal and migrations across the four E_T^{miss} regions are smaller than 10%. The same study is performed on $t\bar{t}$ and $Z(\rightarrow \nu\nu)$+jets events, representing the two main background sources in the SR. Figure 5.21 shows that the migrations across different E_T^{miss} bins are more significant in background rather than in signal events but they are in any case larger across adjacent E_T^{miss} regions, as expected. These results, together with the reasonably good agreement of the variables shown in Figures 5.18-5.19, suggest that the current implementation of the truth-level analysis represents sufficiently well the phase-space of the mono-H($b\bar{b}$) analysis at the reconstruction-level. We can therefore proceed to the next step which consists in the actual evaluation of the theory systematic uncertainties.

5.10.2 Evaluation of the theory uncertainties

As anticipated already in Chapter 3, the *factorisation theorem* allows us to express the total cross-section of the hard-scattering process as a function of the PDF of the partons involved in the process and of the cross-section at parton-level. Starting from Equation 3.2, it is possible to write the total cross-section at the n-th order in perturbation theory as:

$$\sigma_{AB\rightarrow X}^{(n)} = \sum_{a,b} \int dx_a dx_b f_{a/A}(x_a, \mu_F^2) f_{b/B}(x_b, \mu_F^2) \times \hat{\sigma}_{ab\rightarrow X}^{(n)}(\hat{s}, \mu_R^2, \mu_F^2). \quad (5.12)$$

The *factorisation scale* μ_F can be interpreted as the scale that separates the long- and short-distance physics. The *renormalisation scale* μ_R corresponds instead to the reference scale introduced in the computation of the QCD coupling constant in order to allow a proper treatment of ultraviolet divergences.

The simulation of signal and background processes is affected by the following main sources of uncertainty:

- **missing higher orders** in the perturbative expansion of the cross-section at parton-level. For all simulated processes the calculation of the cross-section is truncated at a certain order n in perturbation theory. While an exact computation of the cross-section is invariant under changes of μ_F and μ_R, in the absence of a complete set of higher order corrections it is necessary to make a specific choice for the two scales. The effect of the missing higher orders is estimated by varying μ_F and μ_R independently by a factor of 2 [6].

- **PDF and α_s** uncertainties. The determination of the PDF itself from collision data is affected by several aspects that are associated to the experimental uncertainty on the dataset, the uncertainty on the functional form adopted in the

[6] The variations $(\mu_F,\mu_R)=(0.5,2),(2,0.5)\times\mu_{\text{nominal}}$ are excluded in order to avoid large logarithms in the calculation induced by the large scale differences.

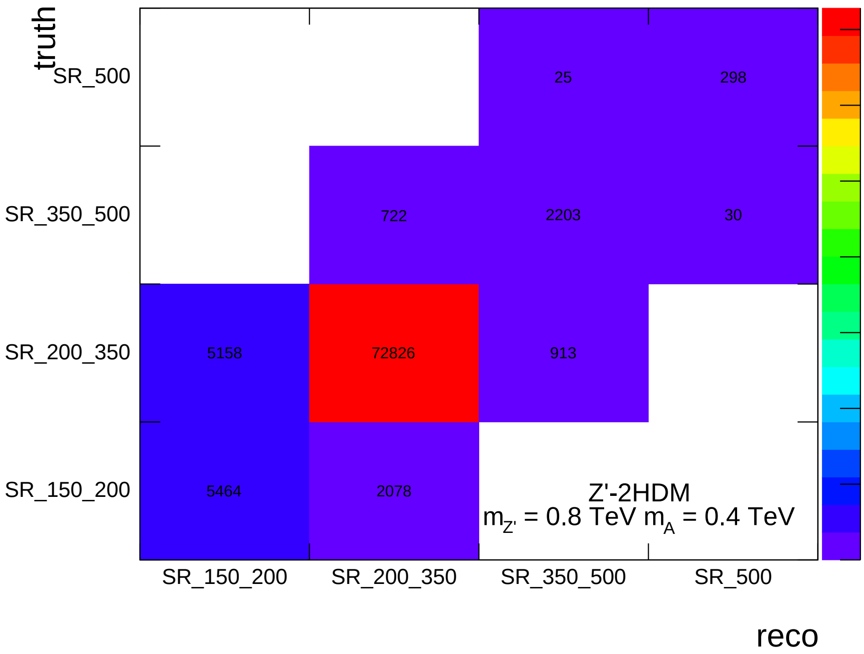

(a)

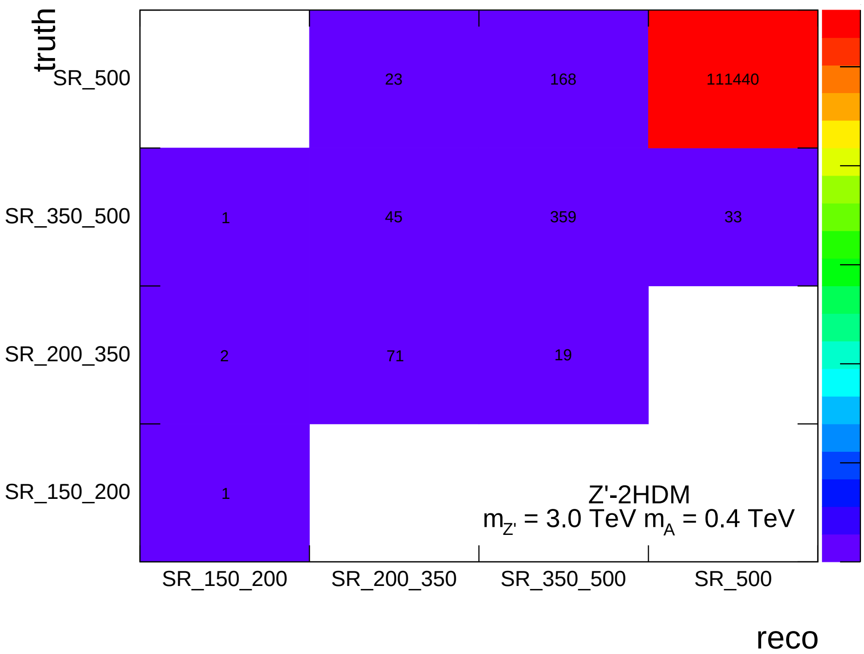

(b)

FIGURE 5.20: Migration matrices showing the number of events passing the SR selection in the four $E_{\mathrm{T}}^{\mathrm{miss}}$ regions, at reconstruction and truth-level, for two representative Z'-2HDM signals corresponding to $m_{Z'} = 0.8$ TeV and $m_A = 0.4$ TeV at the top and $m_{Z'} = 3.0$ TeV and $m_A = 0.4$ TeV at the bottom. The selection is performed inclusively in the number of b-tagged jets.

PDFs fit as well as the experimental determination of α_s. The evaluation of these uncertainties follows the procedure suggested in Ref. [156].

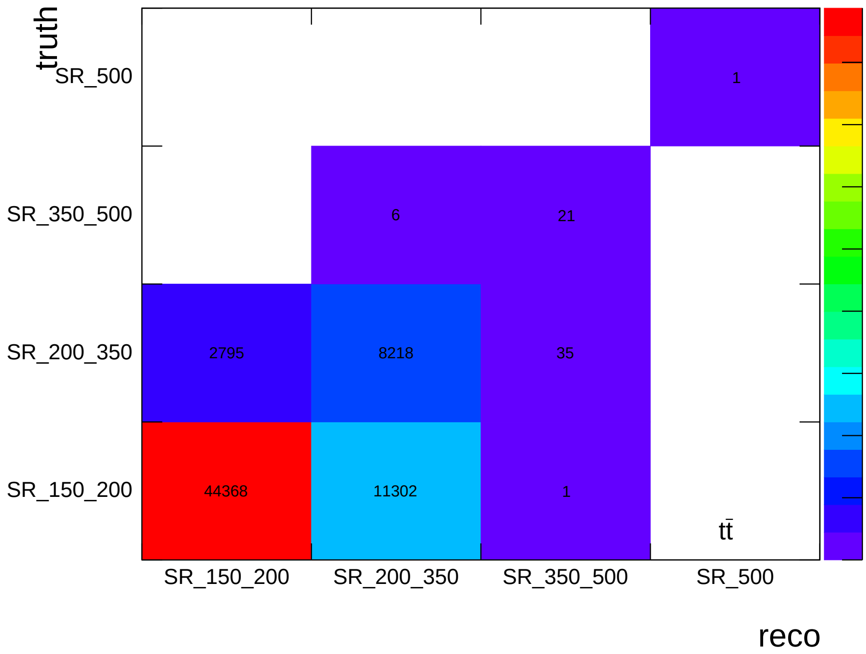

(a)

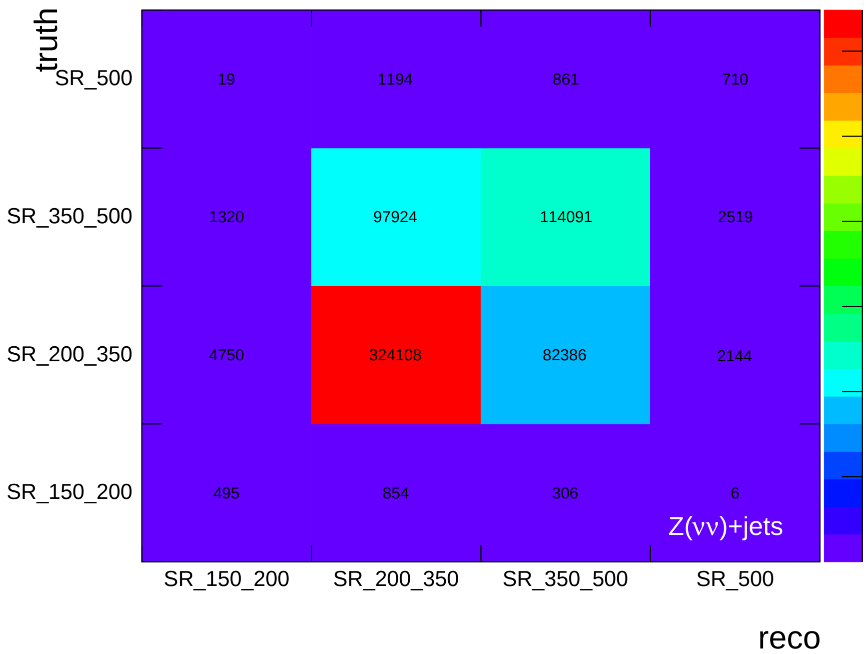

(b)

FIGURE 5.21: Migration matrices showing the number of events passing the SR selection in the four $E_{\mathrm{T}}^{\mathrm{miss}}$ regions, at reconstruction and truth-level, for the $t\bar{t}$ sample (at the top) and a $Z(\rightarrow \nu\nu)$ sample (at the bottom). The selection is performed inclusively in the number of b-tagged jets.

- **parton shower/hadronisation/eigentune** uncertainties. Each MC generator relies on specific models to describe the parton shower, hadronisation and multiple interaction processes. Such models are in practice approximations of QCD calculations and they are based on several free parameters, which need to be optimised (*tuned*) in order to reproduce a good description of the measured observable [139]. The impact due to the chosen values of these parameters is therefore an additional source of uncertainty that needs to be taken into account.

- **matching and merging** uncertainties which are associated to the removal of double-counting arising from interfacing the NLO calculation to parton showers processes and from the combination of final states with different jet multiplicities.

In order to evaluate the impact of the theory uncertainties on the final experimental results, for each variation of the theory parameters two different types of uncertainty are derived on:

- the **shape** on the most discriminating variable used in the final likelihood fit which, in the mono-H($b\bar{b}$) SR, is represented by Higgs candidate mass m_h,
- the **acceptance** of the regions considered for the final statistical analysis.

The shape uncertainty on m_h caused by the variation of a specific theory parameter as well as from a different MC generator can be easily derived as the ratio of m_h histogram obtained for the probed theory uncertainty over the one corresponding to the nominal case. On the other hand, the acceptance uncertainty can be derived as the relative difference of the nominal acceptance for a specific region (SR, CRs, specific $E_{\mathrm{T}}^{\mathrm{miss}}$ bin etc) with respect to a certain variation.

5.10.3 Comparison with previous results: Z'-2HDM signal model

A new estimate of the uncertainties on the Z'-2HDM signal model is derived, in order to compare the impact of the signal modelling uncertainty with respect to the values used in the analysis described in the previous sections. The approach used for the previous publications [152, 129] consists in evaluating the relative difference in the signal acceptance caused by:

- a coherent variation by a factor of 2 of the μ_F and μ_R scales,
- the A14 tune variations with the NNPDF PDF set,
- the comparison between the central value of the default NNPDF2.3LO PDF set with respect the two alternative MSTW2008 [157] and CTEQ6L1 [158] PDF sets,

for each specific $E_{\mathrm{T}}^{\mathrm{miss}}$ bin in the SR. Table 5.8 shows the values of the relative uncertainty on the signal acceptance used in the previous results, for three representative Z'-2HDM scenarios.

The comparison focuses on the estimation of the scale and PDF uncertainty only, due to the unavailability of the A14 tune variations in the new MC samples. Where possible, the procedure to derive these uncertainties follows closely the previous approach: the μ_R and μ_F scale variations are varied by a factor of 2 coherently and the central value of the NNPDF3.0 PDF set is compared with the MMHT and CT14 alternative PDFs [156]. Furthermore, the NNPDF collaboration provides a set of PDFs

Source of uncertainty	E_T^{miss} bin 1	E_T^{miss} bin 2	E_T^{miss} bin 3	E_T^{miss} bin 4
$m_{Z'}$ =0.6 TeV, m_A = 0.3 TeV				
$(\mu_R,\mu_F)\times 2,0.5$	0.333%	0.14%	1.22%	8.0%
NNPDF2.3LO vs MSTW2008/CTEQ6L1	0.0317%	1.82%	7.23%	76.0%
$m_{Z'}$ =1.4 TeV, m_A = 0.6 TeV				
$(\mu_R,\mu_F)\times 2,0.5$	4.64%	0.884%	0.854%	0.378%
NNPDF2.3LO vs MSTW2008/CTEQ6L1	4.27%	3.54%	0.87%	1.13%
$m_{Z'}$ =2.6 TeV, m_A = 0.3 TeV				
$(\mu_R,\mu_F)\times 2,0.5$	-	-	-	0.189%
NNPDF2.3LO vs MSTW2008/CTEQ6L1	-	-	-	0.626%

TABLE 5.8: Old values of the relative difference on signal uncertainty due to scale and PDF variations for three representative Z'-2HDM signal models. The symbol "-" denotes sources of uncertainty that are neglected due to an acceptance lower than 1%.

as a result of the fit on an ensemble of artificial data replicas [159]. The best value is expected to correspond to the mean value of all replicas and the error is given by the standard deviation of this ensemble. The uncertainty due to the PDF variations can therefore be calculated as:

$$\Delta X = \sqrt{\frac{1}{N-1}\sum_i (X_i - X_0)^2} \tag{5.13}$$

where N is the number of PDF replicas available (in this case $N = 100$), X_i is the value of the observable (in this case the integral of the dark Higgs candidate mass distribution) for the i-th PDF variation and X_0 is the mean value of this chosen observable (which is expected to correspond to the one of the nominal sample). This additional source of uncertainty, which was neglected previously, is now properly taken into account.

A comparison for some relevant distributions as E_T^{miss}, number of b-tagged jets and Higgs candidate mass when varying the μ_F and μ_R scales and the PDF choice, for a representative Z'-2HDM scenario with $m_{Z'}$ =1.4 TeV and m_A = 600 GeV, is shown in Figure 5.22 after applying the full SR event selection described in Section 5.10.1. Neither the shape of the m_h or the one of the E_T^{miss} is affected by the considered variations, therefore no shape uncertainties are evaluated for the Z'-2HDM processes.

The new uncertainties are estimated by evaluating the relative difference in the signal acceptance of each E_T^{miss} bin, after applying the full truth-level SR selection described in Section 5.10.1, inclusively in the number of b-tagged jets.

The values of the scale and PDF uncertainties obtained with the new truth-level implementation are shown in Table 5.9 and their impact on the signal strength is compared with the previous results in Table 5.10, after performing the fit to simulated data under the signal hypothesis of three representative Z'-2HDM scenarios. The new signal modelling uncertainty estimates are significantly smaller than the ones adopted in the previous analysis. This can be explained by a better description of the physics process at parton-level in the newer MC simulations as well as a revisited prescription for the estimation of such uncertainties over the last years. The final effect on the

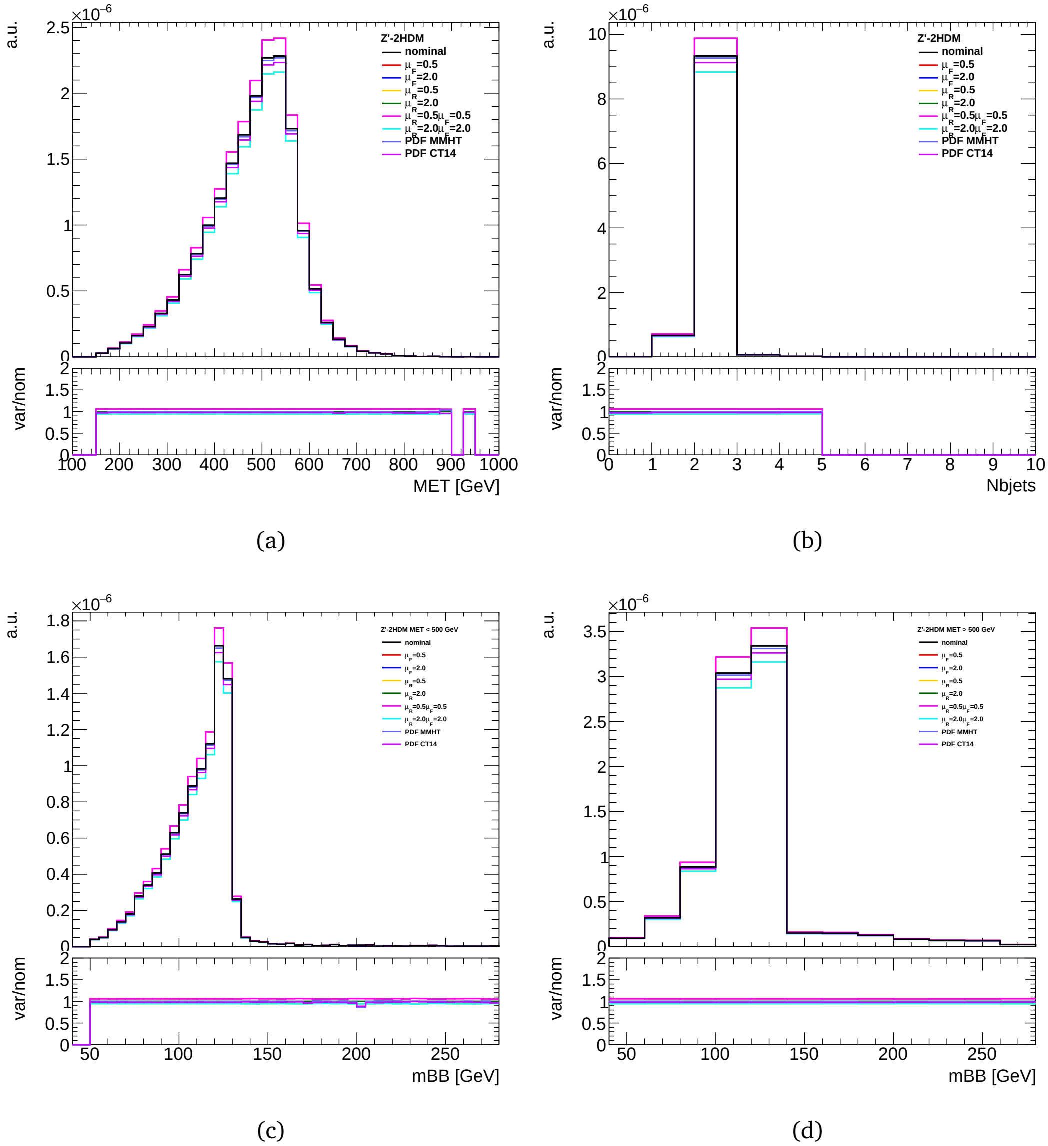

FIGURE 5.22: Comparison of the distribution of $E_{\mathrm{T}}^{\mathrm{miss}}$, number of b-tagged jets and Higgs candidate mass between the nominal case and each systematic variation for Z'-2HDM signal events generated for $m_{Z'}$ = 1.4 TeV and m_A = 600 GeV. At the top, distribution of the $E_{\mathrm{T}}^{\mathrm{miss}}$ and number of b-tagged jets. At the bottom, distribution of Higgs candidate mass for events in the resolved region ($E_{\mathrm{T}}^{\mathrm{miss}} < 500$ GeV) on the left, and in the merged region ($E_{\mathrm{T}}^{\mathrm{miss}} > 500$ GeV) on the right. The nominal sample is shown in black, while the coloured lines represent the different sources of theory uncertainty. All distributions are inclusive in the number of b-tagged jets.

total systematic uncertainty, as shown in Table 5.10, is relatively small in the low and medium $E_{\mathrm{T}}^{\mathrm{miss}}$ regime, as the dominant source of uncertainty originates from the A14 tune variations whose high impact would need a dedicated investigation in the future.

Source of uncertainty	E_T^{miss} bin 1	E_T^{miss} bin 2	E_T^{miss} bin 3	E_T^{miss} bin 4
$m_{Z'}$ =0.6 TeV, m_A = 0.3 TeV				
$(\mu_R,\mu_F)\times 2,0.5$	0.18%	0.20%	(0.32%)	(0.40%)
NNPDF3.0 vs CT14	0.03%	0.12%	(0.25%)	(0.30%)
NNPDF3.0 vs MMHT	0.10%	0.02%	(0.45%)	(0.08%)
NNPDF3.0 standard deviation	0.11%	0.11%	(0.48%)	(0.39%)
$m_{Z'}$ =1.4 TeV, m_A = 0.6 TeV				
$(\mu_R,\mu_F)\times 2,0.5$	(0.15%)	0.12%	0.03%	0.02%
NNPDF3.0 vs CT14	(0.31%)	0.02%	0.02%	0.09%
NNPDF3.0 vs MMHT	(0.23%)	0.09%	0.02%	0.08%
NNPDF3.0 standard deviation	(0.61%)	0.10%	0.06%	0.06%
$m_{Z'}$ =2.6 TeV, m_A = 0.3 TeV				
$(\mu_R,\mu_F)\times 2,0.5$	(0.35%)	(0.45%)	(0.37%)	0.04%
NNPDF3.0 vs CT14	(2.95%)	(0.12%)	(1.29%)	0.02%
NNPDF3.0 vs MMHT	(4.66%)	(0.33%)	(0.74%)	0.02%
NNPDF3.0 standard deviation	(3.00%)	(0.85%)	(0.77%)	0.04%

TABLE 5.9: New values of the relative difference on signal uncertainty due to scale and PDF variations for three representative Z'-2HDM signal models. Brackets are shown around values corresponding to regions with acceptance lower than 1%.

Source of uncert.	Impact [%]		
	(a)	(b)	(c)
b-tagging	4.0	8.0	10
V+jets modelling	3.5	6.0	5.0
Top modelling	3.7	4.8	4.5
MC statistics	1.8	5.4	4.9
SM $Vh(b\bar{b})$	0.8	3.2	2.1
Diboson modelling	0.8	1.5	1.1
Signal modelling	**new: 2.9** **previously: 3.0**	**new: 2.2** **previously: 2.5**	**new: < 0.01** **previously: 1.5**
Luminosity	2.0	2.5	2.5
Small-R jets	1.4	3.0	2.0
Large-R jets	0.2	1.0	2.0
$E_{\mathrm{T}}^{\mathrm{miss}}$	1.2	1.7	1.1
Leptons	0.2	0.8	0.7
Total syst. uncert.	6.5	13	13
Statistical uncert.	2.3	20	22
Total uncertainty	7	24	25

TABLE 5.10: Dominant sources of uncertainty for three representative Z'-2HDM scenarios after the fit to simulated data including the signal: (a) $(m_{Z'}, m_A)$ = (0.6 TeV,0.3 TeV), (b) $(m_{Z'}, m_A)$ = (1.4 TeV,0.6 TeV), and (c) $(m_{Z'}, m_A)$ = (2.6 TeV,0.3 TeV). The effect is expressed as the relative uncertainty on the signal strength, assuming total cross-sections of (a) 452 fb, (b) 3.75 fb, and (c) 2.03 fb. The total uncertainty is the quadrature sum of statistical and total systematic uncertainties.

6 *b*-tagging on Variable-Radius track jets

As already anticipated in Section 4.3, the measurement of the *b*-tagging efficiency in collision data is of crucial importance in order to correct for the imperfections of the detector and the modelling of physics processes in MC simulations. In this chapter, a measurement of the *b*-jet tagging efficiency, for the case of VR track jets, of the high-level algorithms used to analyse the pp collision data recorded by the ATLAS experiment during Run 2 of the LHC is presented.

6.1 *b*-tagging calibration

The *b*-tagging algorithms that are considered in this study are the `MV2c10` BDT and the `DL1` Deep Neural Network. Both taggers have been trained, on calorimeter small-R jets, using a hybrid sample comprising $t\bar{t}$ and Z' events, in order to optimise their performance for both low and high p_{T} jets, as mentioned in Section 4.3. The *b*-tagging performance in data has been found to be very stable with respect to the different pile-up conditions that characterised the ATLAS data taking from 2015 until 2018. Hence it has been possible to combine all the datasets and perform a measurement of the *b*-tagging efficiency using the full statistics from the pp collisions that occurred during Run 2 of the LHC.

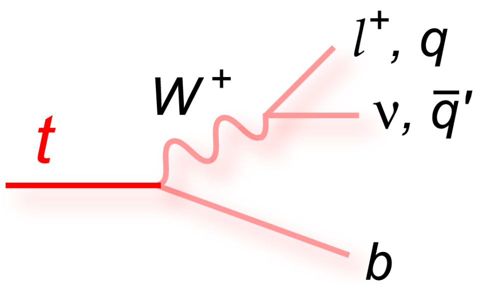

FIGURE 6.1: Illustration of the different final states arising from a top quark decay, depending on the decay mode of the W boson.

In order to achieve a precise measurement of the *b*-tagging efficiency in data, selecting events with a sufficiently high *b*-jet purity is an asset. For this purpose, one of the best candidates for this type of measurement is the top quark (t) which is abundantly produced at the LHC, mostly in pairs with an anti-top quark ($\bar{t}$) through gluon fusion processes, and then decays to a W boson and a bottom quark (b), with a BR close to unity. Depending on the decay mode of the W boson, several different signatures can describe the final state (see Figure 6.1). It is indeed possible to observe:

- a fully **hadronic** final state, in case both W bosons decay to $q\bar{q}'$,
- a **semi-leptonic** final state, in case one W boson decays to $\ell\nu$ and the other decays to $q\bar{q}'$,
- a **di-leptonic** final state, in case both W bosons decay to $\ell\nu$.

All the three channels can potentially be used to perform this type of measurement, although the presence of exactly two leptons, with opposite electric charge, allows to achieve a very pure sample of $t\bar{t}$ events. For this reason, only di-leptonic events are considered in this study. The dominant source of background is represented by events with two real prompt leptons from the decay of the W or Z boson. This includes also single top quark production in association with a W boson and diboson events (WW, WZ, ZZ) where at least two leptons are produced in the electroweak boson decays. By requiring that the two leptons have opposite flavour, the background from $Z \to \ell\ell$ events is significantly reduced. Furthermore, the residual contribution from $Z \to \tau\tau$ events, which populate the low mass region, is further reduced by considering only events with $m_{e\mu} \geqslant 50$ GeV. Background events with additional jets from ISR and FSR or from W+jets processes are suppressed by requiring exactly two reconstructed jets.

In addition to the basic event selection described so far, further dedicated cuts can be applied in order to optimise the sensitivity towards the $t\bar{t}$ signal and they will be discussed more extensively in the following section.

6.1.1 Object and event selection

The events are selected using the single lepton triggers shown in Table 6.1, which require the presence of a high p_{T} electron or muon and provide a fairly constant efficiency for leptons with $p_{\mathrm{T}} > 28$ GeV.

The presence of a PV is required with at least two associated tracks with $p_{\mathrm{T}} > 500$ MeV. Only events recorded in good operating conditions and included in the official GRLs for the 2015-2016, 2017 and 2017 datasets are analysed. The selected data sample corresponds to a total integrated luminosity of 140.5 fb^{-1}, resulting from combining the 2015 ($\mathcal{L}$ = 3.2 fb^{-1}), 2016 ($\mathcal{L}$ = 33.0 fb^{-1}), 2017 ($\mathcal{L}$ = 44.3 fb^{-1}) and 2018 ($\mathcal{L}$ = 60.0 fb^{-1}) datasets.

	2015	2016/2017/2018
muon trigger	HLT_mu20_iloose_L1MU15, HLT_mu40	HLT_mu26_ivarmedium, HLT_mu50
electron trigger	HLT_e24_lhmedium_L1EM20VH, HLT_e60_lhmedium, HLT_e120_lhloose	HLT_e26_lhtight_nod0_ivarloose, HLT_e60_lhmedium_nod0, HLT_e140_lhloose_nod0

TABLE 6.1: Table of the single lepton triggers adopted for the event selection.

VR track jets The reconstruction of VR track jets follows the same criteria described in Section 5.6, in the context of the mono-H($b\bar{b}$) analysis. The events are required to have at least two VR track jets each having $p_T > 5$ GeV, $|\eta| < 2.5$ and at least two constituent tracks. The leading VR track jet is required to have p_T greater than 20 GeV.

Leptons Electrons are required to pass the TIGHTLH criteria defined by the e/γ working group (see Section 4.4). They must have $|\eta| < 1.37$ or $1.52 < |\eta| < 2.47$, in order to be in the fiducial area of the ECAL, and $p_T > 28$ GeV. Muons must pass the TIGHT criteria defined by the muon performance group (see Section 4.5), have $|\eta| < 2.5$ and $p_T > 28$ GeV. A muon is considered as "bad" when reconstructed from high hit multiplicities in the MS (generally associated with very energetic punch-through jets) or from badly measured ID tracks in the jet wrongly matched to the MS segments. An event veto is applied in the presence of such "bad" muons. Lastly, both electrons and muons are required to pass the GRADIENT isolation criteria (defined in Sections 4.4-4.5). Following these criteria, the events are selected if they have exactly one muon and one electron with opposite electric charge.

m_{lj} cut In order to increase the purity of this channel, an additional cut is applied on the invariant mass m_{lj} of the lepton plus jet system. The invariant mass of the combination of a jet and a lepton resulting from the decay of a top quark is expected to be lower than the mass of the top quark. However, the p_T scale of track jets is smaller with respect to the calorimeter jets, as the charged particles only contribute about 70% of the total momentum. The m_{lj} variable is therefore required, for both the two jet plus lepton combinations, to be smaller than 150 GeV (instead of the top quark mass, i.e. 175 GeV). Since there are two leptons and two jets in the event, there are two possible ways to combine them. The combination that is found to be most effective is the one that minimises the summed squared invariant mass of both lj combinations. Following this principle, the distribution of the m_{lj} variable for both leading and subleading jet is shown in Figure 6.2. After applying the cut at 150 GeV on both the two jet plus lepton systems, the purity of the selection increases significantly for $p_T > 100$ GeV, as shown in the bottom panels of Figure 6.3.

Collinear VR track jets removal Depending on their p_T, the two VR track jets can have very different sizes (see Equation 5.5). As no boundary is set on the angular separation between the two jets, it is possible that they highly overlap and potentially become concentric. In these extreme cases, the truth flavour labelling and the track-to-jet association are compromised because they are only based on the ΔR separation between jets and truth hadrons or tracks, respectively. Figure 6.4 shows the distribution of the ΔR between the leading two VR track jets divided by the radius of the smallest (left) and the largest (right) jet among the two. When $\Delta R < R_{\text{min}}$ the axes of the two VR track jets are contained inside the cone of the smaller jet and as a result they have very similar jet axes. In order to avoid an ambiguous b-tagging, such collinear cases are discarded and only events having $\Delta R > R_{\text{min}}$ are retained.

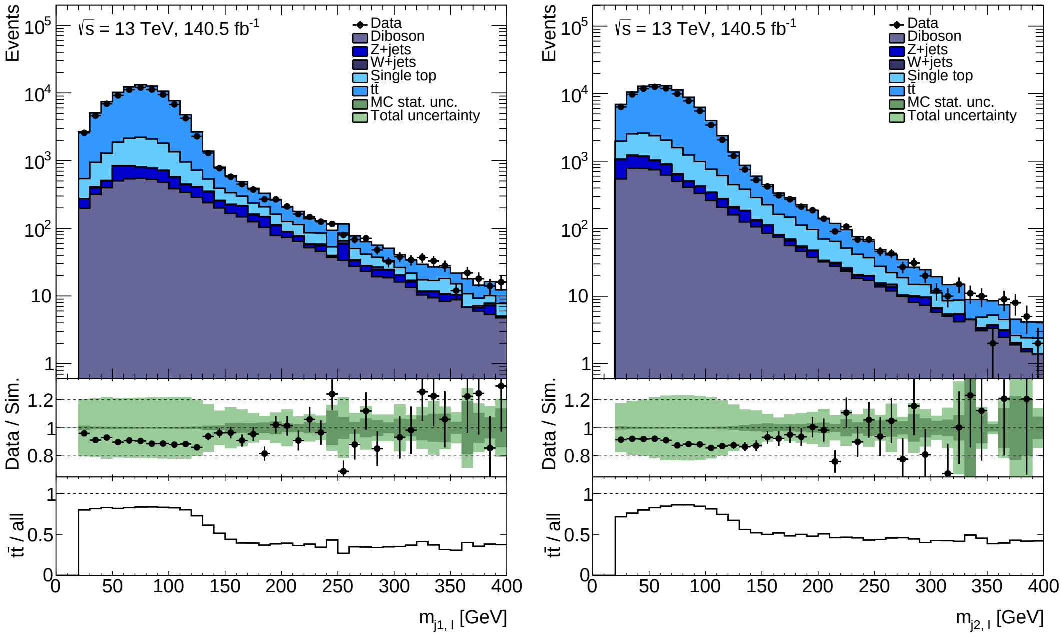

(a) (b)

FIGURE 6.2: Distribution of the lepton plus jet invariant mass for the leading jet (on the left) and subleading jet (on the right). The green band shows the effect of the detector-related and $t\bar{t}$ modelling systematic uncertainties.

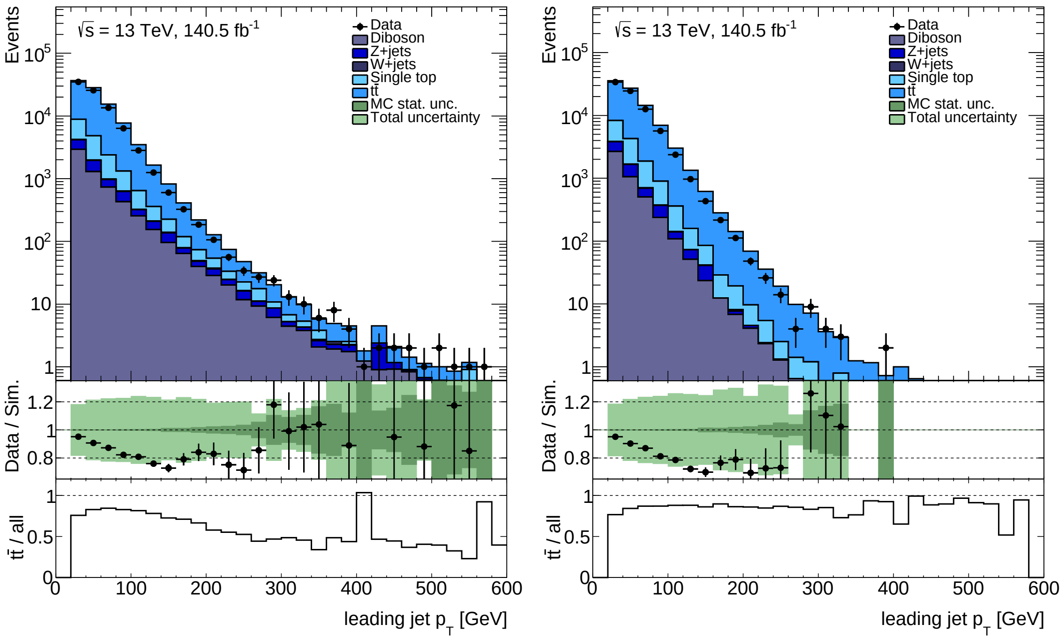

(a) (b)

FIGURE 6.3: Leading jet p_{T} distribution before (on the left) and after (on the right) the lepton plus jet mass cut. The green band shows the effect of the detector-related and $t\bar{t}$ modelling systematic uncertainties.

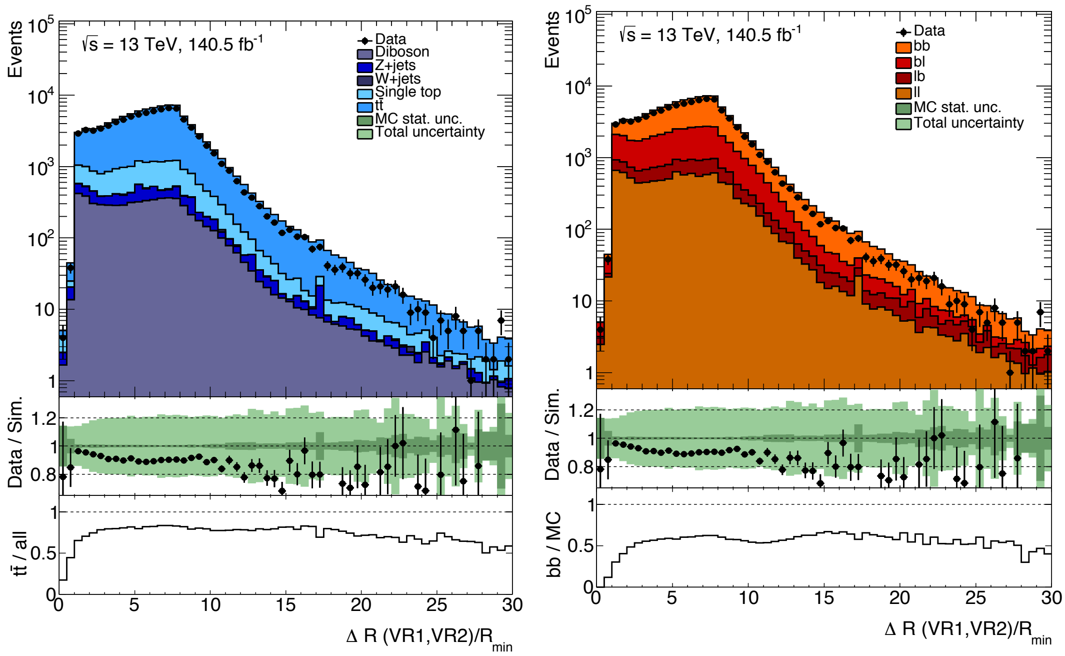

(a) (b)

FIGURE 6.4: Distribution in data and MC of the angular separation between the two VR track jets divided by the radius of the smaller jet, split by process (on the left) and by flavour (on the right). In these plots, the m_{lj} cut is not applied. The green error band shows the effect of detector-related and $t\bar{t}$ modelling systematic uncertainties.

Lastly, in order to identify the flavour content of each jet, tracks and truth hadrons are associated to VR track jets following the standard procedures described in Section 4.3. Events with both VR track jets labelled as b-jets (non b-jets) are indicated as bb (ll). Events with the leading (subleading) VR track jet labelled as b-jet and the subleading (leading) one labelled as non b-jet are identified as bl (lb).

6.1.2 Simulated samples

The nominal $t\bar{t}$ sample is simulated using the POWHEGBOX v2 [137] generator interfaced with PYTHIA 8.230 [138] with the A14 set of tuned parameters [139] and NNPDF2.3LO [135] PDFs in order to simulate the parton shower and hadronisation processes. For the baseline $t\bar{t}$ simulation, the h_{damp} parameter, which gives the cut-off scale of the first gluon emission, is set to 1.5 m_{top}, which is fixed at 172.5 GeV. More details about the tuning of the PYTHIA 8 parameters can be found in Ref. [139].

Alternative $t\bar{t}$ samples are also studied in order to take into account the modelling differences across different MC generators. The differences in the fragmentation and hadronisation processes can be studied by comparing the baseline $t\bar{t}$ sample with the one generated by POWHEGBOX v2 interfaced with HERWIG 7.0.4 [160]. On the other hand, the effects of ISR and FSR can be exploited through an internal reweighting procedure of the nominal sample, which allows to set higher or lower levels of the parton shower radiation. In addition to these internal weights, another alternative POWHEGBOX v2+PYTHIA 8.230 sample with h_{damp} = 3 m_{top} and variation parameter VAR3 [161] is also simulated. Additionally, the variations caused by the matrix element calculation, merging and matching scheme can be evaluated comparing the baseline $t\bar{t}$ sample with the aMC@NLO+PYTHIA 8.230 sample.

The baseline single top Wt channel background samples are generated with POWHEGBOX v2 interfaced with PYTHIA 8.230 and, similarly to the $t\bar{t}$ case, alternative POWHEGBOX v2 + HERWIG 7.0.4 and aMC@NLO+PYTHIA 8.230 samples are also produced, in order to evaluate the variations due to the hadronisation and matrix element calculation. Following the same internal reweighting procedure, also for the single top processes it is possible to exploit the differences due to the parton shower radiation.

Z/W+jets processes are generated by using SHERPA v2.2.1 [133, 134], whereas SHERPA v2.2.2 is used to simulate diboson production (ZZ,WZ and WW).

The uncertainty on the modelling of diboson and Z+jets production processes is estimated by varying the total cross-section by ±5% and ±6%, respectively, as well as varying the factorisation and renormalisation scales through internal reweighting.

6.1.3 Determination of the b-jet efficiency

The b-tagging efficiency in data is extracted by performing a combinatorial likelihood fit in the $e\mu$ channel, after applying all the selection criteria described in Section 6.1.1. A previous application of this method using $t\bar{t}$ events, applied to the case of small-R (R = 0.4) calorimeter jets, is documented in Ref. [162].

In the case of events with exactly two jets, the fraction of events with one b-tagged jet, $f_{1-\text{tag}}$, or two b-tagged jets, $f_{2-\text{tag}}$, can be expressed in the following way:

$$\begin{aligned} f_{1-\text{tag}} &= 2f_{bb}\varepsilon_b(1-\varepsilon_b) + f_{bj}[\varepsilon_j(1-\varepsilon_b) + (1-\varepsilon_j)\varepsilon_b] + (1-f_{bb}-f_{bj})2\varepsilon_j(1-\varepsilon_j) \\ f_{2-\text{tag}} &= f_{bb}\varepsilon_b^2 + f_{bj}\varepsilon_j\varepsilon_b + (1-f_{bb}-f_{bj})\varepsilon_j^2 \end{aligned} \tag{6.1}$$

where f_{bj} and f_{bb} represent the fraction of events with one b-jet and two b-jets, respectively, and ε_b and ε_j are the b- and light-flavour tagging efficiency, respectively. By using these equations, it is possible to determine ε_b by measuring $f_{1-\text{tag}}$ and $f_{2-\text{tag}}$ from data, while f_{bj}, f_{bb} and ε_j are extracted from simulation. This allows the correlation of the jet flavour in the 1-tag and 2-tag region to be properly taken into account, leading to a more precise efficiency measurement. Such measurement is performed in N bins of the jet p_T and this results in $2 \times N^2$ coupled equation. Although it is possible to solve such a system of non-linear equations, it is much simpler to model the same system by using a more flexible and powerful likelihood function and solve the problem numerically by maximising the likelihood.

In general, an extended binned log-likelihood function can be written in the following form:

$$\log \mathcal{L}(\nu_\text{tot}, \hat{\Theta}) = -\nu_\text{tot} + \sum_{i}^{N} n_i \log \nu_i(\nu_\text{tot}, \hat{\Theta}) \tag{6.2}$$

where ν_tot is total number of expected events, $\hat{\Theta} = (\Theta_1,...,\Theta_m)$ represents the set of parameters to be estimated and ν_i (n_i) is the number of expected (observed) events in a given bin i among the total N bins.

In this case, as the fit is performed simultaneously in several bins in the $p_{\text{T},1}$-$p_{\text{T},2}$ plane, it is convenient to indicate with label k the specific $p_{\text{T},1}$-$p_{\text{T},2}$ bin such that $(\log \mathcal{L})_{p_{\text{T},1},p_{\text{T},2}} \equiv (\log \mathcal{L})_k$. The single $(\log \mathcal{L})_k$ term can then be written as:

$$\log \mathcal{L}_k(\nu^k_\text{tot}, \hat{\Theta}) = -\nu^k_\text{tot} + \sum_{w_1,w_2} n^k_{w_1,w_2} \log \nu^k_{w_1,w_2}(\nu^k_\text{tot}, \hat{\Theta}) \tag{6.3}$$

where w_1 and w_2 are the b-tagging discriminant values of the leading and subleading jet in the event and the sum runs over all the b-tagging categories defined by the specific WPs.

The POI for this study is the conditional probability for a b-jet with transverse momentum p_T to have a b-tagging discriminant w falling in a certain bin W, called $\mathcal{P}_{w\in W|f=b,p_\text{T}}$. The total number of POIs is therefore given by the total number of $p_{\text{T},1}$-$p_{\text{T},2}$ bins times the number of b-tagging discriminant bins minus one (as a result of the conservation of probability). The b-tagging efficiency corresponding to a specific cut on the b-tagging discriminant associated to a specific WP is thus given by:

$$\varepsilon_b(p_\text{T}, \text{WP}) = \sum_{w\in WP} \mathcal{P}_{w\in W|f=b,p_\text{T}}. \tag{6.4}$$

The log-likelihood fit function for a given bin k can at this point be rewritten as:

$$\log \mathcal{L}_k(\nu^k_\text{tot}, \mathcal{P}_{w\in W|f=b,p_\text{T}}) = -\nu^k_\text{tot} + \sum_{w_1,w_2} n^k_{w_1,w_2} \log \nu^k_{w_1,w_2}(\nu^k_\text{tot}, \mathcal{P}_{w\in W|f=b,p_\text{T}}) \tag{6.5}$$

in which the rightmost term can be also expressed as:

$$\nu^k_{w_1,w_2}(\nu^k_\text{tot}, \mathcal{P}_{w\in W|f=b,p_\text{T}}) = \nu^k_\text{tot} \cdot \mathcal{P}_{w_1 w_2|k} \tag{6.6}$$

where $\mathcal{P}_{w_1 w_2|k}$ is the conditional probability to get an event with b-tagging weights w_1 and w_2 if $(p_{\text{T},1},\ p_{\text{T},2}) \in k$. We can then split the above equation in terms of the two jet flavours f_1 and f_2 which can be either b or l and, assuming that the b-tagging discriminants of the two jets are independent on each other, obtain the following expression:

$$\nu^k_{w_1,w_2}(\nu^k_{\text{tot}}, \mathcal{P}_{w\in W|f=b,p_{\text{T}}}) = \nu^k_{\text{tot}} \cdot \sum_{f_1,f_2} \mathcal{P}_{f_1,f_2|k} \cdot \mathcal{P}_{w_1\in W_1|f_1,p_{\text{T},1}} \cdot \mathcal{P}_{w_2\in W_2|f_2,p_{\text{T},2}} \tag{6.7}$$

where $\mathcal{P}_{f_1,f_2|k}$ corresponds to the probability for an event to have the two jets labelled with flavours f_1 and f_2 in a given ($p_{\text{T},1}$, $p_{\text{T},2}$) bin and is estimated from simulation. The POIs are represented by the terms $\mathcal{P}_{w\in W|f=b,p_{\text{T}}}$ for events with a b-jet. On the other hand, the conditional probabilities associated to light jets, $\mathcal{P}_{w\in W|f=l,p_{\text{T}}}$, are estimated from simulation after applying specific flavour tagging corrections which take into account the measurement of the light-flavour mistag rate performed by other analysis groups. Lastly, the NPs of the fit are represented by the ν^k_{tot} terms hence to each log-likelihood function $(\log \mathcal{L})_k$ corresponds a specific NP ν^k_{tot} as well as the shared POIs $\mathcal{P}_{w\in W|f=b,p_{\text{T}}}$.

This procedure is performed on all the events passing the selection requirements described in Section 6.1.1, hence considering only the events passing the m_{lj} cut.

6.1.4 Comparison between data and simulation

In Table 6.2, the number of selected events in data and simulation are presented, together with the predicted flavour composition in MC.

Sample	data	Diboson	Z+jets	W+jets	singletop	$t\bar{t}$
Input	36424664	190779.7	30599076.0	2781.8	110703.1	1339386.1
2 leptons	36422632	189659.7	30598916.0	2781.8	110694.7	1339284.5
$e\mu$ channel	810723	48406.0	24524.5	1444.9	55873.5	662164.1
opposite sign	725650	40288.2	21186.3	970.8	51188.9	602631.8
2 jets	109197	13083.1	7052.4	293.9	13009.2	85336.9
$\Delta R(\text{VR}_1, \text{VR}_2) > R_{\text{min}}$	109149	13065.7	7045.3	293.9	12997.9	85312.6
leading jet $p_{\text{T}} > 20$ GeV	85838	6108.2	2522.7	127.3	10242.0	76023.6
jet$_1$ m_{lj} cut	82492	4959.5	2181.9	89.2	9599.0	74668.0
jet$_2$ m_{lj} cut	80843	4678.9	2141.9	81.3	9109.4	73722.0
cc	-	54.8	17.2	0.51	2.20	5.6
lb	-	33.7	28.3	1.32	845.4	3105.4
lc	-	178.8	70.5	2.97	17.4	37.1
bb	-	6.0	14.5	0.53	2184.6	51663.1
bc	-	1.5	0.9	0.14	168.1	720.2
bl	-	25.2	64.1	0.84	5521.9	17141.0
cb	-	3.2	0.6	0.08	41.4	208.7
ll	-	4073.0	1785.2	72.0	307.5	785.0
cl	-	302.8	160.7	2.9	20.9	56.3

TABLE 6.2: Number of selected events in data and simulation and predicted flavour composition in MC, in the $e\mu$ 2 jets channel after all cuts. Data are not split by jet flavour.

Before performing the actual measurement, it is important to check the agreement between data and simulation for some relevant quantities.

Figure 6.5 shows the distributions of the `MV2c10` and `DL1` b-tagging outputs. The same distributions are also shown for the subleading VR track jet in Figure 6.6. Some kinematic distributions are then shown in Figures 6.7-6.8, both for the leading and subleading VR track jet.

As shown in Figures 6.7a-6.8a, a clear mismodelling of the VR track jet p_{T} is present. Moreover, a discrepancy happens to be present also in the distribution of the number of constituent tracks, as shown in Figures 6.7c-6.8c. More detailed studies related to such disagreement are presented below.

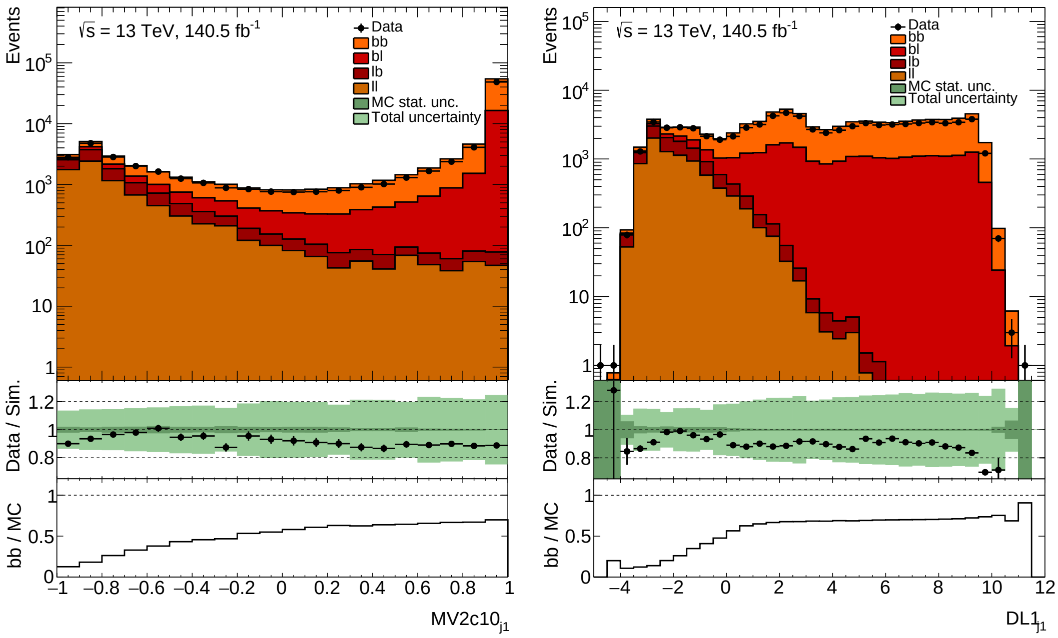

(a) (b)

FIGURE 6.5: Data/MC comparisons for the `MV2c10` and `DL1` tagger of the leading VR track jet, split by event flavour. The green band shows the effect of the detector-related and $t\bar{t}$ modelling systematic uncertainties.

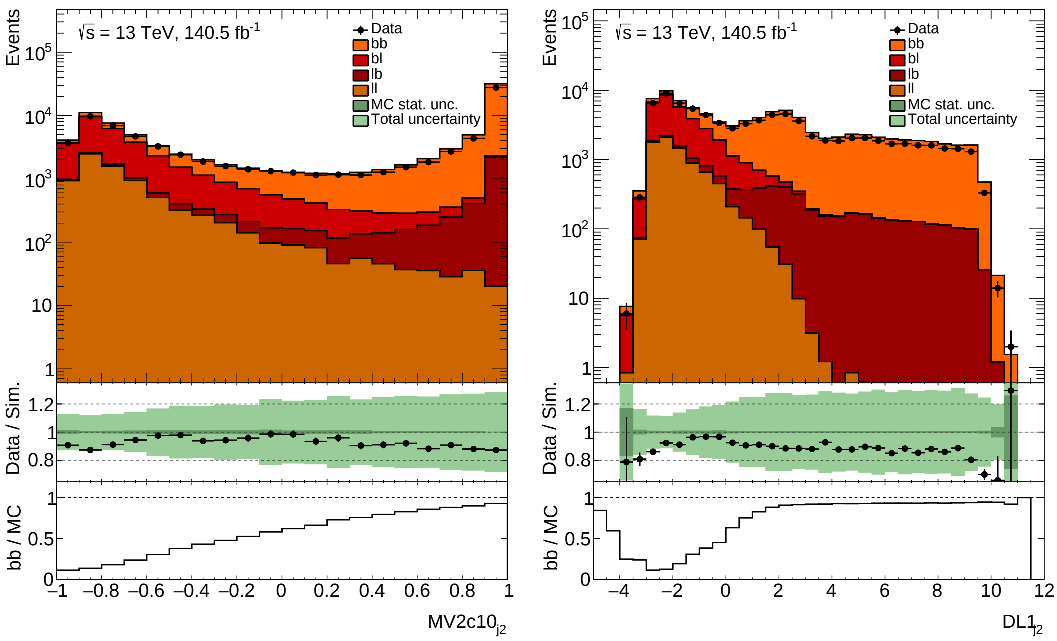

(a) (b)

FIGURE 6.6: Data/MC comparisons for the `MV2c10` and `DL1` tagger of the subleading VR track jet, split by event flavour. The green band shows the effect of the detector-related and $t\bar{t}$ modelling systematic uncertainties.

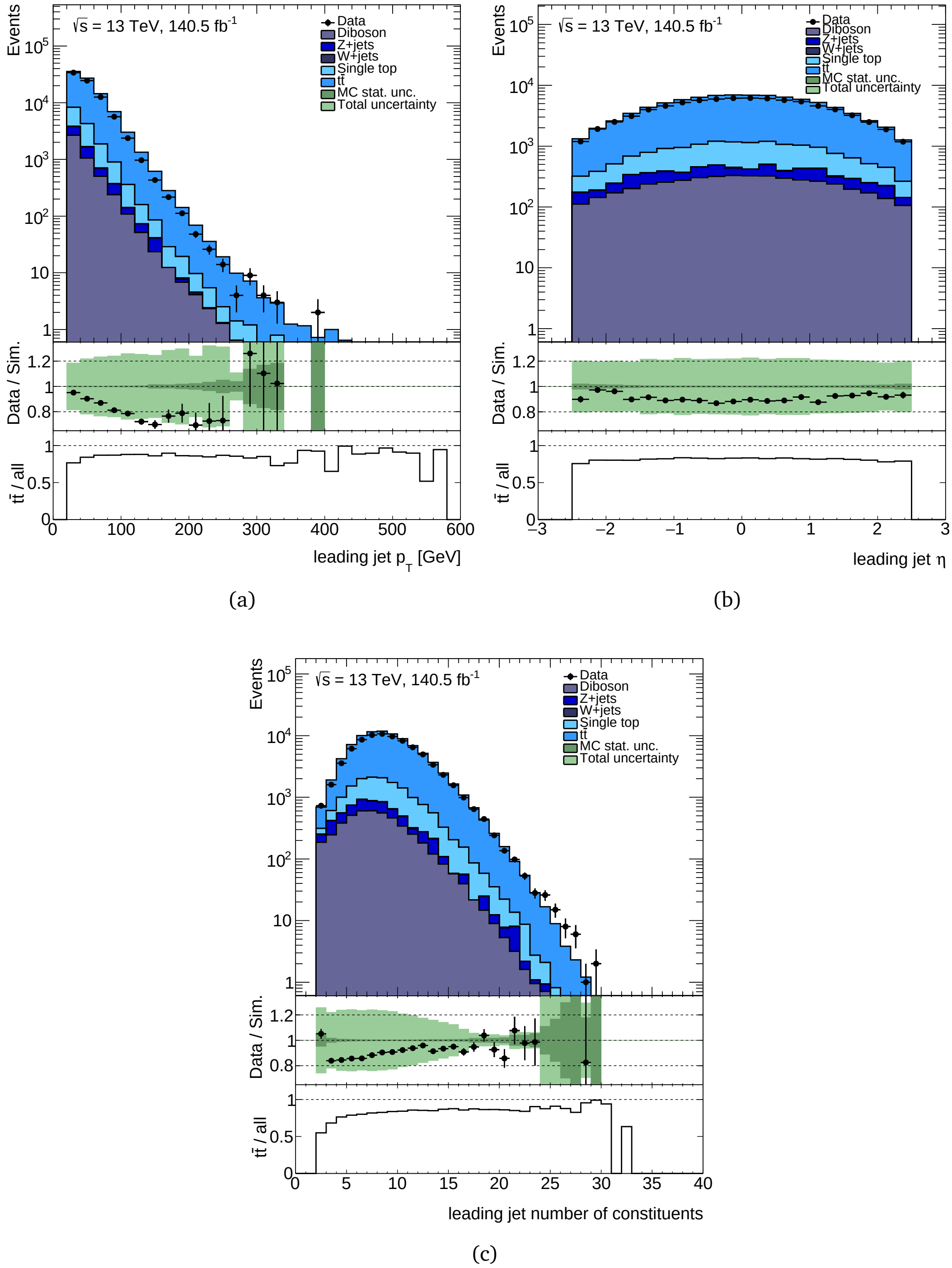

FIGURE 6.7: Data/MC comparisons for the p_{T}, η and number of constituents distributions of the leading VR track jet. The green band shows the effect of the detector-related and $t\bar{t}$ modelling systematic uncertainties.

6.1.5 p_{T} mismodelling studies

In order to understand the origin of the discrepancy between data and simulation observed in the distribution of the VR track jets' p_{T}, several studies have been performed and they are presented in this section. In the following, only the leading jet

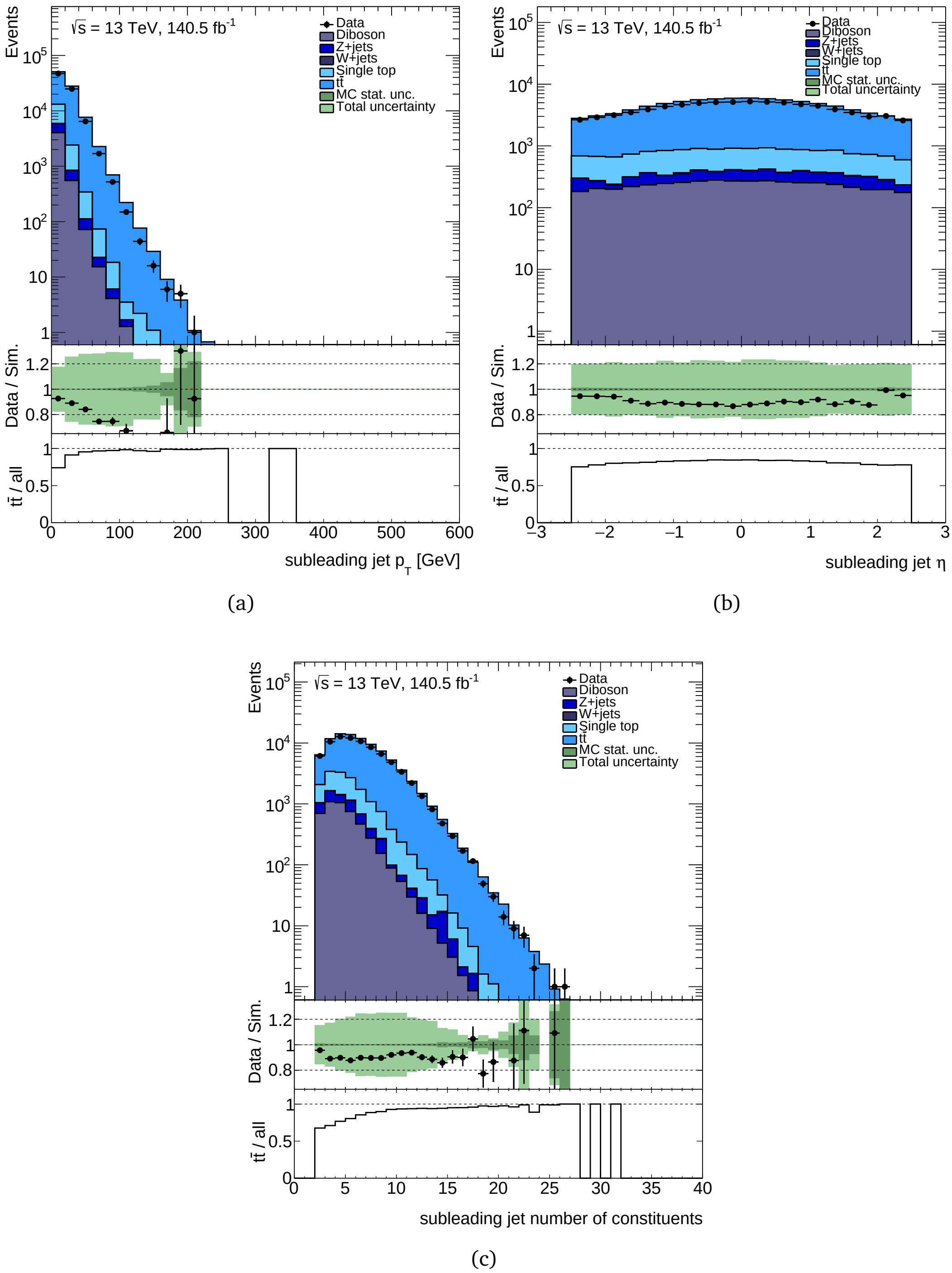

FIGURE 6.8: Data/MC comparisons for the p_{T}, η and number of constituents distributions of the subleading VR track jet. The green band shows the effect of the detector-related and $t\bar{t}$ modelling systematic uncertainties.

p_{T} distributions are shown while the corresponding distributions for the subleading jet are shown in Appendix B.

η dependence The first topic that has been studied is the dependence of the jet p_T distribution with respect to the jet η. For this purpose, Figure 6.9 shows the distribution of the leading VR track jet p_T in two different η bins. Although the slope is more visible when $|\eta| \leqslant 1.4$, a similar disagreement between data and simulation is observed also for $|\eta| > 1.4$.

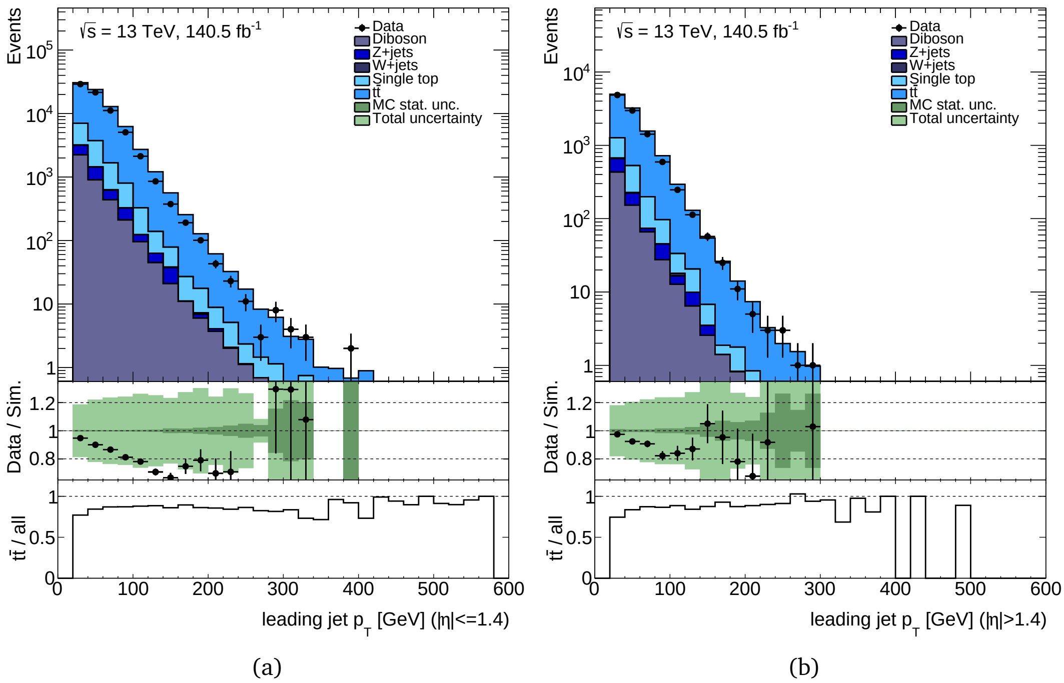

FIGURE 6.9: Data/MC comparison of the leading VR track jet p_T distribution in the two different regions with $|\eta| \leqslant 1.4$ (on the left) and $|\eta| > 1.4$ (on the right). The green band shows the effect of the detector-related and $t\bar{t}$ modelling systematic uncertainties.

μ dependence Another aspect which has been investigated is the presence of fake tracks. As studied by the ATLAS tracking performance group, the fake rate strongly depends on the average number of interactions per crossing $\langle\mu\rangle$ and it is expected to be negligible at low $\langle\mu\rangle$ values. For this reason, the p_T spectra have been derived in three different regions: $\langle\mu\rangle \leqslant 25$, $25 < \langle\mu\rangle \leqslant 35$ and $\langle\mu\rangle > 35$. Figure 6.10 shows these distributions in the three different $\langle\mu\rangle$ regimes, demonstrating that a clear discrepancy between data and MC is present also at low $\langle\mu\rangle$ values. From these studies, it has been concluded that the origin of the jet p_T mismodelling is likely not related to the presence of fake tracks.

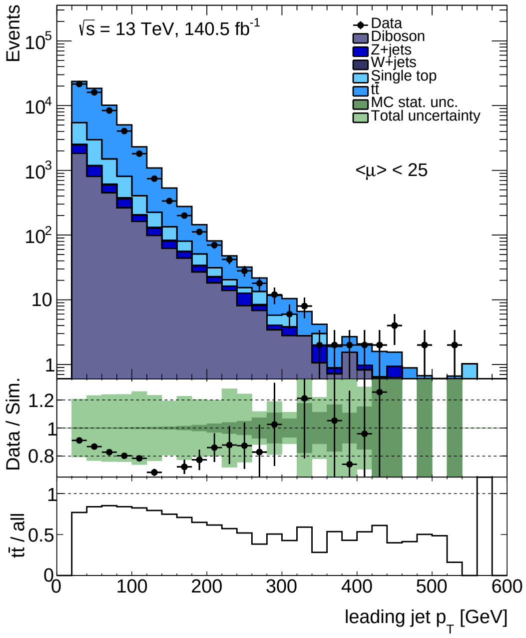

(a)

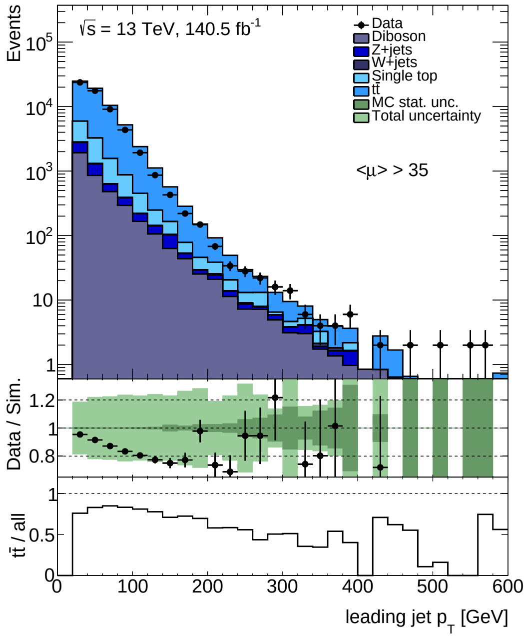

(b)

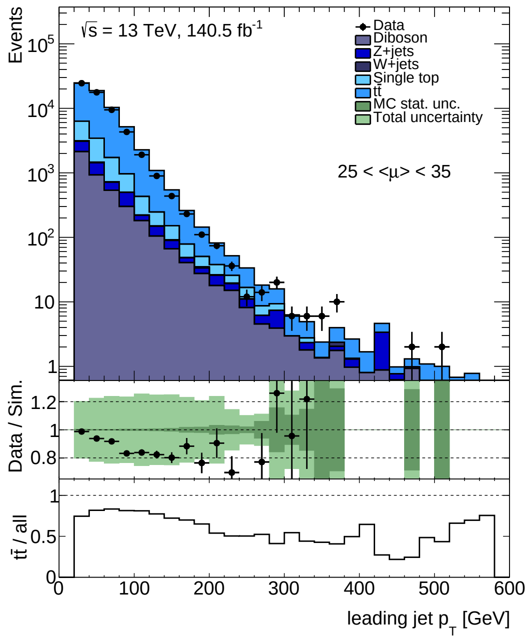

(c)

FIGURE 6.10: Data/MC comparison of the leading VR track jet p_{T} distribution in the low, medium, high $\langle\mu\rangle$ regimes. The green band shows the effect of the detector-related and $t\bar{t}$ modelling systematic uncertainties.

VR track jet constituents An interesting sanity check consists in studying the agreement between data and MC for the main kinematic variables of the tracks contained inside the VR track jets. Figure 6.11 shows the comparison between data and simulation of the main kinematic variables related to such tracks, for both the leading VR track jet. As expected, the p_{T} (and energy) distribution shows the same slope observed in Figures 6.7-6.8.

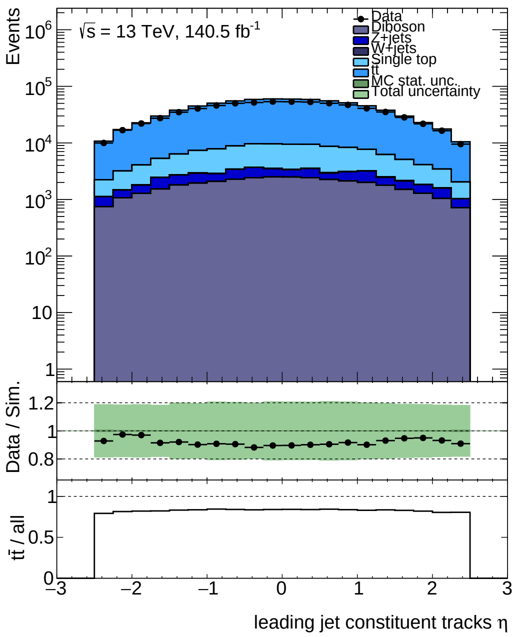

(a)

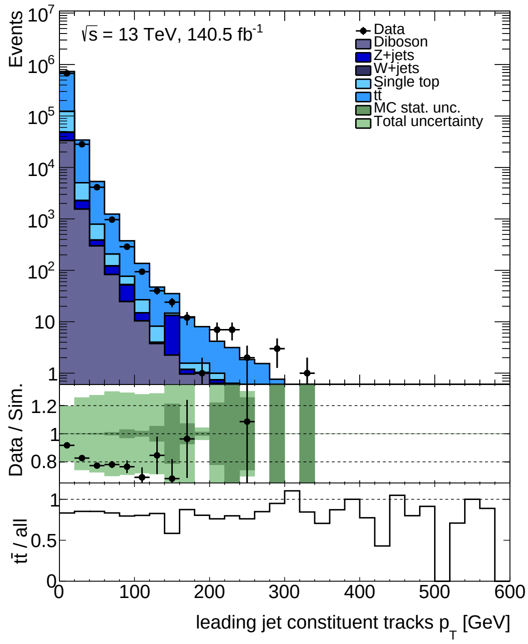

(b)

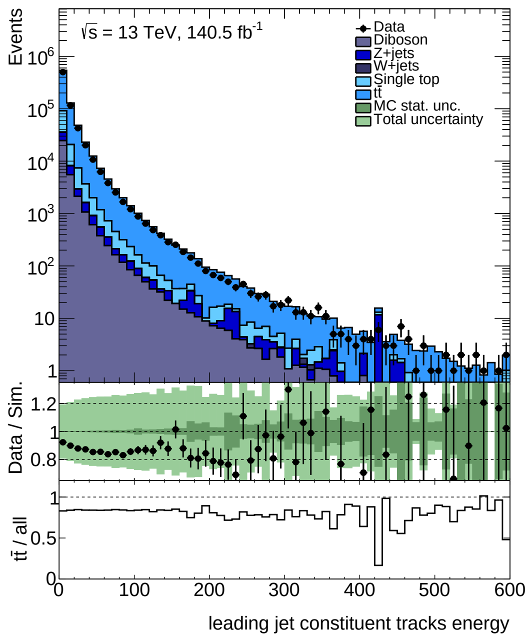

(c)

FIGURE 6.11: Data/MC comparisons of η, ϕ, p_{T} and energy of the tracks contained the leading VR track jet. The green band shows the effect of the detector-related and $t\bar{t}$ modelling systematic uncertainties.

Based on the studies presented so far, there is no clear indication that the observed discrepancy between data and simulation originates from the specific criteria applied in the event selection. It seems instead more likely that a bad modelling of the number and jet energy scale of the constituent tracks inside the VR track jet could be the actual culprit. Moreover, additional studies performed by other analysis groups have shown that a similar disagreement is present also in the case of charm-flavour VR track jets. On the other hand, light-flavour VR track jets do not seem to show the same behaviour. This could be a clear indication that our current understanding of the fragmentation process of heavy flavour VR track jets is not very well understood and requires a closer examination in the future.

6.1.6 Systematic uncertainties

Systematic uncertainties are evaluated one-by-one by replacing the MC nominal sample with a sample affected by a single systematic uncertainty variation, and then repeating the whole procedure.

The systematic uncertainties which are provided as up and down variations are symmetrised. In the case they have opposite impact on the measurement, a symmetric uncertainty corresponding to their difference is calculated. In case instead both up and down variations impact the measurement in the same direction or one of them is compatible with zero, a symmetric uncertainty corresponding to the largest variation is considered. One-sided variations are symmetrised by taking the full difference between the variation and the nominal prediction.

As already anticipated in Section 6.1.2, the impact of the physics modelling of $t\bar{t}$ and non-$t\bar{t}$ processes is estimated by comparing the efficiency measured from the nominal MC simulated samples with respect to alternative MC generators or by using additional internal weights that correspond to the variation of a specific theory parameter. Figure 6.12 shows the impact of the different parameters affecting the modelling of the $t\bar{t}$ processes, which results as the dominant source of systematic uncertainty.

In addition, also experimental uncertainties are taken into account and they correspond to:

- pile-up modelling,
- JES uncertainties as provided by the Jet+$E_{\mathrm{T}}^{\mathrm{miss}}$ ATLAS performance group (including NPs related to sample flavour composition, the sample flavour response and punch-through jets),
- JER uncertainties as studied using the one sided single NP model provided by the Jet+$E_{\mathrm{T}}^{\mathrm{miss}}$ ATLAS performance group,
- muon and electron trigger efficiencies,
- muon track-to-vertex association statistical and systematic uncertainties,
- muon efficiency resolution (separate contributions from MS and ID), scale and isolation uncertainties,
- electron efficiency, resolution and scale uncertainties,
- light mistagging efficiency uncertainty.

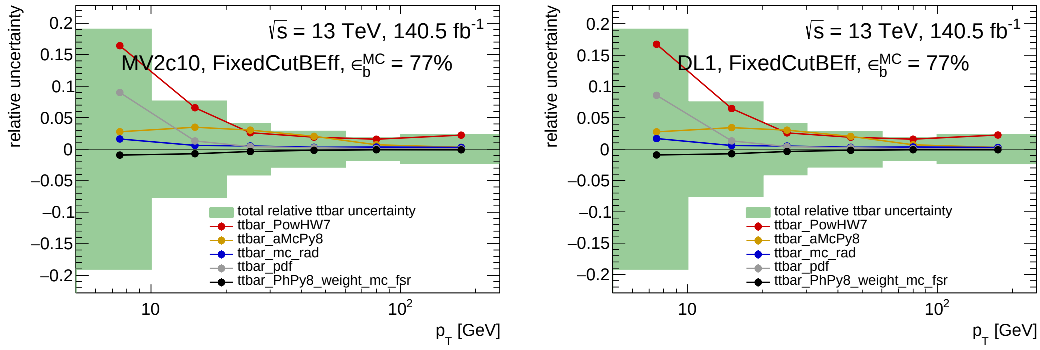

(a) (b)

FIGURE 6.12: Impact of the $t\bar{t}$ modelling systematic uncertainties on the final fit performed on the MV2 and DL1 taggers.

It is worth pointing out that the JES and JER uncertainties have no impact on the final measurement, as expected given that VR track jets are reconstructed from the ATLAS ID tracks only and no information from the ATLAS calorimeter system is used.

Additional uncertainties directly related to the track jets, such as on the tracking reconstruction efficiency and fake rate, have also been studied but they have been found to have a maximum effect of 0.2% and 0.6%, respectively, on the final SFs so they have not been considered for the evaluation of the total systematic uncertainty.

p_{T} mismodelling uncertainty In order to take into account the variations due to the mismodelling observed in the VR track jet p_{T} spectrum (see Figures 6.7a-6.8a), an additional systematic uncertainty has been derived by reweighting the p_{T} spectrum in simulation in order to match the one observed in data, only for events where both VR track jets are labelled as b-jets. The whole calibration procedure is then repeated using the new reweighted p_{T} spectra as input and the central values of the new SFs are compared with the nominal ones. In order to fully exploit the shape differences also at low p_{T}, where narrower p_{T} bins are used in the final likelihood fit, a linear fit of the data/MC slope on the combined 140.5 fb^{-1} dataset is performed for $p_{\mathrm{T}} < 150$ GeV. The results of this linear fit are then used to evaluate a jet p_{T} weight in this region, while for $p_{\mathrm{T}} > 150$ GeV (where much wider bins are used) such weights just correspond to the data/MC ratio values obtained from the histograms in Figure 6.7a. This jet weight is then applied only to bb events which are expected to correspond closely to the actual $t\bar{t}$ signal. As shown in Figure 6.13, by applying this reweighting procedure the agreement between data and simulation improves significantly, proving that the observed discrepancy is mostly present for heavy flavour jets only (although, it is important to notice that this sample has a very small fraction of c- and light-jets).

Finally, the fit is performed again using such reweighted p_{T} spectra as input and the difference with respect to the nominal SFs is presented in Figure 6.14 for both the MV2c10 and DL1 taggers. The impact on the final SFs is very similar for the b-tagging algorithms under study and is around 7% at low p_{T} and 1.5% at high p_{T}. The contribution from this additional systematic uncertainty is taken into account in the final results.

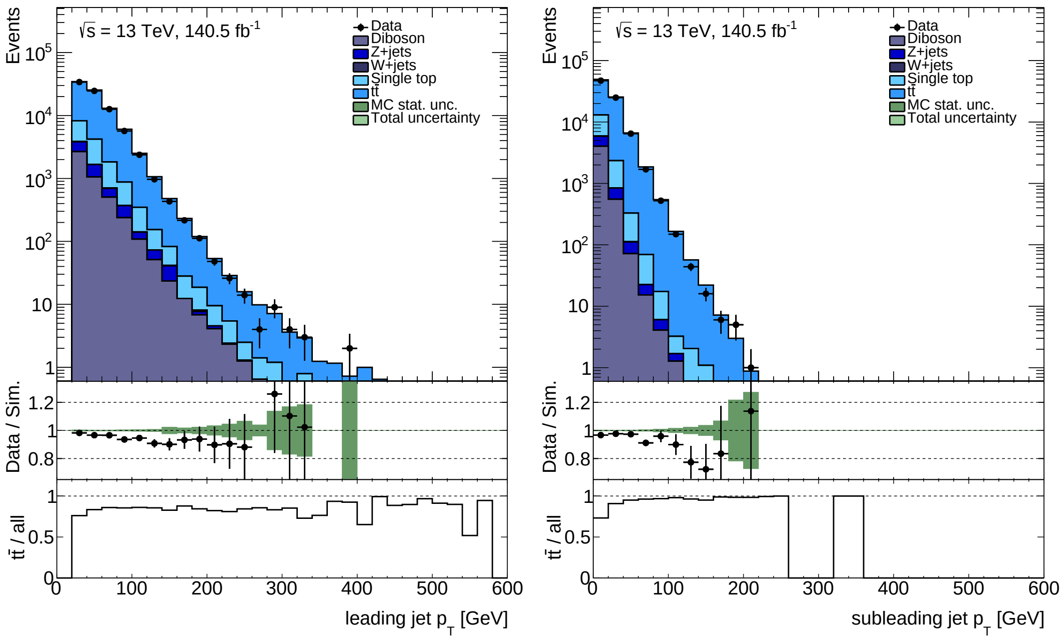

(a) (b)

FIGURE 6.13: Data/MC comparison for the leading and subleading VR track jet p_{T} distributions for the full dataset, after reweighting, after applying the m_{lj} cut. The green band corresponds to the statistical uncertainty only.

6.1.7 Closure test

A closure test is performed by performing the full log-likelihood fit to the simulated events, in order to determine the presence of any possible bias in the results. The total nominal simulated events, which are scaled to the data luminosity, are treated both as pseudo-data and as MC inputs for the likelihood fit, with the expected number of events in each bin taken as the mean of a Poisson distribution to estimate the statistical uncertainty. Figure 6.15 shows the results of the MC closure test for the b-tagging algorithms under study. No significant bias is observed. In fact, the small deviations observed are consistent with the Poisson uncertainty due to limited data statistics and are taken into account in the final fit as an additional source of uncertainty.

6.1.8 Results

After having performed all the necessary tests and having excluded any substantial bias in the procedure, it is finally possible to extract the b-jet tagging efficiency in data. Figures 6.16-6.17 show the results of this measurement as a function of the jet p_{T} for the 77% WP of the algorithms under study.

A global Pearson's χ^2 [163] is computed in order to evaluate the goodness of the fit and its value divided by the number of degrees of freedom obtained for the nominal measurement varies from 1.04 to 1.30 for the two b-tagging algorithms considered in this study. The fraction of events with a specific jet flavour is shown in Figures 6.18-6.19.

The normalisation of the simulated MC events is one of the NPs of the fit, hence the number of MC is allowed to float and match the one in data, as shown in Figure 6.20.

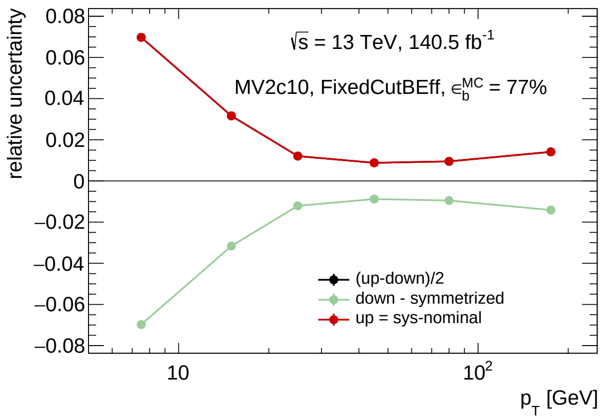

(a)

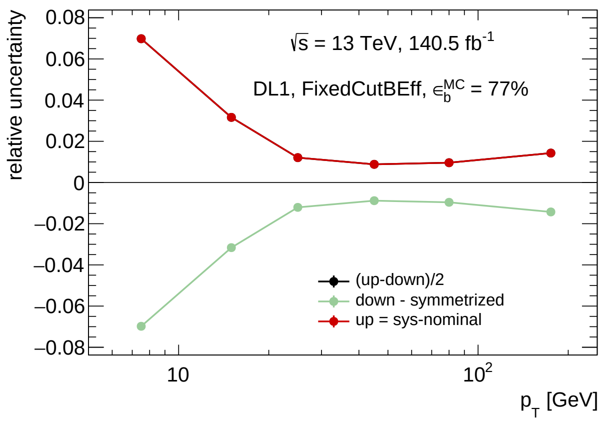

(b)

FIGURE 6.14: Relative differences in the final b-tagging SFs, due to the effect of the p_{T} reweighting for the 77% FixedCut WPs of the `MV2c10` (at the top) and `DL1` tagger (at the bottom).

The lowest p_{T} bin, associated to jets with p_{T} between 5 GeV and 10 GeV, was found to have a significantly smaller b-tagging efficiency in data and a very large impact of the systematic uncertainty, compared to the other calibrated p_{T} bins. In order to understand whether such low p_{T} jets do actually originate from the top quark decay (rather than being associated to additional QCD radiation), several studies investigating the correlation between the b-hadron p_{T} and the b-labelled jet p_{T} as well as the possibility of double labelling (see Section 6.2) have been performed. Based on these studies, such low p_{T} jets seem to behave similarly to the jets with $p_{\mathrm{T}} > 10$ GeV; hence it is plausible that the observed discrepancy between data and simulation is due to a genuine lower bb purity, as shown in Figure 6.18. More studies would then be needed in order to improve the b-jet purity in this region therefore at the moment only the results for jets with p_{T} higher than 10 GeV are recommended to be used within the ATLAS collaboration.

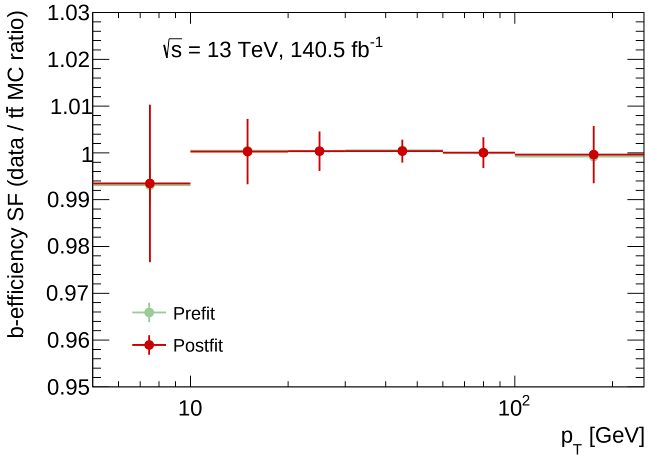

(a)

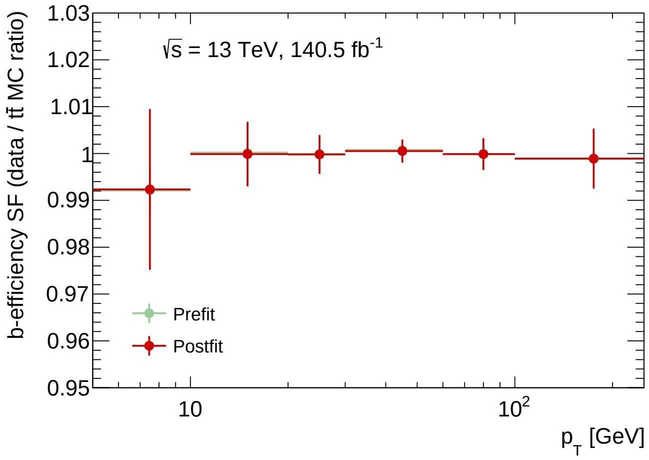

(b)

FIGURE 6.15: Values of the *b*-tagging efficiency SFs, before and after the nominal fit, using MC simulated events as pseudo-data, for the `MV2c10` (at the top) and `DL1` (at the bottom) tagger.

6.1.9 A new approach: the sidebands fit

The results presented above are obtained performing the *standard* likelihood fit described in Section 6.1.3, in which only events passing the m_{lj} cut are used and the flavour composition of the sample is directly estimated from simulation. However, as the physics modelling of the $t\bar{t}$ processes represents the main source of systematic uncertainty, it is reasonable to believe that a more precise measurement can be achieved by introducing $p_{T,1}$-$p_{T,2}$ dependent flavour correction factors in the current likelihood function. This is what the *sidebands fit* does. This new approach has been developed recently [112] and it consists in using the m_{lj} cut to define a SR and three different CRs. The novelty of this technique is in the fact that all the events in the SR and CRs are used to simultaneously measure the *b*-tagging efficiency as well as the flavour composition, which was otherwise estimated only from simulation in the standard method. In Figure 6.21 an illustration of the event categorisation adopted in the new fit method is shown. As in the standard method, the events are binned according to the p_T of both the leading and subleading jet in the event. In each of these bins, events are further assigned to the CRs and to the SR. The events in the

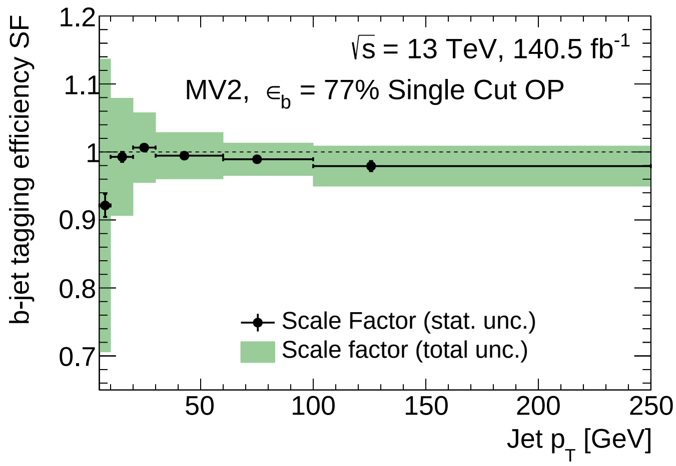

(a)

FIGURE 6.16: Measured b-tagging efficiency corresponding to the 77% of the MV2c10 algorithm. The error band includes both statistical and systematic uncertainty.

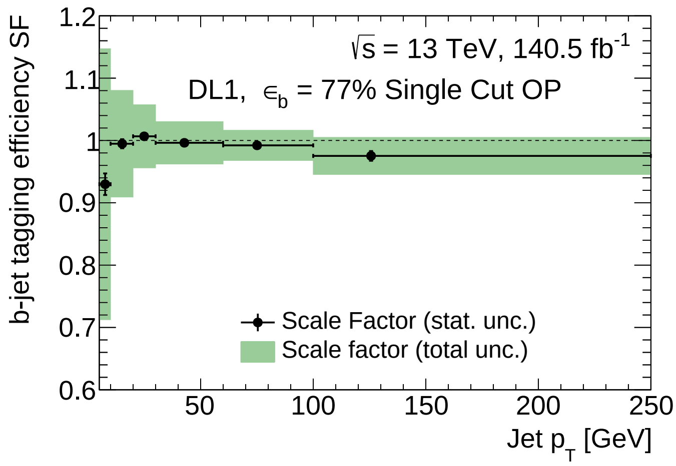

(a)

FIGURE 6.17: Measured b-tagging efficiency corresponding to the 77% of the DL1 algorithm. The error band includes both statistical and systematic uncertainty.

SR are then classified according to the b-tagging discriminant of the two jets. Again, the POI of the final fit is the b-tagging efficiency which is now estimated during the minimisation procedure together with the correction factors applied to the flavour fractions, in each $p_{T,1}$-$p_{T,2}$ bin.

As shown in Figure 6.22, the m_{lj} variable has a very poor discrimination power for jets with p_T lower than 10 GeV, making the sidebands fit not feasible in this region. Therefore in the following only jets with p_T higher than 10 GeV are considered.

A comparison between the two different methods is presented for the case of the 77% b-tagging efficiency WP of the MV2c10 tagger and the DL1 tagger.

As shown in Figure 6.23, the impact of the $t\bar{t}$ modelling uncertainties is significantly reduced with the sidebands fit approach. This allows to improve the precision of the measurement, as shown in Figure 6.24, despite the increased data statistical uncertainty which is expected given the larger number of parameters estimated by

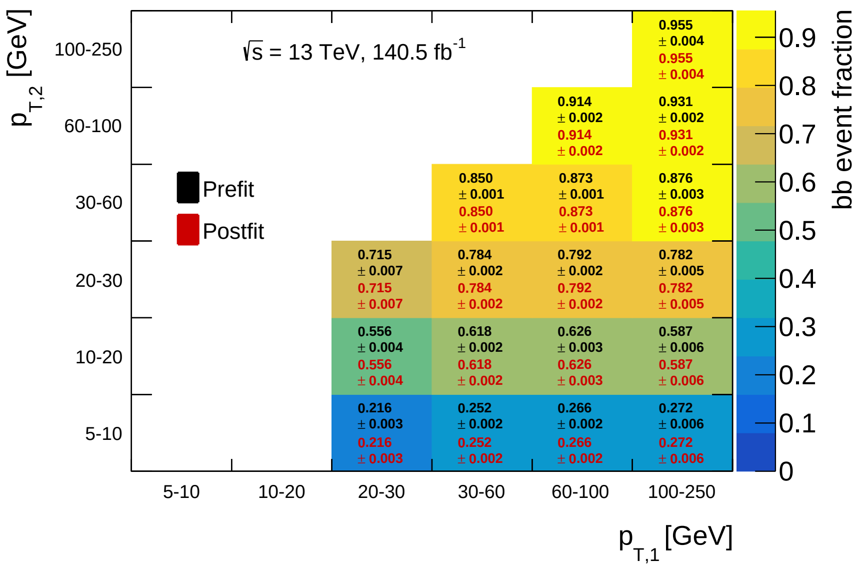

(a)

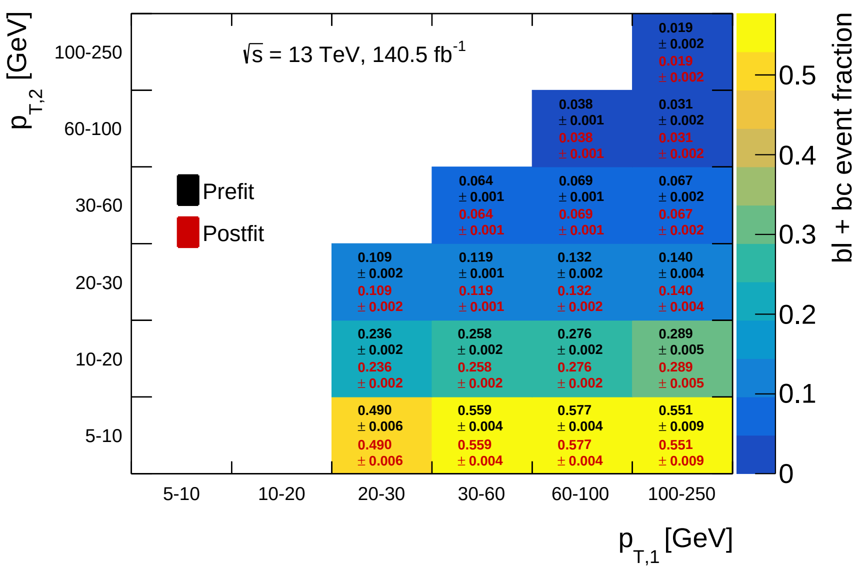

(b)

FIGURE 6.18: Flavour fractions in the $p_{T,1}$-$p_{T,2}$ plane.

the different likelihood fit. Nevertheless, it is relevant to point out that the in the original publication of the sidebands fit method performed on small-R calorimeter jets [112], the uncertainty related to the matrix element calculation of the $t\bar{t}$ process is not taken into account as its impact has found to be excessively high with respect to the standard method. A possible explanation for such behaviour can be due to the different choice of the PYTHIA8 tuned parameters adopted in the alternative aMC@NLO+PYTHIA 8.230 sample which can affect the measurement of FSR sensitive variables. The same strategy is therefore also applied in the case study of VR track jets.

The ratio of $p_{T,1}$-$p_{T,2}$ dependent flavour fractions estimated with the new sidebands fit with respect to the values estimated from simulation are shown in Figures 6.25-6.26, for the case of the MV2c10 algorithm. The largest deviations are

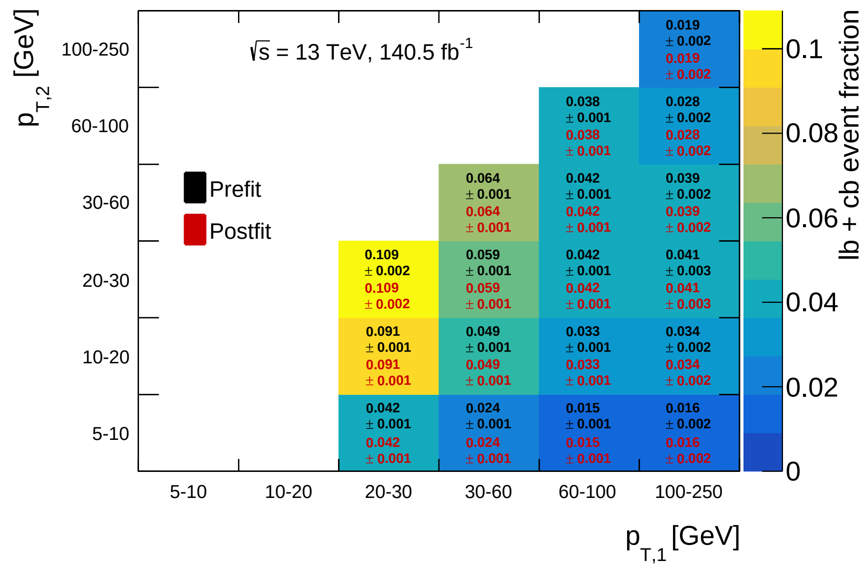

(a)

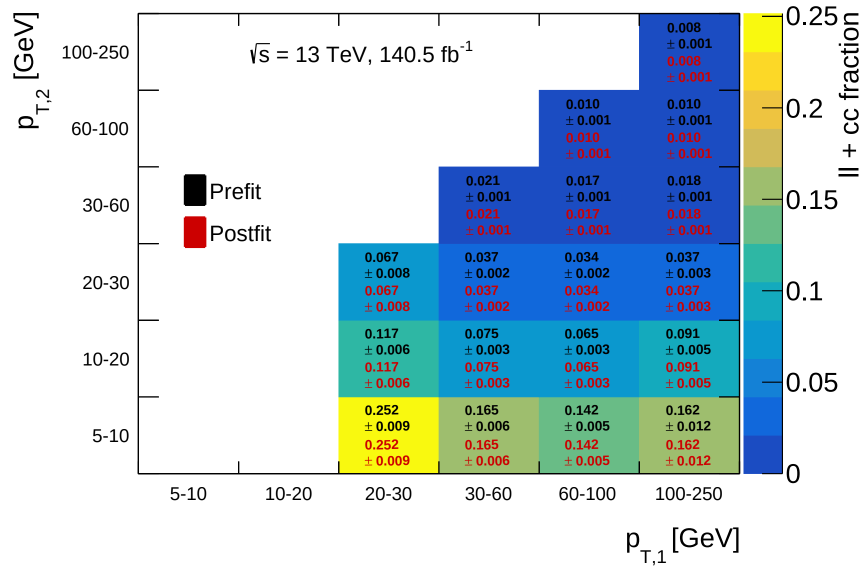

(b)

FIGURE 6.19: Flavour fractions in the $p_{T,1}$-$p_{T,2}$ plane.

present for the *bl*, *lb* and *ll* categories, which are better estimated using the new dedicated CR_{BL}, CR_{LB}, CR_{LL} regions.

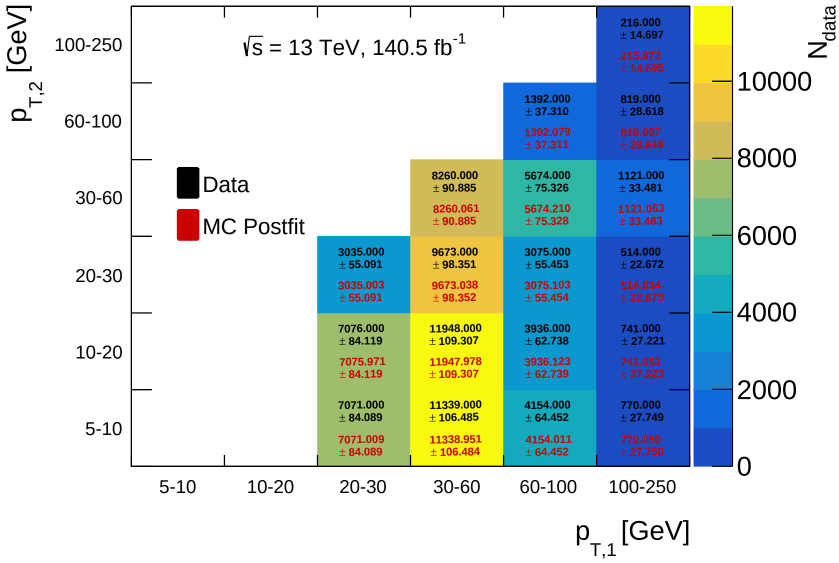

(a)

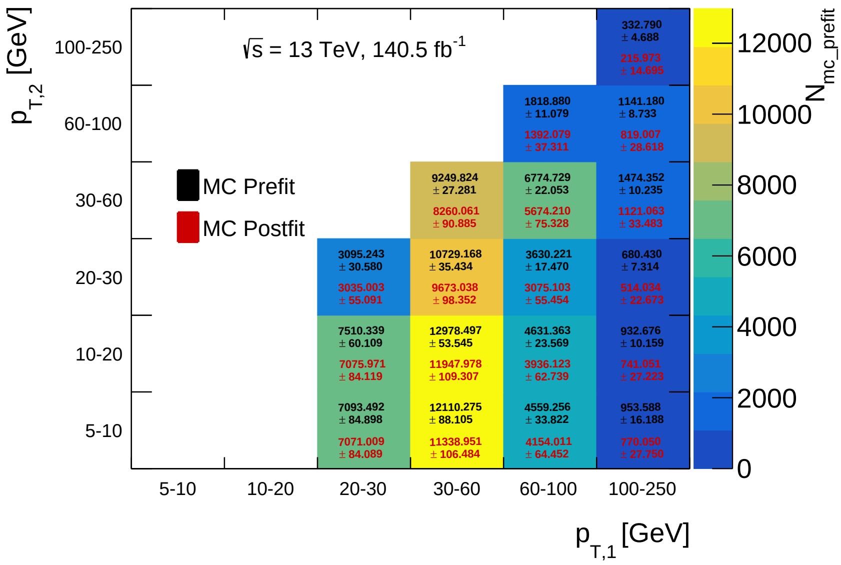

(b)

FIGURE 6.20: Number of events, in simulation and data, in the $p_{T,1}$-$p_{T,2}$ plane, before and after the fit.

6.2 Correlation and truth labelling studies

Additional studies have been performed in order to learn more about the b-jet purity of the $t\bar{t}$ events used for this measurement and they are presented below.

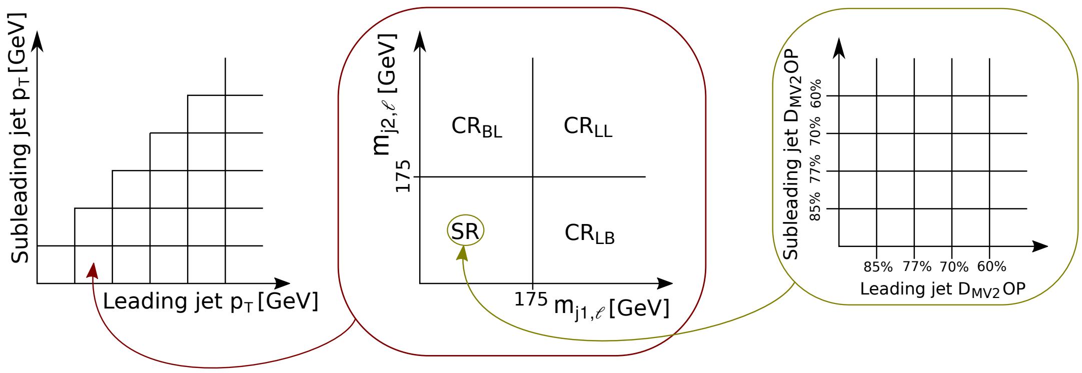

FIGURE 6.21: Schematic illustration of the event categorisation adopted in the new "sidebands fit". Figure taken from Ref. [112].

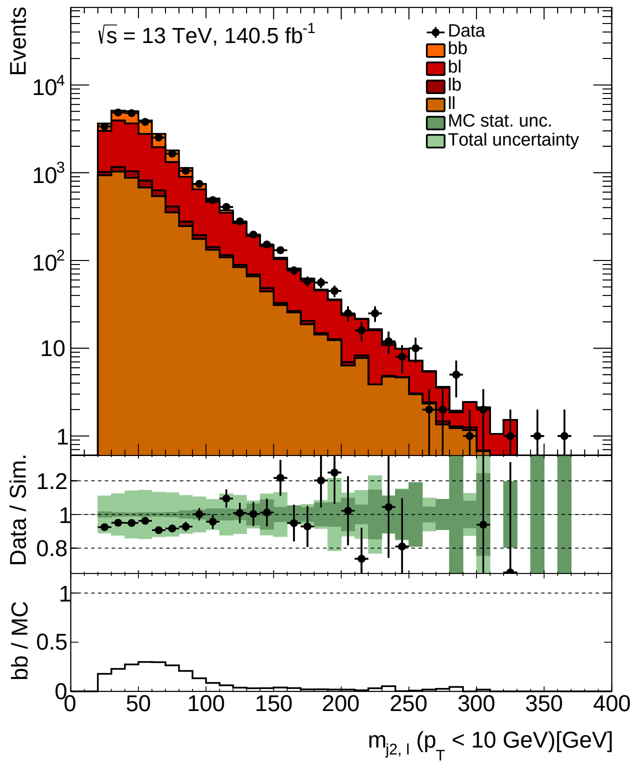

FIGURE 6.22: Distribution of the lepton plus invariant mass for events in which the subleading jet has p_T lower than 10 GeV. The green band shows the impact of statistical and $t\bar{t}$ modelling systematic uncertainties.

Investigating the flavour labelling The *standard* labelling scheme recommended by the flavour tagging working group, as described in Section 4.3, consists in assigning a label to each jet whenever it is matched to at least one truth heavy flavour hadron. Therefore this scheme is not sensitive to the possibility that a jet is matched to a single or more than one truth hadron. However, an additional *extended* flavour labelling scheme has been recently introduced and it allows for double labels in case more than one heavy flavour hadron is matched to the jet. As this calibration is performed using di-leptonic $t\bar{t}$ events, each jet is expected to be matched, in most of the cases, to exactly one truth b-hadron. Therefore, one way to investigate whether the b-jets under study do actually originate from the top quark decay is to compare

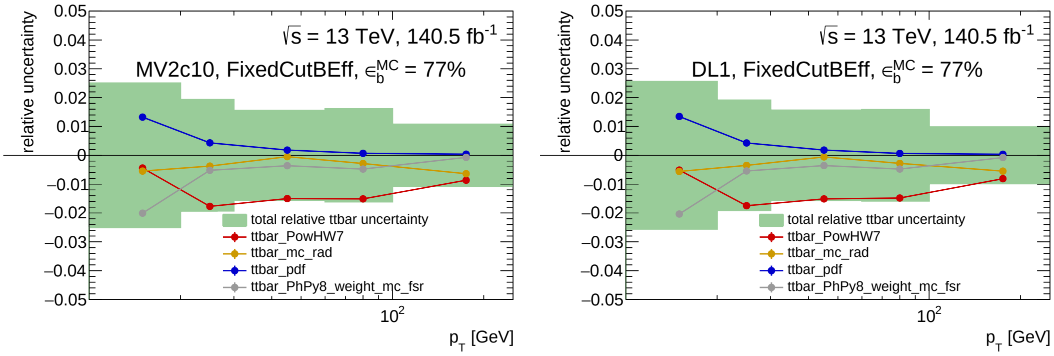

(a) (b)

FIGURE 6.23: Impact of the $t\bar{t}$ modelling uncertainties using the sidebands fit approach, for the case of the MV2c10 tagger (on the left) and DL1 tagger (on the right).

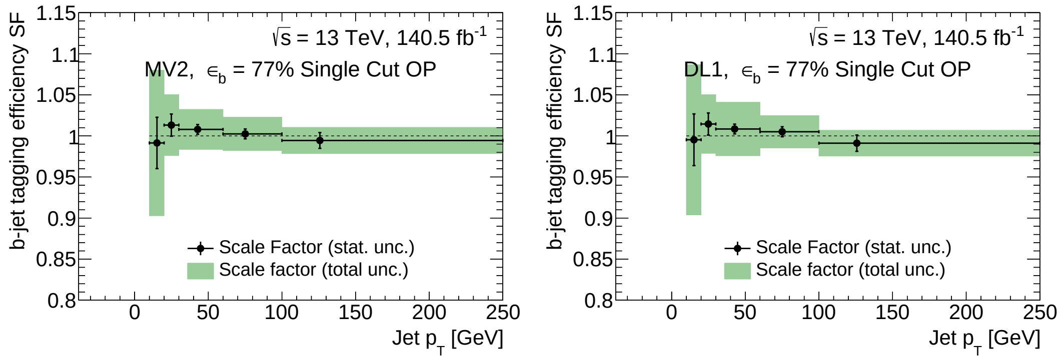

(a) (b)

FIGURE 6.24: Measured b-tagging SFs using the sidebands fit method, for the case of the MV2c10 tagger (on the left) and DL1 tagger (on the right).

the *standard* and *extended* labelling schemes. Figure 6.27 shows the p_T spectrum of all the jets which are labelled as b-jets in $t\bar{t}$ signal events (before including the m_{lj} cut) in the two labelling schemes. When using the *extended* scheme, a jet is labelled as b-jet anytime it is matched to one or two truth b-hadrons or to one b-hadron and one c-hadron. Following this procedure, by construction the blue dashed curve (corresponding to the *standard* labelling) is expected to cover the exact red area (corresponding to the *extended* labelling). The green and yellow dashed lines represent instead the jets that are matched either to two truth b-hadrons or to one truth b-hadron and one c-hadron. The bottom panel shows that the fraction of b-jets subject to double labelling is very small and contributes to less than 3% in the whole p_T range considered for the calibration.

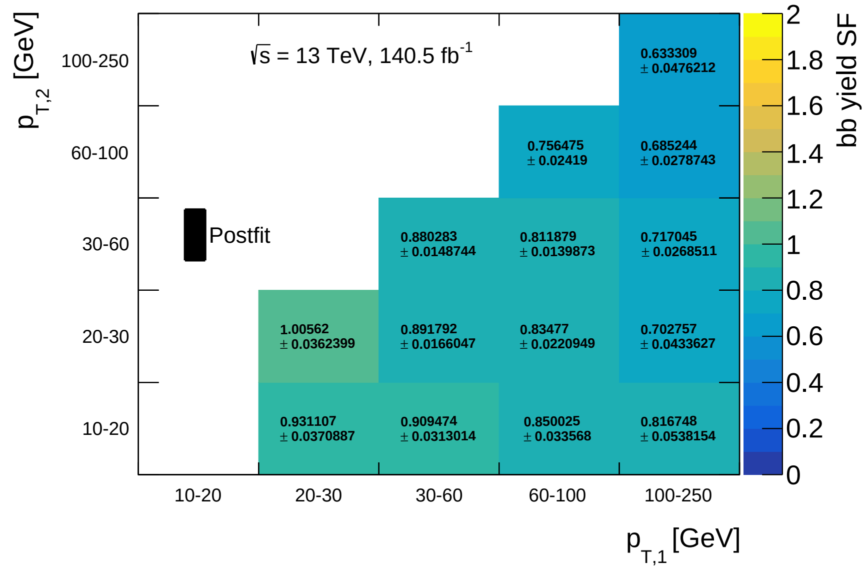

(a)

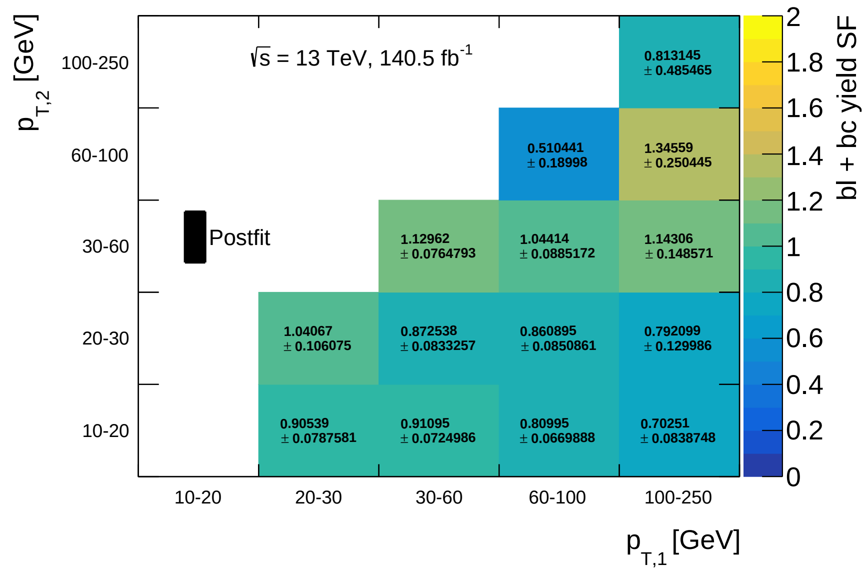

(b)

FIGURE 6.25: Ratio between the pre-fit and post-fit value of the event flavour fractions obtained after performing the sidebands fit on the `MV2c10` tagger.

Correlations Another interesting way to exploit the origin of the *b*-jets under study is to look at the correlation between the *b*-labelled jet p_{T} and the *b*-hadron p_{T}. For this study, only the $t\bar{t}$ nominal sample has been analysed and for each jet identified as a *b*-jet, through the *standard* labelling scheme, the correlation with respect to the p_{T} of the closest truth *b*-hadron is evaluated. Figure 6.28 shows a quite strong correlation in the whole p_{T} range. As expected, the p_{T} of the *b*-jet is softer than the one of the *b*-hadron, due to the missing neutral component of the track jets hence most of the events lies below the diagonal.

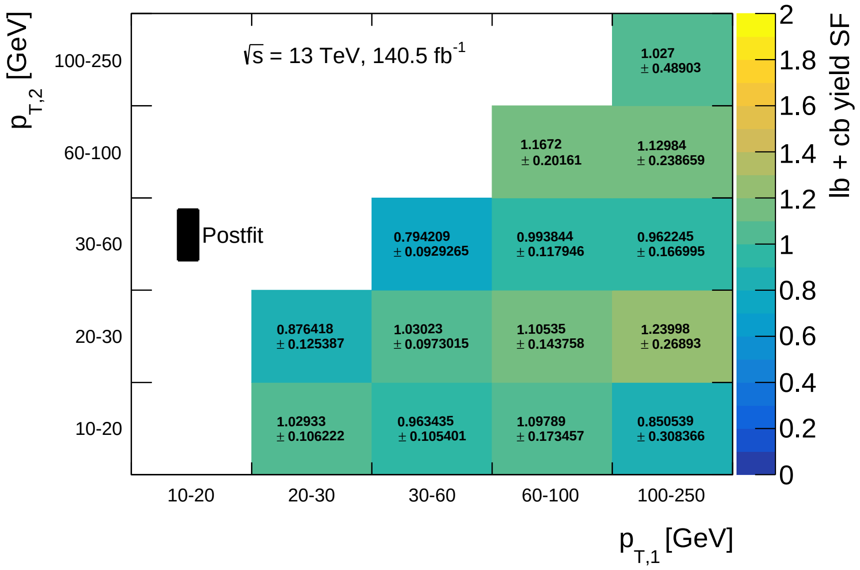

(a)

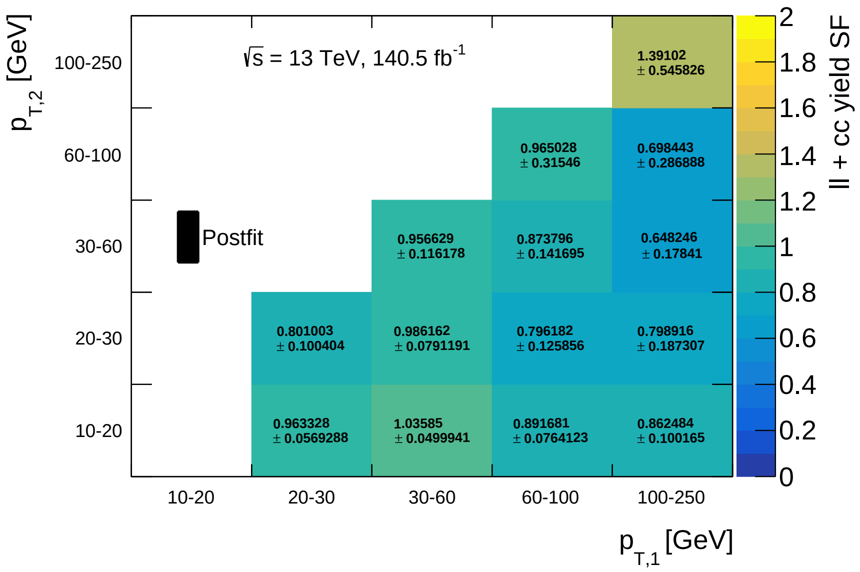

(b)

FIGURE 6.26: Ratio between the pre-fit and post-fit value of the event flavour fractions obtained after performing the sidebands fit on the MV2c10 tagger.

6.3 Ghost association studies

As motivated in Section 6.1.1, it has been decided not to calibrate the VR track jets that are almost collinear with any jet in the event, in order to mitigate the ambiguity in the association of truth hadrons and tracks to the jet. However, this conservative choice, which has a negligible impact on the di-leptonic $t\bar{t}$ events used for the measurement of the b-tagging efficiency, can instead affect the sensitivity of several analyses focusing on very boosted environments, in which VR track jets are preferably used due to their ability to better disentangle the two-prong structure of a very energetic large-R jet. It is hence crucial to understand whether the jets ending up in

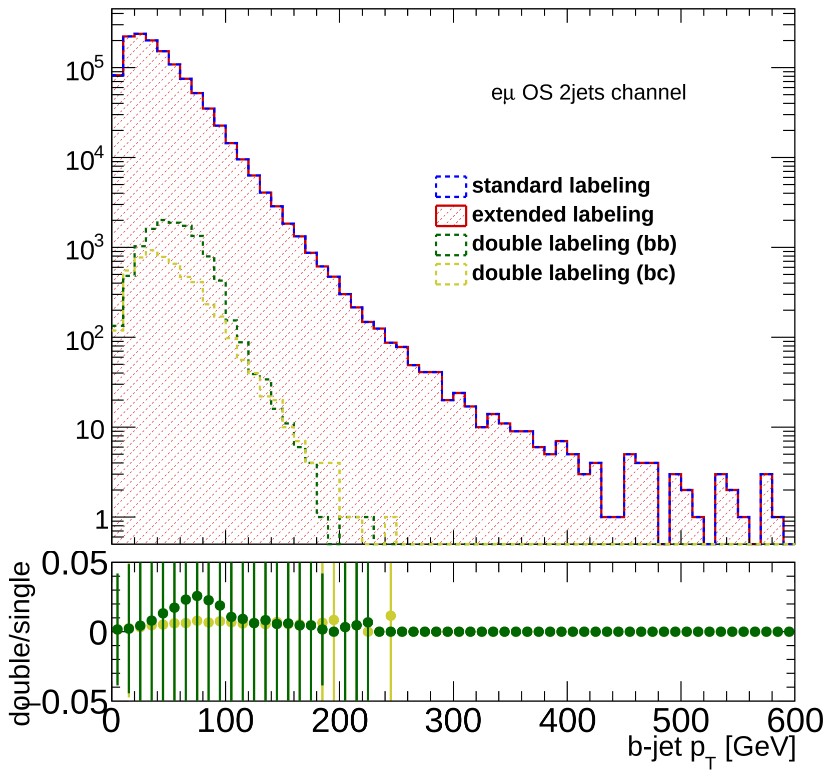

FIGURE 6.27: *b*-jet p_{T} spectrum of the $t\bar{t}$ signal sample. Each jet is labelled as a *b*-jet if it is matched to a truth b-hadron, following the standard and the extended scheme.

such collinear cases are actually problematic for our *b*-tagging algorithms.

A viable way to study the impact of these events on *b*-tagging is to compare the standard *cone* association with respect to the GA [164] (see Section 4.2.3). The metric of the anti-k_t algorithm causes the clustering process to start from the hardest objects. Hence, when performing the GA, a preference is also given in associating tracks or truth hadrons to the highest p_{T} jets first. This ensures that, in the collinear cases described above, the tracks or truth hadrons associated to the softest jets certainly could not be previously associated to the hardest jets. This feature should mitigate the ambiguity caused by the purely ΔR-based approach in which a low p_{T} jet can potentially remove tracks and truth hadrons from a high p_{T} jet, just based on its angular separation.

In order to make this comparison, two VR track jets collections have been analysed:

- the *standard* collection with ΔR track-to-jet association,
- the *Ghost Tag* collection with track-to-jet GA.

For consistency between the track-jet association and the truth labelling used for *b*-tagging, for the standard jets the usual ΔR-based truth flavour labelling scheme is adopted while for the *Ghost Tag* jets the truth hadrons are matched to jet following the GA procedure.

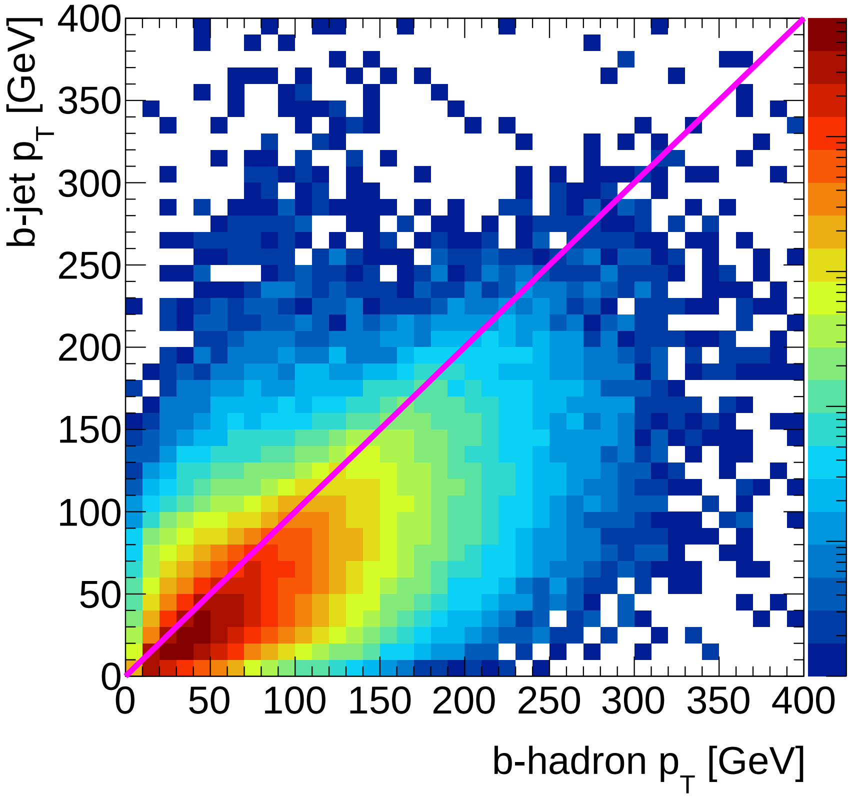

FIGURE 6.28: Correlation between the b-jet p_{T} and the b-hadron p_{T} (always considering the closest b-hadron), in the $e\mu$ (opposite sign) 2 jets region before m_{lj} cut. In pink it is shown the diagonal corresponding to the events in which the b-jet p_{T} is equal to the b-hadron p_{T}.

For this purpose, simulated MC events in which Higgs bosons are generated as decay products of RS gravitons G^* in a benchmark model with a warped extra dimension, $G^* \rightarrow HH \rightarrow b\bar{b}b\bar{b}$, with a graviton mass equal to 2750 GeV, have been analysed. The events are simulated using the `MadGraph5 aMC@NLO` generator, while parton showering, hadronisation and the underlying event were simulated with PYTHIA 8.230 using the leading-order NNPDF2.3 PDF set and the ATLAS A14 set of tuned parameters. The events are required to have at least two large-R jets and only the VR track jets contained inside the cone of either the leading or the subleading large-R jet are considered for this study.

Figures 6.29a-6.29b show the fairly good stability of the `MV2c10` b-tagging output for the two jet collections, also in the case of collinear VR track jets. Despite some differences present at low values (which can then be associated to light-flavour jets), no significant discrepancies are observed among the two jet collections.

On the other hand, Figures 6.30a-6.30b show the impact of the different labelling scheme, which is certainly not negligible for collinear VR track jets. The deviation at low p_{T} in Figure 6.30b seems to indicate that, when using the ΔR association to identify the truth flavour content of the jet, more low p_{T} jets are labelled as b-jets with respect to the GA scheme. Furthermore, as this feature seems to be pronounced only in the case of concentric VR track jets, it is reasonable to believe that, in such pathological cases, several low p_{T} jets are actually able to steal tracks from the higher p_{T} jets and be wrongly labelled as b-jets, as suspected initially.

It is then possible to combine these results and compare the fraction of b-tagged jets (using the 77% WP of the MV2c10 tagger) over the truth labelled b-jets, in the two different schemes, as shown in Figures 6.33a-6.33b.

Lastly, Figure 6.30b can also be compared directly with Figure 6.32b which shows, as expected based on the previous arguments, that the fraction of low p_T jets which are labelled as light jets is higher when using the GA with respect to the ΔR association scheme.

It is also interesting to make the same comparison for a similar RS sample corresponding to a smaller graviton mass. In appendix B.2 it is possible to see the same distributions for the case of a RS graviton mass equal to 900 GeV.

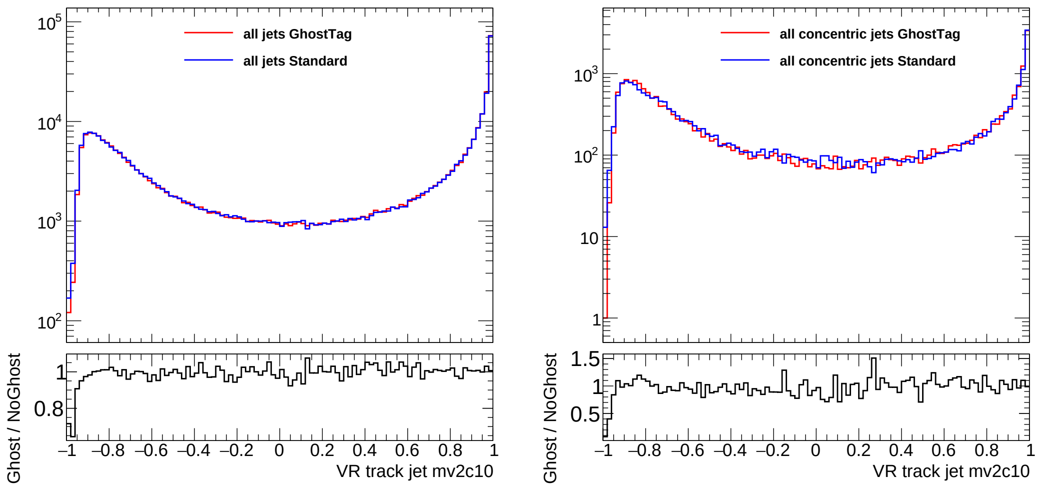

(a) (b)

FIGURE 6.29: MV2c10 distribution of the VR track jets associated either to the leading or subleading large-R jet in the event. On the left, all jets are shown. On the right, only concentric jets ($\Delta R < R_{\min}$) are shown.

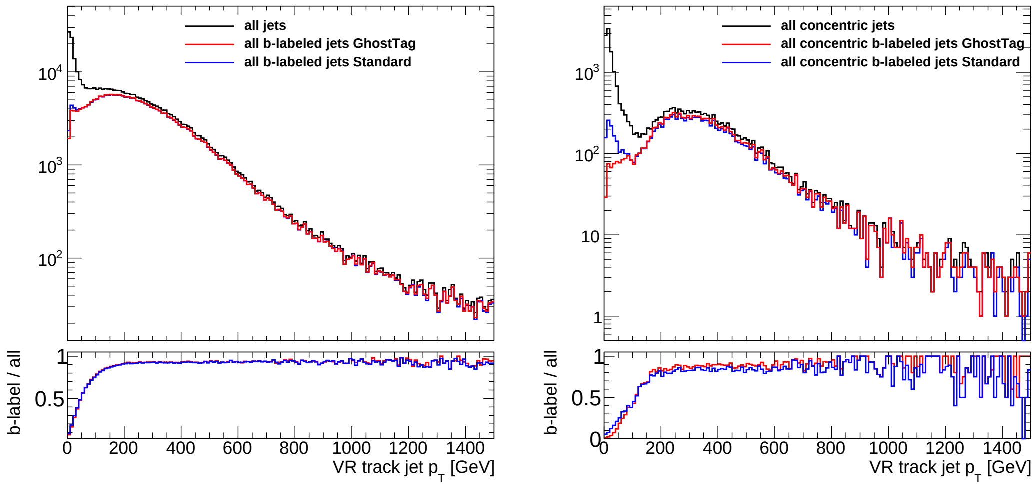

(a) (b)

FIGURE 6.30: p_{T} distribution of the VR track jets associated either to the leading or subleading large-R jet in the event, showing the fraction of jets labelled as b-jets at truth level. On the left, all jets are shown. On the right, only concentric jets ($\Delta R < R_{\mathrm{min}}$) are shown.

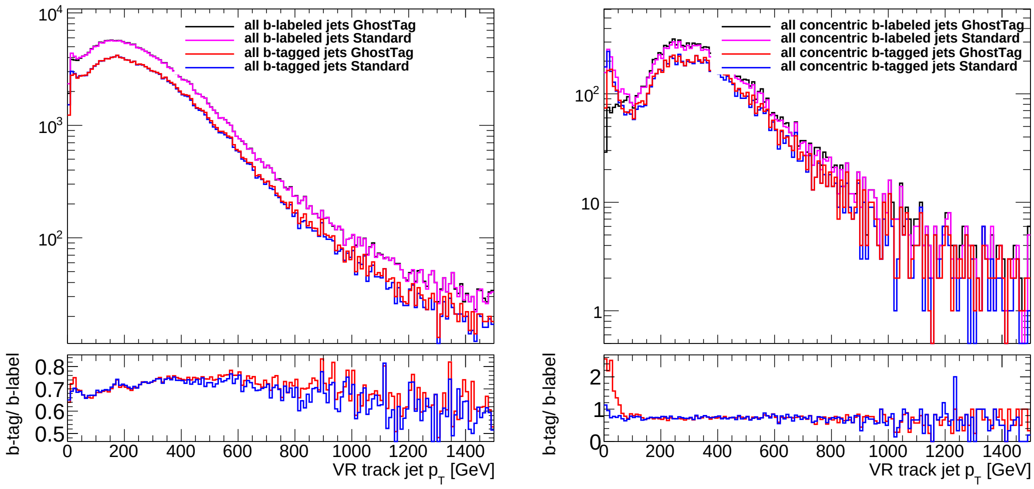

(a) (b)

FIGURE 6.31: p_{T} distribution of the VR track jets associated either to the leading or subleading large-R jet in the event, showing both the b-tagged jets (77% WP) and truth labelled b-jets, in the two different schemes. On the left, all jets are shown. On the right, only concentric jets ($\Delta R < R_{\mathrm{min}}$) are shown.

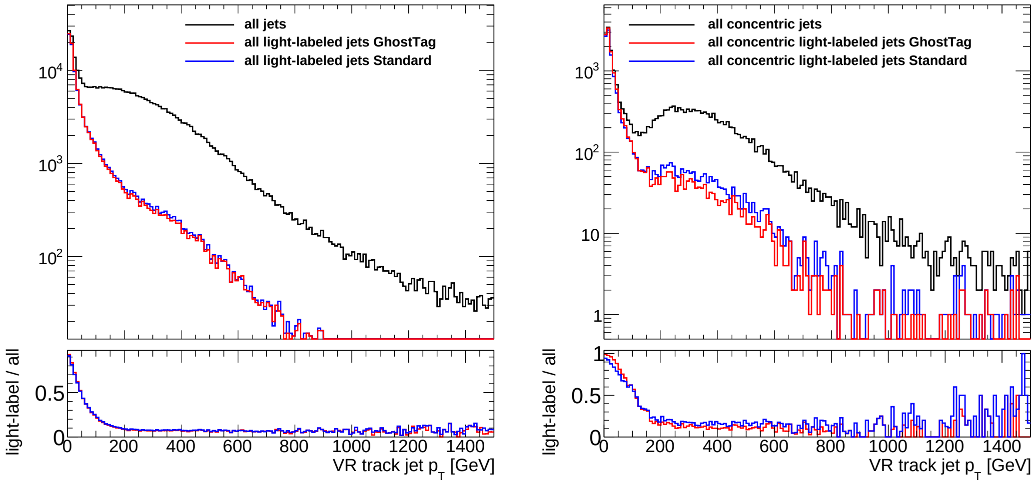

(a) (b)

FIGURE 6.32: p_{T} distribution of the VR track jets associated either to the leading or subleading large-R jet in the event, showing the fraction of jets labelled as light-jets at truth level. On the left, all jets are shown. On the right, only concentric jets ($\Delta R < R_{\mathrm{min}}$) are shown.

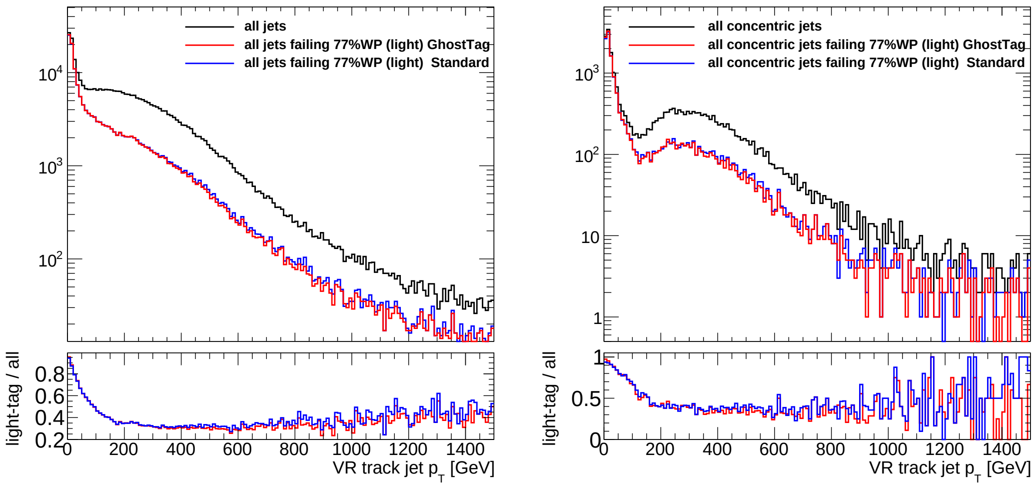

(a) (b)

FIGURE 6.33: p_{T} distribution of the VR track jets associated either to the leading or subleading large-R jet in the event, showing both the jets failing the 77% `MV2c10` WP and truth labelled light jets, in the two different schemes. On the left, all jets are shown. On the right, only concentric jets ($\Delta R < R_{\mathrm{min}}$) are shown.

7 The mono-S($b\bar{b}$) reinterpretation

This chapter is aimed at describing the usage of the RECAST framework [165] in order to interpret the results of the ATLAS mono-H($b\bar{b}$) search, presented in Chapter 5, in the context of a new model predicting DM production in association with a hypothetical dark Higgs boson, with an unknown mass m_s, decaying to b-quarks [166].

7.1 What does *recast* mean?

As described in Chapter 5, the final results of the mono-H($b\bar{b}$) analysis are interpreted only in the context of the Z'-2HDM model which is used as a benchmark of the search. This is similar to the case of several other experimental searches performed at the LHC, in which only a few new physics models are considered for the final interpretation of the results. However, many BSM searches are often sensitive to a broader class of models than the ones they were originally designed to test. Moreover, the number of new physics theory models has increased significantly over the last decades; hence it becomes even more crucial to be able to probe these new theories with any of the existing BSM searches. As we approach the beginning of Run 3 of the LHC, it is essential to "turn every stone" and look at any accessible corner of the theory space in order to test for the existence of new physics at the energy scales that we are currently probing.

Developing a solid analysis strategy represents a significant investment in time as well as in human and computational resources, hence it is not practical to build up a new search for any alternative signal hypothesis. In view of a steadily increasing sensitivity to a growing number of BSM scenarios, what is needed is instead a powerful reinterpretation framework in order to reach the full potential of the results from experimental collaborations.

When building up a new analysis strategy, which is motivated by a specific signal model, the crucial step consists in identifying a phase space region that is efficient for the signal model under study, while rejecting as much SM background as possible. Such region, which is optimised for a specific signal model, can still provide a good sensitivity to other models as long as the final state signatures are fairly similar. Once the event selection of the analysis is fixed, it is possible to reuse the background estimates and the observed data and to interpret the results in terms of a new signal hypothesis, as the only missing piece of information is the expected signal yield of the new model. This procedure is usually called *recasting*.

Figure 7.1 shows the comparison between the workflow of a full analysis, from the event generation of signal and background processes to the final estimate needed for the statistical interpretation, and that of a reinterpretation. It is clear that, provided that the background and data yields are actually reusable, the reinterpretation process should just consist in a single step that involves only the signal workflow.

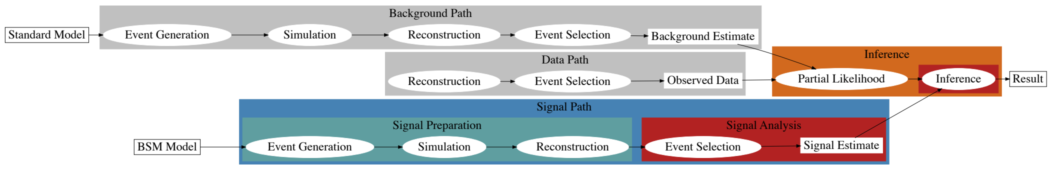

(a)

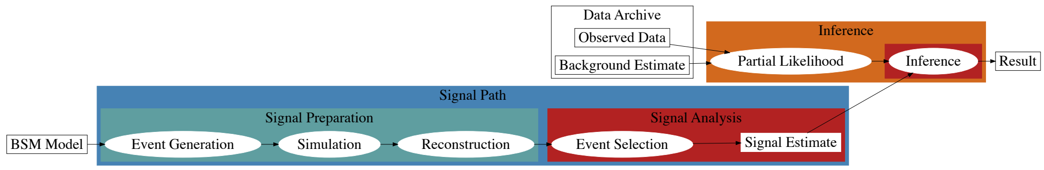

(b)

FIGURE 7.1: Comparison between the computational workflow required for a full analysis (at the top) and that of a reinterpretation (at the bottom).

While this problem seems to have in principle a relatively straightforward solution, in practice the actual bottleneck that has prevented in several cases to achieve these results is that either the specific version of the analysis framework is not available anymore or the knowledge about how to use it has been lost due to the unavailability of the original authors of the analysis. Originally introduced in Ref. [165], the RECAST framework is designed to facilitate this process and overcome this sort of issues. The essential ingredient consists in *preserving* the analysis in a way that allows new collaborators to re-execute it independently. This is achieved in RECAST through the use of re-executable declarative workflow and modern cloud computing technologies.

Let us see in more details how an analysis can be preserved in RECAST.

7.1.1 How to preserve an analysis?

Preserving an existing analysis means in practice preserving the whole workflow, consisting of several interdependent steps needed for the final statistical evaluation, such that it can be re-executed on new inputs. This means that the software behind each step must be archived, the correct usage of the software must be captured in parametrised job templates and the workflow structure must also be preserved.

The first step consists in archiving the software by building `Docker` container images [167, 168], which act as a snapshot of a filesystem that includes the analysis software and its dependencies. In the case of the mono-H($b\bar{b}$) analysis, two separate software repositories are used, one for the main event selection and one for the statistical analysis, hence two `Docker` container images are produced. For both repositories, the image building is integrated into the Continuous Integration (CI) configuration provided by the version control application `GitLab` [169] such that the software is preserved automatically each time the source code is modified.

Once the two `Docker` images are ready, it is possible to capture the workflow structure as well as the correct usage of the software, by using a specific workflow description language. Job templates specifying the commands required to execute the code and the workflow graph structure can now be retained. For this study, the `yadage` language [170] which captures the workflow graph structure as `YAML` documents is used.

Before moving forward with the reinterpretation of the dark Higgs model, the entire workflow has been validated with the Z'-2HDM signal samples from the original analysis. As show in Table 7.1, the exclusion limits can be reproduced by the reinterpretation workflow with sufficient precision.

$m_{Z'}[GeV]$	m_A [GeV]	exp. limit on σ [pb] (RECAST)	obs. limit on σ [pb] (RECAST)	exp. limit on σ [pb] (ATLAS-CONF-2018-039)	obs. limit on σ [pb] (ATLAS-CONF-2018-039)
400	300	$0.0965^{+0.0378}_{-0.0270}$	0.0910	0.0966	0.0913
400	400	$0.0260^{+0.0102}_{-0.0073}$	0.0256	0.0260	0.0256
600	400	$0.3124^{+0.1224}_{-0.0873}$	0.2588	0.3123	0.2588
800	300	$0.0109^{+0.0043}_{-0.0030}$	0.0135	0.0109	0.0135
800	400	$0.0130^{+0.0051}_{-0.0036}$	0.0145	0.0130	0.0145
800	500	$0.0260^{+0.0102}_{-0.0073}$	0.0282	0.0260	0.0282
1000	500	$0.0070^{+0.0027}_{-0.0019}$	0.0088	0.0070	0.0088
1200	700	$0.0047^{+0.0018}_{-0.0013}$	0.0055	0.0047	0.0055
1400	500	$0.0011^{+0.0004}_{-0.0003}$	0.0011	0.0011	0.0011
1400	700	$0.0023^{+0.0009}_{-0.0006}$	0.0023	0.0023	0.0023
1400	800	$0.0028^{+0.0011}_{-0.0008}$	0.0030	0.0029	0.0030
1600	300	$0.0008^{+0.0003}_{-0.0002}$	0.0006	0.0008	0.0006
1600	600	$0.0009^{+0.0004}_{-0.0003}$	0.0008	0.0009	0.0008
1800	500	$0.0008^{+0.0003}_{-0.0002}$	0.0006	0.0008	0.0006
1800	800	$0.0009^{+0.0004}_{-0.0003}$	0.0008	0.0009	0.0008
2000	400	$0.0008^{+0.0003}_{-0.0002}$	0.0006	0.0008	0.0006
2000	600	$0.0008^{+0.0003}_{-0.0002}$	0.0006	0.0008	0.0006
2000	700	$0.0008^{+0.0003}_{-0.0002}$	0.0006	0.0008	0.0006
2000	800	$0.0008^{+0.0003}_{-0.0002}$	0.0006	0.0008	0.0006
2200	400	$0.0008^{+0.0003}_{-0.0002}$	0.0006	0.0008	0.0006
2200	500	$0.0008^{+0.0003}_{-0.0002}$	0.0006	0.0008	0.0006
2200	600	$0.0008^{+0.0003}_{-0.0002}$	0.0006	0.0008	0.0006
2400	300	$0.0008^{+0.0003}_{-0.0002}$	0.0006	0.0008	0.0006
2400	400	$0.0008^{+0.0003}_{-0.0002}$	0.0006	0.0008	0.0006
2400	500	$0.0008^{+0.0003}_{-0.0002}$	0.0006	0.0008	0.0006
2400	700	$0.0008^{+0.0003}_{-0.0002}$	0.0006	0.0008	0.0006
2600	300	$0.0008^{+0.0003}_{-0.0002}$	0.0006	0.0008	0.0006
2600	500	$0.0008^{+0.0003}_{-0.0002}$	0.0006	0.0008	0.0006
2600	700	$0.0008^{+0.0003}_{-0.0002}$	0.0006	0.0008	0.0006
2800	300	$0.0009^{+0.0003}_{-0.0002}$	0.0006	0.0009	0.0006
2800	400	$0.0009^{+0.0003}_{-0.0002}$	0.0006	0.0009	0.0006
2800	500	$0.0009^{+0.0003}_{-0.0002}$	0.0006	0.0009	0.0006
2800	600	$0.0008^{+0.0003}_{-0.0002}$	0.0006	0.0008	0.0006
3000	200	$0.0009^{+0.0004}_{-0.0003}$	0.0007	0.0009	0.0007
3000	300	$0.0009^{+0.0004}_{-0.0003}$	0.0006	0.0009	0.0007
3000	400	$0.0009^{+0.0004}_{-0.0003}$	0.0007	0.0009	0.0007
3000	600	$0.0009^{+0.0003}_{-0.0002}$	0.0007	0.0009	0.0007

TABLE 7.1: Comparison of upper limits on production cross-sections of Z'-2HDM models obtained with RECAST and the original analysis.

7.2 A proof of concept: the dark Higgs model

The signal used for this reinterpretation is the dark Higgs model [166]. As already anticipated in Section 2.5, several exotic searches at the LHC rely on new BSM theories in which DM interacts with SM particles via the exchange of one or more mediators, such as the spin-1 Z' boson or any additional Higgs boson carrying spin 0. All these models must predict the correct DM relic abundance which, in this context, is strongly determined by the properties of these new mediator particles. In the last years, experimental results have strongly constrained the parameter space in which the DM particles can obtain their relic abundance from direct annihilation into SM particles. This complication can be significantly reduced in case the DM particle is not the lightest state in the dark sector, opening new annihilation channels. This represents the main theoretical motivation behind the dark Higgs model, in which the DM particle is generated via a Higgs mechanism in the dark sector. The resulting dark Higgs boson s can be lighter than the DM particle χ, such that the DM relic abundance is dominantly determined by the $\chi\chi \to ss$ process, followed by decays of the s boson to SM particles.

The predicted signature of the dark Higgs model consists then in a certain amount of $E_{\mathrm{T}}^{\mathrm{miss}}$ due to DM pair production and the SM particles from the decay of the dark Higgs boson s. It is therefore possible to exploit the process $s \to b\bar{b} + E_{\mathrm{T}}^{\mathrm{miss}}$. The new mono-S($b\bar{b}$) signature is then identical to the mono-H($b\bar{b}$) final state, with the only exception represented by the mass of the dark Higgs candidate s which in this new framework is a free parameter of the model.

7.2.1 Theoretical framework

The dark Higgs model postulates the presence of a Higgs mechanism in the dark sector that is responsible for the origin of masses of the DM particles. Furthermore, the presence of an additional mediator Z' allows the model to be probed also at colliders through different channels, as illustrated in Figure 7.2.

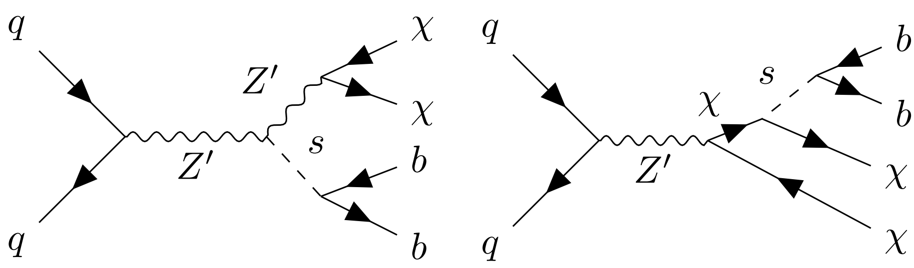

FIGURE 7.2: Process leading to a dark Higgs signal with $E_{\mathrm{T}}^{\mathrm{miss}}$ from DM particles χ and decay of the dark Higgs s to b-quarks. Figure taken from Ref. [171].

In this new model, the DM particle χ is a Majorana fermion, whose mass is obtained from the VEV w of a complex Higgs field S. It couples axially to a new Z' boson which is associated to a new $U(1)'$ gauge group[1]. The symmetry breaking gives rise

[1]The discussion can be extended to the case of a Dirac fermion DM candidate. However, this implies also vectorial couplings to the Z' boson and additional dependence on other free parameters. For simplicity, the original theory paper focuses on a more constrained scenario with only four parameters [166].

to a mass for the Z' boson, as S carries charge q_S under the new gauge group, as well as a new state: the dark Higgs boson s. The interaction Lagrangian is given by:

$$\mathcal{L}_\chi = -\frac{1}{2} g_\chi Z'^\mu \bar{\chi}\gamma^5\gamma_\mu\chi - g_\chi \frac{m_\chi}{m_{Z'}} s\bar{\chi}\chi + 2g_\chi Z'^\mu Z'_\mu (g_\chi s^2 + m_{Z'}s). \quad (7.1)$$

The DM sector is coupled to the SM by postulating vector couplings of the Z' boson to quarks by gauging baryon number, with the following interaction Lagrangian:

$$\mathcal{L}_{q-Z'} = -g_q Z'^\mu \bar{q}\gamma_\mu q. \quad (7.2)$$

Axial-vector couplings of the Z' boson to quarks as well as additional couplings of the Z' to SM leptons would also be possible but they would require a modification of the model in order to guarantee SM gauge invariance and they would introduce further constraints. For simplicity, these two possibilities are not taken into account. In this context, the dark Higgs model can be considered a simplified version of the gauge baryon models [172, 173, 174, 175].

The independent parameters of the model are the mass of the DM particle m_χ; the mass of the Z' boson $m_{Z'}$; the coupling g_χ of the DM particle with the dark Higgs boson s; and the coupling of the Z' boson to quarks g_q. The considered model focuses on the case in which the dark Higgs boson s is the lightest state in the dark sector and the relic abundance is dominantly set by the process $\chi\chi \rightarrow ss$. A non-zero mixing between the dark Higgs boson and the SM Higgs boson ensures that the dark Higgs boson is unstable and can decay to SM particles.

Figure 7.3 shows the BR of the relevant decay processes involving the dark Higgs boson, calculated with `MadGraph5 aMC@NLO` 2.6.6 [140]. The decay to b-quarks dominates for $m_s < 160$ GeV until the possibility of a decay to a pair of W, Z or even h bosons opens up. The sensitivity of the mono-S($b\bar{b}$) search is hence limited at higher masses where the model should be probed with other signatures.

7.2.2 Simulated samples

The signal samples are generated by calculating the hard-scattering matrix elements at LO with `MadGraph5 aMC@NLO` 2.6.2 while the modelling of the parton shower and underlying event is performed by `Pythia 8.230`, allowing for up to one additional jet in the event. In order to remove the overlap between the matrix element and the parton shower, the `CKKW-L` merging procedure [176, 177] is applied, in which the matching scale is set to 40 GeV. The NNPDF3.0 PDF set with a value of the strong coupling constant equal to 0.13 and the A14 set of tuned parameters of `Pythia` are used.

The parameter space of the model is scanned for $m_{Z'}$ from 0.5 TeV to 3.5 TeV, in steps of 0.5 TeV, and for m_s from 50 GeV to 150 GeV, in steps of 20 GeV, assuming a DM particle with mass m_χ equal to 200 GeV. The choice of m_χ is mostly motivated by the need for complementarity to a search probing the $s \rightarrow W^+W^-$ channel which is currently in preparation. In general, little dependence of the signal kinematics on m_χ has been observed and, as the cross-section decreases beyond sensitivity for large values of m_χ, choosing the value of 200 GeV allows us to probe an accessible region of the parameter space. The values of g_q and g_χ are fixed respectively to the values of 0.25 and 1.0, following the conventional coupling choices for vector mediator simplified model searches at the LHC [178, 58]. Lastly, the value of the mixing angle θ is set to 0.01, following the choice made in theory paper [166].

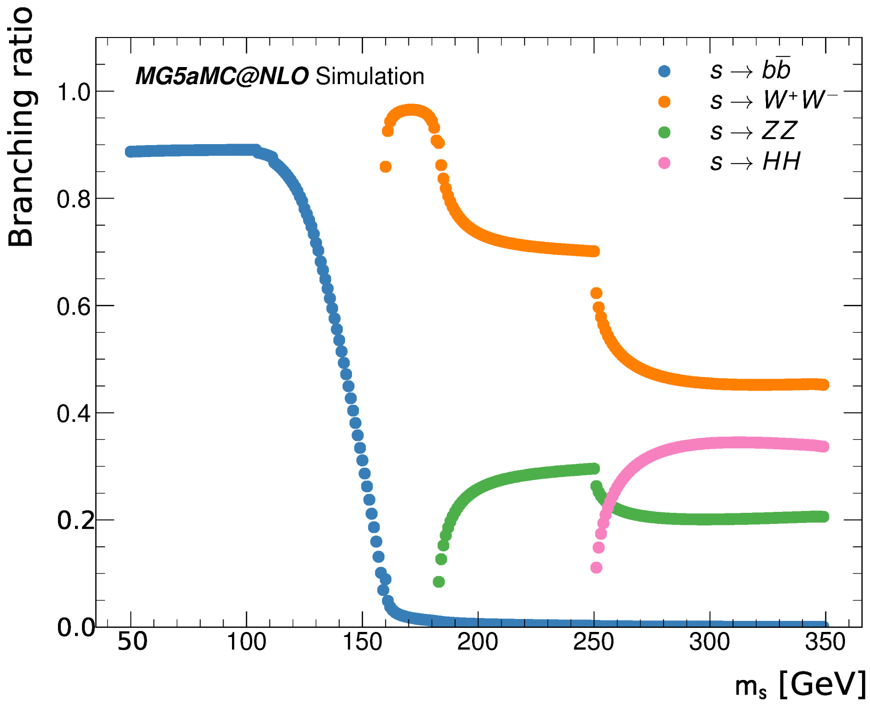

FIGURE 7.3: Branching ratio of the dark Higgs boson s decay to b-quarks, W^+W^-, ZZ and hh. The branching ratio was computed using `MadGraph5 aMC@NLO` 2.6.6 [140] at leading order. Figure taken from Ref. [171].

7.2.3 Signal modelling uncertainties

As the background prediction is the same as in the original analysis, all the systematic uncertainties related to detector effects and the modelling of the SM background can be applied also for the interpretation of this new model. The only additional source of uncertainty that needs to be evaluated separately is related to the theory modelling of the dark Higgs signal.

The theory modelling uncertainties on the dark Higgs signal model are estimated by applying the full SR event selection described in Chapter 5 (see Table 5.1) on particle-level objects, using the same analysis framework and strategy already described in Section 5.10.

The systematic uncertainties related to the theory modelling of the dark Higgs signal samples are estimated by varying the model parameters and comparing the signal event yield, after applying the SR selection at truth-level, using only events with exactly two b-tagged jets.

The uncertainties on the renormalisation and factorisation scales are determined by varying μ_R and μ_F independently by factors of 2 and quoting the largest deviation from the nominal signal yield as uncertainty for each of the four $E_{\mathrm{T}}^{\mathrm{miss}}$ categories. Furthermore, also the uncertainty associated to the NNPDF PDF set is evaluated as the standard deviation of the 100 PDF replicas, following the same approach described in Section 5.10.3.

Figures 7.4-7.5 show the impact of the scale and PDF variations on the distribution of the dark Higgs boson candidate for a representative mass point. From this comparison, it is also possible to see that neither the scale nor PDF variations alter significantly the shape of the dark Higgs candidate mass distribution; therefore only the relative differences concerning the normalisation are computed in this study, as they represent the leading source of uncertainty.

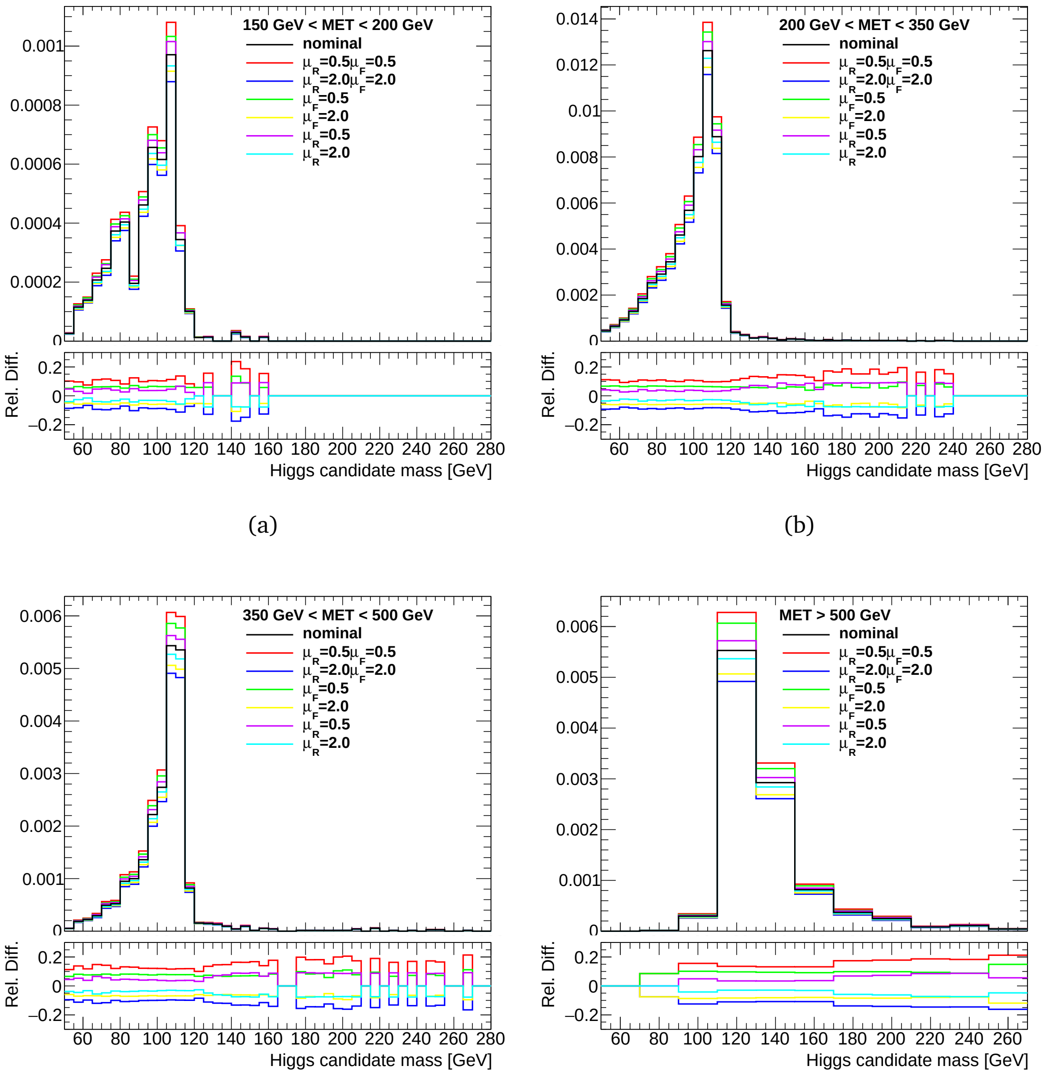

(a) (b)

(c) (d)

FIGURE 7.4: Distributions of the dark Higgs candidate mass in the four $E_{\mathrm{T}}^{\mathrm{miss}}$ regions for a dark Higgs signal with $m_{Z'} = 1$ TeV, $m_s = 110$ GeV and $m_\chi = 200$ GeV. Together with the nominal distribution also the variations corresponding to different choices of μ_R and μ_F are shown, after applying the full SR selection at generator-level.

The values of the relative signal theory uncertainty due to the scale and PDF variations are shown in Table 7.2 for each mass point.

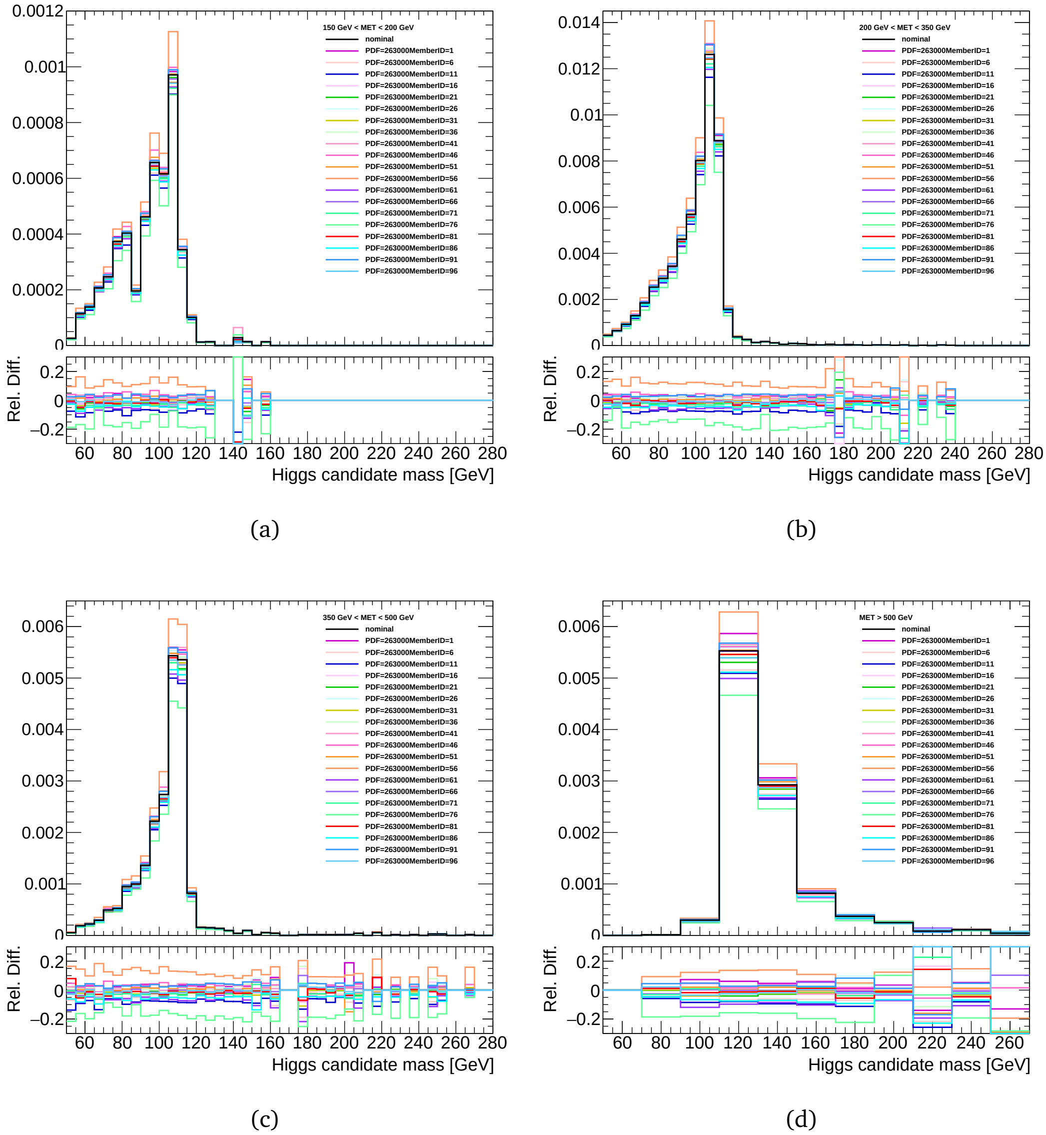

FIGURE 7.5: Distributions of the dark Higgs candidate mass in the four $E_{\mathrm{T}}^{\mathrm{miss}}$ regions for a dark Higgs signal with $m_{Z'} = 1$ TeV, $m_s = 110$ GeV and $m_\chi = 200$ GeV. Together with the nominal distribution also a subset of the 100 PDF variations are shown, after applying the full SR selection at generator-level.

7.2.4 Results

Following the same strategy defined in the context of the mono-H($b\bar{b}$) analysis, in order to establish the presence of a potential signal, a profile likelihood fit is performed simultaneously in all SRs and CRs, using the dark Higgs as alternative signal hypothesis.

Figure 7.6 shows the distribution of the Higgs candidate mass in the four different $E_{\mathrm{T}}^{\mathrm{miss}}$ bins used in the analysis for the observed data, corresponding to an integrated luminosity of 79.8 fb^{-1}, and for the simulated background, before and after the background-only profile likelihood fit. The distributions follow exactly the ones obtained in the original analysis, presented in Figure 5.13, except for the new overlaid signal model which is scaled to an arbitrary cross-section. Similarly, Figure 7.7

DSID	$m_{Z''}$	m_s	scale uncertainty [in %] for $E_{\mathrm{T}}^{\mathrm{miss}}$ [GeV]				PDF uncertainty [in %] for $E_{\mathrm{T}}^{\mathrm{miss}}$ [GeV]			
	[GeV]	[GeV]	150 - 200	200 - 350	350 - 500	500+	150 - 200	200 - 350	350 - 500	500+
311378	500	50	6.2	10.8	17.5	12.0	3.8	4.4	4.2	5.1
311379	1000	50	9.1	11.9	16.7	13.7	4.4	4.3	5.0	5.9
311380	1500	50	11.3	13.6	17.6	12.8	5.3	4.9	5.6	6.2
311381	2000	50	14.3	14.7	18.6	13.9	5.6	5.8	6.9	6.5
311382	2500	50	14.1	16.5	20.2	14.9	7.5	7.0	9.0	7.4
311383	3000	50	16.6	17.0	20.3	16.2	9.2	9.2	9.7	9.5
311384	500	70	7.5	9.0	13.7	11.7	4.0	4.1	4.1	5.7
311385	1000	70	10.1	10.4	14.4	13.5	4.3	4.4	4.6	6.0
311386	1500	70	12.7	11.8	14.7	13.8	5.0	5.0	5.1	5.8
311387	2000	70	14.0	13.4	15.6	14.3	6.1	6.0	5.9	6.4
311388	2500	70	14.8	14.8	17.3	15.1	6.3	7.2	6.9	7.9
311389	3000	70	16.3	15.8	18.1	16.1	8.8	8.6	9.2	9.5
311390	500	90	9.0	9.0	10.2	11.2	4.0	4.1	4.1	5.2
311391	1000	90	11.4	10.3	12.6	13.7	4.3	4.5	4.6	5.7
311392	1500	90	12.2	11.5	12.4	13.4	5.2	5.1	5.1	5.9
311393	2000	90	14.8	13.2	14.0	14.1	5.7	5.9	5.9	6.4
311394	2500	90	15.4	14.8	15.5	15.0	7.9	7.0	7.5	7.9
311395	3000	90	17.5	15.6	16.6	16.1	8.8	8.9	8.6	9.5
311396	500	110	8.6	8.6	10.4	11.8	4.3	4.2	4.4	4.7
311397	1000	110	10.8	10.3	12.3	13.8	4.5	4.4	4.9	5.7
311398	1500	110	12.4	11.5	12.2	13.8	5.0	4.9	5.0	5.9
311399	2000	110	14.6	13.2	13.5	14.2	6.0	5.9	6.0	6.4
311400	2500	110	16.3	14.4	14.9	15.0	8.1	7.1	7.5	7.9
311401	3000	110	16.0	15.6	16.0	16.1	9.6	8.7	9.2	9.4
312356	3500	50	16.5	18.7	22.2	17.0	16.4	12.1	12.4	12.2
312357	3500	70	17.1	16.9	19.1	17.3	15.2	11.4	11.9	12.4
312358	3500	90	18.4	17.1	17.5	17.1	14.3	11.4	11.7	12.3
312359	3500	110	17.8	17.0	17.1	17.2	11.1	11.2	11.7	12.3
312360	500	130	8.7	8.4	10.4	11.4	4.0	4.1	4.2	4.6
312361	1000	130	10.0	10.0	12.2	14.2	4.3	4.4	4.7	5.5
312362	1500	130	13.0	11.5	12.2	14.0	4.8	4.9	5.2	6.2
312363	2000	130	13.5	13.1	13.7	13.9	6.0	5.8	6.0	6.6
312364	2500	130	14.6	14.2	14.9	15.2	7.2	7.2	7.1	7.8
312365	3000	130	16.9	15.6	15.9	16.1	11.0	8.8	9.0	9.4
312366	500	150	8.0	8.3	10.6	12.0	4.3	4.2	4.5	5.3
312367	1000	150	9.5	9.7	11.8	13.4	4.8	4.5	4.8	5.5
312368	1500	150	12.3	11.3	12.3	13.5	5.5	5.0	5.1	6.0
312369	2000	150	13.2	12.7	13.4	14.0	6.2	5.8	6.1	6.4
312370	2500	150	14.1	14.1	14.8	15.0	6.6	7.1	7.3	7.6
312371	3000	150	15.8	15.6	16.1	16.1	7.8	9.1	9.1	9.5
312372	3500	150	17.3	16.5	17.1	17.0	12.7	11.3	11.8	12.2
312373	3500	130	18.6	17.0	16.8	17.1	12.6	11.5	11.7	12.0

TABLE 7.2: List of signal theory uncertainties for the dark Higgs signal model for simulated MC samples with different mass of the Z' boson $m_{Z'}$, mass of the dark Higgs boson m_s and mass of the DM candidate $m_\chi = 200$ GeV.

shows the SM background yield in the resolved and merged $E_{\mathrm{T}}^{\mathrm{miss}}$ bins, compared with the observed data, before and after the background-only fit. The new signal hypothesis is also shown in red for a representative mass point.

As no deviation from the SM prediction is observed, it is possible to extract exclusion limits on the dark Higgs model, by deriving an upper limit on the observed signal strength μ as a function of $m_{Z'}$ and m_s. Figure 7.8 shows the expected and observed 95% CL upper limits on μ for the dark Higgs model under study in the ($m_{Z'}$,m_s) plane.

The expected and observed upper limits on μ shown separately in Figure 7.8 can also be presented as exclusion contours in the ($m_{Z'}$,m_s) plane, as illustrated in Figure 7.9. The dashed (solid) black line corresponds to the expected (observed) limit, while the green and yellow bands represent respectively the $\pm\ 1\sigma$ and $\pm\ 2\sigma$ uncertainty on the expected limit. The region on the left of the black line is excluded at

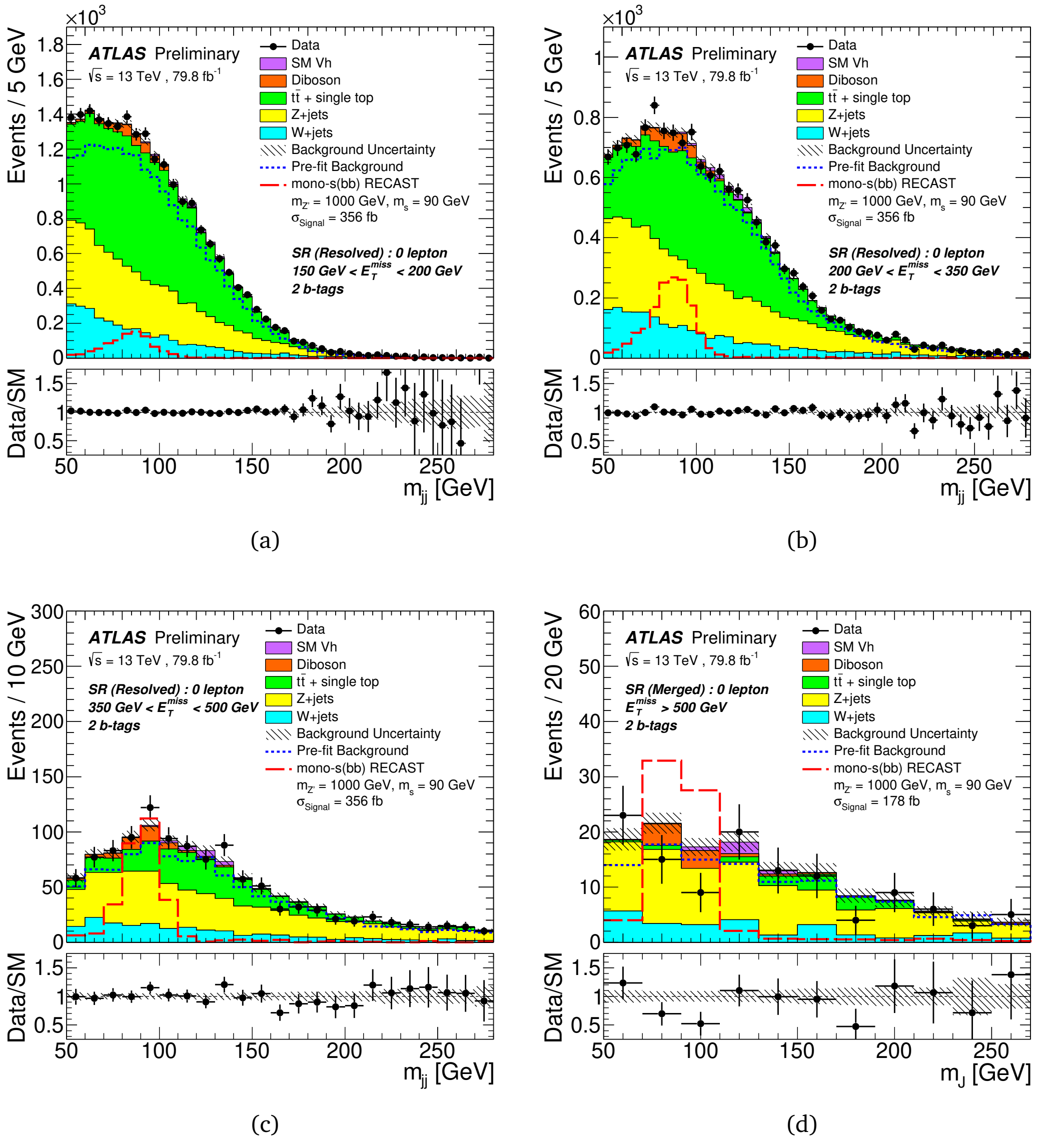

FIGURE 7.6: Distributions of the Higgs candidate mass m_h, calculated as the invariant mass m_{jj} of the dijet system in the resolved regime and as the mass of the leading large-R jet m_J in the boosted regime. The SM expectation is shown before the fit (dashed blue line) and after the fit (solid histograms). The expected signal distribution for a representative dark Higgs model is also shown and is scaled to a cross-section of 356 (178) fb in the resolved (merged) region. Figures taken from Ref. [171].

95% CL. A Z' boson with mass lower than 3.2 TeV is excluded for $m_s = 90$ GeV. In a large part of the phase space, the observed limits are stronger than the expected ones. This behaviour can be explained by the under-fluctuation of data for 70 GeV $< m_s <$ 110 GeV, shown in Figure 7.6, in the merged region, which drives the sensitivity of the search at high $m_{Z'}$. The sensitivity decreases for $m_s >$ 130 GeV due to the diminishing BR for the $s \to b\bar{b}$ process, as shown in Figure 7.3.

It is also important to highlight explicitly the region of the phase space which is compatible with the measurement of the relic abundance performed by the PLANCK collaboration [22] (see Section 2.2). The predicted relic abundance in the dark Higgs

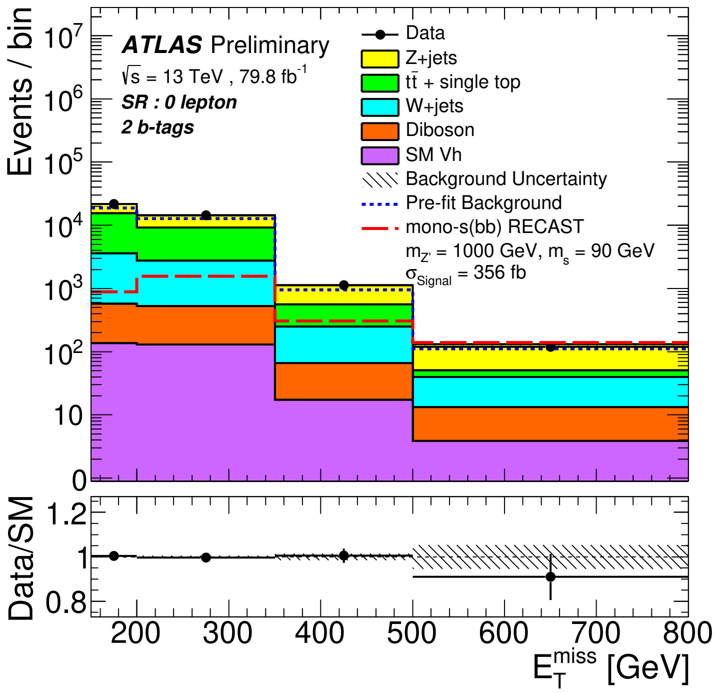

FIGURE 7.7: $E_{\mathrm{T}}^{\mathrm{miss}}$ distribution for the resolved and merged signal regions combined showing the comparison between the observed data and the SM background before and after the background-only fit. Figure taken from Ref. [171].

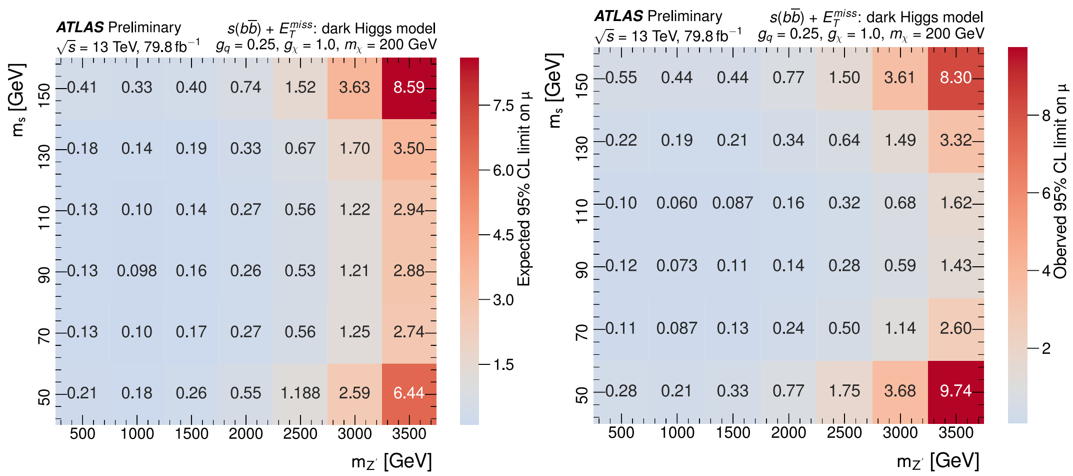

(a) (b)

FIGURE 7.8: 95% CL exclusion limits on the signal strength μ for the dark Higgs model with parameters m_χ = 200 GeV, $g_q = 0.25$, $g_\chi = 1.0$ and different values of $m_{Z'}$ and m_S. The expected exclusion limits are shown on the left, while the observed exclusion limits are shown on the right. Figures taken from Ref. [171].

model strongly depends on the coupling parameters and on the DM mass, allowing various choices of the parameters to satisfy the constraints set by PLANCK. In this particular case, only the region on the left of the pink dashed line in Figure 7.9 are able to satisfy these requirements. We can therefore conclude that the whole region of the parameter space probed with this analysis strategy is excluded.

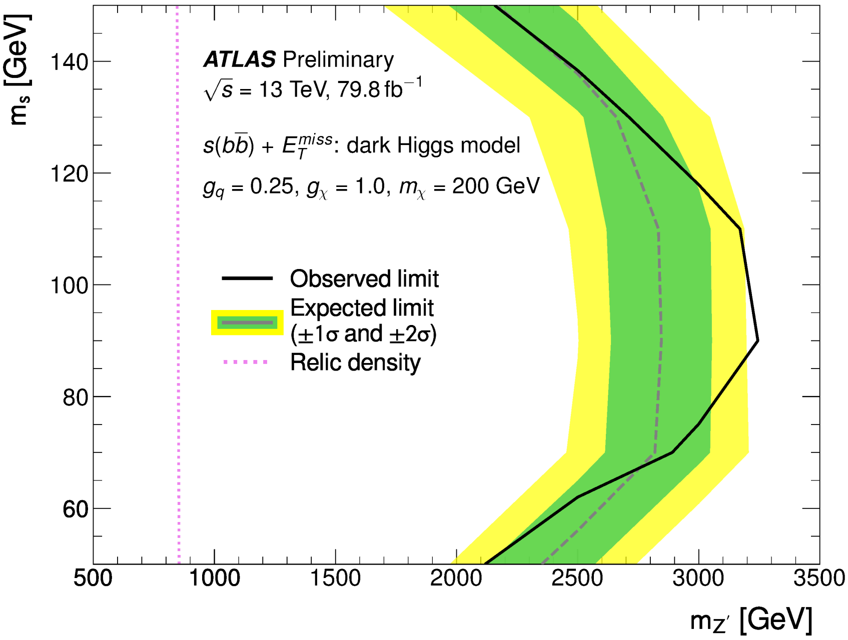

FIGURE 7.9: Exclusion contour for the dark Higgs model with parameters $m_\chi = 200$ GeV, $g_q = 0.25$, $g_\chi = 1.0$ in the ($m_{Z'}$,m_A) plane. The pink dotted curve corresponds to the set of points for which the expected relic density is consistent with the PLANCK measurement [22]. The region on the right of the curve corresponds to a predicted relic abundance which is higher, hence not consistent, with this measurement. Figures taken from Ref. [171].

The results of this work have been published in the form of an ATLAS public note [171] and presented at the 6th Dark Matter @ LHC 2019 workshop [179] in August 2019.

8 Conclusions and outlook

Understanding the nature of DM represents nowadays one of the biggest challenges in physics and cosmology. Being surrounded by an enormous amount of matter whose origin is still unknown is a fair reason to cause headaches to the whole scientific community.

The search presented in this thesis exploits the mono-H($b\bar{b}$) signature with the ATLAS experiment at the LHC. The strategy behind this (and any other similar mono-X) analysis relies on the fact that if it is possible to produce DM particles from an initial state of two SM particles, then DM would leave the detector without interacting with it. The key ingredient of this type of searches is therefore the presence of a large amount of $E_{\mathrm{T}}^{\mathrm{miss}}$ recoiling against a visible object: in this case a SM Higgs boson decaying to b-quarks.

Among the several mono-X searches currently performed at the LHC, the mono-H($b\bar{b}$) channel has definitely a leading role, as it allows to probe a substantial region of the phase space and at the same time it yields results complementary to several other searches.

For the analysis of the Run 2 data of the LHC, recorded from 2015 until 2017 and corresponding to 80 fb^{-1} of integrated luminosity, the mono-H($b\bar{b}$) analysis has focused mostly on improving its sensitivity in the high energy regime. A better sensitivity has indeed been achieved by applying b-tagging to VR track jets in the *boosted* regime, for the first time within the ATLAS collaboration, outperforming previous results by up to a factor of 3 in the high mass regime.

Applying b-tagging to VR track jets also implies a dedicated calibration of the b-tagging performance in collision data. The study performed in this context allowed a deeper investigation of the features, and complications, of the VR track jet algorithm, of which the whole ATLAS collaboration could profit.

While improving the sensitivity of a single search is a worthy cause, being able to reuse (or rather *recast*) existing results and reinterpret them under a new signal model hypothesis is probably equally important. Even more now as we approach the beginning of Run 3 of the LHC, new BSM scenarios can open up and experimental physicists must be ready to analyse the data in view of potential new alternative signal models. For this reason, the mono-H($b\bar{b}$) results presented in this thesis have been reinterpreted in the context of a new signal model predicting the existence of a new dark Higgs boson s with an unknown mass, making use of the infrastructure provided by the RECAST framework.

It is now intriguing to understand what is the actual sensitivity of the mono-H($b\bar{b}$) search using the full dataset recorded by the ATLAS experiment during the Run 2 of the LHC, with almost a doubled amount of integrated luminosity. In order to exploit the full potential of the mono-H($b\bar{b}$) search, several improvements and updates are foreseen for the future analysis and they are discussed below.

A new signal model For the future iteration of the mono-H($b\bar{b}$) analysis, aimed at exploiting the full statistical power of the Run 2 of the LHC, the results are planned to be interpreted also in the context of the 2HDM+a signal model [180, 181]. Compared to other 2HDM models, which extend the Higgs sector with two complex scalar doublets leading in total to five Higgs bosons with different CP properties, the 2HDM+a theoretical model includes an additional pseudo-scalar singlet a mediating the interaction between SM and fermion DM particles. This singlet mixes with the CP-odd component of the 2HDM Higgs doublets, with the mixing angle θ and the mass of the additional pseudo-scalar a being free parameters of the model [182]. Within this framework, the mono-H($b\bar{b}$) signature can arise through two different channels: the gluon-gluon fusion and the b-initiated production, as shown in Figure 8.1. In the Type-II 2HDM models, the qqA coupling scales like $\cot\beta$ (see Section 5.1) for up-type quarks and like $\tan\beta$ for down-type quarks. Therefore coupling to bottom quarks is preferred over coupling to top quarks for high $\tan\beta$ values and as a result the b-initiated contribution dominates for $\tan\beta > 0.5$. The coupling Aha scales instead like $\cos(\theta)\sin(\theta)$.

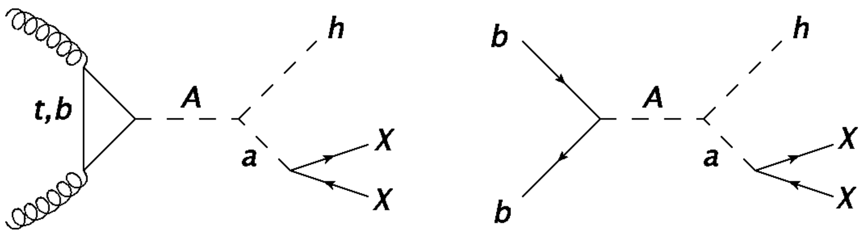

FIGURE 8.1: Feynman diagrams corresponding to the gluon-gluon fusion (left) and b-initiated production (right) of the $h+E_{\mathrm{T}}^{\mathrm{miss}}$ final state.

The 2HDM+a signal model is going to be used as additional benchmark model for the full Run 2 analysis, along with the Z'-2HDM model (with an extended ($m_{Z'}$-m_A) parameter grid). Compared to the Z'-2HDM model, which allows us to easily probe a particularly boosted signature, 2HDM+a events present in general a much softer $E_{\mathrm{T}}^{\mathrm{miss}}$ spectrum. Interpreting the results under these two signal assumptions would allow us to extend the impact of the mono-H($b\bar{b}$) results both in the low and high mass region.

A new b-tagging algorithm Another potential change in the full Run 2 analysis concerns the usage of `DL1r` as b-tagging algorithm for both small-R jets in the resolved region and VR track jets in the merged region, in place of the current `MV2c10` tagger. As already anticipated in Section 4.3, the `DL1r` b-tagging algorithm is expected to provide a better discrimination against light and charm jets, due to a more accurate description of the b-jet properties achieved by taking into account the correlations among all tracks associated to the jet. Furthermore, given its significant improvement with respect to the previous `MV2` algorithms, the `DL1r` is going to be used as default b-tagging algorithm within the ATLAS collaboration. For all these reasons, the impact of the `DL1r` tagger has been studied also in the context of the mono-H($b\bar{b}$) analysis, for both the resolved and merged region. The study is performed on simulation using events corresponding to the pile-up conditions of the data collected during

2018, accounting for 60 fb^{-1} of integrated luminosity. While in the resolved region no significant improvement is observed and the sensitivity of the search seems to remain stable on varying of the b-tagging algorithm, a more significant improvement is observed in the merged region. In fact, in the merged (resolved) region the fraction of events with two b-jets increase by a 13% (3-4%) when using the `DL1r` algorithm, with respect to the `MV2c10` algorithm, as can be concluded by comparing the numbers in Table 8.1 with respect to the ones in Table 8.2. Dedicated studies about the expected gain in terms of the sensitivity of the Z'-2HDM signal model are shown in Appendix C.

Flavour category	$E_{\mathrm{T}}^{\mathrm{miss}}$: 150-200 GeV	$E_{\mathrm{T}}^{\mathrm{miss}}$: 200-350 GeV	$E_{\mathrm{T}}^{\mathrm{miss}}$: 350-500 GeV	$E_{\mathrm{T}}^{\mathrm{miss}}$: >500 GeV
bb	0.834	0.815	0.774	0.533
bc	0.071	0.076	0.080	0.060
bl	0.077	0.081	0.085	0.132
cc	0.0088	0.014	0.030	0.069
cl	0.005	0.009	0.021	0.096
ll	0.004	0.005	0.010	0.110

TABLE 8.1: Fraction of Z+jets events corresponding to different b-tagging categories achieved using the `MV2c10` tagger.

Flavour category	$E_{\mathrm{T}}^{\mathrm{miss}}$: 150-200 GeV	$E_{\mathrm{T}}^{\mathrm{miss}}$: 200-350 GeV	$E_{\mathrm{T}}^{\mathrm{miss}}$: 350-500 GeV	$E_{\mathrm{T}}^{\mathrm{miss}}$: >500 GeV
bb	0.858	0.840	0.805	0.601
bc	0.069	0.073	0.068	0.111
bl	0.059	0.064	0.068	0.111
cc	0.008	0.013	0.028	0.068
cl	0.004	0.007	0.018	0.079
ll	0.002	0.003	0.007	0.079

TABLE 8.2: Fraction of Z+jets events corresponding to different b-tagging categories achieved using the `DL1r` tagger.

A new event selection In preparation for the analysis of whole dataset collected during the Run 2 of the LHC, a complete revaluation of the criteria characterising the baseline event selection has been performed with the aim of retaining only the cuts showing a powerful rejection against background and at the same time reducing the level of complexity of the analysis. While performing this optimisation procedure, several cuts, as $\Delta\phi(j_1,j_2)$ and $\Delta\phi(E_{\mathrm{T}}^{\mathrm{miss}},h)$ (see Section 5.4.1), have found to be inefficient and have been removed from the baseline selection. At the same time new cuts have been introduced, leading to an overall better sensitivity of the search, for both the Z'-2HDM and 2HDM+a (both in gluon-gluon fusion or b-induced production mode) benchmark signal models. In particular, a new variable that works as a proxy of the top quark mass, called $m_T^{b,\mathrm{min/max}}$, is able to provide a very strong rejection power against the semileptonic $t\bar{t}$ background. Assuming that the contribution of semileptonic $t\bar{t}$ background in the 0ℓ SR is due to an unidentified or mis-reconstructed lepton, it is possible to associate to the t and $\bar{t}$ quark the following variable:

$$m_T^{b_{\text{min/max}}} = \sqrt{2p_{\text{T}}^{b_{\text{min/max}}} E_{\text{T}}^{\text{miss}} (1 - \cos\Delta\phi(b_{\text{min/max}}, E_{\text{T}}^{\text{miss}}))} \tag{8.1}$$

where b_{min} and b_{max} represent, respectively, the closest and furthest b-tagged jet with respect to the direction of the $E_{\text{T}}^{\text{miss}}$ vector.

Additional studies have also showed that, in the case of Z'-2HDM signal processes, adding a requirement on the maximum allowed number of jets in the event would lead to a significant increase in sensitivity. However, applying such cut would reduce the sensitivity for the 2HDM+a signals when they originate from gluon-gluon fusion. In order to maximise the sensitivity for a large variety of signal models, the SR can be therefore divided into different jet multiplicities. Preliminary studies have showed that this might be a promising way to achieve an overall good sensitivity. Nevertheless, the impact of such criteria will need to be studied in the context of the final statistical analysis once the new likelihood fit procedure is established.

A Theory uncertainties for the full Run 2 mono-H($b\bar{b}$) analysis

A dedicated estimation of the theory modelling uncertainties is performed for the 2HDM+a signal model which is going to be used as additional benchmark model for the final interpretation of the mono-H($b\bar{b}$) full Run 2 results (see Chapter 8), as well as for the main background sources affecting the SR, which are represented by the $t\bar{t}$ and $Z(\rightarrow \nu\nu)$+jets processes. For all the three processes, the new uncertainties are derived after performing the full SR selection at truth-level, as described in Section 5.10.1, and inclusively in the number of b-tagged jets.

Although so far the theory modelling uncertainties have only been treated as up and down variations of the expected MC normalisation separately in each region, in preparation for the analysis of the full Run 2 dataset it is possible to consider a new approach in which acceptance differences across different regions are instead evaluated as the relative acceptance difference across different regions A and B. The final acceptance uncertainty can therefore be expressed as:

$$\sigma_{\text{acceptance}} = \sqrt{\sum_{i}^{M} \left(1 - \frac{n_A^{\text{var i}} / n_B^{\text{var i}}}{n_A^{\text{nom}} / n_B^{\text{nom}}} \right)^2} \tag{A.1}$$

where M is the total number of variations and n_A (n_B) is the final number of events in the specific region A (B). This new approach is expected to give a bit more freedom to the final likelihood fit as it would allow the normalisation of a specific region A to vary with respect to region B by a certain amount. The set of coupled regions A and B can be represented by: SR $\leftrightarrow$ 1-μ CR, SR $\leftrightarrow$ 2ℓ CR, $E_{\text{T}}^{\text{miss}}$ bin i $\leftrightarrow$ $E_{\text{T}}^{\text{miss}}$ bin j, resolved regime $\leftrightarrow$ merged regime.

As this study focuses on the implementation of truth-level analysis for the 0ℓ SR only relative acceptance uncertainties across different $E_{\text{T}}^{\text{miss}}$ bins, as well as between the resolved and merged 0ℓ region, are considered.

2HDM+a signal model For the 2HDM+a signal process, the error due to variations of the μ_R and μ_F scales, as well as the one on the NNPDF3.0 PDF set, is evaluated, following the same strategy described in Section 5.10.2. The effect of the μ_R and μ_F scale variations is illustrated in Figures A.1-A.2 for two representative 2HDM+a scenarios associated, respectively, to the b-induced production of a A boson with m_A = 1.8 TeV and a a boson with m_a = 150 GeV and the gluon-gluon fusion production of a A boson with m_A = 1.6 TeV and a a boson with m_a = 250 GeV. In the first case, it is possible to appreciate that variations in the μ_R scale have no impact on the nominal distribution, as expected given that b-initiated production of 2HDM+a signal is not a QCD process. On the other hand, the effect of both the μ_R and μ_F scales can be observed in the second case, where the A and a bosons are produced through gluon-gluon fusion.

Tables A.1-A.3 show the variation of the signal acceptance across the different E_T^{miss} regions for each source of uncertainty, while the error on the NNPDF3.0 PDF set is shown in Tables A.2-A.4.

Type of migration	μ_F=0.5	μ_R=0.5	μ_F=2.0	μ_R=2.0	μ_R=0.5,μ_F=0.5	μ_R=2.0,μ_F=2.0
E_T^{miss} bin 1 ↔ E_T^{miss} bin 2	2.6%	–	1.9%	–	2.6%	1.9%
E_T^{miss} bin 2 ↔ E_T^{miss} bin 3	4.7%	–	3.5%	–	4.7%	3.5%
Merged ↔ Resolved	10.2%	–	8.9%	–	10.2%	8.9%

TABLE A.1: Acceptance differences due to the variation of the μ_R and μ_F scales across the four E_T^{miss} bins in the SR for 2HDM+a signal process with m_A = 1.8 TeV and m_a = 150 GeV from an initial state of b-quarks.

E_T^{miss} region	PDF relative uncertainty
E_T^{miss} bin 1	0.42%
E_T^{miss} bin 2	0.31%
E_T^{miss} bin 3	2.22%
E_T^{miss} bin 4	6.90%

TABLE A.2: PDF error for each E_T^{miss} bin of SR for 2HDM+a signal process with m_A = 1.8 TeV and m_a = 150 GeV from an initial state of b-quarks.

Type of migration	μ_F=0.5	μ_R=0.5	μ_F=2.0	μ_R=2.0	μ_R=0.5,μ_F=0.5	μ_R=2.0,μ_F=2.0
E_T^{miss} bin 1 ↔ E_T^{miss} bin 2	2.3%	0.7%	1.9%	0.6%	1.6%	1.4%
E_T^{miss} bin 2 ↔ E_T^{miss} bin 3	3.5%	1.0%	3.0%	0.9%	2.5%	2.2%
Merged ↔ Resolved	4.3%	1.3%	4.0%	1.1%	3.1%	2.9%

TABLE A.3: Acceptance differences due to the variation of the μ_R and μ_F scales across the four E_T^{miss} bins in the SR for 2HDM+a signal process with m_A = 1.6 TeV and m_a = 250 GeV originating from a gluon-gluon fusion process.

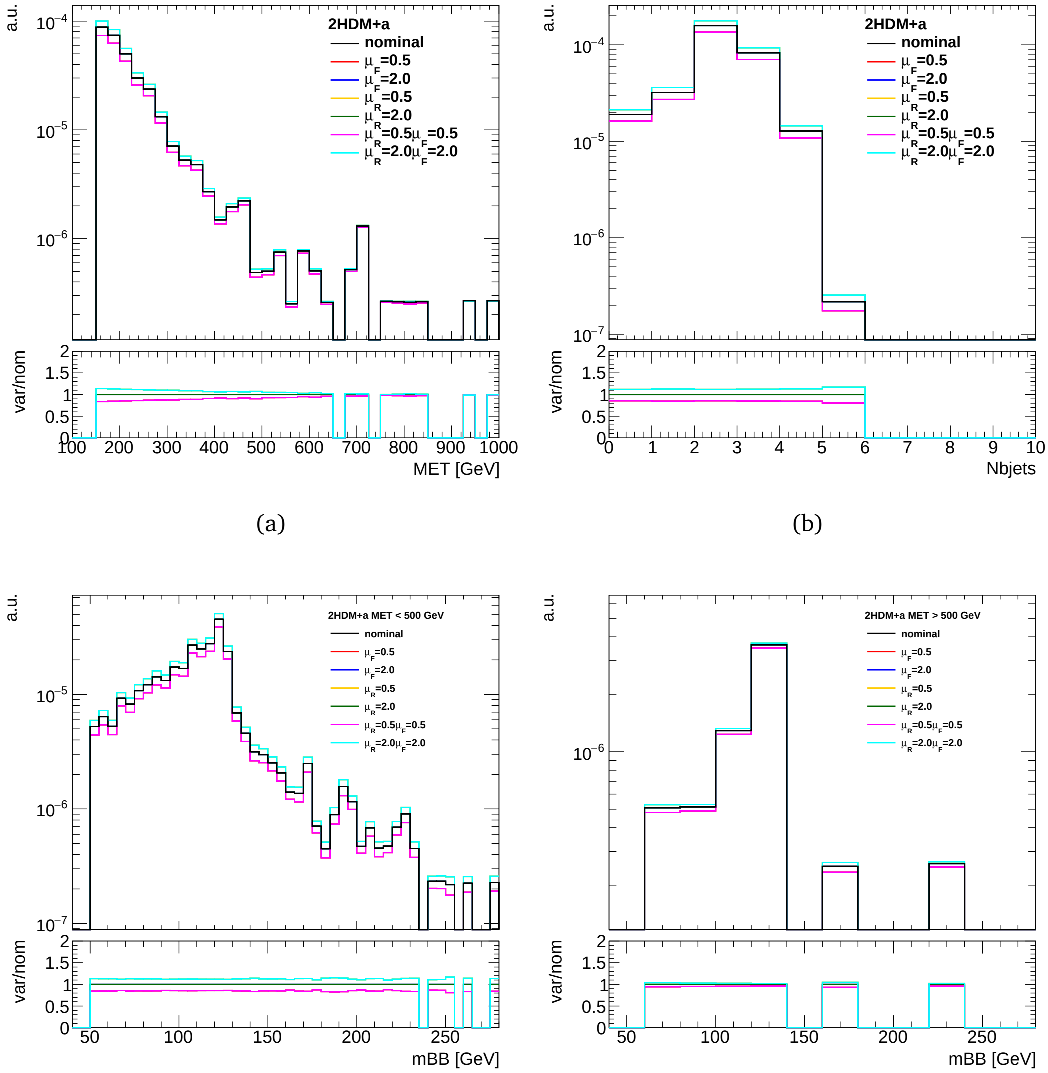

(a) (b)

(c) (d)

FIGURE A.1: Comparison of the distribution of E_T^{miss}, number of b-tagged jets and Higgs candidate mass between the nominal case and each systematic variation for 2HDM+a signal events generated for m_A = 1.8 TeV and m_a = 150 GeV from an initial state of b-quarks. At the top, distribution of the E_T^{miss} and number of b-tagged jets. At the bottom, distribution of Higgs candidate mass for events in the resolved region (E_T^{miss} < 500 GeV) on the left, and in the merged region (E_T^{miss} > 500 GeV) on the right. The nominal sample is shown in black, while the coloured lines represent the different sources of theory uncertainty. All distributions are inclusive in the number of b-tagged jets.

$t\bar{t}$ background Following the same procedure discussed in Section 6.1.2, in the context of the b-tagging calibration of VR track jets based on $t\bar{t}$ events, in order to estimate the uncertainty on the modelling of $t\bar{t}$ processes the following variations are considered:

- matrix element, through a comparison of the aMC@NLO with respect to the nominal POWHEGBOX generator,

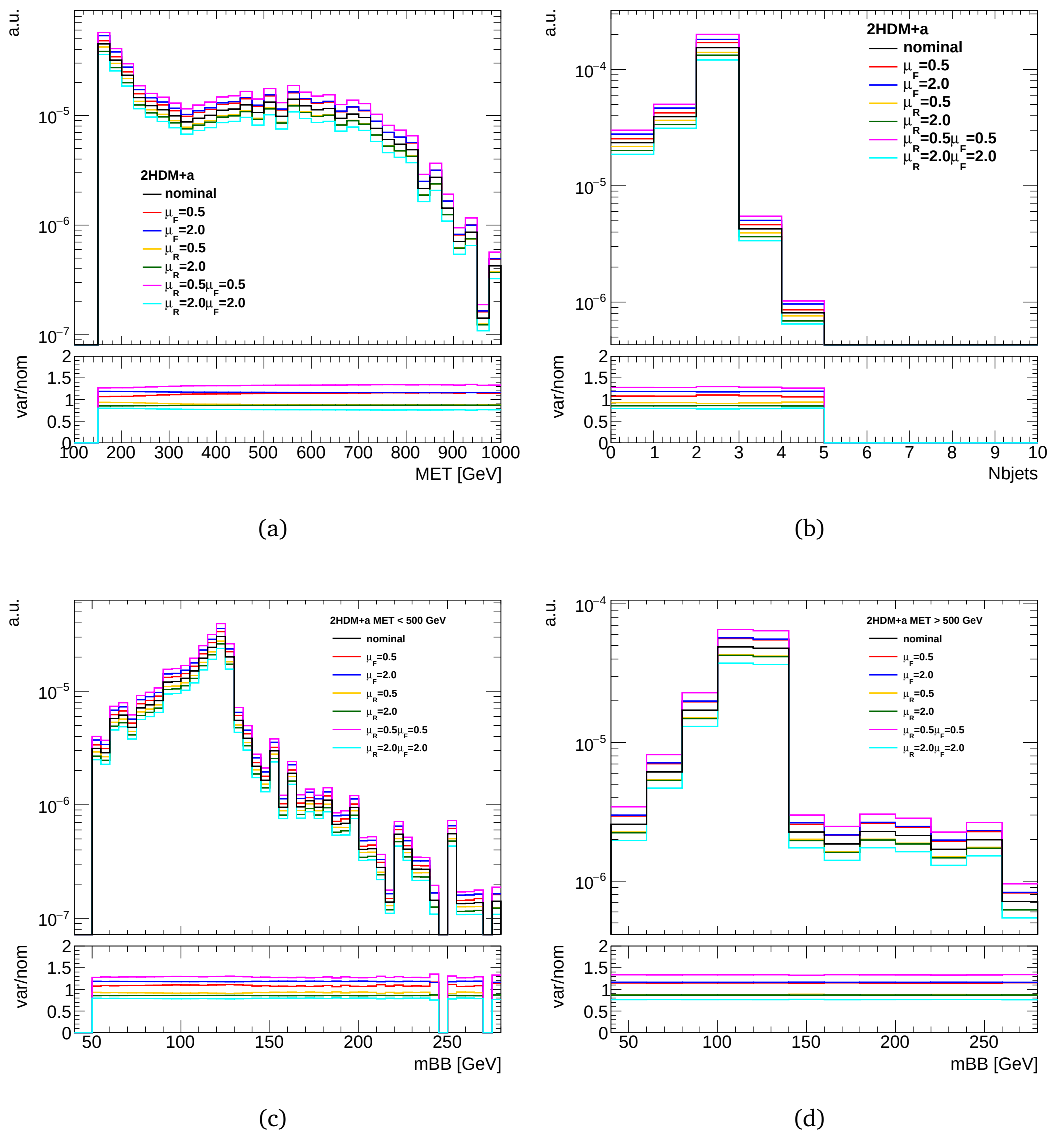

FIGURE A.2: Comparison of the distribution of $E_{\mathrm{T}}^{\mathrm{miss}}$, number of b-tagged jets and Higgs candidate mass between the nominal case and each systematic variation for 2HDM+a signal events generated for m_A = 1.6 TeV and m_a = 250 GeV from a gluon-gluon fusion process. At the top, distribution of the $E_{\mathrm{T}}^{\mathrm{miss}}$ and number of b-tagged jets. At the bottom, distribution of Higgs candidate mass for events in the resolved region ($E_{\mathrm{T}}^{\mathrm{miss}} < 500$ GeV) on the left, and in the merged region ($E_{\mathrm{T}}^{\mathrm{miss}} > 500$ GeV) on the right. The nominal sample is shown in black, while the coloured lines represent the different sources of theory uncertainty. All distributions are inclusive in the number of b-tagged jets.

- parton shower and hadronisation, through a comparison of the POWHEGBOX V2 with respect to the nominal POWHEGBOX generator,
- ISR and FSR, through internal weights available in the baseline POWHEGBOX MC sample.

For simplicity, the uncertainties related to the PDF choice are ignored in this study as they are expected to have a relatively small impact (see also Section 6.1.6). Figure A.3

E_T^{miss} region	PDF relative uncertainty
E_T^{miss} bin 1	0.83%
E_T^{miss} bin 2	0.29%
E_T^{miss} bin 3	2.1%
E_T^{miss} bin 4	3.3%

TABLE A.4: PDF error for each E_T^{miss} bin of SR for 2HDM+a signal process with m_A = 1.6 TeV and m_a = 250 GeV originating from a gluon-gluon fusion process.

shows a comparison for some relevant variables of the different sources of uncertainty with respect to the nominal case. The largest deviation in the E_T^{miss} and m_h shape is caused by the different modelling of the parton shower and hadronisation processes, representing the dominant source of uncertainty also on the acceptance across E_T^{miss} regions, as illustrated in Figure A.5.

Type of migration	ISR down	ISR up	FSR down	FSR up	Matrix Element	Parton Shower/Hadronisation
E_T^{miss} bin 1 $\leftrightarrow$ E_T^{miss} bin 2	0.7%	3.0%	0.7%	0.8%	3.5%	28.8%
E_T^{miss} bin 2 $\leftrightarrow$ E_T^{miss} bin 3	1.5%	2.3%	6.6%	0.6%	1.5%	30.5%
Merged $\leftrightarrow$ Resolved	8.5%	4.2%	17.2%	3.2%	22.7%	5.4%

TABLE A.5: Acceptance differences across the four E_T^{miss} bins in the SR for $t\bar{t}$ processes.

$Z(\to \nu\nu)$+jets background For the evaluation of the modelling uncertainties associated to the $Z(\to \nu\nu)$ plus jets processes, two sources of uncertainty are considered:

- variations on the μ_R and μ_F scales, through internal weights available in the nominal SHERPA V2.2.1 sample,
- parton shower/hadronisation/PDF, through a comparison of the nominal SHERPA V2.2.1 sample with respect to the `MadGraph` generator.

Again, the comparison of the distribution of E_T^{miss}, m_h and number of b-tagged jets between the nominal case and each variation is shown in Figure A.4. The largest uncertainty comes from the direct MC comparison with respect to the MADGRAPH generator, which shows higher tails in E_T^{miss} and m_h with respect to the SHERPA events. Similarly to what has been shown earlier, Tables A.6 to A.8 show the relative acceptance difference across the different E_T^{miss} regions, which is dominated by the comparison between SHERPA V2.2.1 and MADGRAPH generators. As the normalisation of the $Z(\to \nu\nu)$ plus jets background in the final likelihood fit is treated differently depending on the flavour composition of the event, different numbers are derived for Z+ll, cl and HF (bb, bc, bl, cc) jets events.

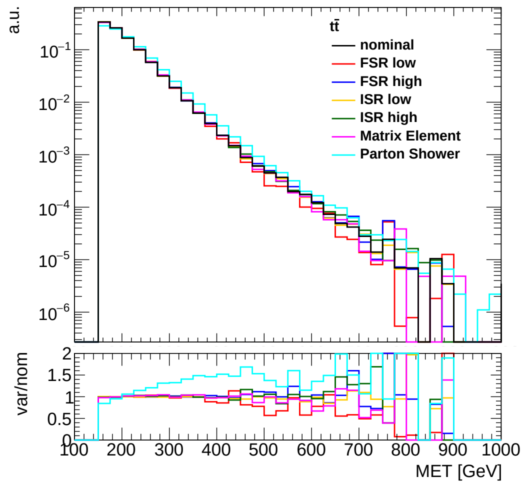

(a)

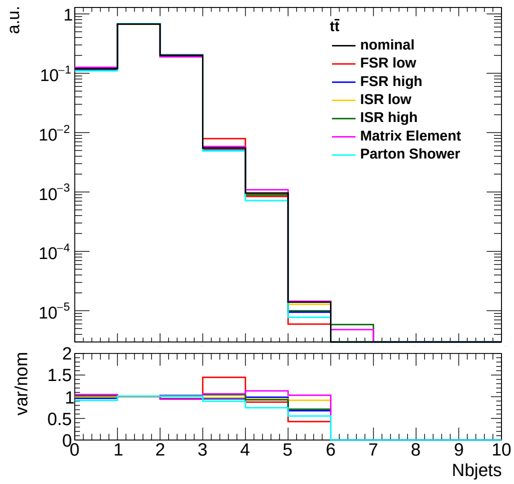

(b)

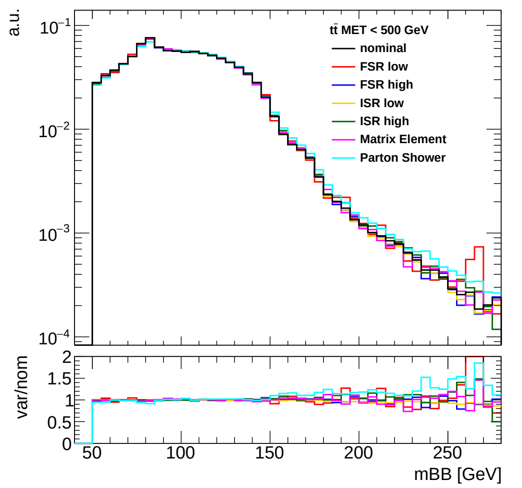

(c)

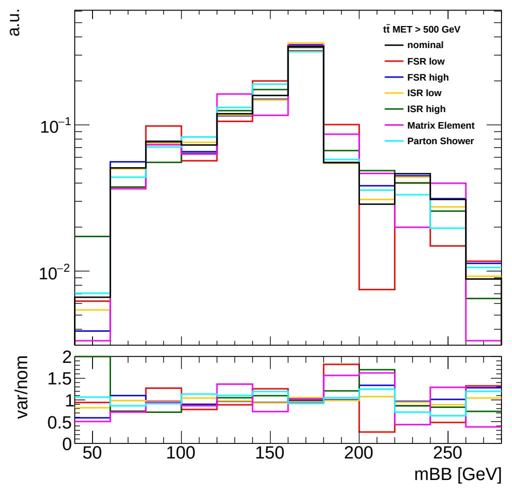

(d)

FIGURE A.3: Comparison of the distribution of $E_{\mathrm{T}}^{\mathrm{miss}}$, number of b-tagged jets and Higgs candidate mass between the nominal case and each systematic variation for $t\bar{t}$ events. At the top, distribution of the $E_{\mathrm{T}}^{\mathrm{miss}}$ and number of b-tagged jets. At the bottom, distribution of Higgs candidate mass for events in the resolved region ($E_{\mathrm{T}}^{\mathrm{miss}} < 500$ GeV) on the left, and in the merged region ($E_{\mathrm{T}}^{\mathrm{miss}} > 500$ GeV) on the right. The nominal sample is shown in black, while the coloured lines represent the different sources of theory uncertainty. All distributions are inclusive in the number of b-tagged jets and scaled to unity in order to isolate the shape differences.

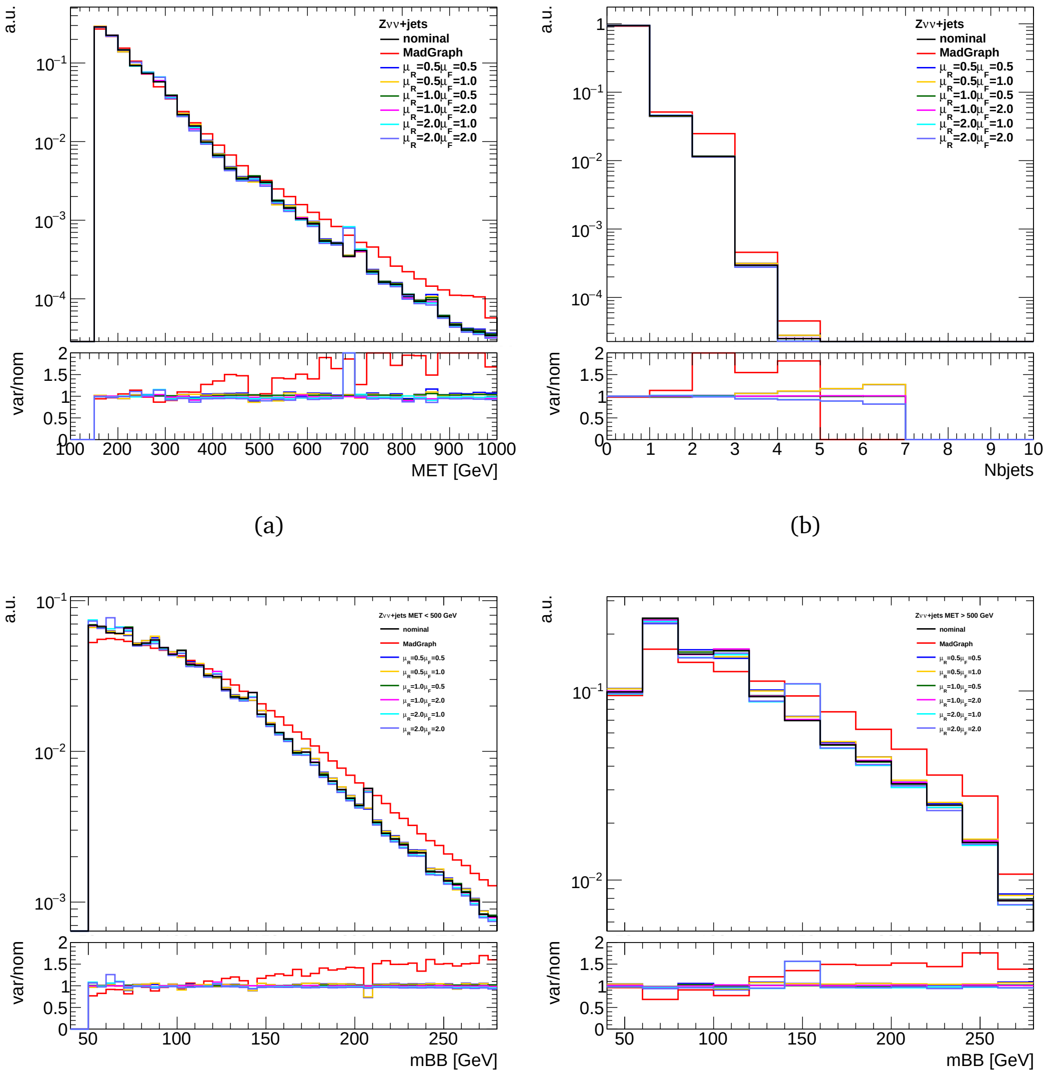

(a) (b)

(c) (d)

FIGURE A.4: Comparison of the distribution of $E_{\mathrm{T}}^{\mathrm{miss}}$, number of b-tagged jets and Higgs candidate mass between the nominal case and each systematic variation for $Z(\rightarrow \nu\nu)$+jets events. At the top, distribution of the $E_{\mathrm{T}}^{\mathrm{miss}}$ and number of b-tagged jets. At the bottom, distribution of Higgs candidate mass for events in the resolved region ($E_{\mathrm{T}}^{\mathrm{miss}} < 500$ GeV) on the left, and in the merged region ($E_{\mathrm{T}}^{\mathrm{miss}} > 500$ GeV) on the right. The nominal sample is shown in black, while the coloured lines represent the different sources of theory uncertainty. All distributions are inclusive in the number of b-tagged jets and scaled to unity in order to isolate the shape differences.

Type of uncertainty	E_T^{miss} bin 1 ↔ E_T^{miss} bin 2	E_T^{miss} bin 2 ↔ E_T^{miss} bin 3	Merged ↔ Resolved
μ_R=0.5,μ_F=0.5	1.9%	2.0%	0.2%
μ_R=0.5,μ_F=1.0	2.2%	4.1%	1.3%
μ_R=1.0,μ_F=0.5	1.0%	1.6%	1.2%
μ_R=1.0,μ_F=2.0	0.3%	4.9%	2.8%
μ_R=2.0,μ_F=1.0	3.2%	5.4%	1.4%
μ_R=2.0,μ_F=2.0	5.9%	12.5%	2.9%
MadGraph	7.0%	22.1%	30.0%

TABLE A.6: Acceptance differences across the four E_T^{miss} bins in the SR for $Z(\rightarrow \nu\nu)+ll$ jets processes.

Type of uncertainty	E_T^{miss} bin 1 ↔ E_T^{miss} bin 2	E_T^{miss} bin 2 ↔ E_T^{miss} bin 3	Merged ↔ Resolved
μ_R=0.5,μ_F=0.5	3.2%	2.1%	6.1%
μ_R=0.5,μ_F=1.0	2.9%	0.3%	4.0%
μ_R=1.0,μ_F=0.5	0.2%	2.6%	2.9%
μ_R=1.0,μ_F=2.0	0.5%	2.3%	3.0%
μ_R=2.0,μ_F=1.0	4.6%	9.1%	8.0%
μ_R=2.0,μ_F=2.0	3.8%	10.2%	10.4%
MadGraph	12.6%	15.5%	31.6%

TABLE A.7: Acceptance differences across the four E_T^{miss} bins in the SR for $Z(\rightarrow \nu\nu)+cl$ processes.

Type of uncertainty	E_T^{miss} bin 1 ↔ E_T^{miss} bin 2	E_T^{miss} bin 2 ↔ E_T^{miss} bin 3	Merged ↔ Resolved
μ_R=0.5,μ_F=0.5	2.2%	3.3%	3.1%
μ_R=0.5,μ_F=1.0	0.8%	2.8%	1.0%
μ_R=1.0,μ_F=0.5	1.6%	0.6%	2.7%
μ_R=1.0,μ_F=2.0	0.2%	0.4%	2.1%
μ_R=2.0,μ_F=1.0	2.4%	1.3%	1.6%
μ_R=2.0,μ_F=2.0	2.8%	1.9%	3.4%
MadGraph	7.0%	19.7%	20.2%

TABLE A.8: Acceptance differences across the four E_T^{miss} bins in the SR for $Z(\rightarrow \nu\nu)$+HF jets processes.

B *b*-tagging calibration of VR track jets

B.1 p_T mismodelling studies

Shower weights variations As concluded from the studies presented in Section 6.1.6, the jet p_T data/MC mismodelling seems to be most evident in the case of heavy flavour jets (similar studies in the context of the charm and light jet calibrations support this observation). Therefore, it is worth investigating, through the internal weights available in the PowhegBox v2+Pythia 8.230 $t\bar{t}$ nominal MC sample, whether the FSR variations are sensitive to this issue. For this purpose, the nominal $t\bar{t}$ p_T spectrum is compared with the FSR up and down variations, as shown in Figure B.1-B.2. The differences due to such variations are too tiny and do not seem to have any impact on the jet p_T shape.

Figures B.3 to B.5 show instead the results of the η and μ dependence studies, as well as the distribution of the constituent tracks inside the VR track jets, for the case of the subleading VR track jet.

B.2 Ghost association studies

In the following, a comparison between the *standard* and *ghost tag* VR track jet collection for a RS graviton sample, as shown in Section 6.3, for the case of a graviton mass equal to 900 GeV.

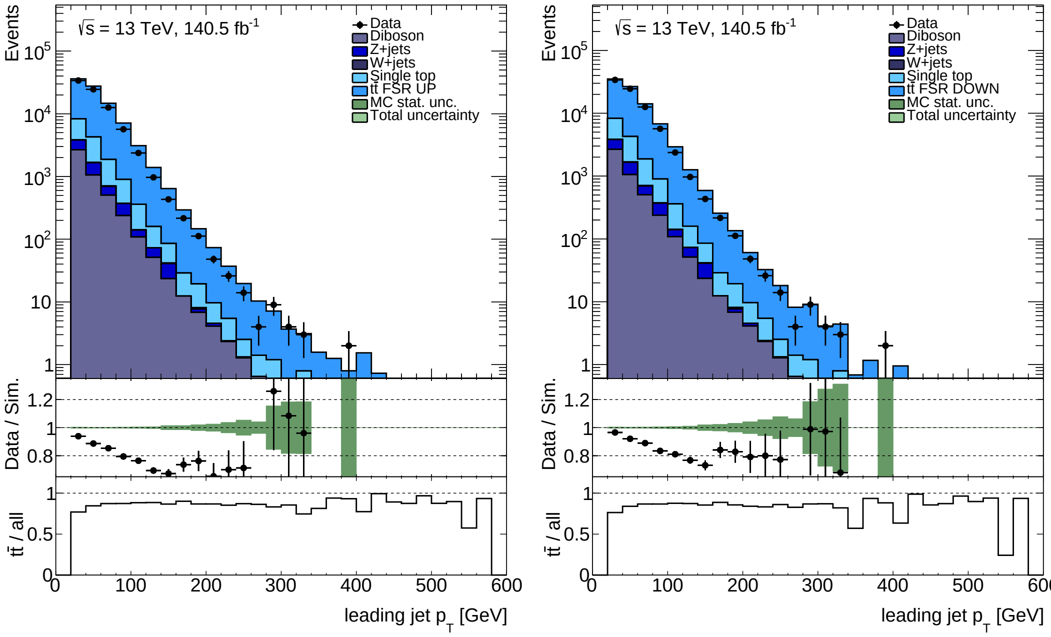

(a) (b)

FIGURE B.1: Distribution of the leading VR track jet p_{T}, comparing the effect of the up (on the left) and down (on the right) variations of FSR on the $t\bar{t}$ MC sample. The green band shows only the effect of the statistical uncertainty.

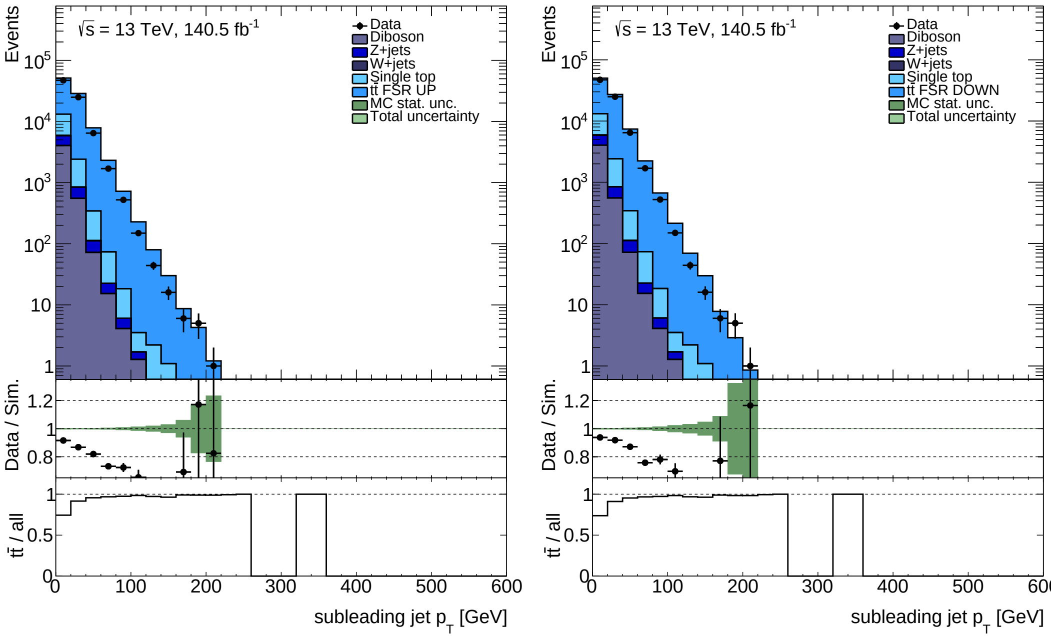

(a) (b)

FIGURE B.2: Distribution of the subleading VR track jet p_{T}, comparing the effect of the up (on the left) and down (on the right) variation of FSR on the $t\bar{t}$ MC sample. The green band shows only the effect of the statistical uncertainty.

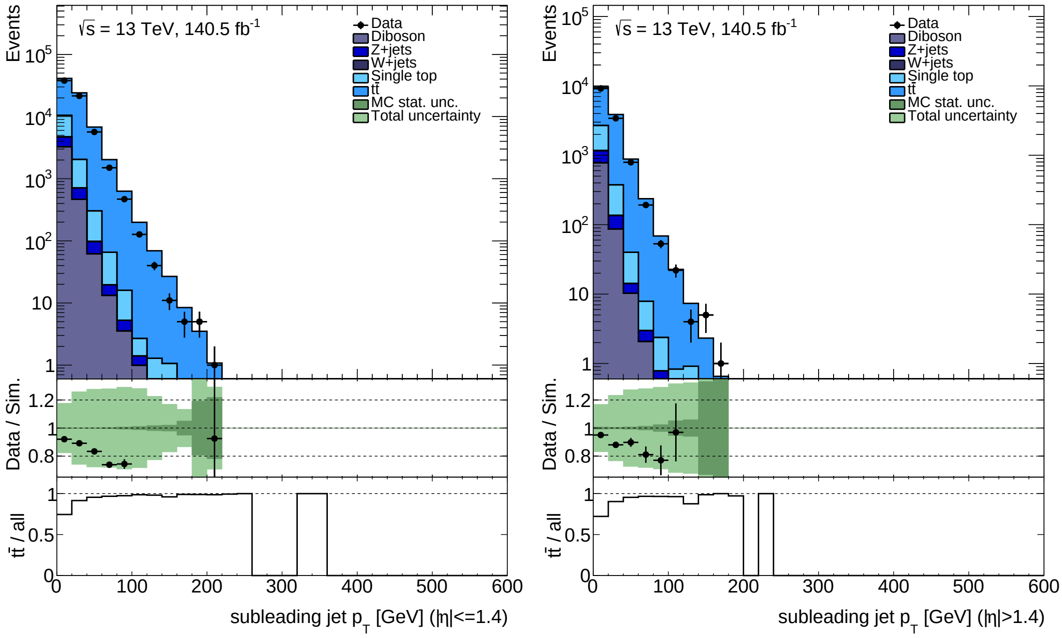

(a) (b)

FIGURE B.3: Data/MC comparison of the subleading VR track jet p_T distribution in the two different regions with $|\eta| \leqslant 1.4$ (on the left) and $|\eta| > 1.4$ (on the right). The green band shows the effect of the detector-related and $t\bar{t}$ modelling systematic uncertainties.

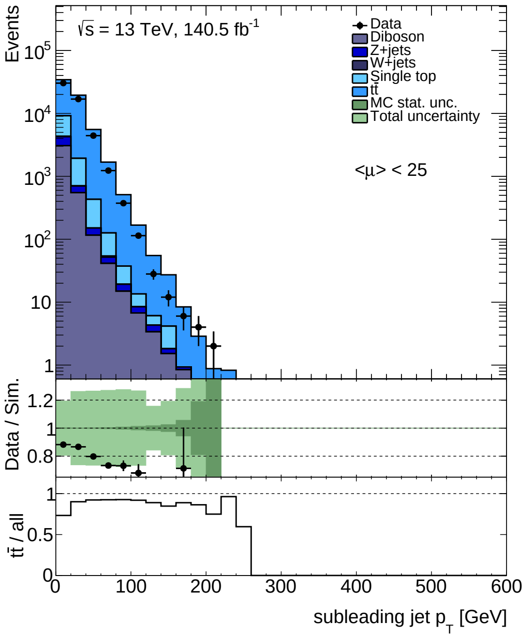

(a)

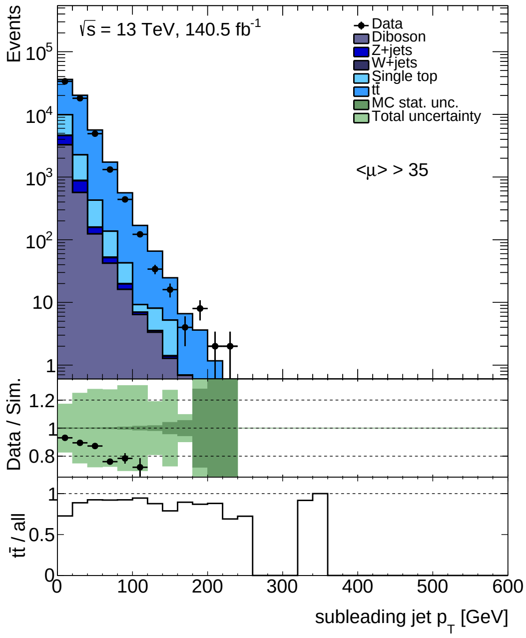

(b)

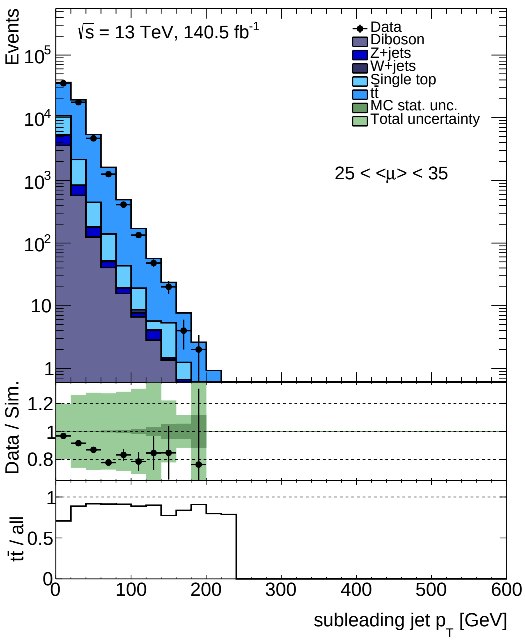

(c)

FIGURE B.4: Data/MC comparison of the subleading VR track jet p_T distribution in the low, medium, high $\langle \mu \rangle$ regimes. The green band shows the effect of the detector-related and $t\bar{t}$ modelling systematic uncertainties.

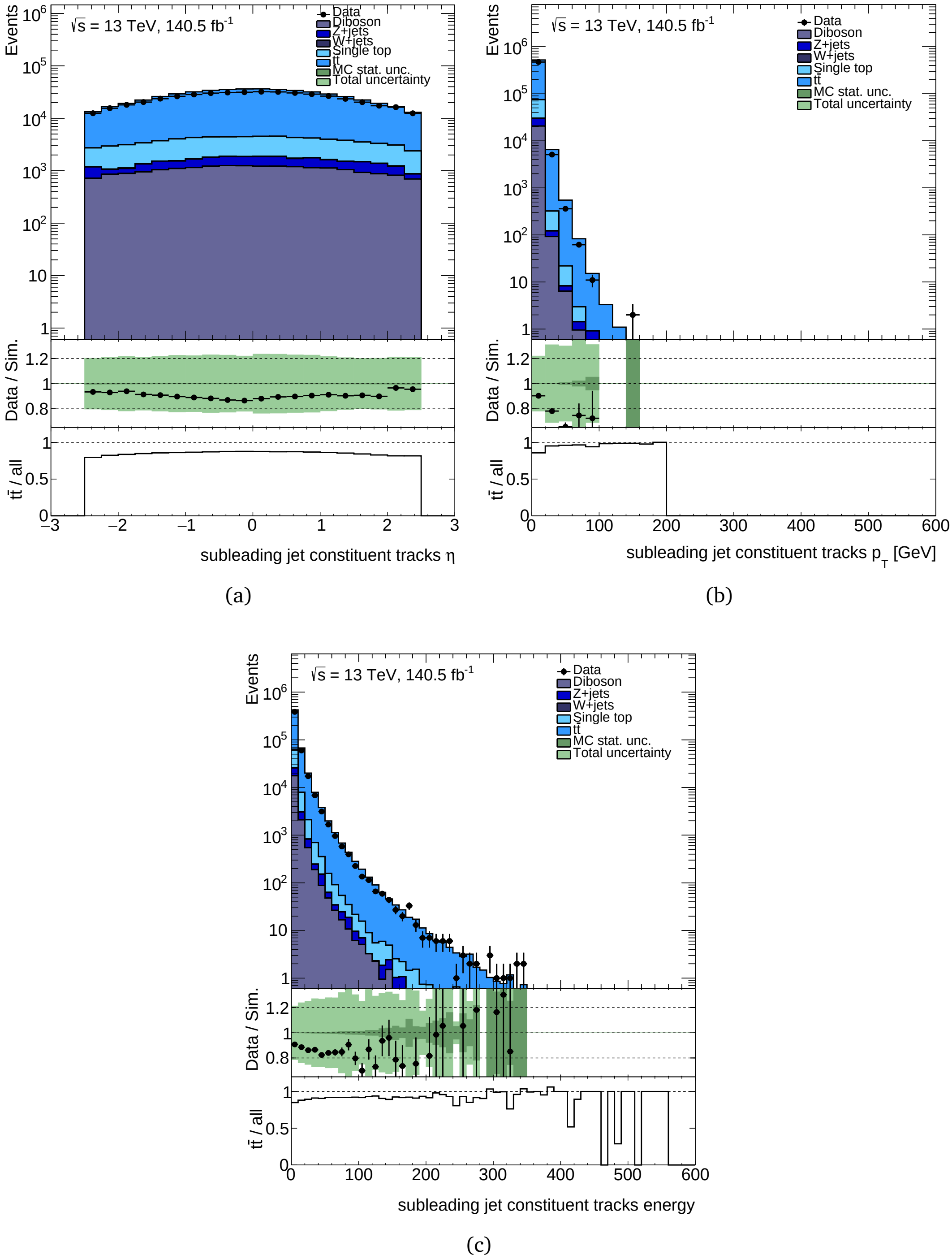

FIGURE B.5: Data/MC comparisons of η, ϕ, p_{T} and energy of the tracks contained the subleading VR track jet. The green band shows the effect of the detector-related and $t\bar{t}$ modelling systematic uncertainties.

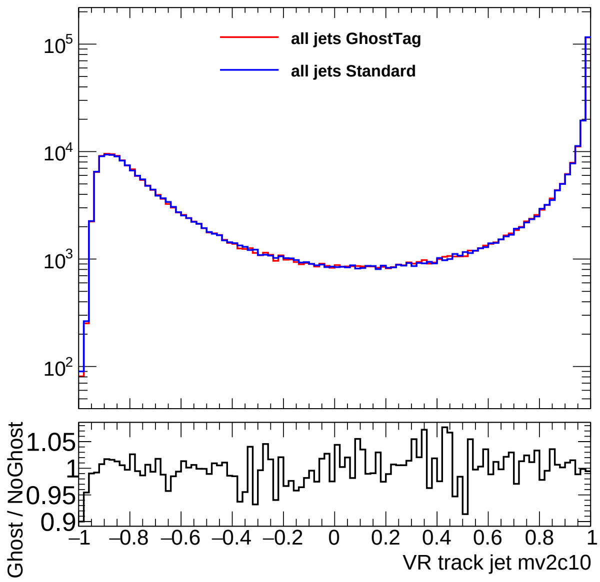

(a)

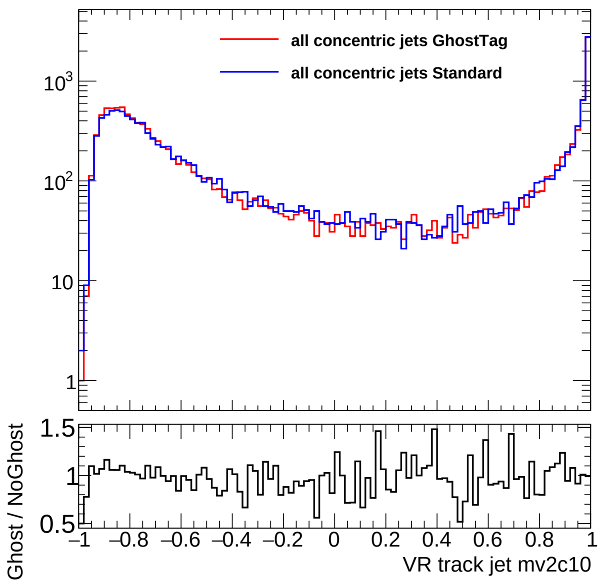

(b)

FIGURE B.6: `MV2c10` distribution of the VR track jets associated either to the leading or subleading large-R jet in the event. At the top, all jets are shown. At the bottom, only concentric jets ($\Delta R < R_{\text{min}}$) are shown.

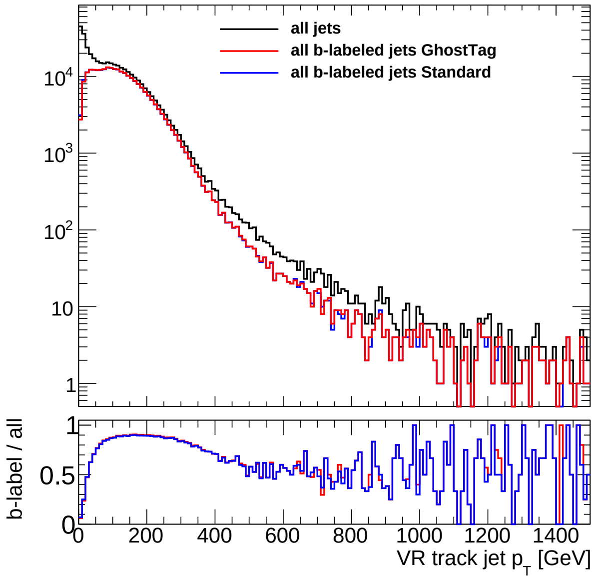

(a)

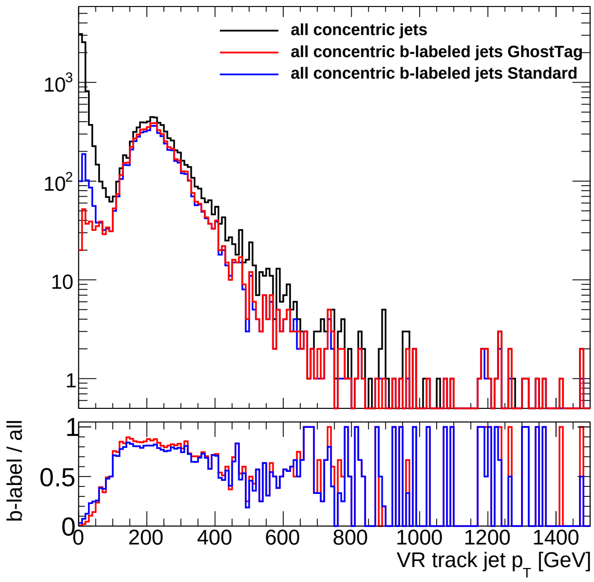

(b)

FIGURE B.7: p_{T} distribution of the VR track jets associated either to the leading or subleading large-R jet in the event, showing the fraction of jets labelled as b-jets at truth level. At the top, all jets are shown. At the bottom, only concentric jets ($\Delta R < R_{\mathrm{min}}$) are shown.

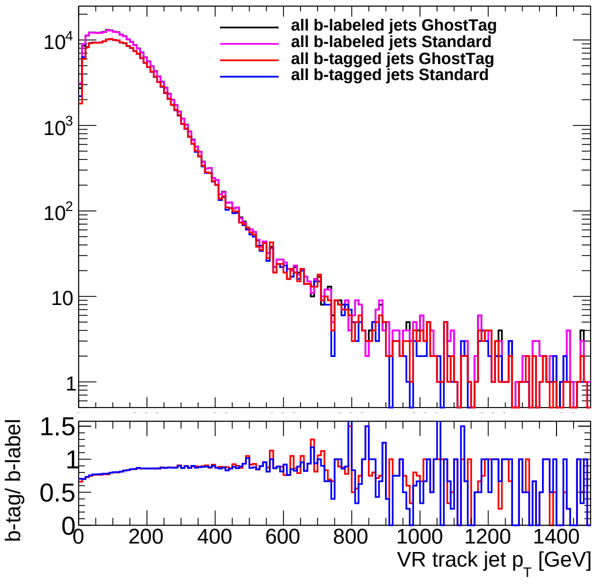

(a)

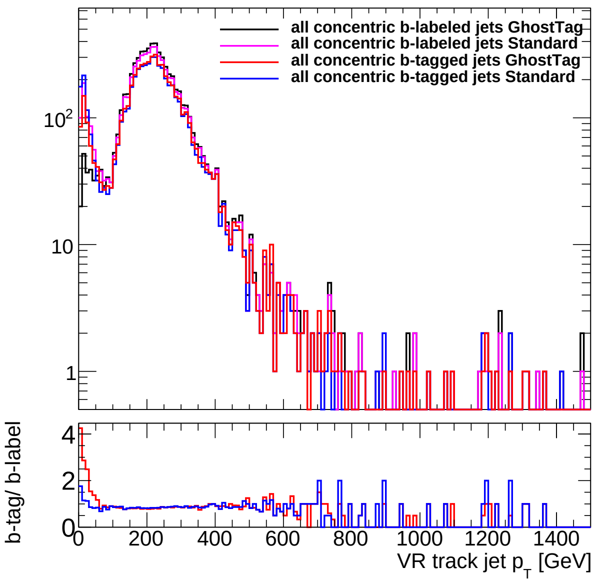

(b)

FIGURE B.8: p_{T} distribution of the VR track jets associated either to the leading or subleading large-R jet in the event, showing both the b-tagged jets (77% WP) and truth labelled b-jets, in the two different schemes. At the top, all jets are shown. At the bottom, only concentric jets ($\Delta R < R_{\min}$) are shown.

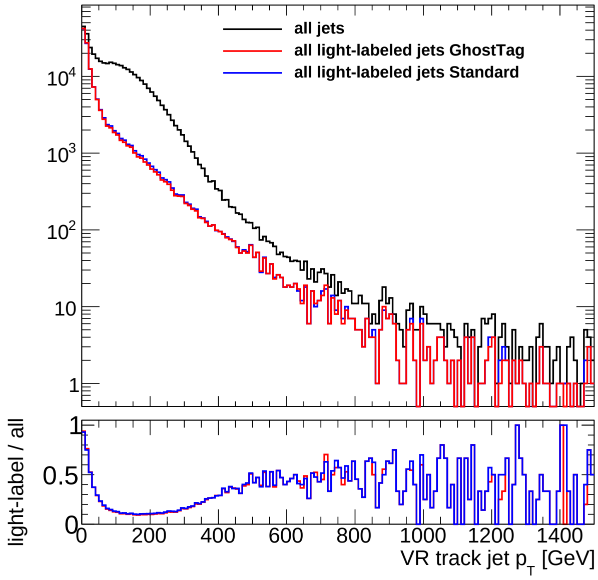

(a)

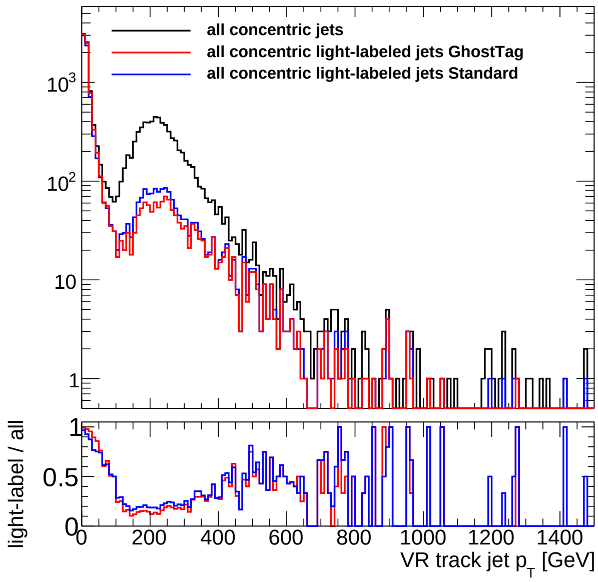

(b)

FIGURE B.9: p_{T} distribution of the VR track jets associated either to the leading or subleading large-R jet in the event, showing the fraction of jets labelled as light-jets at truth level. At the top, all jets are shown. At the bottom, only concentric jets ($\Delta R < R_{\mathrm{min}}$) are shown.

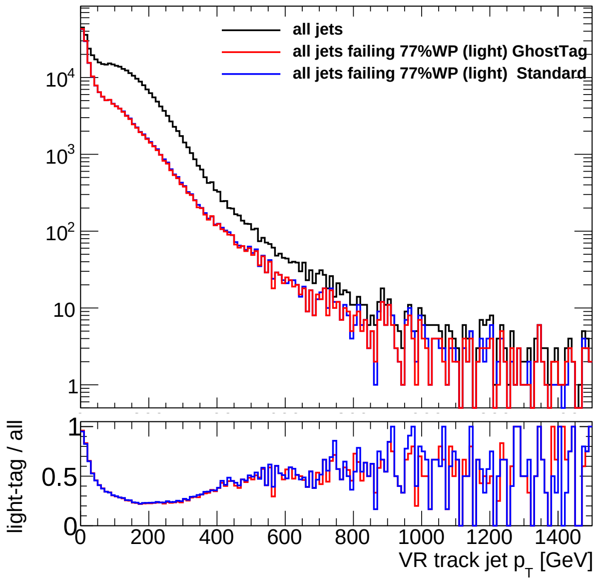

(a)

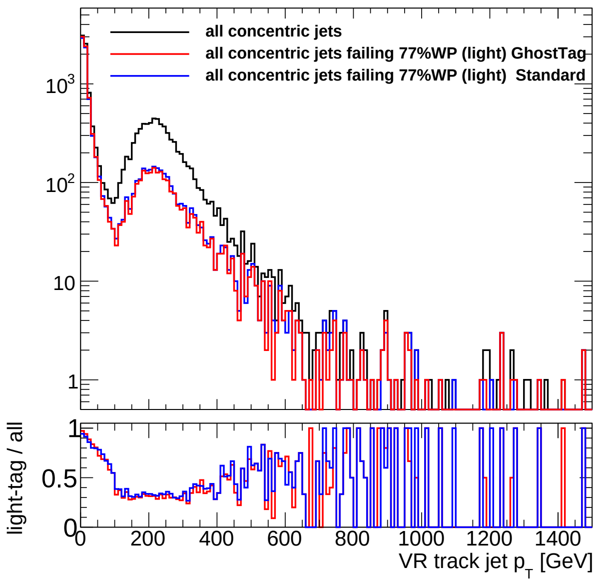

(b)

FIGURE B.10: p_{T} distribution of the VR track jets associated either to the leading or subleading large-R jet in the event, showing both the jets failing the 77% MV2c10 WP and truth labelled light jets, in the two different schemes. At the top, all jets are shown. At the bottom, only concentric jets ($\Delta R < R_{\mathrm{min}}$) are shown.

C Additional material for the full Run 2 mono-H($b\bar{b}$) analysis

Following the strategy described in Section 8, the new event selection criteria are summarised in Table C.1.

Resolved	**Merged**
lowest unprescaled $E_{\mathrm{T}}^{\mathrm{miss}}$ trigger	
veto on baseline light leptons and τ-leptons	
extended τ-veto	
$E_{\mathrm{T}}^{\mathrm{miss}} > 150$ GeV	
min $\Delta\Phi(E_{\mathrm{T}}^{\mathrm{miss}}$,Central+Forward jets$_{1,2,3}) > 20^{\circ}$	
$E_{\mathrm{T}}^{\mathrm{miss}} < 500$ GeV	$E_{\mathrm{T}}^{\mathrm{miss}} > 500$ GeV
N(central small-R jets) ≥ 2	N(central large-R jets) ≥ 1
N(b-tagged small-R jets) ≥ 1	N(b-tagged associated track jets)≥ 1
$\mathcal{S} > 12$	—
p_{T} (Higgs candidate) > 100 GeV if $E_{\mathrm{T}}^{\mathrm{miss}} < 350$ GeV p_{T} (Higgs candidate) > 300 GeV if $E_{\mathrm{T}}^{\mathrm{miss}} \geq 350$ GeV	— —
$m_T^{\mathrm{b,min}} > 170$ GeV	—
$m_T^{\mathrm{b,max}} > 200$ GeV	—
b-tag requirement on	
small-R jets	VR track jets

TABLE C.1: Summary of the resolved and merged event selection applied in the 0ℓ channel. $\mathcal{S}$ denotes the object based $E_{\mathrm{T}}^{\mathrm{miss}}$ significance.

C.1 The DL1r *b*-tagging algorithm

Figure C.1 shows the comparison, in terms of expected signal significance, between the DL1r and MV2c10 taggers for both the resolved and merged region using events with exactly two *b*-tagged jets. The same results are shown for events with a Higgs candidate mass inside the [70, 140] GeV window in Figure C.2.

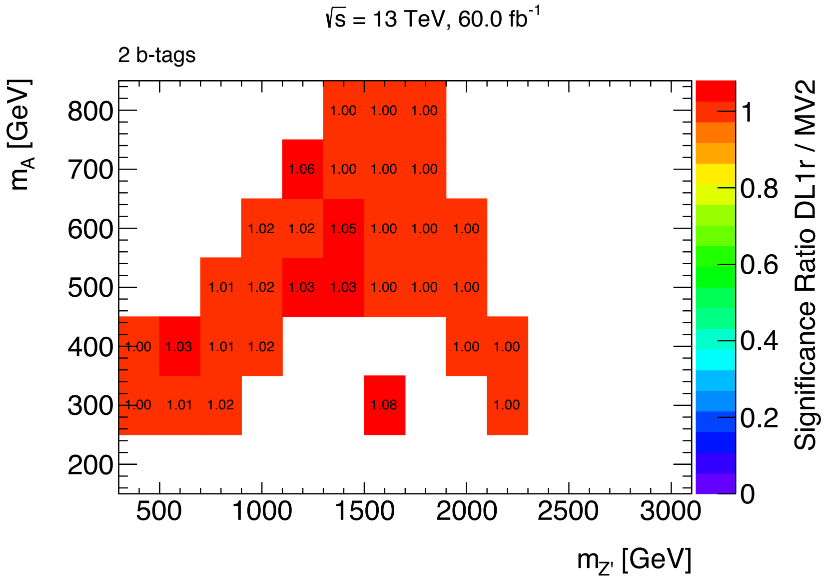

(a)

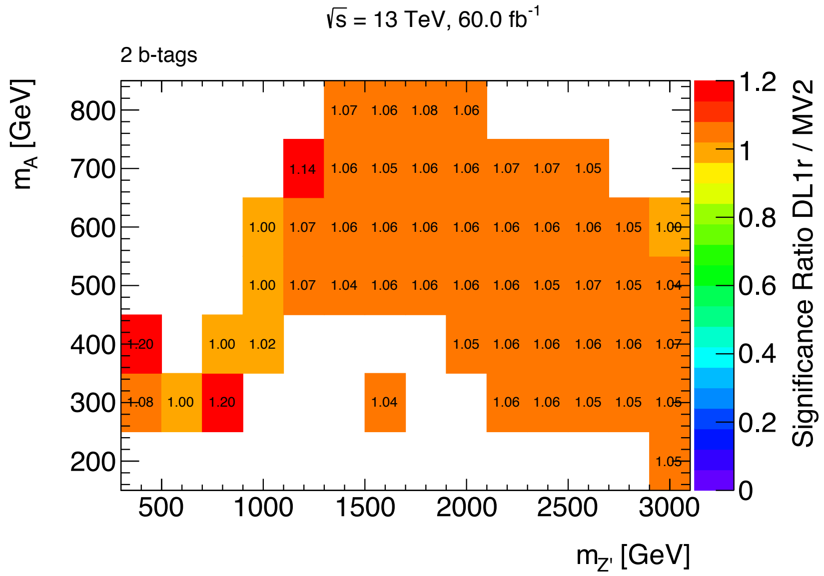

(b)

FIGURE C.1: Ratio of the expected signal significance achieved by the usage of the DL1r tagger with respect to the MV2c10, which has been adopted in all the previous iterations of the mono-H($b\bar{b}$) analysis, for the case of the resolved region (on the left) and merged region (on the right). Events are required to have exactly two *b*-tagged jets.

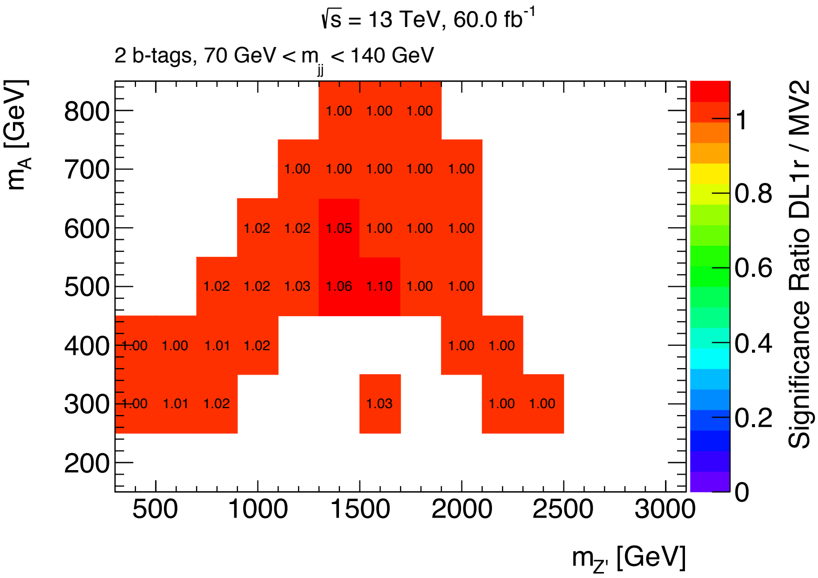

(a)

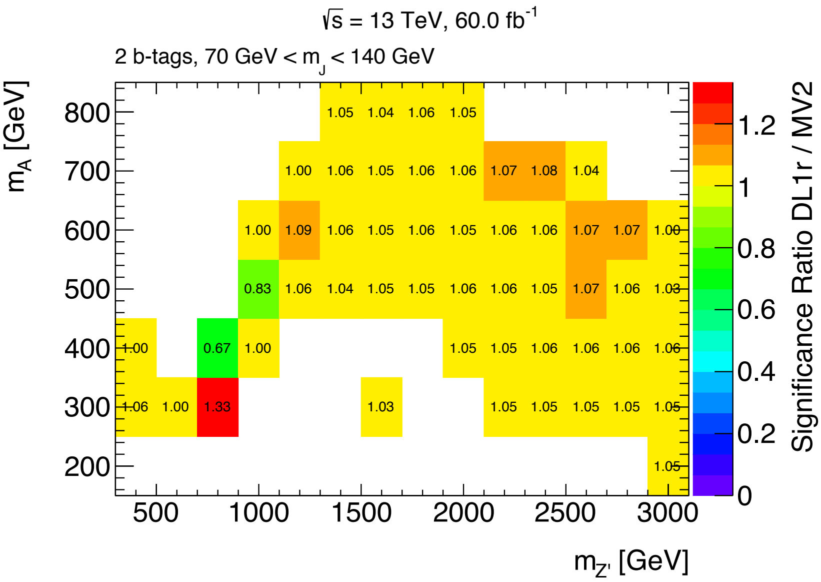

(b)

FIGURE C.2: Ratio of the expected signal significance achieved by the usage of the `DL1r` tagger with respect to the `MV2c10`, which has been adopted in all the previous iterations of the mono-H($b\bar{b}$) analysis, for the case of the resolved region (on the left) and merged region (on the right). Events are required to be inside the Higgs mass window m_h = [70,140] GeV and to have exactly two b-tagged jets.

Summary

Have you ever played *hide-and-seek*?

It may be a long shot but I believe this game works a bit like the search for Dark Matter at the Large Hadron Collider (LHC). The seeker can win the game only if *all* the hidden players have been found. Catching the majority of them is not enough. Well, when a proton-proton collision occurs at the LHC a large number of particles is produced, and they all give rise to a different signal in our detectors. For each of these particles, a list of the relevant properties is filled out and used to trace back the event they actually originated from. Only after *all* the *visible* particles have been recognised, we can tell whether something is still *missing*... or rather it is *invisible*.

The Standard Model (SM) of particle physics is the quantum relativistic theory that is able to explain three of the four interactions between the fundamental constituents of matter. We know that atomic nuclei can exist because of the strong force that confines quarks and gluons inside the proton. Moreover, the knowledge of the electroweak force allowed us to understand the principles of the radioactive decays and the interaction between different families of quarks and leptons. The missing piece of the theory was found in 2012, when the Higgs boson was discovered by the ATLAS and CMS experiments at the LHC. The discovery of the Higgs boson has been essential in order to acknowledge the robustness of the SM theory, which otherwise would have not been able to explain how fundamental particles acquire their mass. The list of the subatomic constituents of matter known up to the present day, after the inclusion of the Higgs boson, is illustrated in Figure S.1.

Having discovered such a special particle like the Higgs boson was indeed a great achievement but it might still be heartbreaking to realise that all the matter that we are able to explain within the Standard Model framework accounts for just about 5% of the whole Universe!

In fact, we still ignore the nature of the 95% of the world around us. We only know that more than 80% of the matter in the Universe should be made of Dark Matter, as inferred from astrophysical and cosmological observations. It is *dark* because it does not seem to interact with ordinary matter, therefore it results as undetectable by our current instruments. Nevertheless, such information turns out to be very precious: if Dark Matter is supposed to interact very weakly with ordinary matter, it means that if we were able to produce Dark Matter at the LHC we should observe an imbalance in the energy measured by the detector. At the LHC, the incoming protons travel along the beam line, therefore in the initial state the momentum in the transverse plane is zero... and it will remain zero as the total

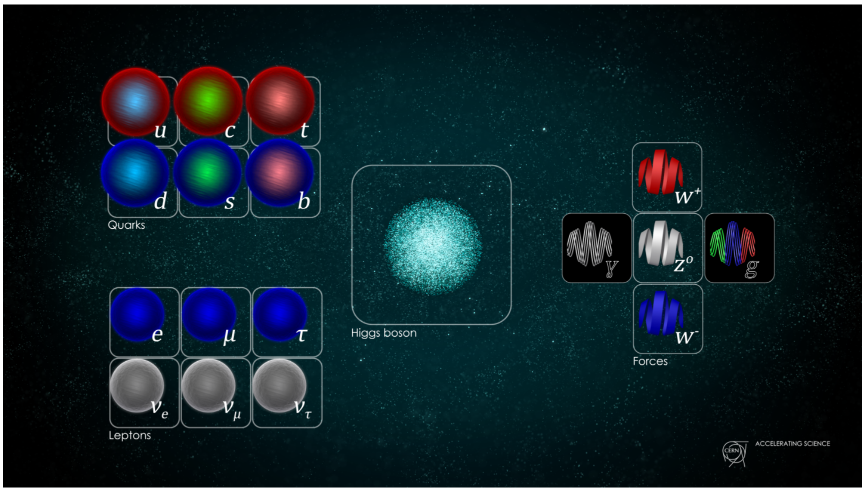

FIGURE S.1: Scheme of all elementary particles predicted by the Standard Model of elementary particles. Figure taken from Ref. [183].

momentum must be conserved. If the measurement indicates otherwise, there must be particles escaping detection (like neutrinos).

The negative sum of the momenta of all the particles in the transverse plane of the detector is called *missing transverse momentum* and it is usually referred to as $E_{\mathrm{T}}^{\mathrm{miss}}$. The search for Dark Matter at the LHC follows the strategy of looking for events with a large amount of $E_{\mathrm{T}}^{\mathrm{miss}}$ that cannot be related to any Standard Model particle. Of course, if there were only Dark Matter in the event we would not see anything: the presence of an additional *measurable* object X allows us to select the interesting event. This is what we usually refer to as a $E_{\mathrm{T}}^{\mathrm{miss}}$ plus X signature.

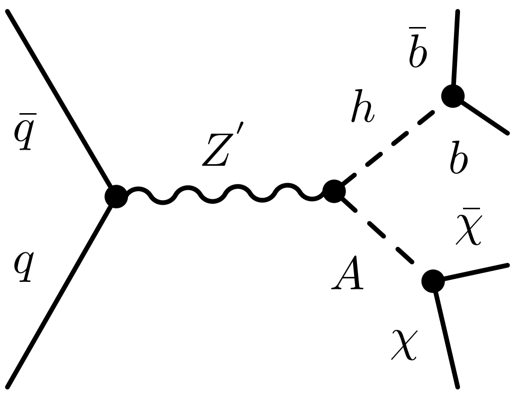

FIGURE S.2: The leading-order contribution of the production of DM and a Higgs boson through a new Z' mediator coupled to a pseudo-scalar Higgs boson A, where the latter decays primarily to a pair of Dark Matter particles ()$\chi\bar{\chi}$). Figure taken from Ref. [130].

An interesting choice is to use the Higgs boson itself, which mostly decays to a pair of b-quarks, as a proxy and look for the so-called mono-H($b\bar{b}$) events. The two b-quarks in the final state recombine with other elementary particles to generate *hadrons*. We can identify the presence of the b-quark by reconstructing the corresponding spray of particles (*jet*) that has been produced. The higher the amount of $E_{\mathrm{T}}^{\mathrm{miss}}$ from the Dark Matter particles, the higher the energy available to the Higgs boson, thus the topology of the event can be very different. In order to enhance the sensitivity of the analysis, two regimes are therefore distinguished: the resolved case (low/medium $E_{\mathrm{T}}^{\mathrm{miss}}$) and the merged (or *boosted*) case (high $E_{\mathrm{T}}^{\mathrm{miss}}$). In the former case, the two b-quarks originating from the decay of the Higgs boson give rise to two separate jets, while in the latter case the angular separation between the two quarks becomes so small that it is more convenient to reconstruct the Higgs boson as a single jet with a larger radius (R).

The expected signal is therefore characterised by the presence of two separate small-R jets or a single large-R jet, and a certain amount of $E_{\mathrm{T}}^{\mathrm{miss}}$ coming from Dark Matter particles. The selected jets are required to exhibit an inner structure consistent with the fragmentation of two b-quarks. It is possible to produce such final state in several beyond Standard Model theories, like the Z'-2HDM model. In this scenario, the Higgs boson is produced by a new vector boson particle, Z', together with an additional pseudo-scalar Higgs boson, A, which is assumed to decay primarily to a pair of Dark Matter particles. A Feynman diagram showing the production mechanism of Dark Matter together with a Standard Model Higgs boson, in the Z'-2HDM scenario, is shown in Figure S.2.

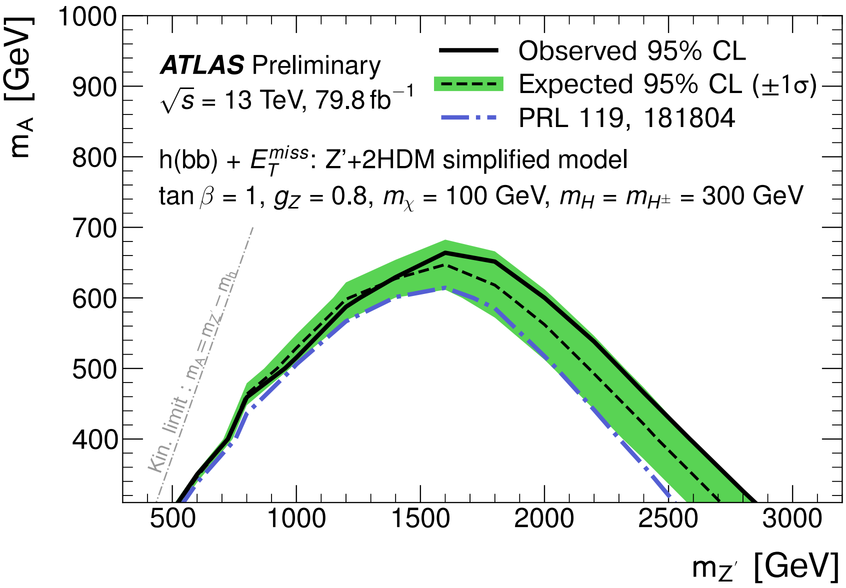

FIGURE S.3: Exclusion contours for the Z'-2HDM scenario in the ($m_{Z'}$,m_A) plane for $\tan\beta = 1$, $g_Z = 0.8$, and $m_\chi = 100$ GeV. Observed limits from previous results at $\sqrt{s} = 13$ TeV and 36.1 fb^{-1} of integrated luminosity (see Ref. [129]) are also shown (dash-dotted line). Figure taken from Ref [130].

A key ingredient in this kind of exotic searches is the ability of identifying the *flavour* of the Higgs boson's decay products. Although the $H \rightarrow b\bar{b}$ is the most probable decay channel, its signature may be very similar to the one of other uninteresting events that are predicted by the Standard Model. It is therefore crucial to employ a powerful reconstruction technique that allows us to distinguish heavy flavour quarks, like b-quarks, from lighter flavour quarks. Such classification exploits several interesting quantities that can be measured by the ATLAS detector, like the distance of the tracks inside the jet with respect to the actual interaction point, as well as the presence of a secondary vertex in the event. This procedure, commonly called b-tagging, can be very challenging in case of a very energetic jet as the resulting decay products tend to be very close to each other. In such a dense environment, dedicated new techniques must be employed. In the case of the mono-H($b\bar{b}$) search, applying b-tagging on Variable-R track jets in the *boosted* regime represented the solution to this problem. The main feature of the Variable-R technique consists in adjusting the size of the jet under study depending on its energy, instead of employing a fixed radius parameter. In this way, we reduce the possibility for the two sub-jets inside the Higgs boson to overlap and have their flavour misidentified. Thanks to this new b-tagging technique, the sensitivity of the mono-H($b\bar{b}$) analysis improved by up to a factor of 3 in the very high $E_{\mathrm{T}}^{\mathrm{miss}}$ regime, and it has been possible to exclude a significant region of the parameter space of the Z'-2HDM model, as shown in Figure S.3.

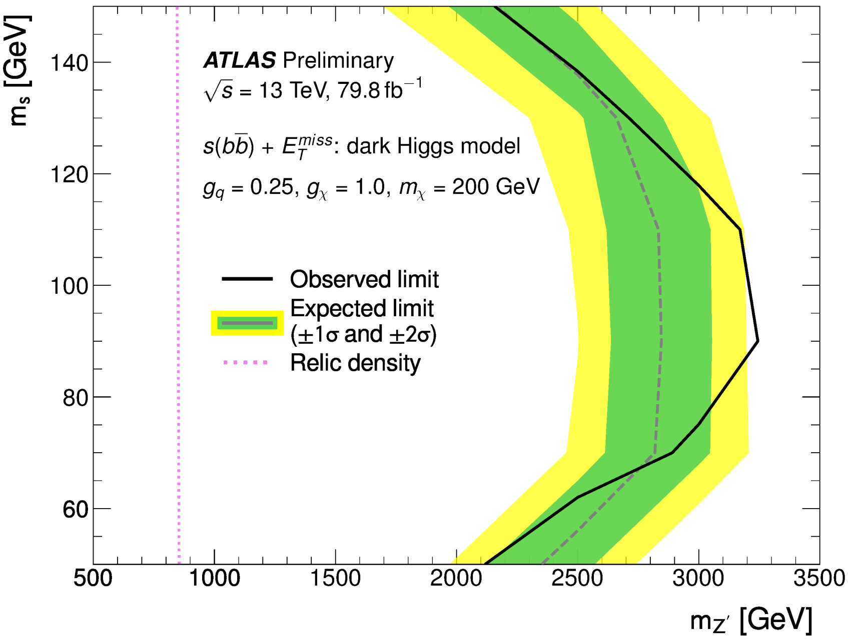

FIGURE S.4: Exclusion contour for the dark Higgs model with parameters m_χ = 200 GeV, g_q = 0.25, g_χ = 1.0 in the ($m_{Z'}$,m_A) plane. The pink dotted curve corresponds to the set of points for which the expected relic density is consistent with the PLANCK measurement [22]. The region on the right of the curve corresponds to a predicted relic abundance which is higher, hence not consistent, with this measurement. Figures taken from Ref. [171].

There are several other beyond Standard Model processes with a signature similar to the one of the mono-H($b\bar{b}$) search, thus it seems very limiting to probe the existence of just one new physics model. It is much more interesting to interpret the observed results in the context of a bunch of several different theory models. As a proof of concept of the fact that a proper analysis preservation can actually help us reach this goal, we have reinterpreted the mono-H($b\bar{b}$) analysis results in view of an alternative beyond Standard Model scenario that predicts the existence of a *dark* Higgs boson s, leading to the so-called mono-S($b\bar{b}$) final state. As shown in Figure S.4, the parameter space of the dark Higgs model probed in this study is largely excluded. However, a more accurate tuning of the theory parameters used in the simulation of the signal events might allow probing a more realistic scenario, consistent with the relic abundance measurements. As a new period of data taking of the LHC is approaching, being able to easily reinterpret the data observed by a single analysis represents a key aspect in the search for physics beyond the Standard Model. The increasing number of alternative theory models obliges experimental physicists to fully exploit the potential of their results.

Coming back to the first words of this summary, if we want to *win* this game, we should be able to look at *every* corner that is accessible at the probed energy scale and find *all* the hidden players. In this context, it is important to improve the reconstruction techniques currently adopted at the LHC while continuing to achieve critical Standard Model precision measurements. The analysis of the data collected during Run 2 of the LHC has already excluded a significant region of the theory parameter space... unfortunately without leaving any trace of new physics. This is the challenge that must be taken up during the upcoming Run 3 of the LHC, which might still be able to open the door to a whole new chapter of the particle physics history.

Samenvatting

Heb je ooit *verstoppertje* gespeeld?

Het is misschien wat ver gezocht, maar ik denk dat dit spelletje een beetje werkt als de zoektocht naar donkere materie bij de Large Hadron Collider (LHC). De zoeker kan het spel alleen winnen als *alle* verborgen spelers zijn gevonden. Het merendeel vinden is niet genoeg. Welnu, wanneer een proton-protonbotsing plaatsvindt bij de LHC, wordt er een groot aantal deeltjes geproduceerd en ze geven allemaal aanleiding tot een ander signaal in onze detectoren. Voor elk van deze deeltjes wordt een lijst met de relevante eigenschappen bijgehouden en gebruikt om de botsing te traceren waaruit ze daadwerkelijk afkomstig zijn. Pas nadat *alle zichtbare* deeltjes zijn herkend, kunnen we zien of er nog iets *ontbreekt*... of liever *onzichtbaar* is.

Het standaardmodel (SM) van de deeltjesfysica is de kwantumrelativistische theorie die drie van de vier interacties tussen de fundamentele componenten van materie kan verklaren. We weten dat atoomkernen kunnen bestaan vanwege de sterke kracht die quarks en gluonen opsluit in het proton. Bovendien stelde de kennis van de elektrozwakke kracht ons in staat de principes van het radioactieve verval en de interactie tussen verschillende families van quarks en leptonen te begrijpen. Het ontbrekende stukje van de theorie werd gevonden in 2012, toen het Higgsdeeltje werd ontdekt door de ATLAS- en CMS-experimenten bij de LHC. De ontdekking van het Higgsdeeltje is essentieel geweest in de erkenning van de robuustheid van het SM dat anders niet had kunnen verklaren hoe fundamentele deeltjes hun massa verkrijgen. De lijst van de tot op heden bekende subatomaire componenten van materie, na opname van het Higgsdeeltje, wordt geïllustreerd in figuur S.1.

De ontdekking van zo'n speciaal deeltje als het Higgsdeeltje was inderdaad een geweldige prestatie, maar het kan nog steeds teleurstellend zijn om te beseffen dat alles wat we kunnen verklaren binnen het raamwerk van het standaardmodel slechts zo'n 5% van het hele universum omvat!

In feite negeren we nog steeds de aard van de overige 95% van de wereld om ons heen. We weten alleen dat meer dan 80% van de materie in het heelal gemaakt moet zijn van donkere materie, zoals afgeleid uit astrofysische en kosmologische waarnemingen. Het is *donker* omdat het geen interacties lijkt te hebben met gewone materie, waardoor het ook niet waarneembaar is met onze huidige instrumenten. Desalniettemin blijkt dergelijke informatie erg kostbaar: als verondersteld wordt dat donkere materie zeer zwakke interacties heeft met gewone materie, betekent dit dat als we donkere materie zouden kunnen produceren met de LHC, we een onbalans zouden moeten waarnemen in de energie gemeten door de detector. Bij de LHC de

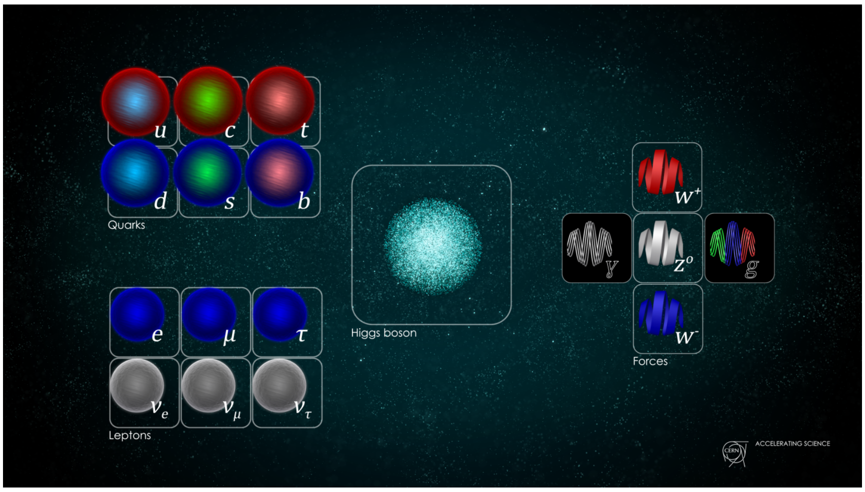

FIGURE S.1: Schema van alle elementaire deeltjes voorspeld door het standaardmodel van elementaire deeltjes. Figuur overgenomen uit Ref. [183].

inkomende protonen langs de bundellijn lopen, is de impuls in het transversale vlak in de begintoestand nul... en deze blijft nul omdat de totale energie behouden moet worden. Als de meting anders aangeeft, moeten er deeltjes ontsnappen aan detectie (zoals neutrino's).

De negatieve som van de momenta in het transversale vlak van de detector over alle deeltjes wordt *ontbrekende transversale impuls* genoemd en meestal geschreven als $E_{\mathrm{T}}^{\mathrm{miss}}$. De zoektocht naar donkere materie aan de LHC volgt de strategie van het zoeken naar botsingswaarnemingen met een grote hoeveelheid $E_{\mathrm{T}}^{\mathrm{miss}}$ die niet gerelateerd kunnen worden aan een standaardmodeldeeltje. Natuurlijk, als er alleen donkere materie geproduceerd wordt bij een botsing, zouden we niets zien: de aanwezigheid van een extra *meetbaar* object X stelt ons in staat om een interessante waarneming te selecteren. Dit is wat we gewoonlijk een $E_{\mathrm{T}}^{\mathrm{miss}}$ plus X- signatuur noemen.

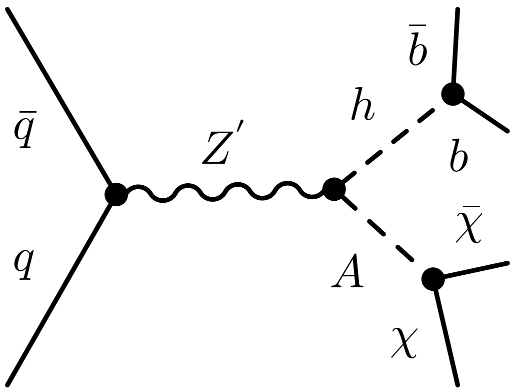

FIGURE S.2: De laagste-orde bijdrage aan de productie van donkere materie en een Higgs- deeltje door een nieuwe Z'-mediator gekoppeld aan een pseudo-scalair Higgs-deeltje A, waarbij dit laatstgenoemde deeltje voornamelijk vervalt tot een paar donkere materiedeeltjes ($\chi\bar{\chi}$). Figuur overgenomen uit Ref. [130].

Een interessante keuze is om het Higgs deeltje, dat meestal vervalt tot een paar b- quarks, als proxy te gebruiken en te zoeken naar de zogenaamde mono-H($b\bar{b}$)-waarnemingen. De twee uitgaande b-quarks combineren ieder met andere elementaire deeltjes om *hadronen* te genereren. We kunnen de aanwezigheid van een b-quark identificeren door de corresponderende spray van deeltjes die geproduceerd wordt (*jet*) te reconstrueren. Hoe hoger de hoeveelheid $E_{\mathrm{T}}^{\mathrm{miss}}$ van de donkere materie- deeltjes, des te hoger is de beschikbare energie die geassocieerd is met het Higgsdeeltje. De topologie van de botsingswaarnemingen kan dus heel verschillend zijn. Om de sensitiviteit van de analyse te vergroten, wordt er daarom onderscheid gemaakt tussen twee typen waarnemingen: gevallen binnen het scheidend vermogen (laag / gemiddeld $E_{\mathrm{T}}^{\mathrm{miss}}$) en de versmolten (of *boosted*) gevallen (hoge $E_{\mathrm{T}}^{\mathrm{miss}}$). In het eerste geval leiden de twee b-quarks die afkomstig zijn van het verval van het Higgsdeeltje tot twee afzonderlijke jets, terwijl in het tweede geval de hoekscheiding tussen de twee quarks zo klein wordt dat het handiger is om het Higgsdeeltje te reconstrueren als een enkele jet met een grotere straal (R).

Het verwachte signaal wordt daarom gekenmerkt door de aanwezigheid van twee afzonderlijke kleine-R jets of een enkele grote-R jet en een bepaalde hoeveelheid $E_{\mathrm{T}}^{\mathrm{miss}}$ afkomstig van donkere materie-deeltjes. De geselecteerde jets moeten een innerlijke structuur vertonen die consistent is met de fragmentatie van twee b-quarks. Het is mogelijk om een dergelijke eindtoestand te produceren in verschillende hypothetische uitbreidingen van het standaardmodel, zoals het Z'-2HDM-model. In dit scenario wordt het Higgsdeeltje geproduceerd door een nieuw vectorboson, Z', samen met een nieuw pseudo-scalair Higgsdeeltje, A, waarvan wordt aangenomen dat het primair vervalt naar een paar donkere materie-deeltjes. Een Feynman-diagram dat het productiemechanisme van donkere materie samen met een standaardmodel Higgsboson toont, in het Z'-2HDM-scenario, staat afgebeeld in figuur S.2.

Een belangrijk ingrediënt in dit soort exotische zoektochten is het vermogen om de *smaak* van de vervalproducten van het Higgsboson te identificeren. Hoewel de $H \to b\bar{b}$ het meest waarschijnlijke vervalkanaal is, kan de signatuur erg lijken op die van andere oninteressante waarnemingen die worden voorspeld door het standaardmodel. Het is daarom cruciaal om een krachtige reconstructietechniek toe te passen waarmee we zware smaak kunnen onderscheiden quarks, zoals b-quarks, van quarks met een lichtere smaak. Een dergelijke classificatie maakt gebruik van verschillende interessante grootheden die door de ATLAS- detector kunnen worden gemeten, zoals de afstand van de deeltjessporen binnen een jet ten opzichte van het werkelijke interactiepunt, evenals de aanwezigheid van een secundaire vertex in het botsingsevent. Deze procedure, gewoonlijk b-tagging genoemd, kan zeer uitdagend zijn in het geval van een zeer energetische jet, aangezien de resulterende vervalproducten de neiging hebben zeer dicht bij elkaar te liggen. In een dergelijke dichte omgeving moeten speciale nieuwe technieken worden gebruikt. In het geval van de mono-H($b\bar{b}$)-zoektocht was het toepassen van b-tagging op Variable-R track jets voor de *boosted* gevallen de oplossing voor dit probleem. Het belangrijkste kenmerk van de Variable-R-techniek is het aanpassen van de grootte van de onderzochte jet aan de hand van zijn energie, in plaats van een vaste straalparameter te gebruiken. Op deze manier verkleinen we de mogelijkheid dat de twee subjets afkomstig het Higgsdeeltje elkaar overlappen en dat hun smaak verkeerd wordt geïdentificeerd. Dankzij deze nieuwe b-tagging-techniek verbeterde de gevoeligheid van de mono-H($b\bar{b}$) analyse met een factor drie in het zeer hoge $E_{\mathrm{T}}^{\mathrm{miss}}$- regime, en was het mogelijk om een

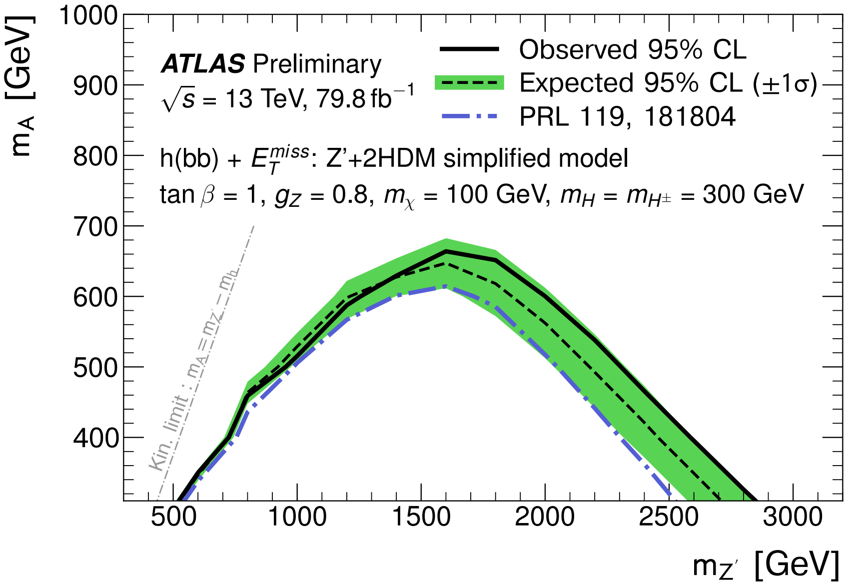

FIGURE S.3: Uitsluitingscontouren voor het Z'-2HDM-scenario in het $(m_{Z'}, m_A)$-vlak voor $\tan\beta = 1$, $g_Z = 0.8$ en $m_\chi = 100$ GeV. Waargenomen limieten van eerdere resultaten bij $\sqrt{s} = 13$ TeV en 36.1 fb^{-1} aan geïntegreerde luminositeit (zie Ref. [129]) zijn ook getoond (stippellijn). Figuur overgenomen uit [130].

significant gebied van de parameterruimte van het Z'-2HDM-model uit te sluiten, zoals weergegeven in figuur S.3.

Er zijn andere hypothetische uitbreidingen van het standaardmodel met een signatuur die lijkt op die van de mono-H($b\bar{b}$)-zoektocht, dus het lijkt erg beperkend om het bestaan van slechts èèn nieuw natuurkundemodel te onderzoeken. Het is veel interessanter om de waargenomen resultaten te interpreteren in de context van een aantal verschillende theoretische modellen. Als proof-of-concept van het feit dat een goede bewaring van de analyse ons daadwerkelijk kan helpen dit doel te bereiken, hebben we de mono-H($b\bar{b}$)- analyseresultaten opnieuw geïnterpreteerd aan de hand van een alternatieve hypothetische uitbreidingen van het standaardmodel met het bestaan van een *donker* Higgsdeeltje s dat leidt tot de zogenaamde mono-S($b\bar{b}$) eindtoestand. Zoals weergegeven in figuur S.4, is de parameterruimte van het donkere Higgsmodel dat in dit onderzoek is onderzocht grotendeels uitgesloten. Een nauwkeurigere afstemming van de theorieparameters die worden gebruikt bij de simulatie van het signaal kan het mogelijk maken om een realistischer scenario te onderzoeken, consistent met de metingen van de relikwie-overvloed (relic abundance). Nu een nieuwe periode van dataverzameling bij de LHC in aantocht is, vormt het gemakkelijk kunnen herinterpreteren van de gegevens van een enkele analyse, een belangrijk aspect in de zoektocht naar natuurkunde buiten het standaardmodel. Het toenemende aantal alternatieve theoretische modellen verplicht experimentele natuurkundigen om het potentieel van hun resultaten volledig te benutten.

Terugkomend op de eerste woorden van deze samenvatting, als we dit spel willen *winnen*, moeten we in staat zijn om in *elke* hoek die toegankelijk is met de huidige energieschaal te kijken en *alle* verborgen spelers te vinden. In deze context is het belangrijk om de reconstructietechnieken die momenteel bij de LHC worden gebruikt te

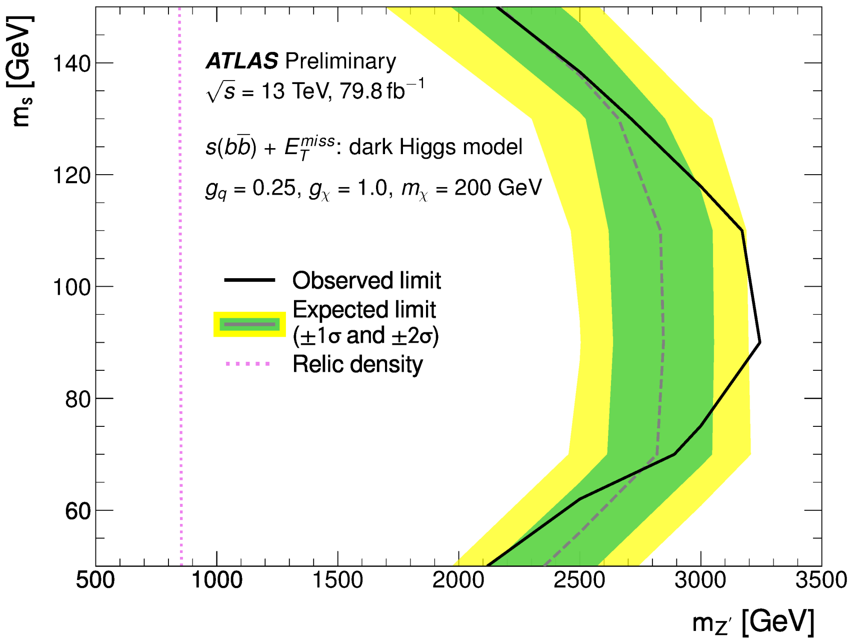

FIGURE S.4: Uitsluitingscontour voor het donkere Higgs-model met parameters m_χ = 200 GeV, g_q = 0.25, g_χ = 1.0 in het ($m_{Z'}$, m_A)-vlak. De roze gestippelde curve komt overeen met de set punten waarvoor de verwachte relikwiedichtheid (relic density) consistent is met de PLANCK-meting [22]. Het gebied aan de rechterkant van de curve komt overeen met een voorspelde relikwie-overvloed (relic abundance) die hoger en dus niet consistent is met deze meting. Cijfers overgenomen uit Ref. [171].

verbeteren, terwijl de kritische standaardmodel-precisiemetingen worden voortgezet. De analyse van de data verzameld tijdens Run 2 van de LHC heeft al een aanzienlijk deel van de theorieparameterruimte uitgesloten... helaas zonder enig spoor van nieuwe fysica achter te laten. Dit is de uitdaging die moet worden aangegaan tijdens de komende Run 3 van de LHC, die misschien nog steeds de deur kan openen naar een heel nieuw hoofdstuk in de geschiedenis van de deeltjesfysica.

List of Figures

List of Tables

Acronyms

2HDM Two Higgs Doublet Model.

ALICE A Large Ion Collider Experiment.

ATLAS A Toroidal LHC ApparatuS.

BBN Big Bang Nucleosynthesis.

BCM Beam Conditions Monitor.

BDT Boosted Decision Tree.

BIB Beam Induced Background.

BR Branching Ratio.

BSM Beyond Standard Model.

CB Combined muon.

CDM Cold Dark Matter.

CERN Conseil Européen pour la Recherche Nucléaire.

CHAMPs Charged Massive Particles.

CI Continuous Integration.

CKM Cabibbo-Kobayashi-Maskawa.

CL Confidence Level.

CMB Cosmic Microwave Background.

CMS Compact Muon Solenoid.

CR Control Region.

CSCs Cathode Strip Chambers.

CT Calorimeter-Tagged muon.

CTP Central Trigger Processor.

DE Dark Energy.

DGLAP Dokshitzer-Gribov-Lipatov-Altarelli-Parisi.

DM Dark Matter.

DNN Deep Neutral Network.

DxAOD Derived Analysis Object Data.

ECAL Electromagnetic Calorimeter.

EFT Effective Field Theory.

EMB Barrel Electromagnetic Calorimeter.

EMEC End-Cap Electromagnetic Calorimeter.

EVNT Event Generator Output.

FCal Forward Calorimeter.

fJVT Forward-JVT.

FR Fixed-Radius.

FSR Final State Radiation.

GA Ghost Association.

GRLs Good Run Lists.

GSC Global Sequential Calibration.

HCAL Hadronic Calorimeter.

HDM Hot Dark Matter.

HEC End-Cap Hadronic Calorimeter.

HF Heavy Flavour.

HLT High Level Trigger.

IBL Insertable B-Layer.

ID Inner Detector.

IP Impact Parameter.

IRC Infrared and Collinear.

ISR Initial State Radiation.

JER Jet Energy Resolution.

JES Jet Energy Scale.

JVF Jet Vertex Fraction.

JVT Jet Vertex Tagger.

L1 First Level Trigger.

L1Calo L1 calorimeter trigger.

L1Muon L1 muon trigger.

L1Topo L1 topological trigger.

LAr Liquid Argon.

LCW Local Calibration Weighting.

LEP Large Electron Positron collider.

LHC Large Hadron Collider.

LHCb LHC beauty.

LLR Log-Likelihood Ratio.

LO Leading Order.

LSP Lightest Supersymmetric Particle.

LUCID LUminosity Cherenkov Integrating Detector.

MC Monte Carlo.

MDTs Monitored Drift Tubes.

MOND MOdified Newtonian Dynamics.

MS Muon Spectrometer.

MVA Multivariate.

NLO Next-to-Leading Order.

NNLO Next-to-Next-to-Leading Order.

NP Nuisance Parameter.

PDF Parton Density Function.

PMNS Pontecorvo-Maki-Nakagawa-Sakata.

POI Parameter Of Interest.

PS Proton Synchrotron.

PSB Proton Synchrotron Booster.

PV Primary Vertex.

QCD Quantum ChromoDynamics.

QED Quantum ElectroDynamics.

RECAST Request Efficiency Computation for Alternative Signal Theories.

RMS Root Mean Squared.

RNN Recurrent Neural Networks.

ROS Read-Out System.

RPCs Resistive Place Chambers.

RS Randall–Sundrum.

SA Standalone muon.

SCT Semi-Conductor Tracker.

SD Spin Dependent.

SFs Scale Factors.

SI Spin Independent.

SiA SiliconAssociatedForward muon.

SM Standard Model.

SMT Soft Muon Tagger.

SPS Super Proton Synchrotron.

SR Signal Region.

ST Segmented-Tagged muon.

SUSY SUperSYmmetry.

SV Secondary Vertex.

TDAQ Trigger and Data Acquisition.

TGCs Thin Gap Chambers.

TileCal Tile Calorimeter.

TLA Trigger-object Level Analysis.

TRT Transition Radiation Tracker.

TST Track-based Soft Term.

UE Underlying Events.

UED Universal Extra-Dimensions.

vdM van der Meer.

VEV Vacuum Expectation Value.

VR Variable-Radius.

WDM Warm Dark Matter.

WIMP Weakly Interactive Massive Particle.

WP Working Point.

xAOD Analysis Object Data.

Bibliography

[1] C.-N. Yang and R. L. Mills, *Conservation of Isotopic Spin and Isotopic Gauge Invariance*, Phys. Rev. **96** (1954) 191.

[2] S. L. Glashow, *Partial Symmetries of Weak Interactions*, Nucl. Phys. **22** (1961) 579.

[3] S. Weinberg, *A Model of Leptons*, Phys. Rev. Lett. **19** (1967) 1264.

[4] A. Salam, *Weak and Electromagnetic Interactions*, Conf. Proc. **C680519** (1968) 367.

[5] PARTICLE DATA GROUP collaboration, *Review of Particle Physics*, Phys. Rev. **D98** (2018) 030001.

[6] BELLE collaboration, *Observation of a resonance-like structure in the $\pi^{\pm}\psi'$ mass distribution in exclusive $B \to K\pi^{\pm}\psi'$ decays*, Phys. Rev. Lett. **100** (2008) 142001 [0708.1790].

[7] LHCB collaboration, *Observation of the resonant character of the $Z(4430)^{-}$ state*, Phys. Rev. Lett. **112** (2014) 222002 [1404.1903].

[8] LHCB collaboration, *Observation of $J/\psi p$ Resonances Consistent with Pentaquark States in $\Lambda_b^0 \to J/\psi K^- p$ Decays*, Phys. Rev. Lett. **115** (2015) 072001 [1507.03414].

[9] D. J. Gross and F. Wilczek, *Ultraviolet Behavior of Nonabelian Gauge Theories*, Phys. Rev. Lett. **30** (1973) 1343.

[10] H. D. Politzer, *Reliable Perturbative Results for Strong Interactions?*, Phys. Rev. Lett. **30** (1973) 1346.

[11] F. Englert and R. Brout, *Broken symmetry and the mass of gauge vector mesons*, Phys. Rev. Lett. **13** (1964) 321.

[12] P. W. Higgs, *Broken symmetries and the masses of gauge bosons*, Phys. Rev. Lett. **13** (1964) 508.

[13] P. Higgs, *Broken symmetries, massless particles and gauge fields*, Physics Letters **12** (1964) 132 .

[14] G. S. Guralnik, C. R. Hagen and T. W. B. Kibble, *Global conservation laws and massless particles*, Phys. Rev. Lett. **13** (1964) 585.

[15] J. Ellis, *Higgs Physics*, in *Proceedings, 2013 European School of High-Energy Physics (ESHEP 2013): Paradfurdo, Hungary, June 5-18, 2013*, pp. 117–168, 2015, 1312.5672, DOI.

[16] ATLAS collaboration, *Observation of a new particle in the search for the Standard Model Higgs boson with the ATLAS detector at the LHC*, *Phys. Lett.* **B716** (2012) 1 [1207.7214].

[17] CMS collaboration, *Observation of a new boson at a mass of 125 GeV with the CMS experiment at the LHC*, *Phys. Lett.* **B716** (2012) 30 [1207.7235].

[18] T. Kajita, *Nobel Lecture: Discovery of atmospheric neutrino oscillations*, *Rev. Mod. Phys.* **88** (2016) 030501.

[19] A. B. McDonald, *Nobel Lecture: The Sudbury Neutrino Observatory: Observation of flavor change for solar neutrinos*, *Rev. Mod. Phys.* **88** (2016) 030502.

[20] J. W. Cronin, CP *symmetry violation: The search for its origin*, *Science* **212** (1981) 1221.

[21] V. L. Fitch, *The discovery of charge conjugation—parity asymmetry*, *Science* **212** (1981) 989 [https://science.sciencemag.org/content/212/4498/989.full.pdf].

[22] PLANCK collaboration, *Planck 2018 results. VI. Cosmological parameters*, 1807.06209.

[23] F. Zwicky, *Die Rotverschiebung von extragalaktischen Nebeln*, *Helv. Phys. Acta* **6** (1933) 110.

[24] V. C. Rubin and W. K. Ford, Jr., *Rotation of the Andromeda Nebula from a Spectroscopic Survey of Emission Regions*, *Astrophys. J.* **159** (1970) 379.

[25] M. Milgrom, *A Modification of the Newtonian dynamics as a possible alternative to the hidden mass hypothesis*, *Astrophys. J.* **270** (1983) 365.

[26] R. H. Sanders, *The published extended rotation curves of spiral galaxies: confrontation with modified dynamics*, *Astrophys. J.* **473** (1996) 117 [astro-ph/9606089].

[27] H. Dahle, *A compilation of weak gravitational lensing studies of clusters of galaxies*, astro-ph/0701598.

[28] M. Markevitch, *Chandra observation of the most interesting cluster in the Universe*, astro-ph/0511345.

[29] NASA, "NASA Finds Direct Proof of Dark Matter." http://chandra.harvard.edu/.

[30] D. Clowe, M. Bradac, A. H. Gonzalez, M. Markevitch, S. W. Randall, C. Jones et al., *A direct empirical proof of the existence of dark matter*, *Astrophys. J.* **648** (2006) L109 [astro-ph/0608407].

[31] G. Bertone, D. Hooper and J. Silk, *Particle Dark Matter: Evidence, candidates and constraints*, *Phys. Rept.* **405** (2005) 279 [hep-ph/0404175].

[32] G. B. Gelmini, *The Hunt for Dark Matter*, in *Proceedings, Theoretical Advanced Study Institute in Elementary Particle Physics: Journeys Through the Precision Frontier: Amplitudes for Colliders (TASI 2014): Boulder, Colorado, June 2-27, 2014*, pp. 559–616, 2015, 1502.01320, DOI.

[33] J. Rich and G. Smoot, *Fundamentals of cosmology*, *Physics Today* **55** (2002) 64.

[34] G. Gelmini and P. Gondolo, *DM Production Mechanisms*, 1009.3690.

[35] G. Gamow, *The origin of elements and the separation of galaxies*, *Phys. Rev.* **74** (1948) 505.

[36] R. A. Alpher and R. C. Herman, *On the relative abundance of the elements*, *Phys. Rev.* **74** (1948) 1737.

[37] G. Gamow, *The Evolution of the Universe*, *Nature* **162** (1948) 680.

[38] PLANCK collaboration, *Planck 2018 results. I. Overview and the cosmological legacy of Planck*, 1807.06205.

[39] K. Griest and D. Seckel, *Three exceptions in the calculation of relic abundances*, *Phys. Rev. D* **43** (1991) 3191.

[40] D. Feldman, Z. Liu and P. Nath, *The Stueckelberg Z' Extension with Kinetic Mixing and Milli-Charged Dark Matter From the Hidden Sector*, *Phys. Rev.* **D75** (2007) 115001 [hep-ph/0702123].

[41] D. M. Jacobs, G. D. Starkman and B. W. Lynn, *Macro Dark Matter*, *Mon. Not. Roy. Astron. Soc.* **450** (2015) 3418 [1410.2236].

[42] L. Chuzhoy and E. W. Kolb, *Reopening the window on charged dark matter*, *JCAP* **0907** (2009) 014 [0809.0436].

[43] J. D. Simon and M. Geha, *The Kinematics of the Ultra-Faint Milky Way Satellites: Solving the Missing Satellite Problem*, *Astrophys. J.* **670** (2007) 313 [0706.0516].

[44] J. R. Primack, *The Nature of Dark Matter*, *Frascati Phys. Ser.* **24** (2002) 449 [astro-ph/0112255].

[45] R. D. Peccei and H. R. Quinn, *CP Conservation in the Presence of Instantons*, *Phys. Rev. Lett.* **38** (1977) 1440.

[46] S. Dodelson and L. M. Widrow, *Sterile neutrinos as Dark Matter*, *Phys. Rev. Lett.* **72** (1994) 17 [hep-ph/9303287].

[47] E. W. Kolb, D. J. H. Chung and A. Riotto, *WIMPzillas!*, *AIP Conf. Proc.* **484** (1999) 91 [hep-ph/9810361].

[48] R. Bernabei et al., *Dark Matter particles in the Galactic halo: Results and implications from DAMA/NaI*, *Int. J. Mod. Phys.* **D13** (2004) 2127 [astro-ph/0501412].

[49] R. Bernabei et al., *Final model independent result of DAMA/LIBRA-phase1*, *Eur. Phys. J.* **C73** (2013) 2648 [1308.5109].

[50] G. Adhikari et al., *An experiment to search for Dark Matter interactions using sodium iodide detectors*, *Nature* **564** (2018) 83 [1906.01791].

[51] COSINE-100 collaboration, *Search for a Dark Matter-induced annual modulation signal in NaI(Tl) with the COSINE-100 experiment*, 1903.10098.

[52] XENON collaboration, *Observation of two-neutrino double electron capture in ^{124}Xe with XENON1T*, *Nature* **568** (2019) 532 [1904.11002].

[53] Particle Data Group collaboration, *Review of particle physics*, *Phys. Rev. D* **98** (2018) 030001.

[54] Fermi-LAT collaboration, *The Fermi Galactic Center GeV Excess and Implications for Dark Matter*, *Astrophys. J.* **840** (2017) 43 [1704.03910].

[55] Super-Kamiokande collaboration, *Atmospheric Neutrino Oscillation Analysis With Improved Event Reconstruction in Super-Kamiokande IV*, *PTEP* **2019** (2019) 053F01 [1901.03230].

[56] PAMELA collaboration, *Cosmic-Ray Positron Energy Spectrum Measured by PAMELA*, *Phys. Rev. Lett.* **111** (2013) 081102 [1308.0133].

[57] L. Feng, R.-Z. Yang, H.-N. He, T.-K. Dong, Y.-Z. Fan and J. Chang, *AMS-02 positron excess: new bounds on dark matter models and hint for primary electron spectrum hardening*, *Phys. Lett.* **B728** (2014) 250 [1303.0530].

[58] ATLAS collaboration, *Constraints on mediator-based dark matter and scalar dark energy models using $\sqrt{s} = 13$ TeV pp collision data collected by the ATLAS detector*, *JHEP* **05** (2019) 142 [1903.01400].

[59] G. Busoni et al., *Recommendations on presenting LHC searches for missing transverse energy signals using simplified s-channel models of dark matter*, 1603.04156.

[60] L. Evans and P. Bryant, *LHC Machine*, *JINST* **3** (2008) S08001.

[61] LEP Working Group for Higgs boson searches, ALEPH, DELPHI, L3, OPAL collaboration, *Search for the standard model Higgs boson at LEP*, *Phys. Lett.* **B565** (2003) 61 [hep-ex/0306033].

[62] E. Mobs, *The CERN accelerator complex - August 2018. Complexe des accélérateurs du CERN - Août 2018*, Aug, 2018, https://cds.cern.ch/record/2636343.

[63] S. D. Ellis, J. Huston, K. Hatakeyama, P. Loch and M. Tonnesmann, *Jets in hadron-hadron collisions*, *Prog. Part. Nucl. Phys.* **60** (2008) 484 [0712.2447].

[64] G. Altarelli and G. Parisi, *Asymptotic Freedom in Parton Language*, *Nucl. Phys.* **B126** (1977) 298.

[65] J. M. Campbell, J. W. Huston and W. J. Stirling, *Hard Interactions of Quarks and Gluons: A Primer for LHC Physics*, *Rept. Prog. Phys.* **70** (2007) 89 [hep-ph/0611148].

[66] NNPDF collaboration, *Parton distributions from high-precision collider data*, *Eur. Phys. J.* **C77** (2017) 663 [1706.00428].

[67] M. Benedikt, P. Collier, V. Mertens, J. Poole and K. Schindl, *LHC Design Report. 3. The LHC injector chain*, 2004. DOI.

[68] T. S. Pettersson and P. Lefèvre, *The Large Hadron Collider: Conceptual design*, 1995, https://cds.cern.ch/record/291782.

[69] The ATLAS Collaboration, *LuminosityPublicResultsRun2*, 2019, https://twiki.cern.ch/twiki/bin/view/AtlasPublic/LuminosityPublicResultsRun2.

[70] ATLAS collaboration, *The ATLAS Experiment at the CERN Large Hadron Collider*, *JINST* **3** (2008) S08003.

[71] CMS collaboration, *The CMS Experiment at the CERN LHC*, *JINST* **3** (2008) S08004.

[72] LHCb collaboration, *The LHCb Detector at the LHC*, *JINST* **3** (2008) S08005.

[73] ALICE collaboration, *The ALICE experiment at the CERN LHC*, *JINST* **3** (2008) S08002.

[74] M. Schott and M. Dunford, *Review of single vector boson production in pp collisions at $\sqrt{s} = 7$ TeV*, *Eur. Phys. J.* **C74** (2014) 2916 [1405.1160].

[75] ATLAS collaboration, *ATLAS magnet system: Technical Design Report, 1*, Technical Design Report ATLAS. CERN, Geneva, 1997, https://cds.cern.ch/record/338080.

[76] ATLAS collaboration, *Track Reconstruction Performance of the ATLAS Inner Detector at $\sqrt{s} = 13$ TeV*, Technical Design Report ATLAS. CERN, Geneva, Jul, 2015, https://cds.cern.ch/record/2037683.

[77] M. Capeans, G. Darbo, K. Einsweiler, M. Elsing, T. Flick, M. Garcia-Sciveres et al., *ATLAS Insertable B-Layer Technical Design Report*, 2010, https://cds.cern.ch/record/1291633.

[78] ATLAS collaboration, *ATLAS tile calorimeter: Technical design report*, 1996, https://cds.cern.ch/record/331062.

[79] ATLAS collaboration, *Improved luminosity determination in pp collisions at $\sqrt{s} = 7$ TeV using the ATLAS detector at the LHC*, *Eur. Phys. J.* **C73** (2013) 2518 [1302.4393].

[80] ATLAS collaboration, *Luminosity Determination in pp Collisions at $\sqrt{s} = 7$ TeV Using the ATLAS Detector at the LHC*, *Eur. Phys. J.* **C71** (2011) 1630 [1101.2185].

[81] ATLAS collaboration, *Luminosity determination in pp collisions at $\sqrt{s} = 8$ TeV using the ATLAS detector at the LHC*, *Eur. Phys. J.* **C76** (2016) 653 [1608.03953].

[82] ATLAS/LUCID collaboration, *The new ATLAS/LUCID detector*, in *Proceedings, 4th International Conference on Advancements in Nuclear Instrumentation Measurement Methods and their Applications (ANIMMA 2015): Lisbon, Portugal, April 20-24, 2015*, p. 7465502, 2015, DOI.

[83] S. van der Meer, *Calibration of the Effective Beam Height in the ISR*, 1968, http://cdsweb.cern.ch/record/296752/.

[84] ATLAS collaboration, *ATLAS first level trigger: Technical design report*, 1998, https://cds.cern.ch/record/381429.

[85] ATLAS collaboration, *ATLAS high-level trigger, data acquisition and controls: Technical design report*, 2003, https://cds.cern.ch/record/616089.

[86] ATLAS collaboration, *Performance of the ATLAS Trigger System in 2015*, *Eur. Phys. J.* **C77** (2017) 317 [1611.09661].

[87] R. Frühwirth, *Application of Kalman filtering to track and vertex fitting*, *Nuclear Instruments and Methods in Physics Research Section A: Accelerators, Spectrometers, Detectors and Associated Equipment* **262** (1987) 444 .

[88] T. G. Cornelissen, N. Van Eldik, M. Elsing, W. Liebig, E. Moyse, N. Piacquadio et al., *Updates of the ATLAS Tracking Event Data Model (Release 13)*, Tech. Rep. ATL-SOFT-PUB-2007-003. ATL-COM-SOFT-2007-008, CERN, Geneva, Jun, 2007, https://cds.cern.ch/record/1038095.

[89] ATLAS collaboration, *Reconstruction of primary vertices at the ATLAS experiment in Run 1 proton–proton collisions at the LHC*, *Eur. Phys. J.* **C77** (2017) 332 [1611.10235].

[90] ATLAS collaboration, *Impact Parameter resolutions in di-jet events*, September, 2018, https://atlas.web.cern.ch/Atlas/GROUPS/PHYSICS/PLOTS/IDTR-2018-008/.

[91] W. Lampl, S. Laplace, D. Lelas, P. Loch, H. Ma, S. Menke et al., *Calorimeter clustering algorithms: Description and performance*, 2008, https://cds.cern.ch/record/1099735.

[92] *Monte Carlo Calibration and Combination of In-situ Measurements of Jet Energy Scale, Jet Energy Resolution and Jet Mass in ATLAS*, Tech. Rep. ATLAS-CONF-2015-037, CERN, Geneva, Aug, 2015, http://cds.cern.ch/record/2044941.

[93] ATLAS collaboration, *Performance of jet substructure techniques for large-R jets in proton-proton collisions at $\sqrt{s}$ = 7 TeV using the ATLAS detector*, *JHEP* **09** (2013) 076 [1306.4945].

[94] ATLAS collaboration, *Jet energy measurement with the ATLAS detector in proton-proton collisions at $\sqrt{s} = 7$ TeV*, *Eur. Phys. J.* **C73** (2013) 2304 [1112.6426].

[95] M. Cacciari, G. P. Salam and G. Soyez, *The anti-k_t jet clustering algorithm*, *JHEP* **04** (2008) 063 [0802.1189].

[96] G. P. Salam, *Towards Jetography*, *Eur. Phys. J.* **C67** (2010) 637 [0906.1833].

[97] ATLAS collaboration, *Jet energy scale and uncertainties in 2015-2017 data and simulation*, November, 2018, https://atlas.web.cern.ch/Atlas/GROUPS/PHYSICS/PLOTS/JETM-2018-006/.

[98] ATLAS collaboration, *Jet energy resolution in 2017 data and simulation*, September, 2018, https://atlas.web.cern.ch/Atlas/GROUPS/PHYSICS/PLOTS/JETM-2018-005/.

[99] *Tagging and suppression of pileup jets with the ATLAS detector*, Tech. Rep. ATLAS-CONF-2014-018, CERN, Geneva, May, 2014, https://cds.cern.ch/record/1700870.

[100] *Selection of jets produced in 13TeV proton-proton collisions with the ATLAS detector*, Tech. Rep. ATLAS-CONF-2015-029, CERN, Geneva, Jul, 2015, https://cds.cern.ch/record/2037702.

[101] J. Gonski, *Jet Cleaning in 2016 and the Event Level Cleaning Tool*, Tech. Rep. ATL-COM-PHYS-2017-982, CERN, Geneva, Jun, 2017, https://cds.cern.ch/record/2272136.

[102] J. M. Butterworth, A. R. Davison, M. Rubin and G. P. Salam, *Jet substructure as a new Higgs search channel at the LHC*, *Phys. Rev. Lett.* **100** (2008) 242001 [0802.2470].

[103] D. Krohn, J. Thaler and L.-T. Wang, *Jet Trimming*, *JHEP* **02** (2010) 084 [0912.1342].

[104] ATLAS collaboration, *Performance of jet substructure techniques for large-R jets in proton-proton collisions at $\sqrt{s}$ = 7 TeV using the ATLAS detector*, *JHEP* **09** (2013) 076 [1306.4945].

[105] ATLAS collaboration, *Jet mass reconstruction with the ATLAS Detector in early Run 2 data*, 2016, https://cds.cern.ch/record/2200211.

[106] ATLAS collaboration, *In situ large-R jet energy scale calibration and uncertainties in 2015-2017 data*, July, 2019, https://atlas.web.cern.ch/Atlas/GROUPS/PHYSICS/PLOTS/JETM-2019-05/.

[107] M. Cacciari, G. P. Salam and G. Soyez, *The Catchment Area of Jets*, *JHEP* **04** (2008) 005 [0802.1188].

[108] ATLAS collaboration, *Optimisation and performance studies of the ATLAS b-tagging algorithms for the 2017-18 LHC run*, Tech. Rep. ATL-PHYS-PUB-2017-013, CERN, Geneva, Jul, 2017, https://cds.cern.ch/record/2273281.

[109] ATLAS collaboration, *Secondary vertex finding for jet flavour identification with the ATLAS detector*, Tech. Rep. ATL-PHYS-PUB-2017-011, CERN, Geneva, Jun, 2017, https://cds.cern.ch/record/2270366.

[110] ATLAS collaboration, *Topological b-hadron decay reconstruction and identification of b-jets with the JetFitter package in the ATLAS experiment at the LHC*, Tech. Rep. ATL-PHYS-PUB-2018-025, CERN, Geneva, Oct, 2018, https://cds.cern.ch/record/2645405.

[111] ATLAS collaboration, *Identification of Jets Containing b-Hadrons with Recurrent Neural Networks at the ATLAS Experiment*, Tech. Rep. ATL-PHYS-PUB-2017-003, CERN, Geneva, Mar, 2017, https://cds.cern.ch/record/2255226.

[112] ATLAS collaboration, *ATLAS b-jet identification performance and efficiency measurement with $t\bar{t}$ events in pp collisions at $\sqrt{s} = 13$ TeV*, 1907.05120.

[113] ATLAS collaboration, *Calibration of light-flavour jet b-tagging rates on ATLAS proton-proton collision data at* $\sqrt{s} = 13$ *TeV*, 2018, https://cds.cern.ch/record/2314418.

[114] ATLAS collaboration, *Measurement of b-tagging Efficiency of c-jets in* $t\bar{t}$ *Events Using a Likelihood Approach with the ATLAS Detector*, 2018, https://cds.cern.ch/record/2306649.

[115] ATLAS collaboration, *Measurements of b-jet tagging efficiency with the ATLAS detector using* $t\bar{t}$ *events at* $\sqrt{s} = 13$ *TeV*, *JHEP* **08** (2018) 089 [1805.01845].

[116] ATLAS collaboration, *ATLAS Flavour-Tagging Calibration Results with 80.5* fb^{-1}, March, 2019, http://atlas.web.cern.ch/Atlas/GROUPS/PHYSICS/PLOTS/FTAG-2019-003/.

[117] ATLAS collaboration, *Electron and photon performance measurements with the ATLAS detector using the 2015-2017 LHC proton-proton collision data*, 1908.00005.

[118] ATLAS collaboration, *Muon identification and reconstruction efficiencies in full run-2 dataset*, August, 2019, https://atlas.web.cern.ch/Atlas/GROUPS/PHYSICS/PLOTS/MUON-2019-03/.

[119] ATLAS collaboration, *Muon reconstruction performance of the ATLAS detector in proton–proton collision data at* $\sqrt{s}$ *=13 TeV*, *Eur. Phys. J.* **C76** (2016) 292 [1603.05598].

[120] ATLAS collaboration, *Measurement of the tau lepton reconstruction and identification performance in the ATLAS experiment using pp collisions at* $\sqrt{s} = 13\ TeV$, Tech. Rep. ATLAS-CONF-2017-029, CERN, Geneva, May, 2017, http://cds.cern.ch/record/2261772.

[121] ATLAS collaboration, *Identification and energy calibration of hadronically decaying tau leptons with the ATLAS experiment in pp collisions at* $\sqrt{s}$*=8 TeV*, *Eur. Phys. J.* **C75** (2015) 303 [1412.7086].

[122] ATLAS collaboration, *Performance of missing transverse momentum reconstruction with the ATLAS detector using proton-proton collisions at* $\sqrt{s} =$ *13 TeV*, *Eur. Phys. J.* **C78** (2018) 903 [1802.08168].

[123] *Forward Jet Vertex Tagging: A new technique for the identification and rejection of forward pileup jets*, Tech. Rep. ATL-PHYS-PUB-2015-034, CERN, Geneva, Aug, 2015, https://cds.cern.ch/record/2042098.

[124] ATLAS collaboration, E_T^{miss} *performance in the ATLAS detector using 2015-2016 LHC p-p collisions*, Tech. Rep. ATLAS-CONF-2018-023, CERN, Geneva, Jun, 2018, https://cds.cern.ch/record/2625233.

[125] ATLAS collaboration, *Jet reconstruction and performance using particle flow with the ATLAS Detector*, *Eur. Phys. J.* **C77** (2017) 466 [1703.10485].

[126] ATLAS collaboration, *Missing transverse momentum performance using the full run 2 pp data at 13 TeV*, February, 2019, https://atlas.web.cern.ch/Atlas/GROUPS/PHYSICS/PLOTS/JETM-2019-03/.

[127] ATLAS collaboration, *Object-based missing transverse momentum significance in the ATLAS detector*, Tech. Rep. ATLAS-CONF-2018-038, CERN, Geneva, Jul, 2018, http://cds.cern.ch/record/2630948.

[128] ATLAS collaboration, *Measurement of the Inelastic Proton-Proton Cross Section at $\sqrt{s} = 13$ TeV with the ATLAS Detector at the LHC*, *Phys. Rev. Lett.* **117** (2016) 182002 [1606.02625].

[129] ATLAS collaboration, *Search for Dark Matter Produced in Association with a Higgs Boson Decaying to $b\bar{b}$ using 36 fb^{-1} of pp collisions at $\sqrt{s} = 13$ TeV with the ATLAS Detector*, *Phys. Rev. Lett.* **119** (2017) 181804 [1707.01302].

[130] ATLAS collaboration, *Search for Dark Matter Produced in Association with a Higgs Boson decaying to $b\bar{b}$ at $\sqrt{s} = 13$ TeV with the ATLAS Detector using 79.8 fb^{-1} of proton-proton collision data*, Tech. Rep. ATLAS-CONF-2018-039, CERN, Geneva, Jul, 2018, https://atlas.web.cern.ch/Atlas/GROUPS/PHYSICS/CONFNOTES/ATLAS-CONF-2018-039/.

[131] W. Verkerke and D. P. Kirkby, *The RooFit toolkit for data modeling*, *eConf* **C0303241** (2003) MOLT007 [physics/0306116].

[132] L. Moneta, K. Belasco, K. S. Cranmer, S. Kreiss, A. Lazzaro, D. Piparo et al., *The RooStats Project*, *PoS* **ACAT2010** (2010) 057 [1009.1003].

[133] S. Hoeche, F. Krauss, S. Schumann and F. Siegert, *QCD matrix elements and truncated showers*, *JHEP* **05** (2009) 053 [0903.1219].

[134] T. Gleisberg, S. Hoeche, F. Krauss, M. Schonherr, S. Schumann, F. Siegert et al., *Event generation with SHERPA 1.1*, *JHEP* **02** (2009) 007 [0811.4622].

[135] NNPDF collaboration, *Parton distributions for the LHC Run II*, *JHEP* **04** (2015) 040 [1410.8849].

[136] S. Hoeche, F. Krauss, M. Schonherr and F. Siegert, *QCD matrix elements + parton showers: The NLO case*, *JHEP* **04** (2013) 027 [1207.5030].

[137] S. Frixione, P. Nason and C. Oleari, *Matching NLO QCD computations with Parton Shower simulations: the POWHEG method*, *JHEP* **11** (2007) 070 [0709.2092].

[138] T. Sjostrand, S. Mrenna and P. Z. Skands, *A Brief Introduction to PYTHIA 8.1*, *Comput. Phys. Commun.* **178** (2008) 852 [0710.3820].

[139] *ATLAS Run 1 Pythia8 tunes*, Tech. Rep. ATL-PHYS-PUB-2014-021, CERN, Geneva, Nov, 2014, https://cds.cern.ch/record/1966419.

[140] J. Alwall, R. Frederix, S. Frixione, V. Hirschi, F. Maltoni, O. Mattelaer et al., *The automated computation of tree-level and next-to-leading order differential cross sections, and their matching to parton shower simulations*, *JHEP* **07** (2014) 079 [1405.0301].

[141] S. Agostinelli et al., *Geant4 - a simulation toolkit*, *Nuclear Instruments and Methods in Physics Research Section A: Accelerators, Spectrometers, Detectors and Associated Equipment* **506** (2003) 250 .

[142] ATLAS collaboration, *The ATLAS Simulation Infrastructure*, *Eur. Phys. J.* **C70** (2010) 823 [1005.4568].

[143] ATLAS collaboration, *Characterisation and mitigation of beam-induced backgrounds observed in the ATLAS detector during the 2011 proton-proton run*, *JINST* **8** (2013) P07004 [1303.0223].

[144] ATLAS collaboration, *Search for dark matter produced in association with a Higgs boson decaying to two bottom quarks in pp collisions at $\sqrt{s} = 8$ TeV with the ATLAS detector*, *Phys. Rev.* **D93** (2016) 072007 [1510.06218].

[145] ATLAS collaboration, *Search for dark matter in association with a Higgs boson decaying to b-quarks in pp collisions at $\sqrt{s} = 13$ TeV with the ATLAS detector*, *Phys. Lett.* **B765** (2017) 11 [1609.04572].

[146] D. Krohn, J. Thaler and L.-T. Wang, *Jets with Variable R*, *JHEP* **06** (2009) 059 [0903.0392].

[147] ATLAS collaboration, *Variable Radius, Exclusive-k_T, and Center-of-Mass Subjet Reconstruction for Higgs($\rightarrow b\bar{b}$) Tagging in ATLAS*, Tech. Rep. ATL-PHYS-PUB-2017-010, CERN, Geneva, Jun, 2017, https://cds.cern.ch/record/2268678.

[148] G. Cowan, K. Cranmer, E. Gross and O. Vitells, *Asymptotic formulae for likelihood-based tests of new physics*, *Eur. Phys. J.* **C71** (2011) 1554 [1007.1727].

[149] S. S. Wilks, *The Large-Sample Distribution of the Likelihood Ratio for Testing Composite Hypotheses*, *Annals Math. Statist.* **9** (1938) 60.

[150] A. L. Read, *Modified frequentist analysis of search results (the CL_s method)*, 2000. DOI.

[151] ATLAS collaboration, *Evidence for the $H \rightarrow b\bar{b}$ decay with the ATLAS detector*, *JHEP* **12** (2017) 024 [1708.03299].

[152] ATLAS collaboration, *Search for dark matter in association with a Higgs boson decaying to b-quarks in pp collisions at $\sqrt{s} = 13$ TeV with the ATLAS detector*, *Phys. Lett.* **B765** (2017) 11 [1609.04572].

[153] R. J. Barlow and C. Beeston, *Fitting using finite Monte Carlo samples*, *Comput. Phys. Commun.* **77** (1993) 219.

[154] *10th International Workshop on Boosted Object Phenomenology, Reconstruction and Searches in HEP*, 2018, https://cds.cern.ch/record/2624674.

[155] J. Catmore, J. Cranshaw, T. Gillam, E. Gramstad, P. Laycock, N. Ozturk et al., *A new petabyte-scale data derivation framework for ATLAS*, *Journal of Physics: Conference Series* **664** (2015) 072007.

[156] J. Butterworth et al., *PDF4LHC recommendations for LHC Run II*, *J. Phys.* **G43** (2016) 023001 [1510.03865].

[157] A. D. Martin, W. J. Stirling, R. S. Thorne and G. Watt, *Parton distributions for the LHC*, *Eur. Phys. J.* **C63** (2009) 189 [0901.0002].

[158] J. Pumplin, D. R. Stump, J. Huston, H. L. Lai, P. M. Nadolsky and W. K. Tung, *New generation of parton distributions with uncertainties from global QCD analysis*, *JHEP* **07** (2002) 012 [hep-ph/0201195].

[159] NNPDF collaboration, *A Determination of parton distributions with faithful uncertainty estimation*, *Nucl. Phys.* **B809** (2009) 1 [0808.1231].

[160] *Herwig 7.0/Herwig++ 3.0 release note*, *The European Physical Journal C* **76** (2016) .

[161] ATLAS collaboration, *Studies on top-quark Monte Carlo modelling for Top2016*, Tech. Rep. ATL-PHYS-PUB-2016-020, CERN, Geneva, Sep, 2016, https://cds.cern.ch/record/2216168.

[162] ATLAS collaboration, *Measurements of b-jet tagging efficiency with the ATLAS detector using $t\bar{t}$ events at $\sqrt{s} = 13$ TeV*, *JHEP* **08** (2018) 089 [1805.01845].

[163] K. Pearson, *X. On the criterion that a given system of deviations from the probable in the case of a correlated system of variables is such that it can be reasonably supposed to have arisen from random sampling*, *The London, Edinburgh, and Dublin Philosophical Magazine and Journal of Science* **50** (1900) 157 [https://doi.org/10.1080/14786440009463897].

[164] M. Cacciari and G. P. Salam, *Pileup subtraction using jet areas*, *Phys. Lett.* **B659** (2008) 119 [0707.1378].

[165] K. Cranmer and I. Yavin, *RECAST: Extending the Impact of Existing Analyses*, *JHEP* **04** (2011) 038 [1010.2506].

[166] M. Duerr, A. Grohsjean, F. Kahlhoefer, B. Penning, K. Schmidt-Hoberg and C. Schwanenberger, *Hunting the dark Higgs*, *JHEP* **04** (2017) 143 [1701.08780].

[167] D. Merkel, *Docker: Lightweight Linux containers for consistent development and deployment*, *Linux J.* **2014** (2014) .

[168] D. Bernstein, *Containers and cloud: From lxc to docker to kubernetes*, *IEEE Cloud Computing* **1** (2014) 81.

[169] J. Hethey, *GitLab Repository Management*. Packt Publishing, 2013, https://books.google.ch/books?id=tUYiAgAAQBAJ.

[170] K. Cranmer and L. Heinrich, *Yadage and Packtivity - analysis preservation using parametrized workflows*, *J. Phys. Conf. Ser.* **898** (2017) 102019 [1706.01878].

[171] ATLAS collaboration, *RECAST framework reinterpretation of an ATLAS Dark Matter Search constraining a model of a dark Higgs boson decaying to two b-quarks*, Tech. Rep. ATL-PHYS-PUB-2019-032, CERN, Geneva, Aug, 2019, https://cds.cern.ch/record/2686290.

[172] S. Ohmer and H. H. Patel, *Leptobaryons as Majorana Dark Matter*, *Phys. Rev.* **D92** (2015) 055020 [1506.00954].

[173] M. Duerr and P. Fileviez Pérez, *Theory for baryon number and dark matter at the LHC*, *Phys. Rev. D* **91** (2015) 095001.

[174] M. Duerr and P. Fileviez Perez, *Baryonic Dark Matter*, *Phys. Lett.* **B732** (2014) 101 [1309.3970].

[175] J.-Y. Liu, Y. Tang and Y.-L. Wu, *Searching for Z' Gauge Boson in an Anomaly-Free $U(1)'$ Gauge Family Model*, *J. Phys.* **G39** (2012) 055003 [1108.5012].

[176] L. Lonnblad, *Correcting the color dipole cascade model with fixed order matrix elements*, *JHEP* **05** (2002) 046 [hep-ph/0112284].

[177] L. Lonnblad and S. Prestel, *Matching Tree-Level Matrix Elements with Interleaved Showers*, *JHEP* **03** (2012) 019 [1109.4829].

[178] G. Busoni et al., *Recommendations on presenting LHC searches for missing transverse energy signals using simplified s-channel models of dark matter*, 1603.04156.

[179] *6th Dark Matter @ LHC 2019 workshop*, 2019, https://cds.cern.ch/record/2684364.

[180] S. Ipek, D. McKeen and A. E. Nelson, *A Renormalizable Model for the Galactic Center Gamma Ray Excess from Dark Matter Annihilation*, *Phys. Rev.* **D90** (2014) 055021 [1404.3716].

[181] M. Bauer, U. Haisch and F. Kahlhoefer, *Simplified dark matter models with two Higgs doublets: I. Pseudoscalar mediators*, *JHEP* **05** (2017) 138 [1701.07427].

[182] LHC Dark Matter Working Group collaboration, *LHC Dark Matter Working Group: Next-generation spin-0 dark matter models*, *Phys. Dark Univ.* (2018) 100351 [1810.09420].

[183] *Le modèle standard*, Tech. Rep. OPEN-PHO-CHART-2015-001, CERN, Geneva, Mar, 2015, https://cds.cern.ch/record/2002395.

Acknowledgements

If I look back at myself exactly four years ago, I bet I was sure this moment would have never arrived. But for some reasons, here I am: finally at the end of this thesis. During these last years, I learned a lot about science but probably even more about myself. There have been tough moments that I could overcome only thanks to the incredible people I am so lucky to have in my life. This page is dedicated to all of them, without whom I am sure this thesis would have never seen the light.

First of all, a huge thank to my supervisors, Frank and Nicolo, for the great opportunity you gave me offering me this position at Nikhef. You left me the freedom of choosing my own path but always kept an attentive eye on my research to be sure I did not get lost. Besides the scientific support, I have to thank you for your endless understanding regarding my frequent flights to Edinburgh. You understood that this part of my life was essential to me and you never put any obstacle. For this I will always be grateful to both of you. Last, but not least, thank you for carefully reviewing this manuscript (and in particular for teaching me the difference between "that" and "which"...).

I do not even know where to start thanking my family: my dad Alfredo, my mum Rosella and my sister Flavia. You are my safe place in the whole world. I could not be here without your continuous support and unconditional advice. Mum, dad: you have been always so close to me, helping out with anything I needed despite the long hours of travelling and the effort of moving *me* from one place to another, across countries. I think you will never learn the meaning of the word *distance* and that is why you are simply amazing. Flavia: your advice, always direct and sincere, has worked as a guide to me during these years. Please keep doing so also in the future, I will need it even more.

Thanks also to zio Fabrizio, who has always supported me with wonderful words since I started my bachelor degree course. *Grazie anche a nonna Stella, nonna Teresa, nonno Mario e anche Cuccetta, che non mi hai lasciato sola durante tutti questi anni.*

Thanks to my *brilliant friend* Stefania, from whom I always learn something new. Despite the distance and the unpredictability of both our lives, I never stopped feeling close to you and, after 17 years (!), you are still the person I need to talk to when I need to analyse the craziness of my life.

Thanks to my first flatmate ever, Odeta. You guided me since the very beginning of my complicated relationship with physics and your advice has always been so inspiring in all the moments where I had to take important decisions in my life. I hope one day I will be able to pay you back all the patience that you had since I was a dumb homesick bachelor student.

Thanks also to my *doc*, Marta, one of my biggest and craziest supporters. Every time I hear from you what you think about me I get a dose of positive energy that has been essential to survive during the last years. I missed a lot sharing the apartment with you but I hope life will bring us again very close to each other in the future.

Thanks also to my friends in Ascoli: Patrizia, Federica, Ilaria, Amanda. You supported me since the very beginning and I feel lucky to have you in my life because I know I can always count on you every time I need a sincere advice.

Thanks to Tonino and Susanna, for hosting me in Rome every time I needed. You always made me feel at home and your support, both practical and psychological, has been so precious to me during all these years.

Thanks also to Matteo, Chiara, Gianluca, Andrea and Rebecca, who became part of my life in the last years. The amazing time we have every time we meet again makes me feel even more convinced that we should come back to Rome. I hope this will happen very soon!

Thanks to all my colleagues at Nikhef and at the Radboud University for all the social activities and the nice moments that we shared together. I already know that I will miss them a lot! A special mention goes to the *Ragù* group (Fabrizia, Luca and Peppe), Jeroen, Lucrezia, Michele, Alice, Milo, Elena, Marc, Broos, Marko, Birgit, Federica, Anamika, Lucía, Polina, Daniil, Remco, Alex, Mart, Nadia.

I have to thank the person who, in the first place, motivated me in applying to a PhD position at Nikhef: Lucrezia. I still remember how nervous you were for my interview, probably even more than me. Although we did not end up living in the same apartment in Amsterdam, I am so happy that we shared three years of this experience together. Your advice during all these years has always been so precious: you helped me during the difficult moments and, at the same time, you were present every time I wanted to celebrate or party together. *Ti voglio bene accia!*

I would like to thank again Fabrizia and Jeroen for accepting to be my paranymphs. I chose you because during these four years you became a precious part of my life. Jeroen, thank you also for your patience in translating my summary in dutch. Thank you for being such very good friends. . . and last but not least, thanks for sharing with me and Gianluca the craziness of the *4daagse* period: it is one of the best memories I have of my dutch period.

I cannot hold from dedicating a special thank to Fabrizia, my guiding light of all these fours years. I have always considered myself so lucky to have found amazing people in all the places where I lived but I definitely could not imagine finding a friend like you in Nijmegen as well. We shared so much during these years that I feel we have known each other for a long time. You helped

me a lot in so many occasions, especially when I did not even know I needed help. Yes, I think you have a superpower. I will terribly miss our *girls' nights* but from the bottom of my heart I know that this is just the start of a very long friendship.

Thanks for all the help provided by the incredible secretaries of the HEP department at the Radboud University: Gemma, Gertie and Marjo. Your extremely prompt support has prevented me from living on a street at least for a couple of times and from dealing with terrible bureaucracy. A huge thank also to Ed, to whom I asked over these years so many favours and questions that were often beyond his responsibility.

While working in the ATLAS collaboration, I met so many people who inspired me in many different ways. First of all, I want to thank Sam Meehan who strived to bring out the best of me during these years. Your enthusiasm is a rare thing and you represent to me an exemplary model of how a physicist should behave. I hope we will meet again in the future and that we will not need to look for each other in *Pagine Bianche*. Within the mono-H($b\bar{b}$) group, I want to thank Philipp Gadow, Andrea Matic and Dilia Portillo Quintero, for all the knowledge and support that we shared during these years. I learned a lot from all of you and I wish you the best of luck for your future. I also want to thank Patrick Rieck, for believing in me from the start and for giving me important responsibilities during the CONF note analysis. Lastly, thanks to Giuliano Gustavino and Valerio Ippolito who never stopped mentoring (and making fun of) me since I was a master student in Rome. I really hope our paths will cross again in the future (*#entu*).

Thanks a lot also to the amazing people with whom I spent my secondment at CERN: Alessandra (*e le infinite chiacchierate alle 3 di notte*), Peter (*e le merende con le bomboniere*), Giulia and Grazia (*le mie due anime gemelle musicali, e non solo...*), Lorenzo (*Ascoliii*), Betto (*oooo*), Adele, Marco and Serena (*e la palestra? eh?*), Fefe (*So what?* ♪). You succeeded in an incredible mission: making life in Saint-Genis-Pouilly a lot of fun. You are amazing. I wish a bright future to all of you!

Living abroad can sometimes be very challenging. You can feel lonely not only because you are far away from your family and friends, but also because you can lose connection with the reality of your country. It is then essential to find something that makes you feel at home also when you are many kilometres away, even just for a moment. In my case this was possible thanks to Diego Bianchi and the whole *Propaganda Live* team. Every Friday night I feel a bit like I am living in Rome again and for a few hours you give me the right amount of *pace interiore* that I need.

Lastly, thanks Gianluca for your love, support and rationality. Living in two different countries during these years was not easy, but you made it simple because you believed in us and you brought my feet back on the ground every time sadness and nostalgia were overwhelming me. You are the reason why every single day of my life is simply amazing. I just cannot imagine my life without you and I really hope we will be as happy as we are now for the rest of our lives.